

m

Miscellanea

INGV

Agreement INGV-DPC 2012-2021
Volcanological Programme 2012-2015

**Project V3 – Multi-disciplinary analysis
of the relationships between
tectonic structures and volcanic activity
(Etna, Vulcano-Lipari system)**

Final Report
November 1st, 2014 – June 30th, 2015

29



Direttore Responsabile

Stefano GRESTA

Editorial Board

Luigi CUCCI - Editor in Chief (INGV - RM1)

Raffaele AZZARO (INGV-CT)

Mario CASTELLANO (INGV-NA)

Viviana CASTELLI (INGV-BO)

Rosa Anna CORSARO (INGV-CT)

Mauro DI VITO (INGV-NA)

Antonio GUARNIERI (INGV-BO)

Marcello LIOTTA (INGV-PA)

Mario MATTIA (INGV-CT)

Milena MORETTI (INGV-CNT)

Nicola PAGLIUCA (INGV-RM1)

Umberto SCIACCA (INGV-RM2)

Alessandro SETTIMI (INGV-RM2)

Salvatore STRAMONDO (INGV-CNT)

Andrea TERTULLIANI (INGV-RM1)

Aldo WINKLER (INGV-RM2)

Segreteria di Redazione

Francesca Di Stefano - Referente

Rossella Celi

Tel. +39 06 51860068

redazionecen@ingv.it

in collaborazione con:

Barbara Angioni (RM1)

REGISTRAZIONE AL TRIBUNALE DI ROMA N.178 | 2014, 23 LUGLIO

© 2014 INGV Istituto Nazionale di Geofisica e Vulcanologia

Sede legale: Via di Vigna Murata, 605 | Roma

m

Miscellanea

INGV

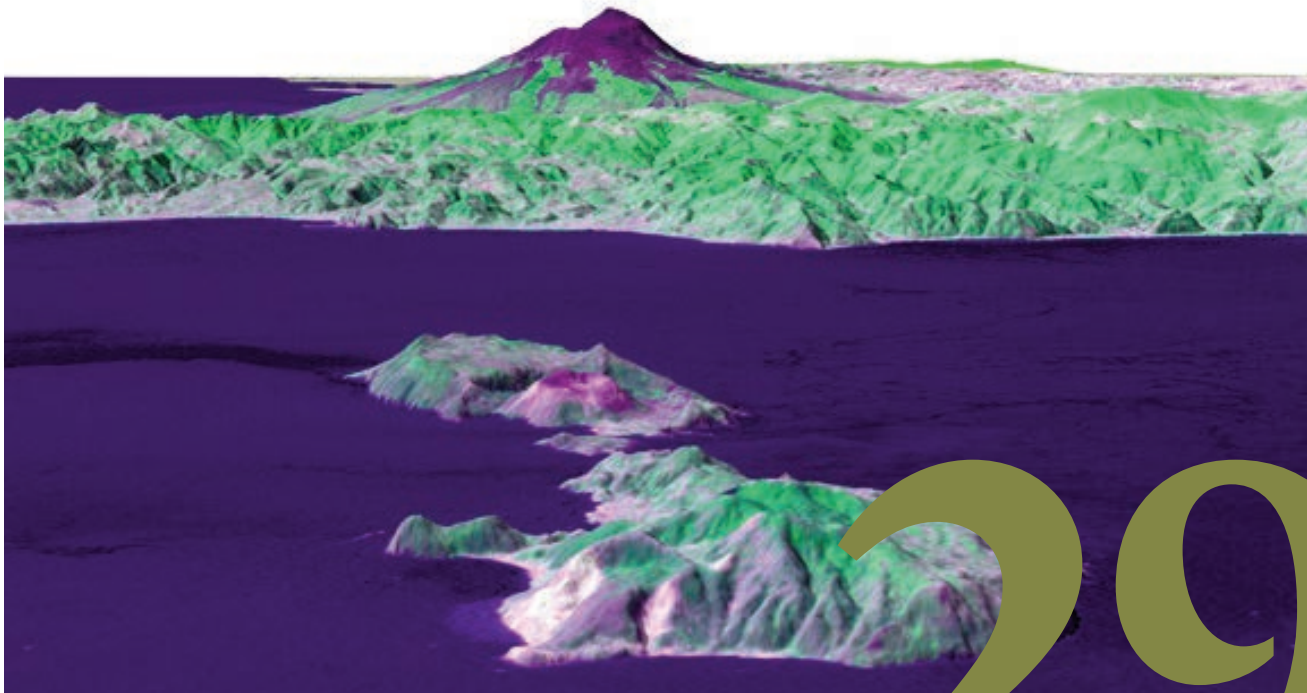
AGREEMENT INGV-DPC 2012-2021
VOLCANOLOGICAL PROGRAMME 2012-2015

**PROJECT V3 – MULTI-DISCIPLINARY ANALYSIS OF THE RELATIONSHIPS
BETWEEN TECTONIC STRUCTURES AND VOLCANIC ACTIVITY
(ETNA, VULCANO-LIPARI SYSTEM)**

Final Report

NOVEMBER 1ST, 2014 – JUNE 30TH, 2015

Editors Raffaele Azzaro, Rosanna De Rosa



29



Project Directors

Raffaele Azzaro, Istituto Nazionale di Geofisica e Vulcanologia - Osservatorio Etneo, Catania

Rosanna De Rosa, Dipartimento di Scienze della Terra, Università della Calabria, Cosenza

DPC Representative

Antonio Ricciardi, Dipartimento di Protezione Civile, Roma

Coordinator of the Volcanological Programme Committee

Francesca Bianco, Istituto Nazionale di Geofisica e Vulcanologia - Osservatorio Vesuviano, Napoli

Web site on the DPC-INGV Volcanological projects

<https://sites.google.com/a/ingv.it/volcpro2014/>

Immagine di frontespizio

Lipari, Vulcano, e l'Etna sullo sfondo, in una immagine 3D da satellite ricostruita da sensori termici, radiometrici e radar
(© ASTER and SRTM Teams, NASA's Jet Propulsion Laboratory, <http://visibleearth.nasa.gov/view.php?id=10388>)

Normazione ortoeditoriale, Revisione testi e Impaginazione

Rossella Celi Centro Editoriale Nazionale INGV
Francesca Di Stefano Centro Editoriale Nazionale INGV

Table of Contents

Riassunto esteso della seconda fase (annualità)	7
Section 1: Report on the project by Directors	11
1. Introduction	13
2. Task of the project	13
3. Scheme of activities	14
4. Deliverables	16
5. Highlight	16
6. Research Units, coordinators and activities	27
7. Management	28
8. Summary of the financial plan	28
Section 2: Scientific Reports of Research Units (RU)	31
RU 1, INGV-CT: R. Azzaro	33
RU 2, INGV-PA: C. Federico	61
RU 3, INGV-CNT: M. Anzidei	73
RU 4, INOGS-TS: A. Saraò	93
RU 5, UNI-CS: R. De Rosa	103
RU 6, UNI-CT: C. Ferlito	123
RU 7, UNI-RM: M. Marsella	153
ANNEX 1	157
ANNEX 2	165

Riassunto esteso della seconda fase (annualità)

Il PROGETTO V3 è focalizzato allo studio di due importanti aree vulcaniche attive presenti in Sicilia, l'Etna e il sistema Vulcano-Lipari. Scopo principale del progetto è quello di investigare le relazioni che intercorrono tra tettonica e dinamiche magmatico-eruttive, e sugli aspetti di pericolosità connessi. Le attività sviluppate nell'ambito del secondo anno rappresentano la continuazione di quanto fatto nel primo anno, con alcuni aggiustamenti operati in relazione alla rimodulazione di alcuni obiettivi legati essenzialmente alla conclusione anticipata di tutti i progetti Vulcanologici e Sismologici attivati nell'ambito della Convenzione C tra DPC e INGV, la cui durata è stata biennale (le ricerche erano state però pianificate su base triennale).

Anche nel secondo anno, il progetto è imperniato su 4 task secondo lo schema riportato in Fig. 1, le cui attività sono complessivamente articolate in 14 work-package (WP) a seconda dell'approccio metodologico e del tematismo affrontato (vedi Tab. 1). Come per il primo anno, sono state finanziate 7 Unità di Ricerca (3 INGV e 4 universitarie/altri enti di ricerca), impegnate su più temi e dal carattere fortemente multidisciplinare (Tabb. 2, 3, 4).

Il progetto ha beneficiato di importanti e concreti collegamenti con altri progetti DPC, in particolare S2 per la parte relativa al Task 1, e di dati di base provenienti da precedenti progetti/convenzioni tra DPC e vari enti di ricerca. In alcuni casi il raggiungimento degli obiettivi è stato possibile grazie a co-finanziamenti con altre iniziative in corso (vedi report delle UR nella Section 2).

Complessivamente il raggiungimento dei *deliverable* previsti alla fine del progetto può ritenersi molto soddisfacente, con una percentuale di completamento dei vari WP mediamente attestata al 100%. Le difficoltà di tipo tecnico-scientifico sono state occasionali e percentualmente limitate ad alcuni sotto-prodotti (evidenziati in rosso in Tab. 1).

Il problema principale che ha condizionato la gestione del progetto è quello di natura amministrativa, già riscontrato nel primo anno di attività. Le UR universitarie, in particolare, hanno sofferto il ritardo con cui le proprie amministrazioni hanno erogato le anticipazioni finanziarie, concesse solo dopo lunghi *iter* a partire dai contratti firmati dalla amministrazione INGV; in alcuni casi, le erogazioni sono state disponibili solo nei mesi di luglio-agosto 2014. Ciò ha reso molto difficile l'organizzazione delle missioni per i rilievi sul campo, e di fatto impedito anche il reclutamento del personale dedicato nei tempi previsti dal progetto (contratti e borse di studio).

Nel seguito vengono brevemente richiamati i principali risultati ottenuti dal progetto, suddivisi per task (a cura dei responsabili), evidenziando in particolare gli "highlights" più significativi. Per gli aspetti metodologici e i risultati di dettaglio delle attività svolte, si rimanda alle relazioni delle singole UR.

- **Task 1 - Valutazione probabilistica della pericolosità sismica nel versante orientale etneo, legata all'attivazione delle faglie locali** (L. Peruzza)

Le attività relative a questo task sono state condotte come pianificato, con una percentuale complessiva di raggiungimenti degli obiettivi del 100%. Da segnalare l'implementazione di nuove versioni dei software usati per il calcolo probabilistico della pericolosità sismica, sviluppati *ad-hoc* per le finalità del progetto. In particolare, il codice di calcolo FiSH, messo a punto nell'ambito del PROGETTO S2, include nuove relazioni di scala tra dimensione della sorgente (faglia) e magnitudo specifiche per i contesti vulcanici quali l'Etna.

Il software CRISIS è stato modificato grazie alla collaborazione con il team messicano di sviluppo (M. Ordaz e collaboratori), e adesso riesce a modellare superfici topografiche 3D complesse come quella etnea, calcolando in modo corretto le distanze sorgente-sito. Tale implementazione si è resa necessaria vista l'estrema variabilità del valore di PGA, anche su brevi distanze, calcolato dalla relazione di attenuazione a scala locale messa a punto per l'Etna. Una simile operazione è stata poi effettuata sulle *routines* del software OpenQuake, grazie all'assistenza tecnica del team di sviluppatori di GEM (M. Pagani e collaboratori) e all'impegno di una borsa di studio, parzialmente finanziata dal progetto V3 (R. Gee).

Sono infine state integrate nei calcoli le caratterizzazioni di risposta di sito, ottenute dalla UR 6, per una fascia del versante sud-orientale dell'Etna. Tale prodotto, in fase di verifica, rappresenta il primo esempio di mappa di hazard *site-specific*, di estensione areale sovracomunale.

- **Task 2 - Relazioni tra strutture tettoniche locali e sistema vulcanico all'Etna** (R. Azzaro)

Le attività previste in questo task, largamente basate su approcci multi-disciplinari sviluppati da differenti gruppi di lavoro/UR, presentano un avanzato grado di completamento, con un sostanziale raggiungimento degli obiettivi previsti. Tra le numerose attività, due sono le risultanze particolarmente

interessanti. In primo luogo, la significativa correlazione trovata nel versante orientale dell'Etna tra zone di faglia attive, distribuzione della sismicità, deformazioni crostali (dati GPS) e circolazione dei fluidi. Questa evidenza apre nuove prospettive nello studio dei processi di fagliazione all'Etna.

In tale settore del vulcano l'orizzonte sismogenetico di riferimento si attesta a profondità di 1-5 km, con i valori più elevati di rilascio sismico nell'area compresa tra la Valle del Bove e Zafferana, dove sono presenti strutture sismogenetiche ad andamento NE-SW la cui attivazione sembra essere particolarmente influenzata da fasi eruttive del vulcano. Il confronto tra i *moment-rate* sismologici, geodetici e geologici per la zona del sistema di faglie delle Timpe conferma che una larga parte della deformazione avviene asismicamente, come da tempo noto da osservazioni di terreno, e fornisce per la prima volta una stima analitica della componente di *creep*, utile per studiare il processo di caricamento di segmenti di faglia bloccati (sismogenetici). Inoltre, è stato verificato come variazioni nello *strain* geodetico legate ad attività vulcanica o sismica, si accompagnino a significativi cambiamenti nella circolazione e nelle caratteristiche chimico-fisiche delle acque di falda. Questa evidenza dimostra il ruolo importante giocato dai fluidi, ed in particolare della pressione di poro, come peraltro dimostrato dai meccanismi focali da tensore momento ottenuti per la faglia Pernicana.

Come secondo punto si evidenzia il contributo dato dai rilievi aeromagnetici e dai profili sismici condotti in mare, alla conoscenza dell'assetto strutturale del basamento sedimentario. L'anomalia magnetica identificata in Val Calanna ha consentito di dettagliare la porzione superiore del vecchio sistema di alimentazione etneo, fortemente alterato, che ha un diametro di circa 5 km; il modello ottenuto è consistente con quelli di altre metodologie geofisiche (gravimetria, magnetotellurica e tomografia sismica). Nell'*off-shore* etneo il dato magnetico evidenzia un settore caratterizzato da piccoli corpi vulcanici superficiali allineati lungo la dorsale di Riposto. Più a sud, al largo di Acireale, i profili sismici hanno consentito di riconoscere due strutture estensionali attive, che rappresentano la continuazione in mare delle faglie di Acireale e S. Tecla. Tra Acitrezza e Catania, le strutture identificate sono invece compressive, probabilmente riconducibili al fronte attivo a *thrust* della Catena Appenninico-Maghebide (estensione della Anticlinale di Catania in mare).

- **Task 3 - Relazioni tra strutture tettoniche regionali e il sistema magmatico Vulcano-Lipari** (R. De Rosa)

Come il precedente, anche questo task è caratterizzato da un approccio multi-disciplinare che coinvolge diversi gruppi di lavoro/UR. Le attività svolte hanno consentito di raggiungere i risultati prefissati con un completamento del task al 100%. Due sono i principali punti focali emersi. Il primo è il tasso significativo di deformazione crostale che interessa il settore meridionale dell'Arcipelago Eoliano, e in particolare il complesso Lipari-Vulcano, situato all'estremità settentrionale della linea tettonica "Tindari-Letojanni". Dati storici e strumentali hanno permesso di evidenziare processi locali estremi come la subsidenza nell'area urbana di Lipari, che presenterà un impatto di protezione civile rilevante nei prossimi decenni. Mappe predittive all'anno 2100 mostrano un innalzamento del livello del mare di 2.2 m, con invasione delle aree abitate prospicienti la costa.

Il secondo punto è l'evidenza di un unico sistema di alimentazione per l'attività magmatica storica di Lipari e Vulcano, come confermato dalle analisi chimiche e mineralogiche sui prodotti delle eruzioni storiche delle due isole, e l'attivazione sin-eruttiva delle strutture N-S che interessano i centri eruttivi più giovani di 20 ka nel settore orientale del sistema Lipari-Vulcano, possibile sede dell'attività magmatica futura. I dati raccolti suggeriscono un modello strutturale in cui da un regime tensionale dominato da movimenti di strike-slip lungo la trascorrente "Tindari-Letojanni", l'intrusione di magma dal basso induce una rotazione del σ_1 da orizzontale a verticale generando un regime estensionale con faglie dirette orientate NS. La modellazione della estesa serie storica (1974-2013) di dati sismologici e di deformazione del suolo, suggerisce la presenza di una sorgente magmatica in deflazione localizzata sotto Vulcanello, a circa 4 km di profondità.

I fluidi magmatici che attualmente alimentano il campo fumarolico di Vulcano hanno dei valori di $^3\text{He}/^4\text{He}$ molto simili ai prodotti latitici della "lava del Roveto" di Vulcanello, e confermano l'ipotesi della presenza di un *reservoir* latitico sotto Vulcanello come attuale sorgente dei gas emessi. Questo *reservoir* superficiale è periodicamente alimentato da fluidi profondi provenienti da un *reservoir* sottostante, caratterizzato da alto $^3\text{He}/^4\text{He}$. Lo studio geochimico ed isotopico dei prodotti latitici delle eruzioni storiche di Lipari e Vulcano, e l'analisi delle inclusioni magmatiche avvalorano la presenza di una sorgente magmatica profonda comune di composizione shoshonitica a 20 km di profondità, che

alimenta camere magmatiche più superficiali, 3-5 km di profondità fino a 1 km, nelle quali il magma differenzia in latite e poi in riolite.

- **Task 4 - Pericolosità legata a fenomeni di instabilità gravitativa di versante a Vulcano e Lipari** (M. Marsella)

L'attività del task ha riguardato l'approfondimento di alcuni aspetti utili alla comprensione dei meccanismi di dissesto dei fianchi del cono della Fossa a Vulcano, ed alla valutazione del loro stato attuale. Uno studio dedicato al riconoscimento e alla mappatura delle aree instabili è stato condotto sull'isola di Lipari, a completamento dell'analisi svolta nel primo anno. A partire dalle conoscenze acquisite, sono state sviluppate tre linee di ricerca relative alla valutazione delle variazioni topografiche legate alla presenza di movimenti di versante e alla definizione di carte di suscettività al dissesto (Sp1), alla mappatura delle aree interessate da attività idrotermale (Sp2) ed alla sperimentazione di metodi innovativi per il monitoraggio di frane attive (Sp3).

Le analisi e i rilievi condotti nel corso del secondo anno hanno permesso di ottenere i seguenti risultati: a) la formazione di un database cartografico che include cartografia raster e numerica, mappe di velocità SAR e carte tematiche (litologia e attività idrotermale); b) l'estrazione e la validazione di una carta di suscettività al dissesto basata sull'analisi automatica di dati morfometrici e classificazioni derivate da dati Lidar; c) la definizione di una procedura utile alla valutazione della stabilità di settori del cono potenzialmente instabili e la sua applicazione al settore nord-est della Fossa (Punte Nere); d) la raccolta di elementi utili alla valutazione di potenziali distacchi (circolazione di fluidi idrotermali, alterazione delle rocce, batimetria di dettaglio, ecc.); e) la verifica della funzionalità del sistema GB-SAR in associazione alla mappature termica in continuo, da utilizzare in caso di riattivazione di fenomeni di dissesto della Forgia Vecchia.

I risultati forniscono un quadro di dettaglio e aggiornato dei fenomeni di dissesto che hanno interessato di recente, o sono tuttora in atto, Vulcano e Lipari, sulla base del quale possono essere implementate valutazioni di rischio, definiti nuovi sistemi di monitoraggio e azioni per la mitigazione dei danni.

Section 1

Report on the project by Directors

1. Introduction

This report presents the final results of the PROJECT V3, aimed at investigating the relationships between tectonic activity and eruptive dynamics in two important active volcanic areas in Sicily - namely Mt. Etna and the Vulcano-Lipari system - and assessing the related hazard features. The activities planned for the second and last year of the project represent the natural extension of the researches undertaken in the first year, though it must be stressed that the original proposal of the project was based on a three-year activity, later reduced by one year according to the guide lines given by the *Commissione Paritetica DPC-INGV* (CP) (transmitted by e-mail on March 23 and May 1, 2014).

Therefore, the activities carried out during the second phase of the project have been ‘compressed’ in order to be concluded at the end of the second year. This implies that the analyses aimed at comparing and integrating different datasets have been completed but that a significant part regarding multidisciplinary interpretations, is not entirely addressed. However, scientific publications in preparation will fill in the gap by shedding light on aspects not tackled in the present report.

The activities reported by each Research Unit (RU) in Section 2 are updated to June 30, 2015. In general, the review for the second year of the project shows a satisfactory balance between planned and completed activities, although it demonstrates the negative impact of the delays in funding and the contraction of the project’s time extent. Funds become available to the external RUs (i.e. not INGV), only in July-August 2014 despite the project officially started already in May 1st. Moreover, delays in funding have severely affected the possibility to hire specialised personnel (in the form of fellowships and other temporary collaborations) as well as the organization of field surveys and operational meetings especially at the beginning of the project’s second phase.

2. Tasks of the project

The overall framework of the PROJECT V3 consists of four tasks with the following contents and structure (Fig. 1).

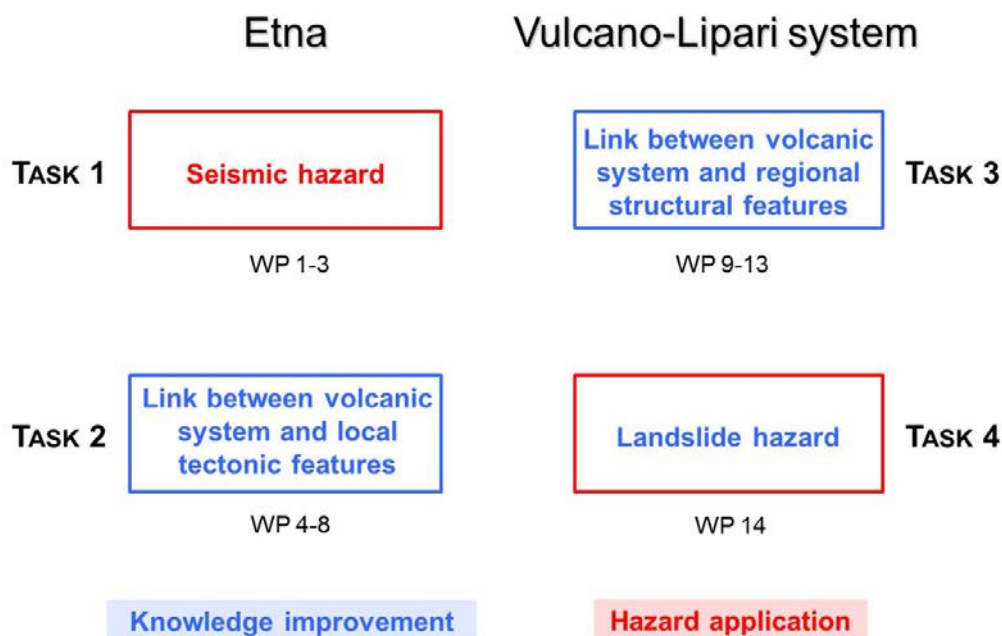


Figure 1. Structure of the Project V3: investigated areas, tasks and related work-packages (WP).

Section 1

Report on the project by directors

A short reminder of the goals of each task:

- **Task 1** focuses on the *probabilistic seismic hazard assessment in the eastern flank of Mt. Etna, due to local volcano-tectonic earthquakes*. The activity is an extension of work undertaken in the DPC-INGV “V4_Flank” Project, improving the probabilistic hazard estimations previously based on macroseismic data (long-term) by also considering the huge instrumental dataset acquired by the seismic monitoring network (INGV-OE 1999-2014). Methodological approach and computation codes are the same as used in the seismological PROJECT S2 (or previous ones), but adapted to consider the features of volcano-tectonic seismicity: fault-based approach, ground-motion (PGA) prediction equations specifically derived for Etna, time-dependent occurrence model (BPT), short exposure times (30, 20, 10 and 5 yrs). The obtained estimations are intended as complementary to seismic hazard map of Italy (50 yrs), to establish priority in the seismic retrofitting of the more exposed municipalities.
- **Task 2** is devoted to analysing the *relationships between local tectonic structures and volcanic system at Mt. Etna* by a multi-disciplinary approach. The distribution of stress in the eastern flank of the volcano is “read” at the surface by the analysis of ground deformation. It is compared with dynamics occurring at depth revealed by seismological data, also with the aims of estimating the seismic efficiency of the area and characterizing the seismic sources. The characterization of the crustal structures responsible for fluid circulation and magma ascent are investigated through geochemical and petrographic analyses in order to detect patterns and variations in the mid- and short-terms. The setting of the sedimentary basement hosting some important volcano-tectonic features (Monte Calanna sub-volcanic body, Timpe fault system in the offshore) is defined by magnetic modelling and seismic profiles, in order to discriminate tectonic processes at the front of the chain from those related to volcano dynamics.
- **Task 3** is conceptually similar - *relationships between regional tectonic structures and the Vulcano-Lipari system* - but investigates at a larger scale the influence of regional tectonics on magmatism in the southern sector of the Aeolian arc. The deformation pattern of the area is analysed by decennial GPS time-series in order to detect possible interactions between the volcano-tectonic systems of Panarea-Lipari-Vulcano and the Aeolian-Tindari-Letojanni line, with emphasis on the effects of the vertical component responsible for subsidence at Lipari. The more rapid time-space dynamics of the Lipari-Vulcano tectonic system is interpreted in the light of the main geophysical/geochemical anomalies recorded during the last 40 years, in order to discern changes linked to the geothermal system from magmatic or tectonic sources. Petrological analyses on the erupted products and structural surveys are used to characterize geometry and composition of the recent volcanic feeding system, ascent magma mechanism and local stress field. A long-term perspective of volcanic/seismic phenomena occurring in the area from the XVI° to XX° centuries, is provided by a historical analysis on coeval documents.
- **Task 4** concerns the *hazard due to gravity flank instability at Vulcano and Lipari*, in response to volcanic activity or other triggering processes. The action is focused on shallow and deep-seated instability phenomena potentially affecting La Fossa cone, while additional analyses are conducted in the SE sector of Vulcano and on the island of Lipari in order to correlate the local deformation processes with large scale dynamics (cfr. Task 3). The multidisciplinary approach includes consolidated surveying methodologies (topographical and photogrammetric datasets, geological and morphological data) integrated with innovative techniques (DInSAR, UAV photogrammetry, Laser and Radar terrestrial surveying). The evaluation of susceptibility to flank failures of La Fossa cone is also based on the role played by the hydrothermal fluids on the alteration of bedrock, and is aimed at providing insights into improving the monitoring system as well as the implementation of mitigation actions.

3. Scheme of activities

The activities planned for the second phase of the PROJECT V3 are organised in 14 work-packages (WP), according to both methodological approaches adopted and the expected results. Each WP is organised in different sub-products (Sp) aimed at investigating diverse issues. The list of WPs is reported in Tab. 1,

together with information on the targets attained and RUs involved in the activity. During the second year, some activities have been integrated in order to finalize the results so that the organization at the end of the project is slightly modified with respect to the initial plan; only in a few cases they have been significantly redefined. The main modifications are indicated in blue.

Table 1. List of work-packages (WP), sub-products (Sp) with results and RUs involved.

	WP	Sp1	Sp2	Sp3	RU
1	Time-dependent occurrence probability for strong earthquakes on the Timpe fault system OK	revision of the average time of occurrence of earthquakes along the Timpe faults	characterisation of seismic sources with high quality instrumental data		1,4
2	Ground-motion prediction equations (PGA from instrumental seismic data) OK	upgrade of spectral GMPE for volcanic earthquakes	amplification functions from H/V noise and modelling		1,6
3	Probabilistic seismic hazard maps OK	maps with/without time-dependency and topography (10% in 30, 20, 10 and 5 yrs)	spectral maps including local site effects (10% in 30, 20, 10 and 5 yrs)		1,4
4	Coulomb stress transfer Partial	fault interaction in the Timpe fault system: implementation of stress simulator			1
5	Dynamics and kinematics of the eastern flank from seismological and ground deformation analyses OK	space-time distribution of seismicity and strain release, also in relation with the main recharging phases of the volcano	earthquake features through the seismic moment tensor	comparison among the scalar geodetic, geologic and seismic moments	1,4
6	Crustal structures and fluid circulation OK	assessment of fluid pressure in relation with the tectonic stress and the magmatic activity, based on time series of geochemical data	detection of phases of increased magma degassing, according to chemical and isotopic data (He isotopes) in peripheral gas manifestations	mapping of the gas emission rates in the Salinelle of Paternò and their temporal evolution	2
7	Geochemistry of magmas and feeding structures Partial	analyses of textures and compositions of crystalline phases: 1928 and 1981 eruptions	pre- and sin-eruptive magma differentiation models and relationship with volcanological evolution and syn-eruptive tectonics: 1928 and 1981 eruptions		1,6
8	Tectonic setting of the sedimentary basement OK	magnetic modelling of the Val Calanna area and off-shore coastal sector	seismic profiles in the offshore south-east of Etna	relationships between on- and offshore structures and definition of deformation processes	1,3,6
9	Deformation of the Lipari-Vulcano-Gulf of Patti system and implications on coastal hazard OK	GPS surveys of the Mts. Nebrodi-Peloritani network and Lipari	updated GPS crustal velocity and strain fields	predictive map of marine ingression for 2100 for Lipari	1,3,7
10	Definition of the time-space dynamics of the Lipari-Vulcano tectonic system OK	definition of areas with common dynamics	ground deformation maps over different time windows		1
11	Relationships between tectonic features and volcanic activity in the southern sector of the Aeolian Arc OK	definition of the Lipari-Vulcano feeding system	characterization of the Lipari-Vulcano active fault systems		5
12	Historical analysis on the space-time relationships between regional earthquakes in the Gulf of Patti-northern Sicily and seismic-volcanic phenomena at Vulcano OK	short monographs of volcanic events and the main earthquakes	final release of the database on earthquakes and volcanic activity		6

Section 1

Report on the project by directors

WP		Sp1	Sp2	Sp3	RU
13	Crustal structures and fluid circulation OK	steaming ground, mofettes, along the Aeolian-Tindari-Letojanni fault system and assessment of geochemical anomalies related to seismic activity and/or ground deformation	mapping of concentrations and fluxes of CO ₂ , H ₂ S and HCl in the fumarolic field of La Fossa in Vulcano	helium isotope analysis in melt inclusions and assessment of the evolution of the magma feeding La fossa cone	2
14	Slope instability hazard maps OK	vector and thematic maps in GIS formats (La Fossa cone and selected sites at Lipari); report on stability analysis of the potential failures detected at La Fossa cone, and on the characteristics of past and active instability phenomena and associated hazard (Vulcano and Lipari)	maps of the hydrothermal alteration facies in the sector between Forgia Vecchia and the 1988 landslide (Vulcano island), soil permeability, moisture content and fracture network; bathymetry of the slope foot map	ground-based radar and thermal infrared reference measurements on the Forgia Vecchia in order to test potential applications for detecting slope movements and weak points of rock mass area	1,2,7

Each WP is considered as the result of the activities of all RU involved, whose contribution is described in the RU Reports (Section 2). A general overview of the WPs indicated in Tab. 1, is presented in the Annex 2.

4. Deliverables

The project is expected to provide two kinds of deliverables: a) hazard maps (hereinafter indicated as D1, D4) and space-time analyses of parameters derived from monitoring and obtained from standard procedures (D2); b) improvements in scientific knowledge, aimed at interpreting the phenomena connected to the interaction between tectonic structures and volcanic activity (D3).

The products planned for the second year of the PROJECT V3, are the following:

- D1** - Probabilistic time-dependent seismic hazard maps of Mt. Etna, expressed in PGA for different exposure times (30, 20 10 and 5 yrs), including topographic and site effects (WP1-sp1-2, WP2-sp1, WP3-sp1);
- D2** - Maps and sections of seismicity, ground deformation maps and strain parameters analysis for Etna and Lipari-Vulcano-Gulf of Patti-Peloritani areas (WP4-sp1, WP5-sp1-3, WP9-sp1-3, WP10-sp1-2, WP12-sp1-2);
- D3** - Reports on magma ascent processes in relation with the tectonic setting, petrological and geochemical features at Etna Vulcano-Lipari-G. di Patti (WP6-sp1-3, WP7-sp1, WP8-sp1-3, WP11-sp1-2, WP13-sp1-2);
- D4** - Flank instability hazard maps due to gravity processes at La Fossa cone (Vulcano) and Lipari (WP14-sp1-3).

On the whole, all the deliverables have been achieved. For details, see the RUs reports in Section 2 and the related electronic materials (listed in Annex 1).

5. Highlights

The overall framework and targets for the four tasks of the PROJECT V3 are consistent with those originally defined. A short summary of the highlights given by the task responsables at the end of the project (2nd year), is reported below.

Task 1 - Probabilistic seismic hazard assessment in the eastern flank of Mt. Etna, due to local volcano-tectonic earthquakes (L. Peruzza)

The activities related to this task have been carried out as planned, with a satisfactory overall percentage of progress. The main highlight concerns the implementation of new versions of the codes used for the calculation of the probabilistic seismic hazard, specifically developed for this project.

In particular, the code FiSH uses new earthquake scaling relationships *ad-hoc* for Etna. This code outputs maximum magnitudes for faults, recurrence times and related uncertainties, and earthquake probabilities and seismicity rates (under Poisson or time-dependent assumptions) to be entered into PSHA (Fig. 2).

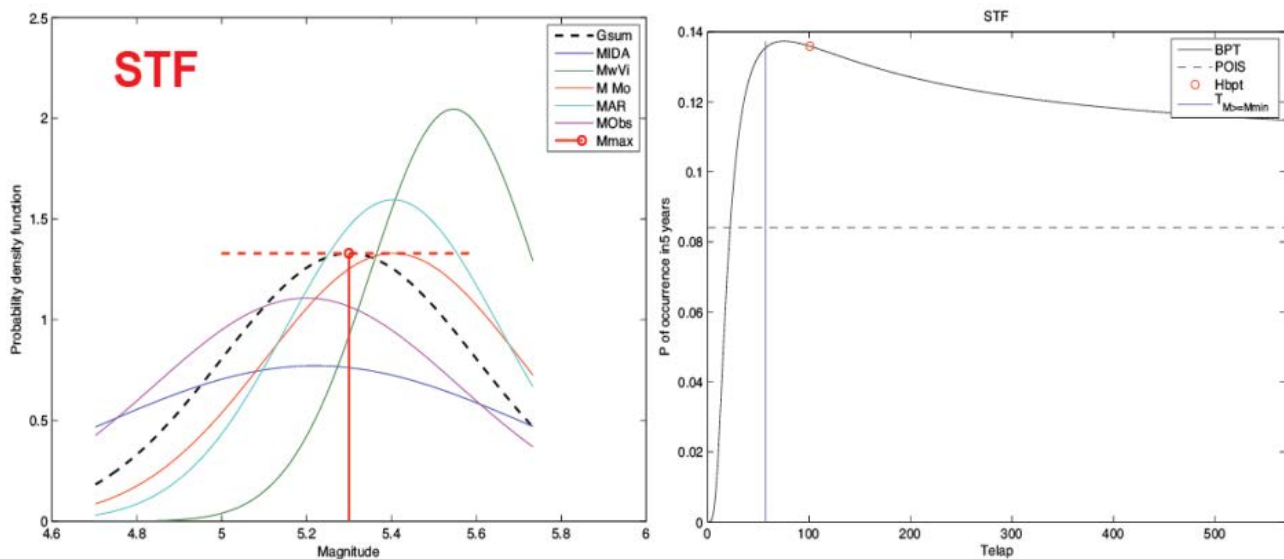


Figure 2. Example of calculations for the S. Tecla f. Left; maximum magnitudes estimated by the code FiSH, following the different approaches used; the dimensions of the curves concur with the relative uncertainties. Right, probabilities of occurrence in the next 5 years for an earthquake equal or higher than M_{\min} , following both poissonian and time-dependent BPT behaviours; the time-dependent probability using the elapsed times from the last M_{\max} earthquake, is indicated with the red circle.

The software CRISIS now accomplishes the general modelling of a 3D surface (effect of topography) in order to compute the proper source-site distances, essential for an exact PGA estimation through local attenuation relationships. This implementation has been feasible by the cooperation with the developer team of CRISIS (M. Ordaz, University of Mexico City) and research visits at OGS, in Nov. 2014 and Feb. 2015. Similar new functionalities have then been implemented in OPENQUAKE, the platform used by GEM (Global Earthquake Model) and by SHARE Project; a grant has been partially funded by V3 Project at INOGS (R. Gee) on these subjects.

The effect of topography is controlled by the source characterization, as it influences the source-to-site distance, and by the ground motion prediction equation used: in the sensitivity tests we performed, it causes a decrease of expected values locally till to 20% (Fig. 3); the role of new topographic distances tends to decrease by increasing the return period the elaborations refer to.

Lastly, the amplification factors obtained by instrumental measures in the eastern flank of Etna by UR 6, have been used in CRISIS too. They give the first seismic hazard site-specific map based on real response data, and clearly illustrate how amplification due to local site can jeopardize the expected ground motion at rock reference sites (Fig. 4).

Section 1

Report on the project by directors

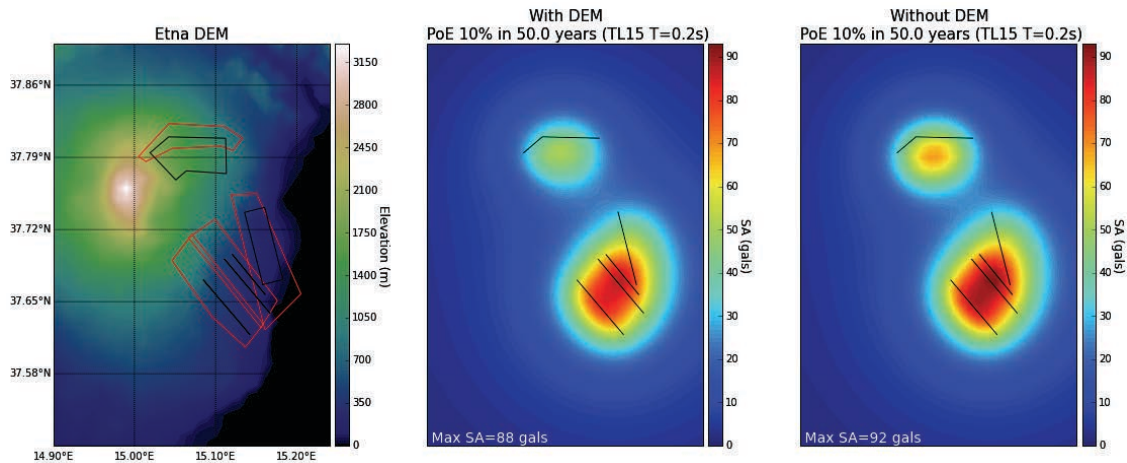


Figure 3. Test on topographic effect using fault sources implemented in OpenQuake during the second semester of V3 Project; faults are modelled with their final geometry, but with arbitrary seismicity rates: TL15 means the last GMPE released by Tusa and Langer in the frame of V3 Project.

Even if these results are preliminary, they can be considered the first example of a new generation of site-specific seismic hazard maps suitable for defining priorities of retrofitting at a local scale.

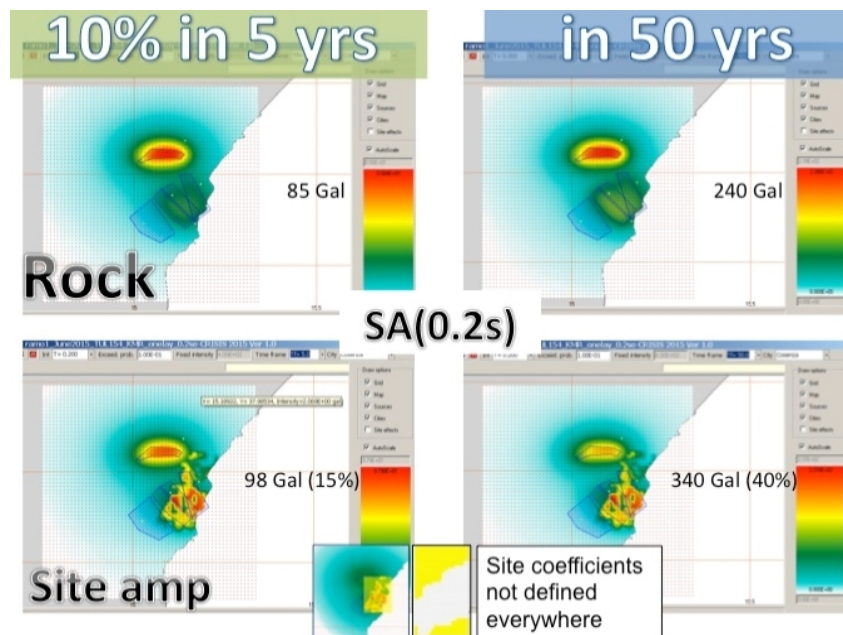


Figure 4. Results obtained by using area sources with G-R calibrated on instrumental and historical data, GMPE derived for the project (WP 2, in RU 1 report) and amplification coefficients calculated from site measurements (WP 2, in RU 6 report). The computations have been done using CRISIS v.2015. Spectral acceleration at 0.2 s. Note the impact of site effects on the final results.

Task 2 - Relationships between local tectonic structures and volcanic system at Mt. Etna (R. Azzaro)

The activities scheduled in this task, based on multi-disciplinary approaches developed by different working groups or RUs, have largely been completed with respect to the scheduled deliverables. The following highlights deserve mention. Firstly, the significant correlations found in the eastern flank of the volcano among active fault zones, seismic patterns (Fig. 5), variations of crustal strain (GPS data) and fluid

circulation in the volcanic rocks (role of pore pressure). This opens new perspectives in the investigation of the faulting process at Etna.

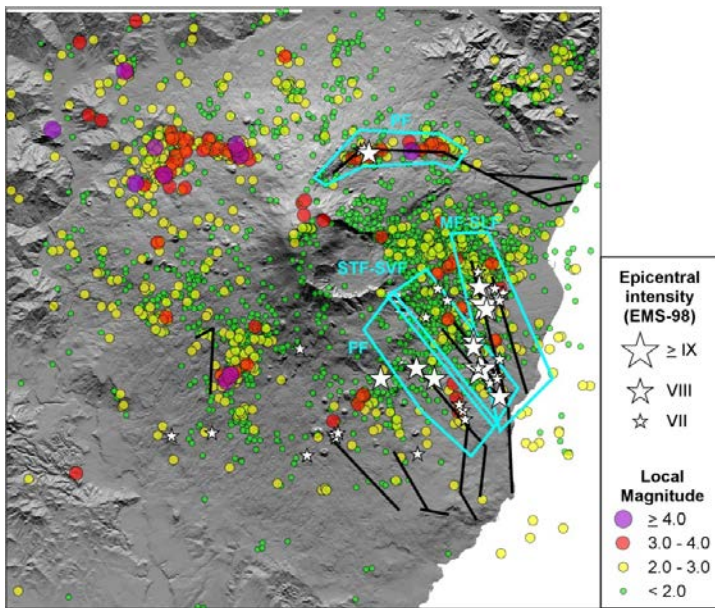


Figure 5. Earthquakes (circles) located from 2005 to 2014 (WP 5 in RU 1 report). Areas in cyan indicate the seismic zones (SZ): Pernicana (PF), Moscarello and S. Leonardello (MF-SLF), S. Tecla and S. Venerina (STF-SVF), Fiandaca (FF). White stars represent the epicenters of historical earthquakes (data from CMTE, 2014).

Shallow seismicity, the main seismogenic layer in the range 1-5 km b.s.l., shows the highest values of strain release between east of Valle del Bove and along the northern termination of the Timpe fault system. Here the scalar geodetic moment-rate, including both elastic and inelastic deformations, does not match that estimated from seismological data, representing only the elastic component responsible for earthquakes (Fig. 6). This study confirms that a large amount of the deformation at Etna occurs aseismically along faults in the eastern flank, as also indicated by field observations, and provides, for the first time, an analytical estimation of creep processes. The misfit may be viewed as a proxy of loading processes on locked fault segments prone to seismic failure.

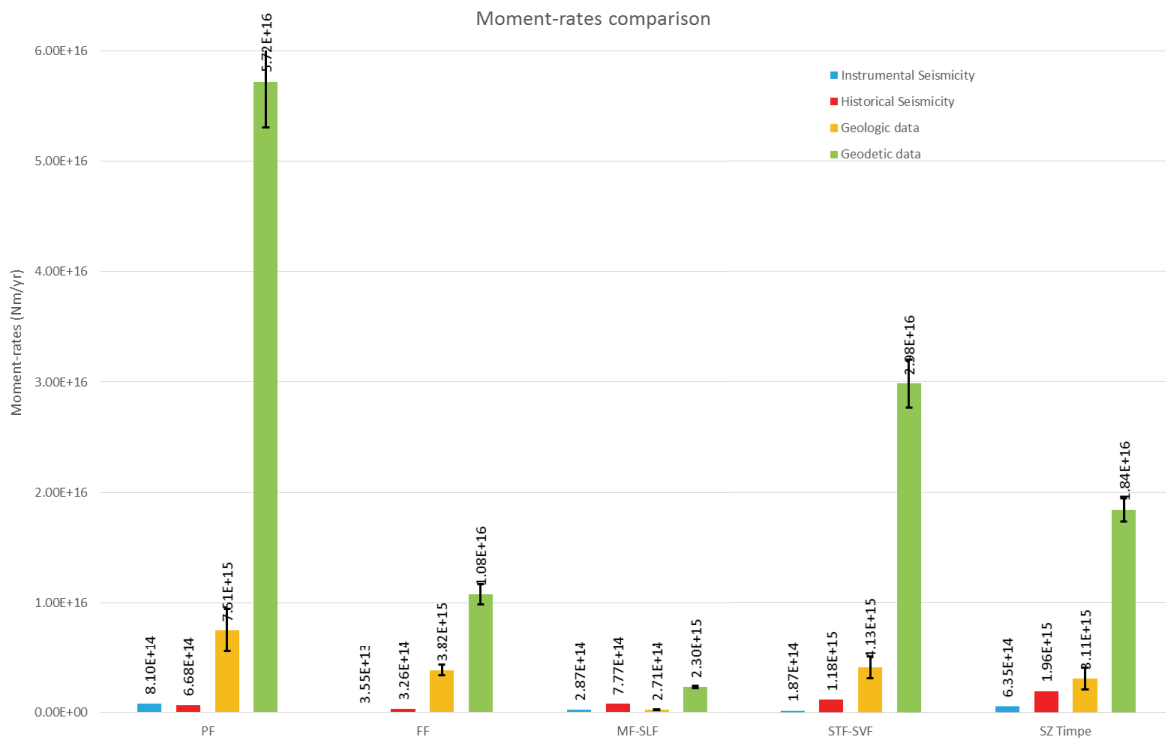


Figure 6. Geological, seismological and geodetic moment-rates obtained for the analysed structures. Fault abbreviations as in Fig. 5.

Section 1

Report on the project by directors

Moreover, variations in the crustal geodetic strain related to volcanic or seismic activity, have been detected to cause changes in the fluid circulation (chiefly groundwater), revealed by the transfer of water in nearby basins and, as a consequence, variations in the water table head and discharge rates (Fig. 7).

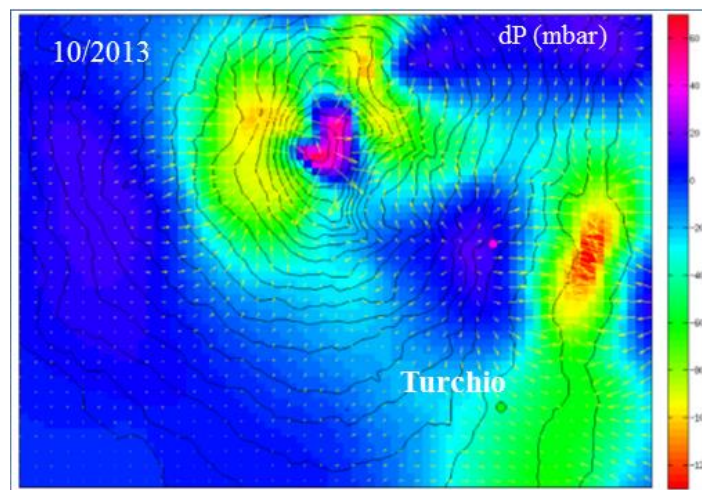


Figure 7. Comparison between variations in the water table head in wells and pore pressure calculated from geodetic strain (WP 6, in RU 2).

Secondly, high-resolution aeromagnetic surveys and seismic profiles shed light on the structural setting of the sedimentary basement and some areas of active deformation. A low magnetized area in Val Calanna has been detected and interpreted as the upper portion of an altered feeder system related to the earliest volcanic centres, with a sub-circular shape of about 5 km diameter centered close to the Mt. Fior di Cosimo area (Fig. 8). The magnetic model is consistent with gravimetric, magnetotelluric and seismic tomography data.

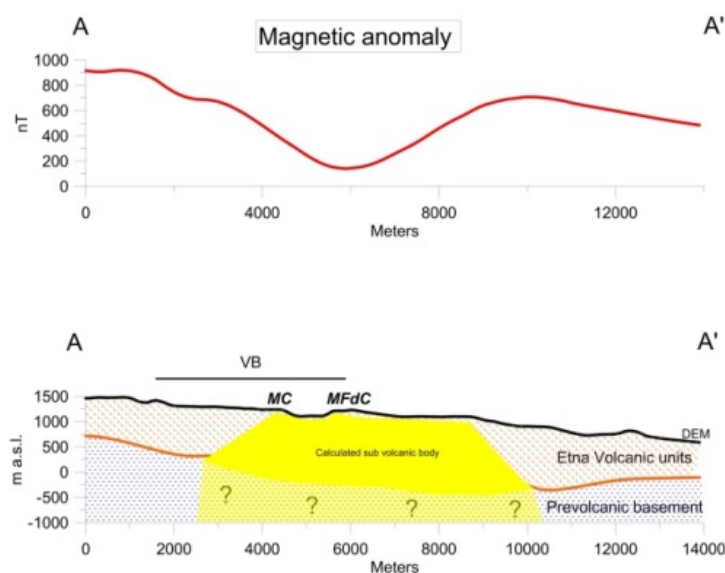


Figure 8. Magnetic model of the Val Calanna area (NS profile). Orange patchwork: magnetic volcanic deposits. Blue patchwork: pre-volcanic, non-magnetic basement. Orange line: basement-volcanic product surface contact. Yellow polygon: sub-volcanic body of Val Calanna. Question marks: area that cannot be modelled using magnetic methods. VB: Valle del Bove., MC: Mt. Calanna. MFdC: Mt. Fior di Cosimo.

In the offshore of Etna, a clear correlation between the magnetic anomaly and the morphological bulge structure evidenced by Chiocci et al. (2011), has been recognized. The high frequency magnetic anomalies aligned along the Riposto ridge represent the effect of shallow localized volcanic bodies above a non-magnetic basement, due to a tabular body confined between the Catania canyon and Alcantara valley (Fig. 9).

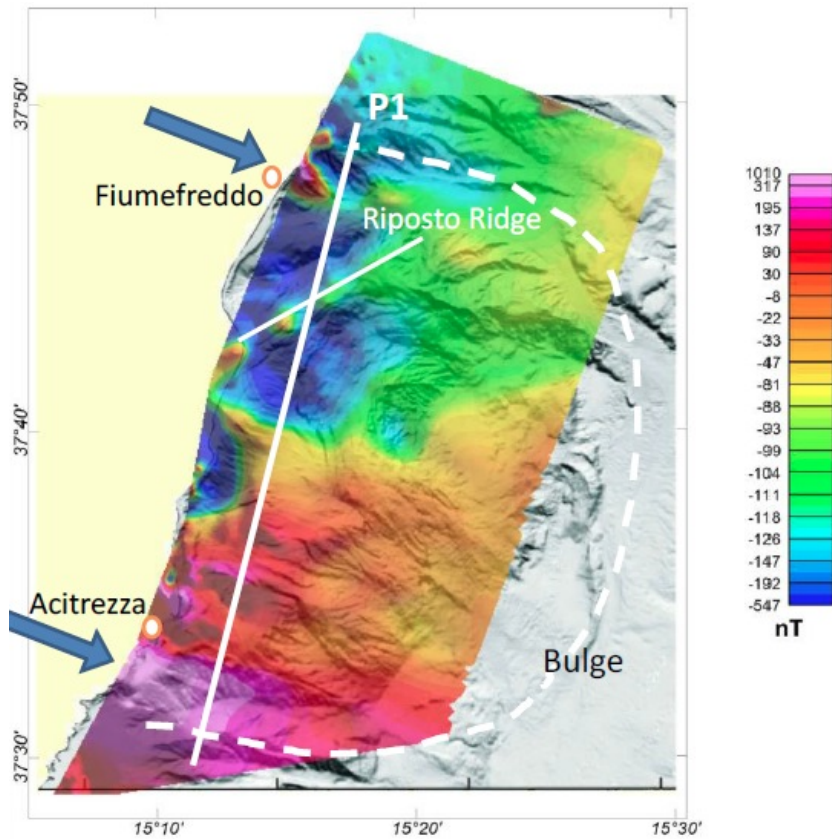


Figure 9. Etna offshore magnetic anomaly. The white dashed line represents the bulge morphology as indicated in Chiocci et al. (2011). The blue arrows indicate the Catania canyon and Alcantara valley positive magnetic anomaly. The white continuous line represents a modeled profile.

Moreover, seismic profiles in the offshore south-east of Etna show an active contractional deformation in Upper Pleistocene deposits in the area of Aci Castello-Acitrezza (Fig. 10), along the offshore extension of the Catania Anticline, and extensional structures along the offshore extension of the Timpe fault system dislocating the 200-100 ky volcanic plateau and also producing ruptures in the seafloor (Fig. 11). Thrusting and folding can be related to the late migration of the Sicilian chain front, whereas extensional faulting to the east is probably part of the major kinematic boundary located in eastern Sicily.

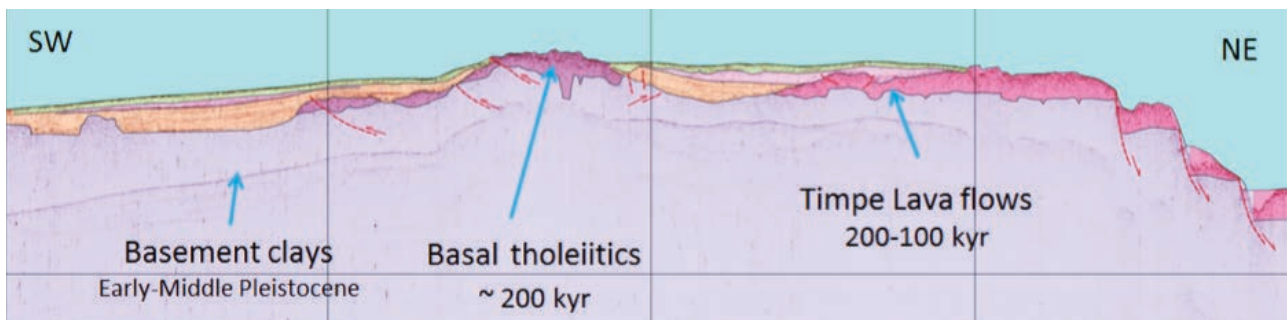


Figure 10. Seismostratigraphic interpretation of a NE-SW oriented sparker line acquired between Capo Mulini and Acitrezza. Note the erosive truncations and unconformities between the seismic units, and the compressive deformation in the southwestern part of the profile.

Section 1

Report on the project by directors

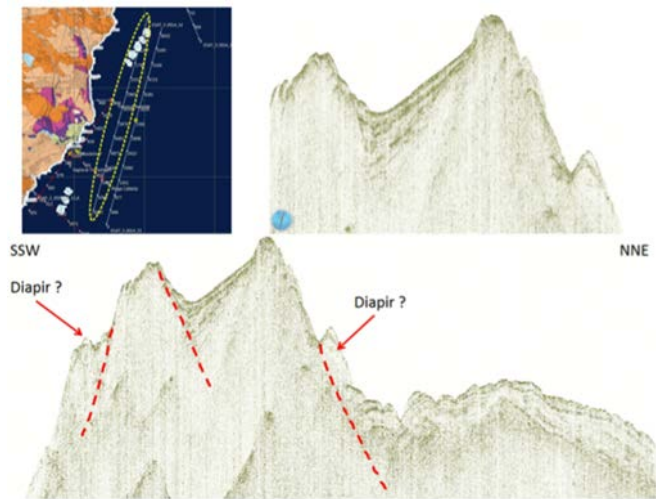


Figure 11. Active horst structure detected along a NNE-SSW trending line. Note that faulting is accompanied by the ascent of what are probably mud diapirs. Top-zoom shows a small triangular-shaped basin with growing strata.

Task 3 - Relationships between regional tectonic structures and the Vulcano-Lipari system (R. De Rosa)

Like the previous task, this one also adopts multi-disciplinary approaches involving different working groups/RUs; the activities carried out in the second year of the project have all been completed as scheduled. Two main highlights can be noted.

First, the relevant rate of crustal deformation (from decennial GPS time-series data) affecting the southern sector of the Aeolian Islands, especially the Vulcano-Lipari complex located at the northern tip of the Tindari-Letojanni line (Fig. 12), with extreme local processes such as the subsidence at Lipari (urban area).

Based on GPS and historical evidence of land subsidence, marine and terrestrial very high resolution DTMs, the project provided values of sea level rise for the coastal area for the harbor zones of Marina Corta and Marina Lunga, at specific times. Results of predictive maps show that the coast of Lipari will be widely flooded in the next decades with a maximum sea level that will rise at 2.2 m in 2100 for the worst scenario (Fig. 13).

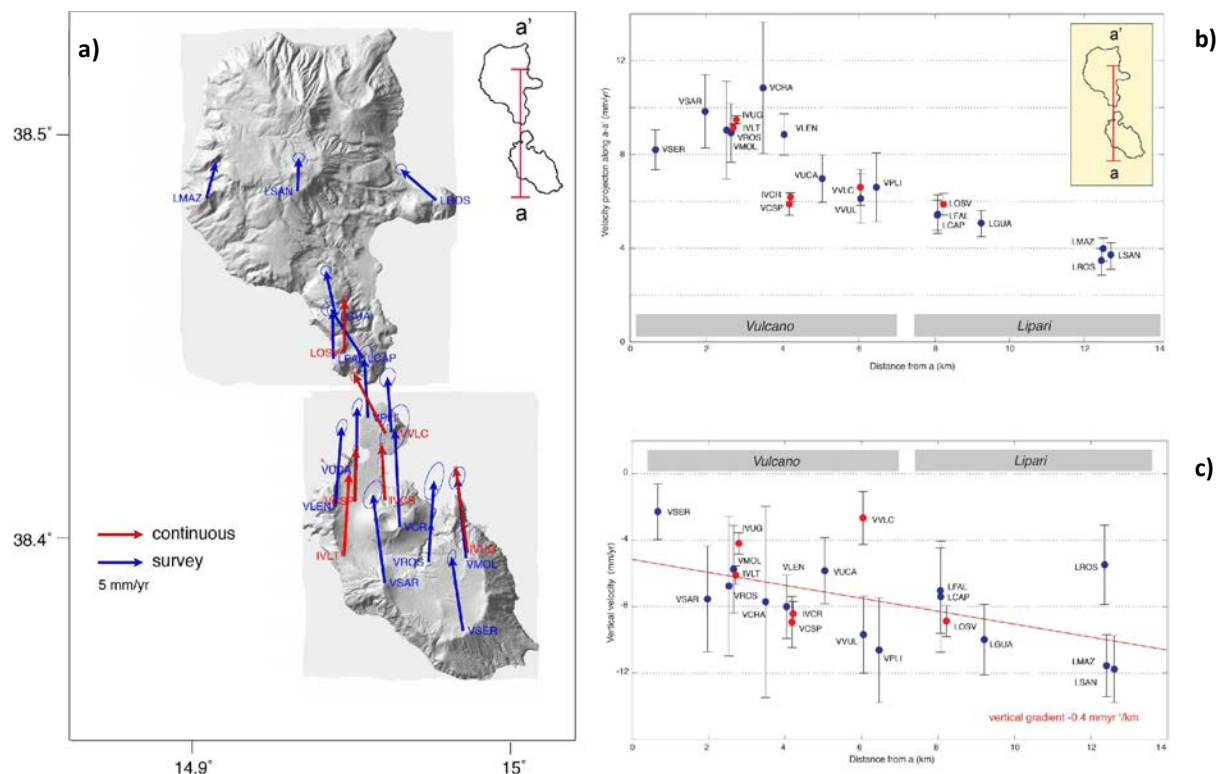


Figure 12. a) The horizontal GPS velocity field for the GPS discrete networks of Lipari-Vulcano; b) GPS and CGPS horizontal velocities projected along cross section a-a'; c) CGPS and GPS vertical velocities along a-a'.

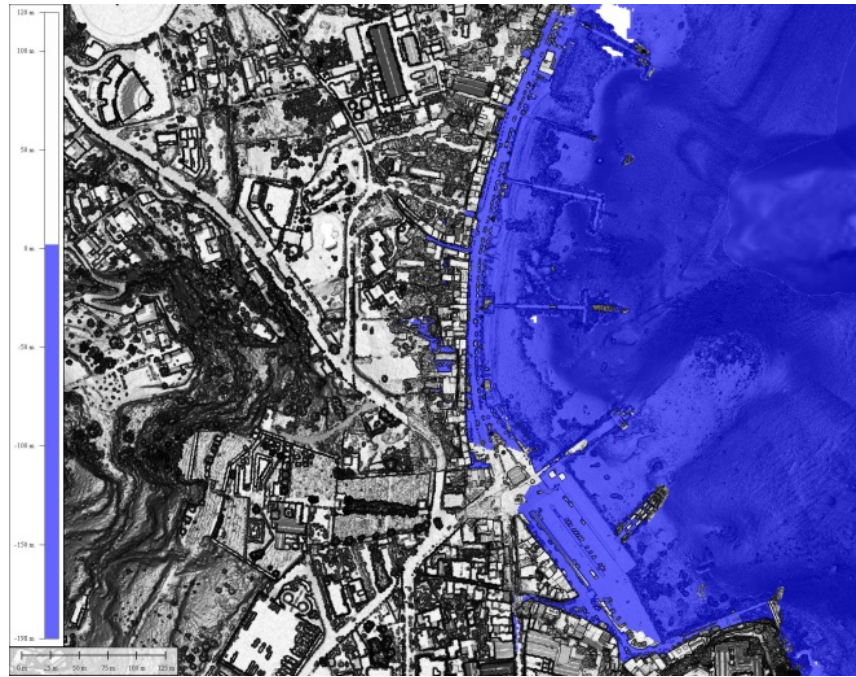


Figure 13. Map of marine flooding for Marina Lunga estimated for 2100: Sea level rise: 2.21 m Scenario: maximum Rahmstorf (2009, PNAS). Blue is sea level with respect to the time of surveys (October 2015). Topography from UAV aerial photogrammetry and bathymetry from multibeam surveys, both performed in this project.

Second, the existence of a common plumbing system feeding the historical eruptions of Lipari and Vulcano, and the dominant magmatic stress field affecting both islands. Overall data indicate that in this sector of the Aeolian Arc the younger than 1 ka eruptive activity, was not accompanied by strong volcano-tectonic earthquakes and occurred contemporaneously at Lipari and Vulcano along a 15 km long, 1 km wide corridor to the East of the Lipari-Vulcano complex. The results of the structural study support a constant EW dominant extensional regime with very limited E-W spatial variation of the activity; any future eruption is thus more likely to occur along this corridor (Fig. 14).

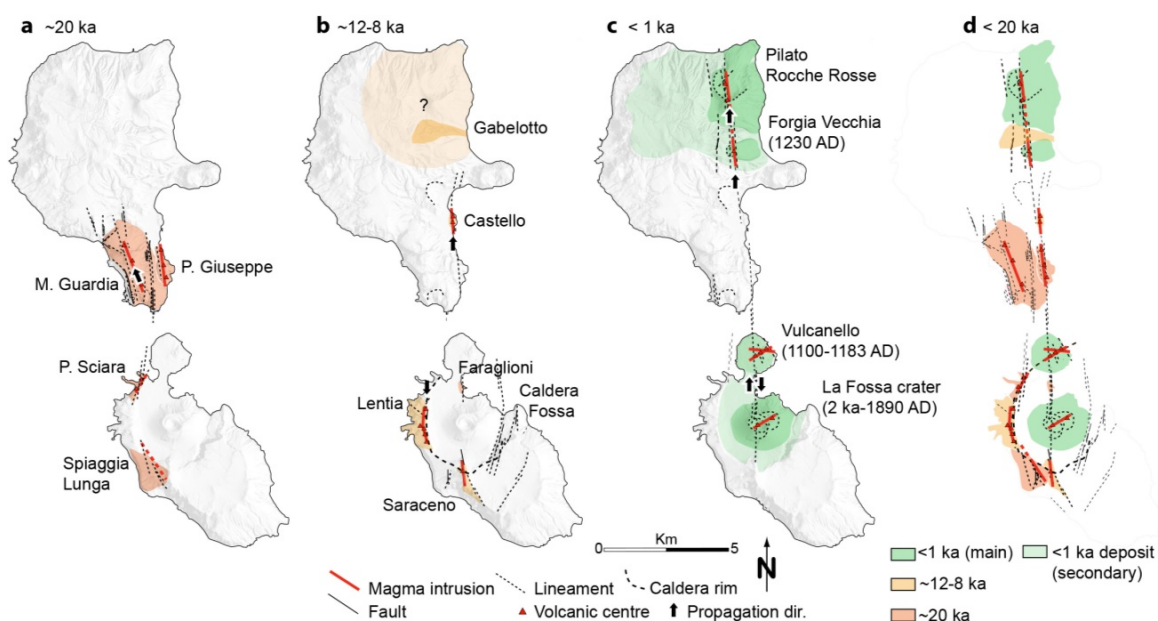


Figure 14. Magmatic-tectonic evolution of Lipari and Vulcano during the last 20 ka.

Section 1

Report on the project by directors

The overall data allows proposing a structural model (Fig. 15) where the maximum effective stress (σ_1) may rotate from horizontal to vertical, transiting from pure right lateral strike-slip faulting along the Tindari fault zone (tectonic-dominant) to an extensive regime (magmatic dominant) inducing normal faulting and extension during transient magma intrusions.

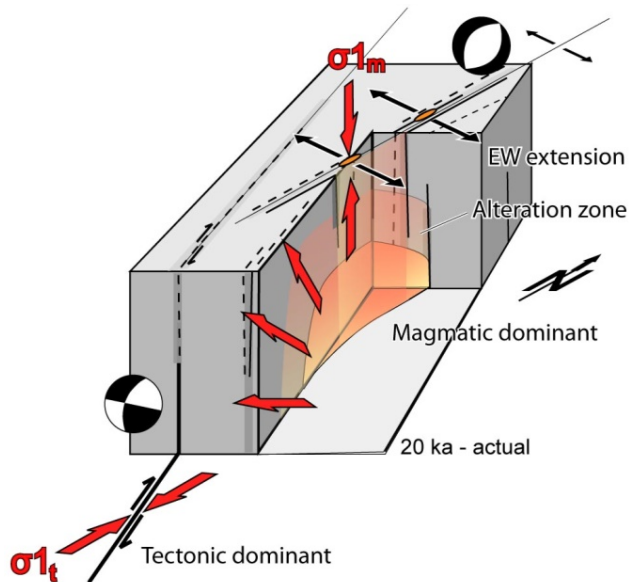


Figure 15. Proposed kinematics model to explain the transition between right lateral oblique motion (South) to normal faulting (North), transiting from tectonic stress (σ_1 horizontal) to magmatic stress (σ_1 vertical), in response to the presence of magma pressure.

The present dynamics of the area obtained from ground deformation and seismic data covering the 1974-2013 period fit well with a deflating source of latitic composition located under Vulcanello at a depth of 4.6 km (Fig. 16).

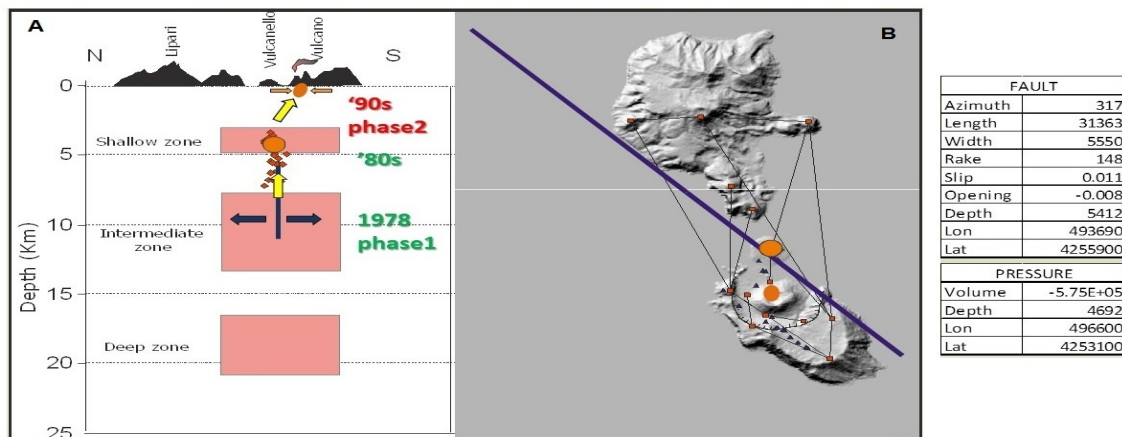


Figure 16. The two sources: (A) a tabular dislocation (regional tectonic) and (B) a magmatic deflating source located under Vulcanello.

The geochemical composition of noble gases of the fumarolic field at la Fossa confirms this hypothesis indicating that this magmatic source is still active and periodically fed by deep fluids coming from the underlying reservoir, having higher $^3\text{He}/^4\text{He}$ ratio (Fig. 17).

Furthermore the isotopic, geochemical and melt inclusions data of the historical latites, indicate a common polibarc system with a 20 km deep shoshonitic magma periodically feeding several shallow magma storage zones (3-5 km, up to 1 km of depth), where processes of assimilation fractional crystallization allow the differentiation of the shoshonitic magma in latitic and rhyolitic melts.

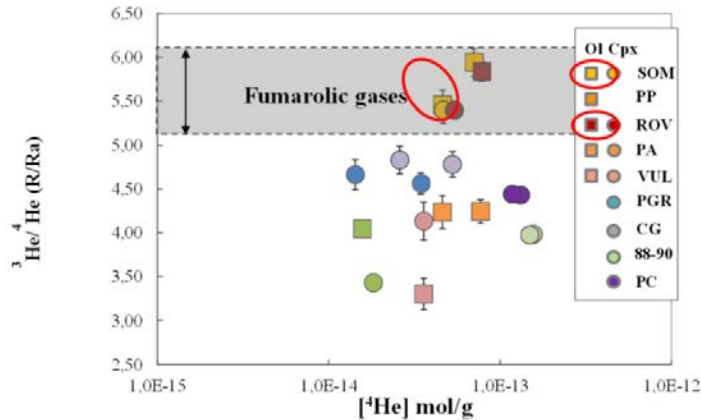


Figure 17. Comparison between $^3\text{He}/^4\text{He}$ ratios measured in fluid inclusions in Vulcano and Vulcanello products and those measured in present fumarolic gases.

Task 4 - Hazard due to gravity flank instability at Vulcano and Lipari (M. Marsella)

The task has carried out an in-depth analysis on some aspects linked to the understanding of the instability mechanisms of the flanks of La Fossa cone (Vulcano Island), and the assessment of their current status. A study devoted to the detection and mapping of unstable areas was also conducted on the island of Lipari, in order to complete the analysis carried out in the first year.

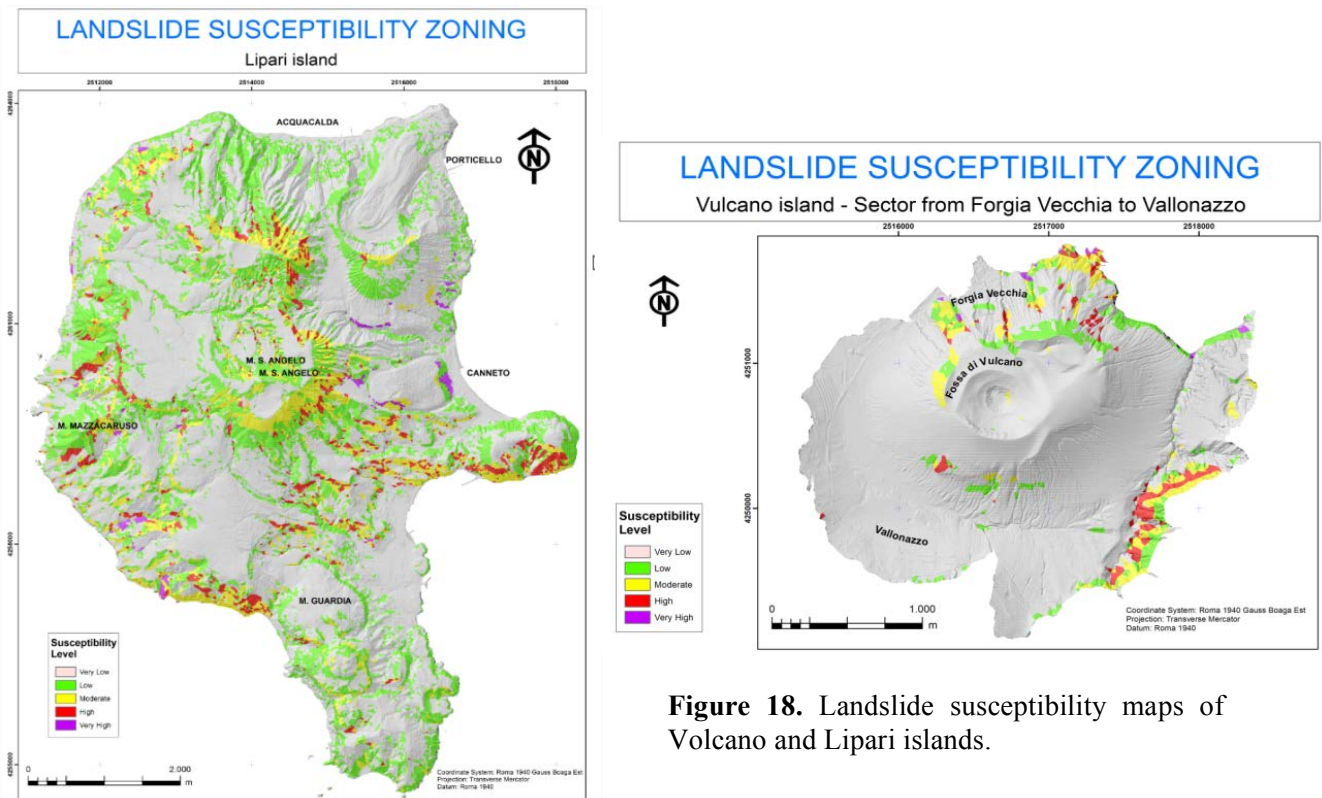


Figure 18. Landslide susceptibility maps of Vulcano and Lipari islands.

Starting from the knowledge gained in previous phases of the project, three lines of research were developed. These aimed at performing a back-analysis for the assessment of the topographic variations due to slope movements and compiling susceptibility-to-instability maps (Sp1, Fig. 18), mapping the areas affected by hydrothermal activity (Sp2, Fig. 19) and testing innovative methods for monitoring of active landslides (Sp3, Fig. 20).

Section 1

Report on the project by directors

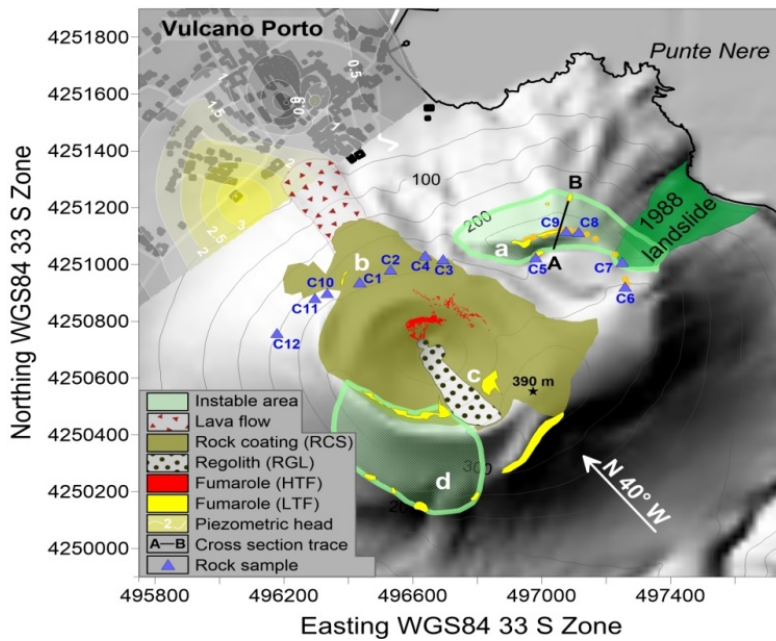


Figure 19. Instability processes related to hydrothermal fluid circulation and alteration.

In detail, the analyses and surveys conducted during the second year yielded the following results:

- building a database that includes a numerical raster cartography, SAR displacement velocity maps and thematic maps (lithology and hydrothermal activity);
- extraction and validation of susceptibility-to-instability maps based on the automatic analysis of morphometric data and Lidar data based classifications;
- defining a procedure to assess the stability of potentially unstable areas of the cone and its application to the NE sector of the La Fossa (Punte Nere);
- collection of elements for the evaluation of potential detachments (circulation of hydrothermal fluids, rock alteration, detailed bathymetry, etc.);
- verification of GB-SAR system functionality in combination with continuous thermal mapping (FLIR) to be used in case of reactivation of instability phenomena of La Forgia Vecchia slope.



Figure 20. Area of acquisition of the Ground-Based Radar GPRI-II with the image of phase.

These results provide a detailed and updated frame of instability phenomena, either recent, or still ongoing, that affected Lipari and Vulcano. On this basis, risk assessments can be implemented, new monitoring systems can be designed and further actions for the mitigation of damage can be planned.

6. Research Units, coordinators and activities

The Research Units participating in the second phase of the PROJECT V3 are the same as those involved in the first year. The only variation is the change in the responsible of RU 3 and his affiliation, M. Chiappini (currently director of INGV-RM2) being replaced by M. Anzidei (INGV-CNT).

The list of RUs related to the task activity is shown in Tab. 2.

Table 2. List of Research Units (RUs), Responsibles and involvement in the tasks of the project.

	RU	Task 1	Task 2	Task 3	Task 4
1	INGV-CT - R. Azzaro	X	X	X	X
2	INGV-PA - C. Federico		X	X	X
3	INGV-CNT - M. Anzidei		X	X	
4	OGS-TS - A. Saraò	X	X		
5	UNI-CS - R. De Rosa			X	
6	UNI-CT - C. Ferlito		X	X	
7	UNI-RM La Sapienza - M. Marsella				X

The list of coordinators of tasks and work-packages is reported in Tab. 3.

Table 3. List of coordinators of Tasks and Work-Packages (WP).

	WP	Task 1 L. Peruzza	Task 2 R. Azzaro	Task 3 R. De Rosa	Task 4 M. Marsella
1	RU 4 - B. Pace	X			
2	RU 1 - H. Langer	X			
3	RU 4 - L. Peruzza	X			
4	RU 1 - M. Mattia		X		
5	RU 1 - O. Cocina		X		
6	RU 2 - C. Federico		X		
7	RU 6 - F. Ferlito		X		
8	RU 1 - S. Branca		X		
9	RU 3 - M. Anzidei			X	
10	RU 1 - S. Gambino			X	
11	RU 5 - R. De Rosa			X	
12	RU 6 - M.S. Barbano			X	
13	RU 2 - P. Madonia			X	
14	RU 7 - M. Marsella				X

Section 1

Report on the project by directors

7. Management

The delay in funding by the administrations of some external RUs has made a number of managerial adjustments to the organization of meetings necessary. The general kick-off meeting has therefore been substituted with operational briefings for individual Tasks/WPs. However, this was not a critical issue since the aforementioned activities are the continuation of the research undertaken in the first year of the project.

In the second phase of the project operational briefings/workshops with individual RUs (dedicated to checking ongoing activities and coordination levels among RUs involved), have been carried out as follows:

- May 9, 2014, RU 1 (WP 4), Catania
- May 29-30, 2014, Task 1 (WP 3), Pisa
- July 10, 2014, RU 6 (WP 12), Catania
- July 18, 2014, RU 6 (WP 8), Catania
- July 21-23, 2014, RUs 1-4 (WP 1, 3), Trieste
- September 10, 2014, RU 1 (WP 5), Catania
- October 2, 2014, RUs 1-7 (WP 14), Catania
- October 16, 2014, RUs 1-6 (WP 2), Catania
- January 14-16, 2015, RU 4 (WP 3, 5), Trieste
- January 21-22, 2015, RU 1 (WP 4, 5, 9, 10, 14), Catania
- February 3-4, 2015, RUs 2, 5, 6 (WP 2, 6, 7, 8, 11, 12, 13, 14), Catania
- February 17, 2015 RUs 3 (WP 8, 9), Roma
- May 9-10, 2015, RUs 3, 5 (WP 9, 11), Lipari
- May 11, 2015, RUs 1, 6 (WP 2), Catania

Final project workshop

- June 10-11, 2015, RUs 1-7, Catania

Quarterly meetings of the Volcanological Projects V1-3 with the *Commissione Paritetica DPC-INGV*, held in Roma:

- July 28, 2014
- November 6, 2014
- February 18, 2015

Conference of the DPC-INGV Volcanological projects:

- June 22-23, 2015, Roma

8. Summary of the financial plan

The financial requests have been agreed on the basis of the activities redefined for the second year of the PROJECT V3. Tab. 4 reports the funds assigned to RUs in the first and second year of activity.

Table 4. Funds to RUs in the first and second year of the project.

RU	Responsible	Institution	1 st year funds	2 nd year funds
1	Azzaro R.	INGV-CT	44.428	41.000
2	Federico C.	INGV-PA	24.428	23.000
3	Anzidei M.	INGV-CNT	19.430	24.500
4	Saraò A.	OGS-TS	19.430	25.000
5	De Rosa R.	UNI-CS	39.428	36.000
6	Ferlito C.	UNI-CT	34.428	36.000
7	Marsella M.	UNI-RM La Sapienza	44.428	35.500
Total			226.000	221.000*

*general contraction defined by the *Convenzione C – DPC-INGV, 2014*.

Details on the distribution of funding to RUs in the second phase of the project, are shown in Fig. 21.

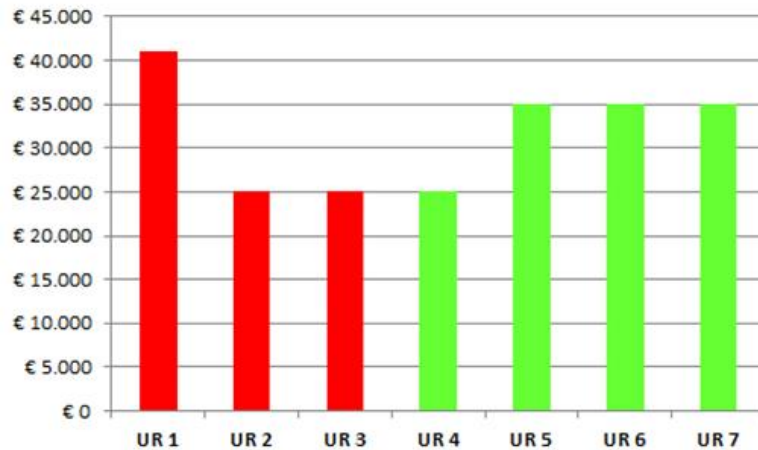


Figure 21. Distribution of the Project V3 funding to RUs in the second phase of the project. Red: INGV; green: other institutions.

The overall distribution between INGV and other institutions according to the guideline of the *Convenzione C – DPC-INGV, 2014*, is given in Fig. 22.

	1 st year	2 nd year	
Total INGV:	88.286	88.500	(40%)
Total other institutions:	137.714	132.500	(60%)

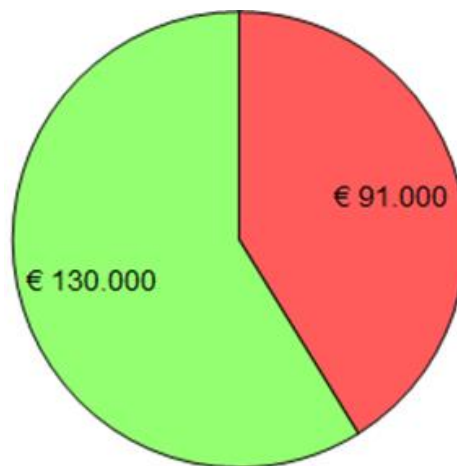


Figure 22. Overall distribution of the Project V3 funding between INGV and other institutions in the second phase of the project. Red: INGV; green: other institutions.

Section 2

Scientific Reports of Research Units (RU)

RU 1, INGV - Sezione di Catania - Osservatorio EtneoResponsible: **Raffaele Azzaro****Activity of RU in phase 2**

RU 1 is involved in tasks 1, 2, 3 and 4 of the project:

- WP 1** (resp. S. D'Amico) - Characterization of the seismic sources from long-term (historical macroseismic catalogue) and short-term data (instrumental catalogue).
- WP 2** (resp. H. Langer) - Upgrade of GMPEs for Etna considering hypocentral depths and spectral ordinate coefficients.
- WP 4** (resp. M. Mattia) - Coulomb stress transfer: installation and set-up of the software on computers of the Faculty of Computer Science (University of Catania); simulations and tests for improving the correct computational process.
- WP 5** (resp. O. Cocina) - 3D relocation of Etna seismicity from 2005 to 2014; comparing the scalar geodetic, geologic and seismic moments to estimate seismic efficiency.
- WP 10** (resp. S. Gambino) - Modeling of deformation sources from 1974-2013 time series of EDM, GPS, levelling and earthquake data.
- WP 14** (resp. L. Lodato) - FLIR and GB-RAR reference measurements on the Forgia Vecchia (Vulcano) in order to test the potential applications for detecting slope movements and weak points of rock mass.

Task 1 - WP 1***Time-dependent occurrence probability for strong earthquakes on the Timpe fault system*****Participants: INGV-CT**

Salvatore D'Amico, Raffaele Azzaro, Graziella Barberi, Tiziana Tuve`

Sp2 - Characterization of the seismic sources (resp. S. D'Amico)

In order to estimate the probability of occurrence and other parameters necessary to WP 3 "Probabilistic seismic hazard maps", it is required the knowledge of the characteristics of seismogenic sources related to volcano-tectonic seismicity. For this purpose were used both long-term (macroseismic catalogue) and short-term data (instrumental catalogue) of the Etnean earthquakes. The latter dataset consists of earthquakes located with 3D model of seismic wave velocities in the framework of WP 5 (Task 2). Although the instrumental catalogue is extended about twenty years, only a dataset consisting of events occurring from 2005 to 2014, was used. Infact, in this time window the overall seismic rate at Etna appears to be stable because it is not affected by the intense seismic sequences such as those occurring during the 2001 and 2002-03 eruptions (Alparone et al., 2015). Moreover, since 2005 the seismic network has undergone upgrades and implementations such that the quality of acquired data is increased (Alparone et al., 2012) and local magnitude (M_l) estimations are also available, which have less uncertainty than the duration magnitude (M_d) previously used.

Seismogenic zones

In order to spatially identify the seismogenic zones (SZ), we used the ones defined in the the first year of the project, because they well represent the simplified geometry of the structural systems recognized in the field (Azzaro et al., 2012a). They also represent the source areas of the strongest earthquakes occurring at Etna in the last 200 years (Fig. 1).

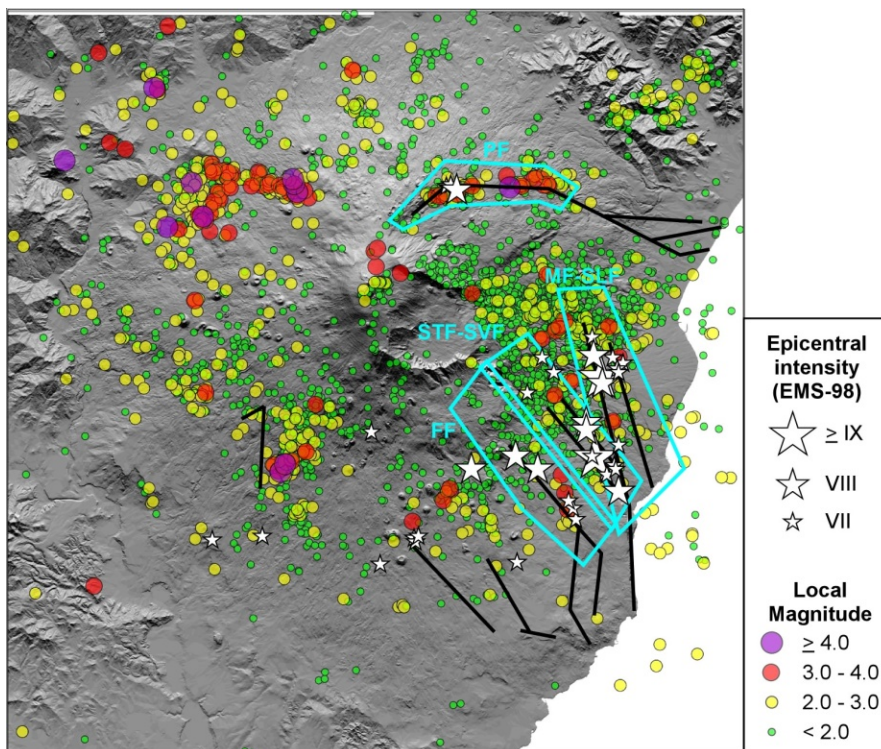


Figure 1. Earthquakes (circles) located from 2005 to 2014 in the framework of WP 5 (Task 2). Areas in cyan indicate the seismic zones (SZ): Pernicana (PF), Moscarello and S. Leonardello (MF-SLF), S. Tecla and S. Venerina (STF-SVF), Fiandaca (FF). White stars represent the epicenters of historical earthquakes (data from CMTE, 2014).

The characterization of the SZ has been made in detail with the estimation of the effective depth, i.e. the seismogenic layer where most of seismic energy is released. For this purpose for each seismic zone we calculated the distribution of the number of earthquakes and strain release vs. depth, with steps of 1 km (Fig. 2). Results indicate that the seismogenic thickness for each SZ is mainly confined in the first 7 km b.s.l., which is in agreement with the overall depth distribution of seismicity in the Mt. Etna area. In particular it is well evident a main seismogenic layer at about 1 km b.s.l. and, in some cases (STF-SVF and MF-SLF), also a second seismogenic layer at about 5 km b.s.l. (Tab. 1).

Seismicity rates

The seismic rate was calculated using the ZMap tools (Wiemer, 2001) by the Frequency Magnitude Distribution (FMD) of the instrumental catalogue (covering about 10 years) for each SZ, to estimate the *a* and *b* coefficients of the Gutenberg-Richter (GR) relationship. Detailed analyses (Fig. 3, Tab. 1) show that the structures belonging to the Timpe fault system (Moscarello, S. Leonardello, S. Tecla, S. Venerina and Fiandaca, see abbreviations in the Fig. 1 caption) have seismicity rates substantially similar, while the Pernicana fault, though it retains about the same annual rate (*a*-value) of earthquakes, it has a much lower *b*-value.

	PF	MF-SLF	STF-SVF	FF
<i>Seism. thickness (km)</i>	-1.0 - 1.0	-1.0 - 5.0	-1.0 - 5.0	-1.0 - 1.0
<i>b-value</i>	0.68 ± 0.09	0.94 ± 0.08	1.12 ± 0.13	0.94 ± 0.24
<i>annual a-value</i>	2.05	2.52	2.70	1.82

Table 1. Seismogenic thickness, *b* and *a* coefficients of Gutenberg-Richter relationship for each SZ, obtained from the instrumental dataset (see WP 5 report).

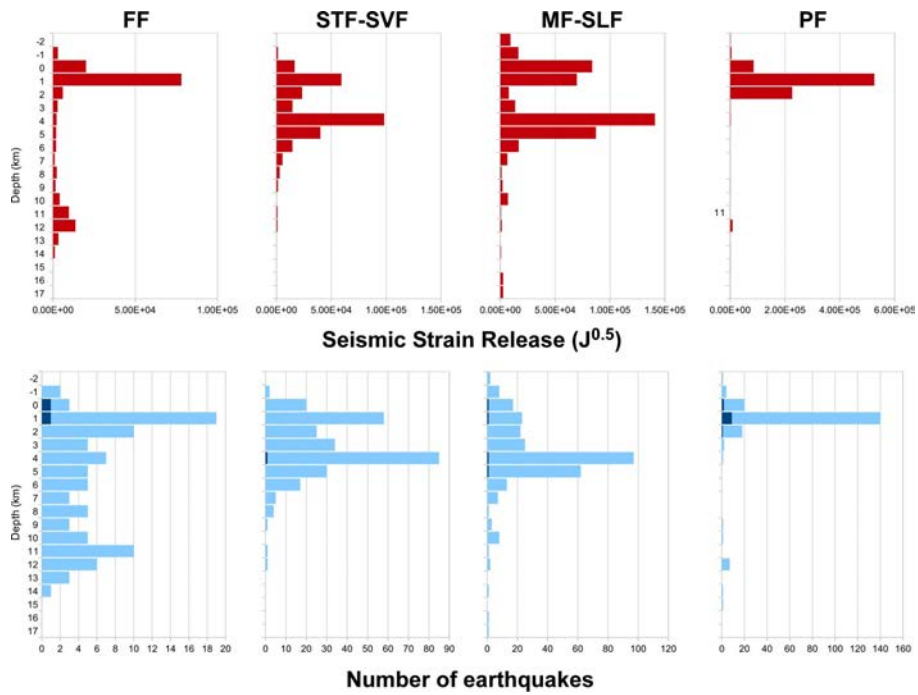


Figure 2. Distributions of seismic strain release (top) and number of earthquakes (bottom) vs. depth. Dark blue histograms indicate the number of earthquakes with $M_L \geq 3.0$.

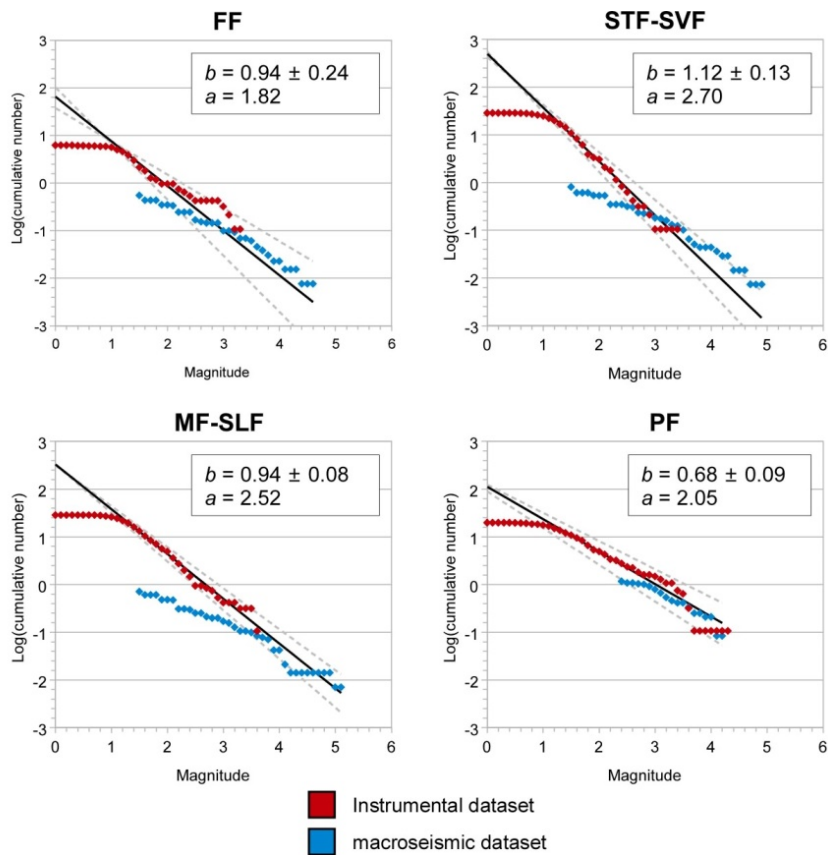


Figure 3. Frequency Magnitude Distribution for each SZ. Red dots refer to the instrumental dataset (see WP 5, Task 2), blue dots to the macroseismic dataset (CMTE, 2014). Dotted lines indicate the uncertainties respect to the Gutenberg-Richter relationship (black line). Data are normalized to one year. Fault abbreviations as in Fig. 1.

Section 2

Scientific Reports of Research Units (RU 1)

FMD were compared with those obtained from the historical macroseismic catalogue, covering a time-span of about 150 years for all SZs except PF which is about 30 years. Since the time-span of the two catalogues is different, FMD were normalized to one year. As shown in Fig. 3, b -values calculated from the instrumental and macroseismic datasets are consistent each other, so we can affirm that instrumental seismicity occurring in the selected nine years time-window may be considered representative for a long-term seismogenic behaviour.

In order to calculate the seismic hazard by using the innovative approach known as smoothed seismicity, a - and b - coefficients of the GR were calculated using a three-dimensional grid with internodal distance of 2 km (Fig. 4). A constant search radius equal to 3 km was used in each node. The results obtained with a number of earthquakes lower than twenty were discarded.

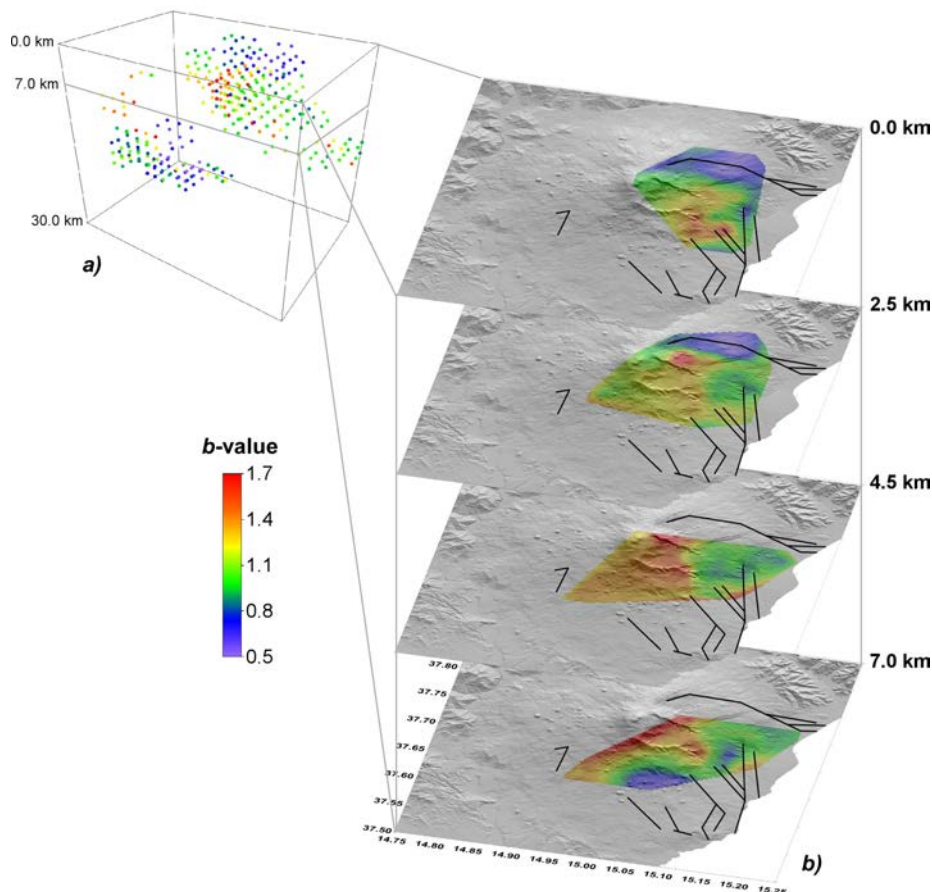


Figure 4. a) 3D distribution of b -value for Mt. Etna; b) contour maps for selected depths within the adopted seismogenic thickness (-1 to 7.00 km b.s.l.).

Task 1 - WP 2, Resp. H. Langer

Ground-motion prediction equations (PGA from instrumental seismic data) (Etna)

Participants: INGV-CT

Horst Langer, Giuseppina Tusa

Sp1 - Upgrade of spectral GMPEs for volcanic earthquakes

Ground motion prediction equations (GMPEs) have been derived for peak ground acceleration (PGA), velocity (PGV) and 5%-damped spectral acceleration (SA) at periods between 0.1 and 5 s for the volcanic

area of Mt. Etna. The dataset consists of 91 earthquakes with magnitudes $3.0 < M_i < 4.8$ and epicentral distances between 0.5 km and 100 km. The geological conditions in the areas are rather specific, with the volcanic edifice overlying a thick sedimentary substratum and strong lateral heterogeneities. In order to account for these characteristics, we divided our data set into two groups: Shallow Events (SE, focal depth < 5 km), and Deep Events (DE, focal depth > 5 km). Signals of DE typically have more high frequencies than those of SE. This difference is clearly visible in the waveforms (Fig. 5). Consequently these differences show up also in the empirical GMPEs. Indeed, for a given magnitude and hypocenter distance, PGA tend to be higher for the DE than for SE.

In order to compare our data to those recorded in other regions in Italy and Europe, we considered two formulations. The proposals by Sabetta and Pugliese (1987, SP87 hereafter) and Ambraseys and Bommer (1996, AMB96 hereafter) formula are given in eq. 1:

$$\text{Log}(Y) = a + b_1 M + c_1 \text{Log} \sqrt{R^2 + h^2} + c_3 \sqrt{(R^2 + h^2)} + e_i S_i \quad (1)$$

where Y is the ground motion parameter, b_1 is the coefficient controlling the magnitude dependence, c_1 describes exponent in the distance dependent amplitude decay, c_3 stands for inelastic attenuation. h is an additional parameter that is sometimes addressed to as “pseudo depth” (km) and incorporates all the factors that tend to limit or reduce motion near the source (Joyner and Boore, 1981). The S_i indicate the soil conditions, with i standing for the soil classes A, B, C, D defined in EC8 building code. The S_i variables of Boolean type are set to 1 if the corresponding soil class is met at a site, whereas the S_i for all other classes is 0. As c_3 is close to 0, the AMB96 converges to the SP87 formulation. We therefore discuss the two versions together.

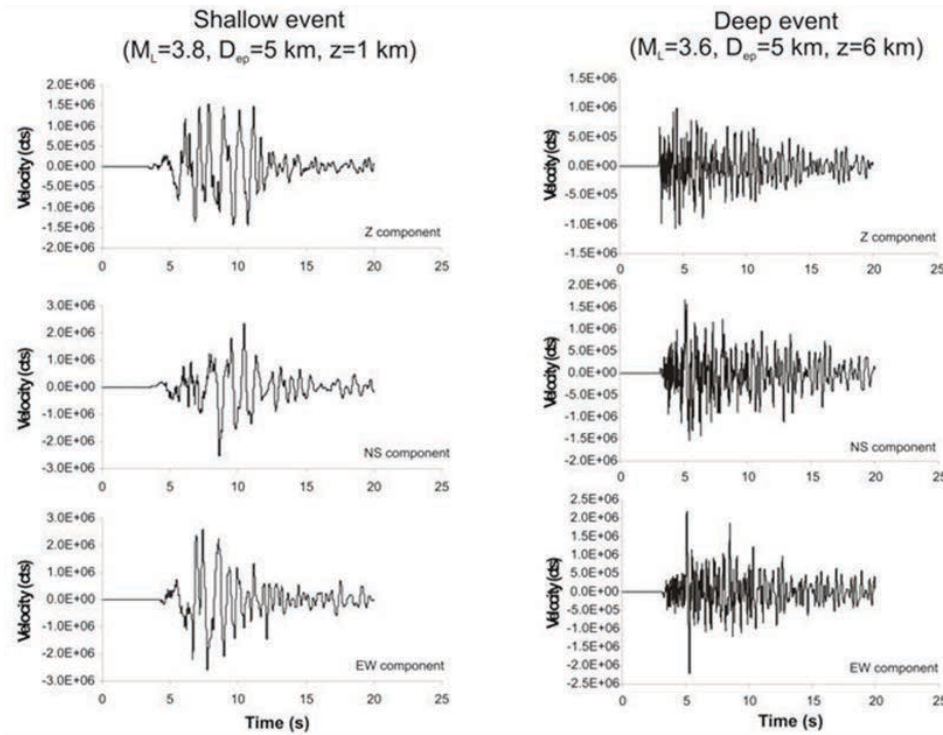


Figure 5. Example of wave forms of a shallow (left) and deeper event (right panel).

A second, more complex formulation was proposed by Boore & Atkinson (2008, BA2008 hereafter). This formulation (see eq. 2) is also used in the Italian standard equation ITA10:

$$\text{Log}(Y) = a + b_1 M + b_2 M^2 + [c_1 + c_2 (M - M_{ref})] \text{Log} \left(\sqrt{R_{ep}^2 + h^2} \right) + c_3 \left(\sqrt{R_{ep}^2 + h^2} - 1 \right) + e_i S_i \quad (2)$$

Both SP87/AMB96 as well as the BA2008 formulations are based on the Joyner-Boor distance, which

Section 2
Scientific Reports of Research Units (RU 1)

converges to the epicentral distance for small sized sources. In Tabs. 2 and 3 we report the results obtained for our data set, distinguishing between shallow and deeper events.

Shallow Events (SE)										
	a	b₁	c₁	h	e_B	e_D	R²	S_{eve}	S_{sta}	S_T
PGA _h (cm/s ²)	-1.183	0.724	-1.716	1.541	0.359	-0.066	0.378	0.221	0.225	0.388
CI95	-1.529	0.656	-1.836	0.717	0.264	-0.190	0.248			
	-0.838	0.792	-1.596	2.366	0.453	0.058	0.508			
PGA _v (cm/s ²)	-1.095	0.685	-1.746	1.235	0.339	-0.084	0.432	0.228	0.215	0.389
CI95	-1.433	0.617	-1.860	-2.002	0.247	-0.208	0.304			
	-0.758	0.754	-1.632	-0.468	0.432	0.040	0.560			
PGV _h (cm/s)	-3.516	0.989	-1.535	2.555	0.445	0.066	0.406	0.150	0.226	0.341
CI95	-3.843	0.929	-1.658	-3.544	0.357	-0.043	0.286			
	-3.188	1.049	-1.411	-1.567	0.532	0.175	0.525			
PGV _v (cm/s)	-3.711	1.000	-1.484	2.134	0.460	0.001	0.442	0.155	0.209	0.331
CI95	-4.019	0.942	-1.597	-3.049	0.377	-0.105	0.328			
	-3.403	1.058	-1.371	-1.219	0.544	0.107	0.556			
Deep Events (DE)										
PGA _h (cm/s ²)	-0.749	0.768	-1.630	8.186	-0.122	-0.137	0.091	0.162	0.274	0.400
CI95	-1.119	0.729	-1.815	-10.278	-0.206	-0.237	-0.025			
	-0.378	0.808	-1.446	-6.095	-0.038	-0.037	0.208			
PGA _v (cm/s ²)	-0.524	0.743	-1.750	8.705	-0.140	-0.081	0.086	0.158	0.248	0.389
CI95	-0.896	0.705	-1.936	-10.699	-0.222	-0.178	-0.028			
	-0.153	0.781	-1.564	-6.711	-0.059	0.016	0.200			
PGV _h (cm/s)	-3.266	0.841	-1.183	5.613	0.064	-0.057	0.170	0.162	0.232	0.361
CI95	-3.548	0.806	-1.320	-7.592	-0.009	-0.147	0.066			
	-2.983	0.877	-1.046	-3.633	0.137	0.033	0.273			
PGV _v (cm/s)	-2.857	0.818	-1.422	8.224	0.027	0.004	0.162	0.170	0.200	0.345
CI95	-3.177	0.784	-1.582	-10.299	-0.045	-0.083	0.061			
	-2.537	0.852	-1.262	-6.149	0.099	0.090	0.262			

Table 2. Coefficients of equation 1 (SP87/AMB96) for the prediction of PGA and PGV, both horizontal (PGA_h and PGV_h) and vertical (PGA_v and PGV_v). CI95 indicates the confidence intervals at 95% level.

Shallow Events (SE)													
	a	b₁	b₂	c₁	c₂	h	c₃	e_B	e_D	R²	S_{eve}	S_{sta}	S_T
PGA _h (cm/s ²)	-0.568	0.475	0.037	-2.054	-0.015	2.317	0.006	0.452	0.477	0.856	0.222	0.221	0.390
CI95	-2.854	-0.750	-0.133	-2.313	-0.175	1.316	0.002	0.340	0.331	RMSE			
	1.717	1.700	0.208	-1.795	0.146	3.318	0.009	0.564	0.623	0.392			
PGA _v (cm/s ²)	-0.726	0.431	0.055	-2.012	-0.095	1.795	0.004	0.413	0.512	0.858	0.227	0.214	0.391
CI95	-3.004	-0.797	-0.117	-2.244	-0.253	0.897	0.001	0.301	0.367	RMSE			
	1.551	1.658	0.226	-1.780	0.063	2.692	0.008	0.525	0.657	0.392			

Shallow Events (SE)													
PGVh (cm/s)	-1.412	0.085	0.094	-1.670	0.171	3.056	0.003	0.479	0.441	0.876	0.150	0.229	0.343
CI95	-3.444	-0.994	-0.056	-1.933	0.026	1.792	-0.001	0.380	0.312	RMSE			
	0.620	1.163	0.244	-1.407	0.315	4.321	0.006	0.578	0.571	0.344			
PGVv (cm/s)	-2.197	0.286	0.070	-1.373	0.161	1.769	-0.001	0.474	0.458	0.880	0.156	0.212	0.333
CI95	-4.141	-0.759	-0.075	-1.569	0.026	0.698	-0.004	0.379	0.335	RMSE			
	-0.253	1.331	0.216	-1.176	0.296	2.840	0.002	0.569	0.582	0.334			
Deep Events (DE)													
	a	b₁	b₂	c₁	c₂	h	c₃	e_B	e_D	R²	S_{eve}	S_{sta}	S_T
PGAh (cm/s ²)	2.527	-0.397	0.094	-1.998	0.315	9.608	0.000	-0.200	0.002	0.708	0.161	0.276	0.399
CI95	0.838	-1.015	0.013	-2.694	0.184	13.474	-0.005	-0.294	-0.124	RMSE			
	4.216	0.221	0.174	-1.301	0.446	5.743	0.006	-0.106	0.129	0.400			
PGAv (cm/s ²)	2.459	-0.407	0.100	-1.956	0.273	9.315	-0.001	0.229	-0.013	0.731	0.157	0.249	0.387
CI95	0.865	-1.005	0.022	-2.611	0.149	5.687	-0.006	0.138	-0.136	RMSE			
	4.054	0.191	0.178	-1.301	0.397	12.944	0.004	0.320	0.109	0.387			
PGVh (cm/s)	-0.623	-0.301	0.099	-1.139	0.285	4.609	-0.003	-0.005	0.092	0.738	0.162	0.233	0.359
CI95	-1.807	-0.849	0.026	-1.447	0.184	1.860	-0.006	-0.084	-0.015	RMSE			
	0.561	0.247	0.171	-0.831	0.385	7.359	0.000	0.073	0.199	0.360			
PGVv (cm/s)	-0.249	-0.400	0.111	-1.264	0.268	6.505	-0.004	-0.040	0.089	0.770	0.168	0.199	0.341
CI95	-1.471	-0.923	0.042	-1.660	0.167	3.294	-0.007	-0.116	-0.015	RMSE			
	0.974	0.124	0.180	-0.868	0.370	9.717	0.000	0.037	0.193	0.342			

Table 3. Coefficients of equation 2 (BA2008) for the prediction of PGA and PGV, both horizontal (PGA_h and PGV_h) and vertical (PGA_v and PGV_v).

From ANOVA (ANalysis Of VAriance) we learn that most of the errors in our GMPEs can be attributed to unmodelled site effects (given by σ_{STA}), whereas errors related to event parameters (σ_{EVE}) are limited. This is particularly evident for the DE group. We carried out a series of statistical tests in order to check the significance and validity of the SP87/AMB model and the BA2008 model. For DE, BA2008 outperforms the simpler models SP87 or AMB96. The Bayesian Information as well as prediction errors during cross-validation reveals that, for SE, the simple SP87 is preferable to the BA2008 model (see Tusa and Langer 2015).

Besides peak ground motion parameters, we also calculated empirical relations for PSA for a number of frequencies. We don't list them here as they can be found in the paper by Tusa and Langer (2015). For a shallow event of $M=4$, we compare the relations to those predicted by ITA10. The results, shown in Fig. 6, underscore particularities for shallow Mt. Etna events. Being comparatively rich in low frequencies, the corresponding spectral values are higher than those predicted by ITA10. On the other hand, PSA for higher frequencies are well below the values given by ITA10.

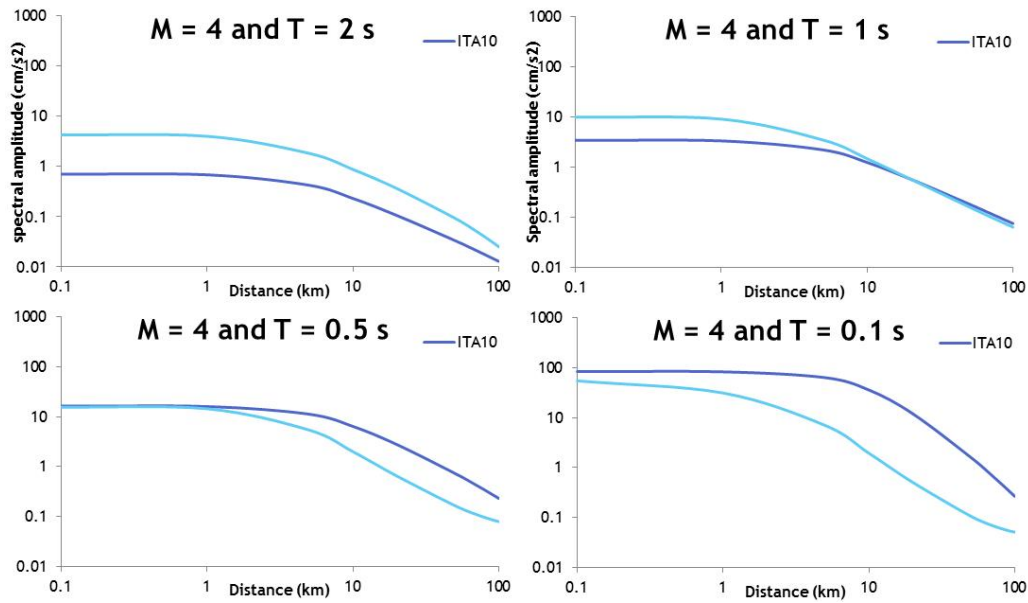


Figure 6. Comparison PSA predicted by ITA10 and the values from Tusa and Langer (2015). The values were obtained for an event of $M=4$.

In the framework of the project empirical GMPEs were exploited for probabilistic seismic hazard analyses (PSHA) focusing on the shallow events occurring on Mt. Etna. The computer codes for PSHA use the hypocenter distance rather than the Joyner-Boore distance considered above. This brings along slight changes in the estimated coefficients of the regression. For the purpose of comparison with ITA10, we cite the values obtained using the formulation in eq (2). In the framework of PSHA we consider both epicenter distance < 30 km as well as 100 km (as before). For horizontal PGA we obtain the coefficients reported in Tab 4.

PGA h (cm/s ²)	a	b ₁	b ₂	c ₁	c ₂	h	c ₃	RMSE	R ²
	-0.033	0.954	-0.083	-2.238	0.311	2.696	-0.006	0.402	0.716
CI 95%	-2.089	0.120	-0.200	-3.356	0.013	4.847	-0.037		
CI 95%	2.022	1.788	0.034	-1.119	0.609	0.545	0.024		

Table 4a. Coefficients of regression model (distance < 30 km, only soil B).

PGA h (cm/s ²)	a	b ₁	b ₂	c ₁	c ₂	h	c ₃	e _B	e _D	RMSE	R ²
	0.329	0.105	0.076	-2.111	0.039	1.553	0.006	0.450	0.457	0.395	0.853
CI 95%	-1.993	-1.136	-0.097	-2.376	-0.125	-0.084	0.003	0.337	0.309		
CI 95%	2.651	1.346	0.248	-1.847	0.204	3.190	0.010	0.562	0.604		

Table 4b. Coefficients of regression model (distance < 100 km).

As before, we also calculated the empirical relations for pseudo spectral acceleration (PSA). Comparing our values to ITA10 (Fig. 7), we find, in principal, similar results as in Fig 6. Note, however, that values for distances up to 30 km are higher as only soil B is considered, which is the widely prevailing soil type available in this distance range.

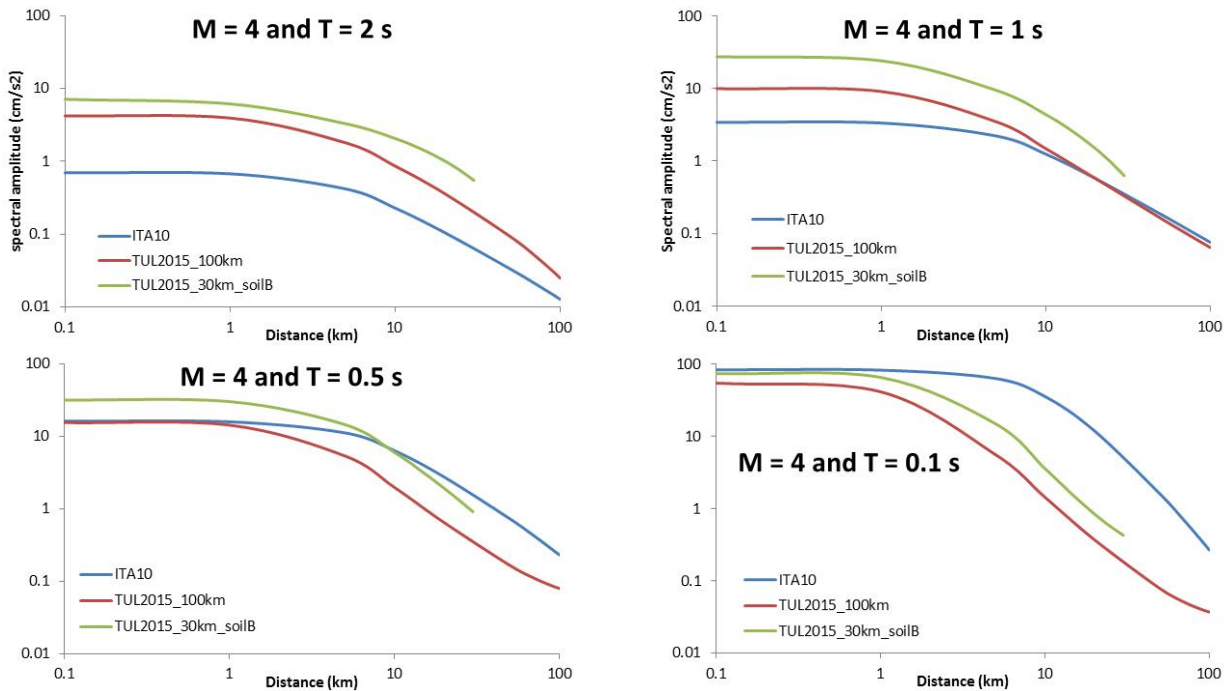


Figure 7. Comparison PSA predicted by ITA10 and our values, using the hypocenter distance instead of the Joyner-Boore measure. The values were obtained for an event of $M=4$.

Task 2 - WP 4, Resp. M. Mattia

Coulomb stress transfer (Etna)

Participants: INGV-CT

Mario Mattia, Valentina Bruno, Danila Scandura

Other institutions

DMI UNI-CT Sebastiano Battiato, Antonino Furnari, Rosario Ruta, Alessandro Di Cunzolo

Sp1 - Fault interaction in the Timpe fault system: implementation of stress simulator

The aim of this WP originally was the investigation of the interactions between faults in the eastern flank of Mt. Etna through a Finite Element Modeling approach (FEM). In the second year of the project, we solved some informatic problems in order to perform computations on computers of the Dipartimento di Matematica e Informatica (UNI-CT). The Coulomb stress changes were calculated by using PYLITH, a parallel finite element code (Aagaard et al., 2009). To study if fault slip is encouraged or discouraged by the stress change due to the movement of another fault, we analyze the Coulomb stress changes on the receiver faults. Based on the Coulomb failure criterion, fault slip is encouraged if the change in Coulomb stress is positive, while it is discouraged if the change is negative. The stress changes were resolved onto the received faults surfaces, using the apparent friction model that considers the Coulomb failure function:

$$\Delta CFF = \Delta\tau + \mu' \Delta\sigma_n$$

where $\Delta\tau$ is the shear stress, $\Delta\sigma_n$ is the normal stress change, μ' is the apparent friction coefficient that includes the effects of pore fluids and the material properties of the fault zone. We fixed μ' to 0.4 as generally used in stress transfer computations on Mt. Etna (Walter et al., 2005; Feuillet et al., 2006).

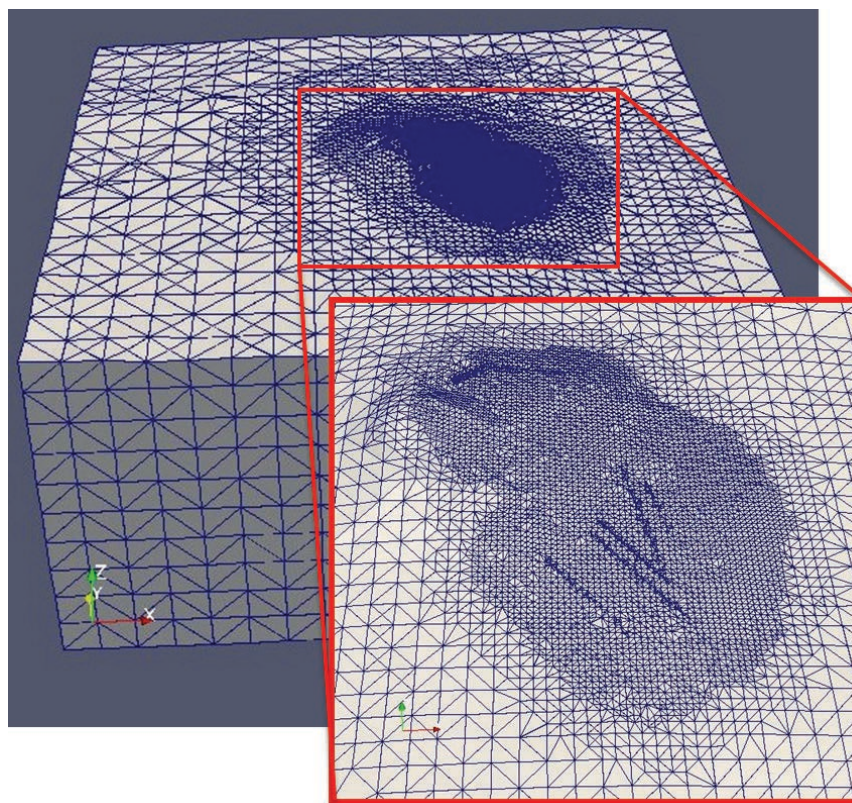


Figure 8. Computational domain created by the LAGRIT code: the mesh resolution is about 300 m around the sources (inset), about 500 m in the 20×20 km area around the summit craters and decreases to 2 km in the periphery of the volcano.

Simple homogeneous half-space models are not very efficient in computing the static stress changes in presence of strong medium heterogeneity and steepest relief, therefore in order to account for the Etna topography and the medium heterogeneity, a 3D finite element model of the volcano was developed to evaluate the Coulomb stress changes. The computational domain is a volume extending 100×100×50 km; in this way we avoid artifacts in the numerical solution, which can arise from the proximity of the external boundaries. Using LAGRIT, a 3D grid generation code from Los Alamos National Laboratory (<http://lagrit.lanl.gov>), the computational domain was meshed into 954,962 isoparametric, and arbitrarily distorted tetrahedral elements connected by 165,399 nodes. The mesh resolution is about 300 m around the sources, about 500 m in the 20×20 km area around the summit craters and decreases to 2 km in the far field (Fig. 8). For boundary conditions, the displacements normal to the lateral boundaries and to the bottom are fixed to zero, while the boundary at the ground surface is free.

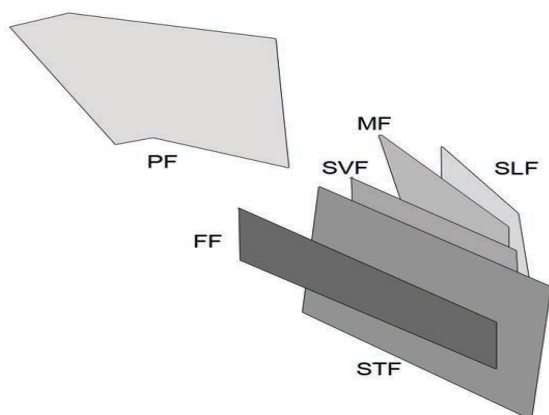


Figure 9. Scheme of the faults included in the model for FEM analysis. Fault abbreviations as in Fig. 1.

The model includes six faults (Fig. 9), whose parameters are summarized in Tab. 5. Each fault embedded in the computational domain, can be considered as both source or receiving structure. The approach we have developed also allows to apply an inhomogeneous slip distribution on the source fault. Several synthetic simulations were conducted in order to test the potentiality of the approach and to highlight the important role of topography in the stress transfer.

The model includes six faults (Fig. 9), whose parameters are summarized in Tab. 5. Each fault embedded in the computational domain, can be considered as both source or receiving structure. The approach we have developed also allows to apply an inhomogeneous slip distribution on the source fault. Several synthetic simulations were conducted in order to test the potentiality of the approach and to highlight the important role of topography in the stress transfer.

PF1:	Pernicana	Fault	SVF:	S. Venerina	Fault
502127,7	4182477	1950	511081	4171517	350
504914,9	4179560	-2150	511081	4171517	-5150
506060,3	4180533	-2366	514613,3	4167236	-5500
504142,1	4184188	1572,22	514613,3	4167236	0
PF2:	Pernicana	Fault	MF:	Moscarello	Fault
504142,1	4184188	1572,22	512375,8	4176079	300
506060,3	4180533	-2366	514564,6	4176623	-5902,73
510405,4	4180244	-3280,14	516559,8	4168846	-6252,73
510313,7	4184046	600	514371	4168302	-50
FF:	Fiandaca	Fault	SLF:	S. Leonardello	Fault
507938,9	4168769	400	513933,4	4174897	0
507938,9	4168769	-1100	515997,9	4175505	-5920,98
512961	4162925	-1700	517178	4171624	-6120,98
512961	4162925	-200	515113,5	4171016	-200
STF:	S. Tecla	Fault			
510217,3	4171018	430			
510217,3	4171018	-5070			
515144,4	4165241	-5550			
515144,4	4165241	-50			

Table 5. 3D coordinates of the faults embedded in the domain.

In Fig. 10 we show one case-study analyzed: we apply an average strike-slip of 0.65 m in the upper part of the Pernicana fault (seismic swarm of April 2010, from Guglielmino et al., 2011). Results show the stress changes over the other faults of the domain. In practice, very shallow seismic activity along the Pernicana fault can't induce meaningful stress transfer to the other faults of the eastern flank of Mt. Etna.

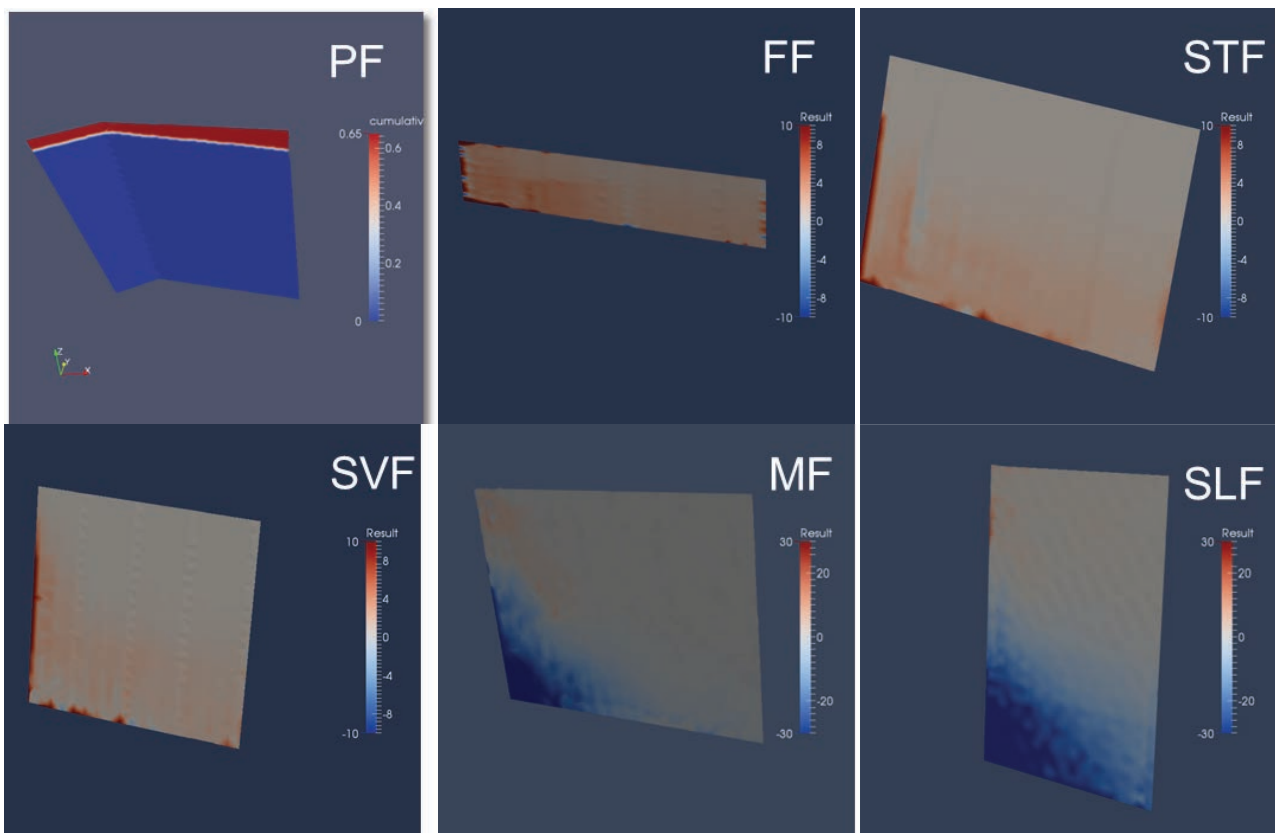


Figure 10. Left top): Distribution of slip in the upper part (250 m) of PF; stress changes on receiving faults of the eastern flank of Etna (Timpe system).

Section 2

Scientific Reports of Research Units (RU 1)

These results are preliminary but represent a valuable toll for a detailed study of fault interactions in a 3D realistic model of Mt. Etna. The FEM approach also permits to add the influence of the different elastic parameters of different lithologies at different depths and the influence of the weight of the volcanic edifice. Of course, it must be underlined that the huge work in which the research team has been involved for resolving many problems related to the large quantities of “computation power” needed for simulations, as well as the configuration of the 3D mesh of the volcano, has prevented to simulate the real cases occurred in the past.

Task 2 - WP 5, Resp. O. Cocina

Dynamics and kinematics of the eastern flank from seismological and ground deformation analyses

Participants: INGV-CT

Salvatore Alparone, Graziella Barberi, Ornella Cocina, Elisabetta Giampiccolo, Vincenza Maiolino, Carla Musumeci, Luciano Scarfi, Andrea Ursino

Other institutions:

INOGS-TS Angela Saraò

Sp1 - Space-time distribution of seismicity and strain release, also in relation with the main recharging phases of the volcano

During the first semester of the second year of the project, we analyzed a selected high quality dataset of earthquakes recorded from January 2005 to December 2013 by a number of digital stations and broadband sensors. In the second semester, we enlarged the dataset considering the 1999-2014 time span, to perform a more complete investigation of the study area. During this period seismicity has been influenced by intense earthquake swarms (for occurrence rate and energy) related to the opening of the eruptive fractures leading to the flank eruptions occurred in 2001, 2002 -2003 and 2008. On this basis, we also analyzed the relationship between the seismicity and the eruptive periods.

Firstly, we studied the seismicity in the whole Etna area and then we focused in two sectors of the eastern flank. A starting dataset of 8,351 1D located earthquakes with M_d between 0.3 e 4.4 has been selected on the basis of the following thresholds: $GAP \leq 250^\circ$, $NO \geq 6$, $RMS \leq 0.40$, ERH and $ERZ \leq 3.0$ km (Fig. 11a).

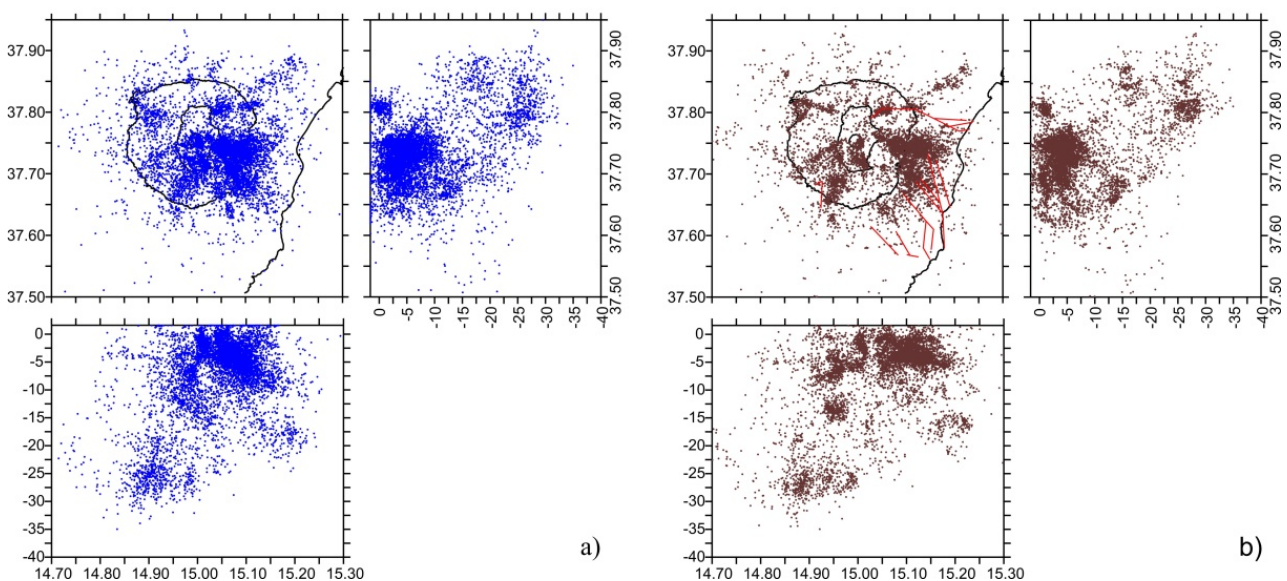


Figure 11. Epicentral maps and vertical cross-sections of the 7,095 earthquakes selected in the 1999 - 2014 time interval and located using: a) a 1D velocity model derived from Hirn et al. (1991); b) the 3D velocity model of Alparone et al. (2012) with TOMODDPS algorithm.

A final dataset of 7,095 seismic events was obtained using the 3D velocity model by Alparone et al. (2012) and TOMODDPS code (Zhang et al., 2009). This algorithm uses a combination of both absolute and differential arrival time readings between couple of events of an earthquakes cluster. It allows a better definition of the seismic clusters improving the quality of earthquake locations. In Fig. 11b it is evident that in the Etna area seismicity is not homogenously distributed and most of earthquakes occur in the eastern flank, involving different seismogenic levels. Shallow seismicity (up to 3 km b.s.l.) is located in the NE area of the volcano (Pernicana-Provenzana fault system) and in a volume located between the central craters and an area towards south. The larger volume is located in the central-eastern sector with seismogenic depths not exceeding 7 km. An area east of the Ragalna fault (Mt. Parmentelli area) involves crustal levels between 12 and 16 km and seems to be related to the recharging phases of the volcano (Cocina et al., 2010; Alparone et al., 2012). A deep seismogenic zone is located in the north western area of Etna, with foci between 20 and 30 km b.s.l.

The distribution of the most energetic and shallower events seems to delineate the limits of the instable sector of the volcano. Moreover, in the deepest levels seismicity appears to be related to the NW-SE trending Timpe fault system (Fig. 12). On the basis of the spatial distribution of seismicity and literature data, we recognised two sectors, A and B, the latter being very important for seismic hazard studies due to morphological evidences of the Timpe faults and the shallowness of the associated seismicity (Fig. 13).

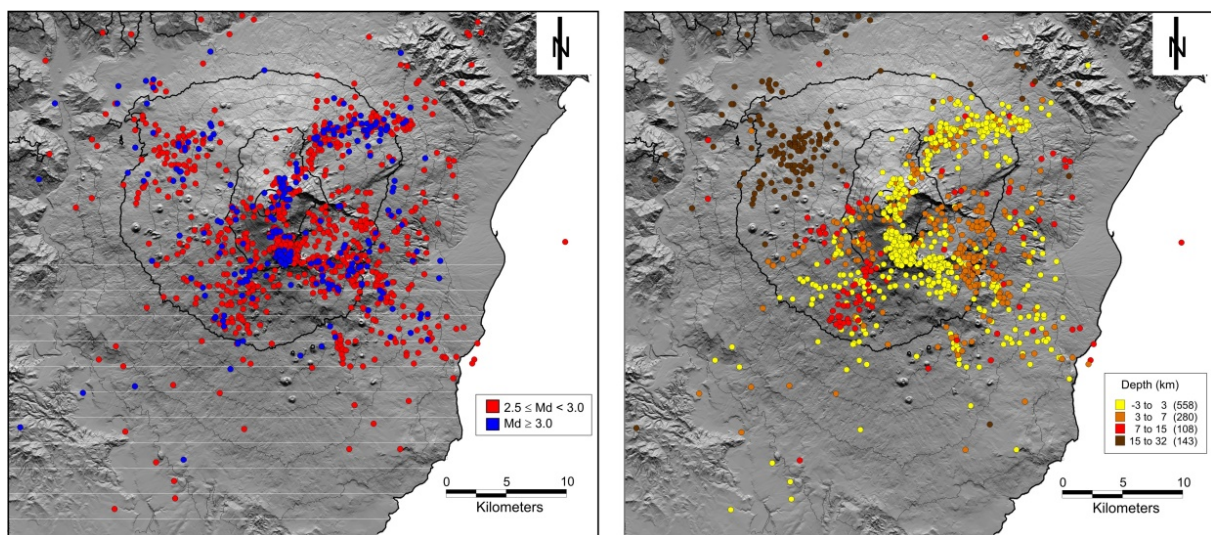


Figure 12. Epicentral map of the $M > 2.5$ seismicity reported according to different magnitude (on the left) and depth (on the right) classes.

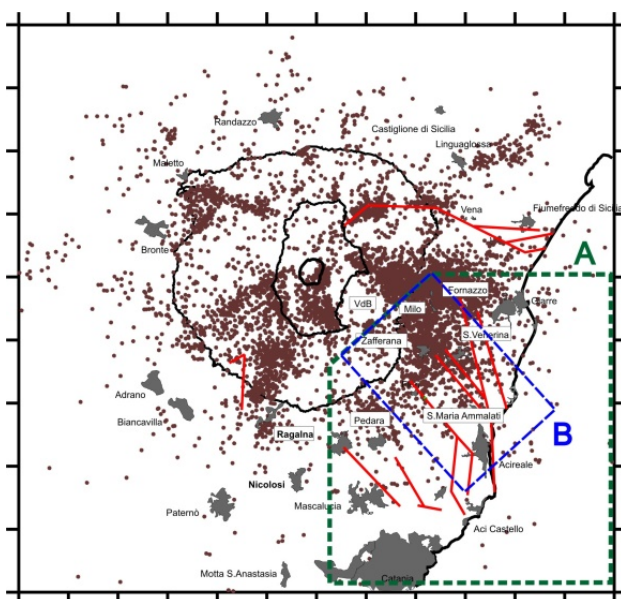


Figure 13. Epicentral map of the 7,095 re-located earthquakes and the identified sectors A and B. The main tectonic elements are also reported (from Azzaro et al., 2013).

Section 2
Scientific Reports of Research Units (RU 1)

The depth distribution of the earthquakes in the whole Etnean area and in sector A, evidences that the most of seismicity is located in the depth range 3-5 km b.s.l. (Fig. 14). With the aim to identify the main seismogenetic sectors, we also investigated the strain release patterns in the whole Etnean area and in sector A.

The time distribution of the earthquake occurrence rate and the strain release evidenced that during the studied period most of the energy release occurs in the eastern sector of the volcano (i.e. the sector located East of central craters).

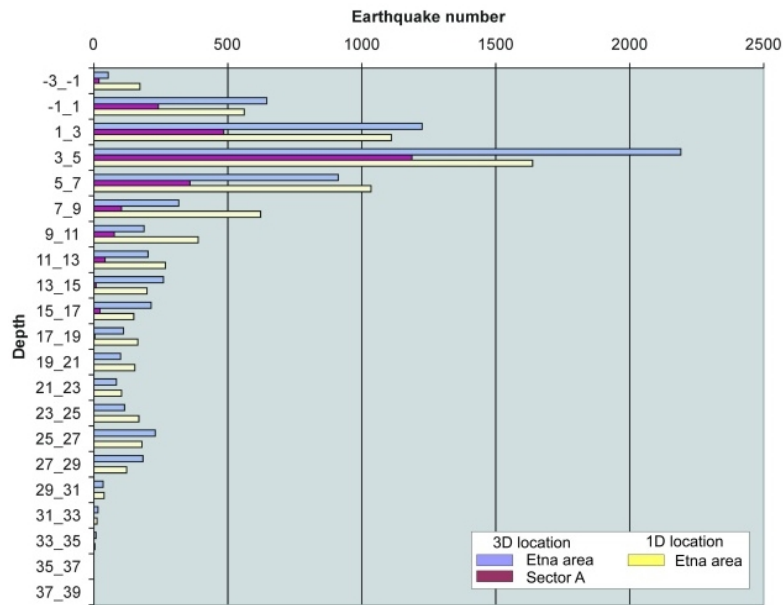


Figure 14. Earthquake depth distribution according to different classes.

Although sector A is not interested by eruptive swarms and does not include seismic activity of the Pernicana fault, it indeed shows a significant strain release (Fig. 15).

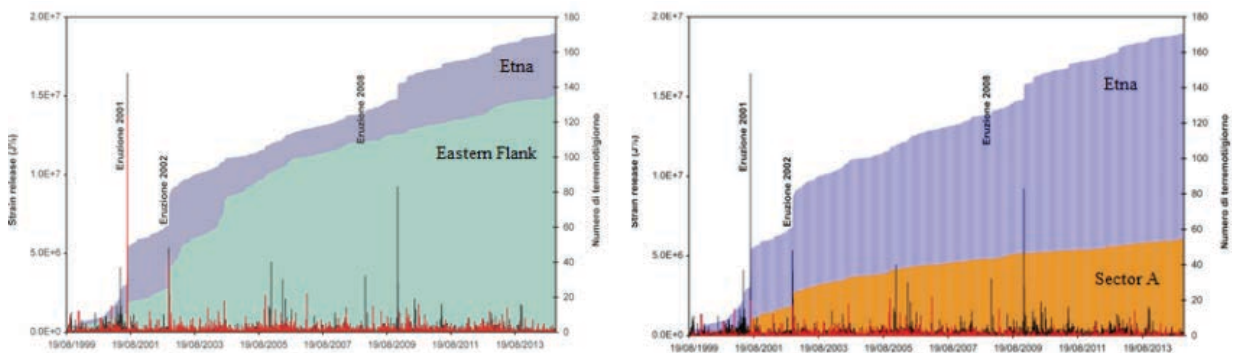


Figure 15. Time distribution of the cumulative strain release and daily occurrence of earthquakes in the Etnean area compared with those in the eastern sector (a) and sector A (b).

Furthermore, we analyzed kinematics of sector B, investigating the seismic swarms occurred during the studied period by excluding the eruptive phases of activity. On the basis of the location of the seismic swarms, five seismogenetic areas have been identified and reported in Fig. 16 (top). The shallowest seismic swarms (up to 3 km b.s.l.) occurred in the area of the Timpe fault system, characterized by major morphostructural evidence (yellow earthquakes). The other four sectors (violet, red, blu and green) include deeper crustal levels from 4 to 7 km b.s.l.

After individuating the main seismogenetic areas in this sector, we also investigate the time distribution of the seismic swarms but we do not identify any direct correlation with the eruptive phases (Fig. 16, bottom).

An important result is related to the spatial distribution of the strain release of the earthquakes occurred in sector A (Fig. 17). The highest values are due to the seismicity occurred in sector B, particularly in the volumes located between Zafferana and Valle del Bove (VdB in Fig. 13) and along the Fiandaca and S. Tecla faults, in the first 3 km of depth. The volume located in the northwestern part of sector B between Zafferana and Valle del Bove, seems to be influenced by the eruptive phases (Fig. 17a-b).

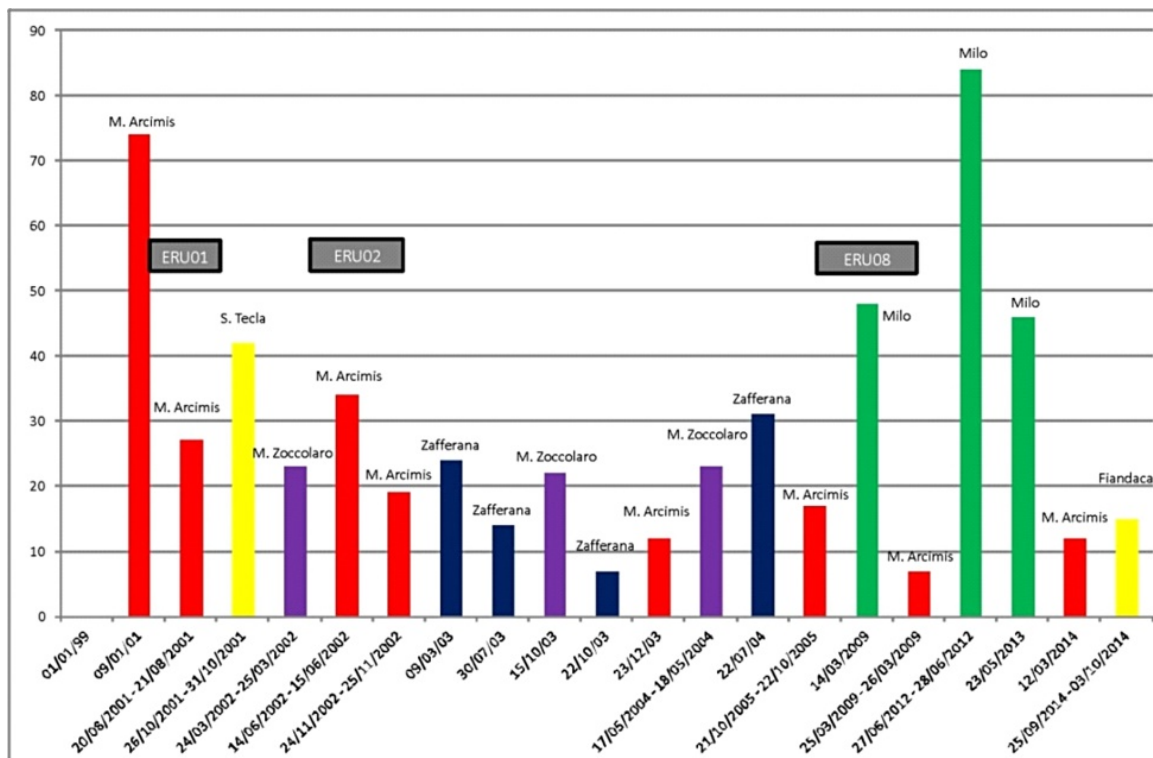
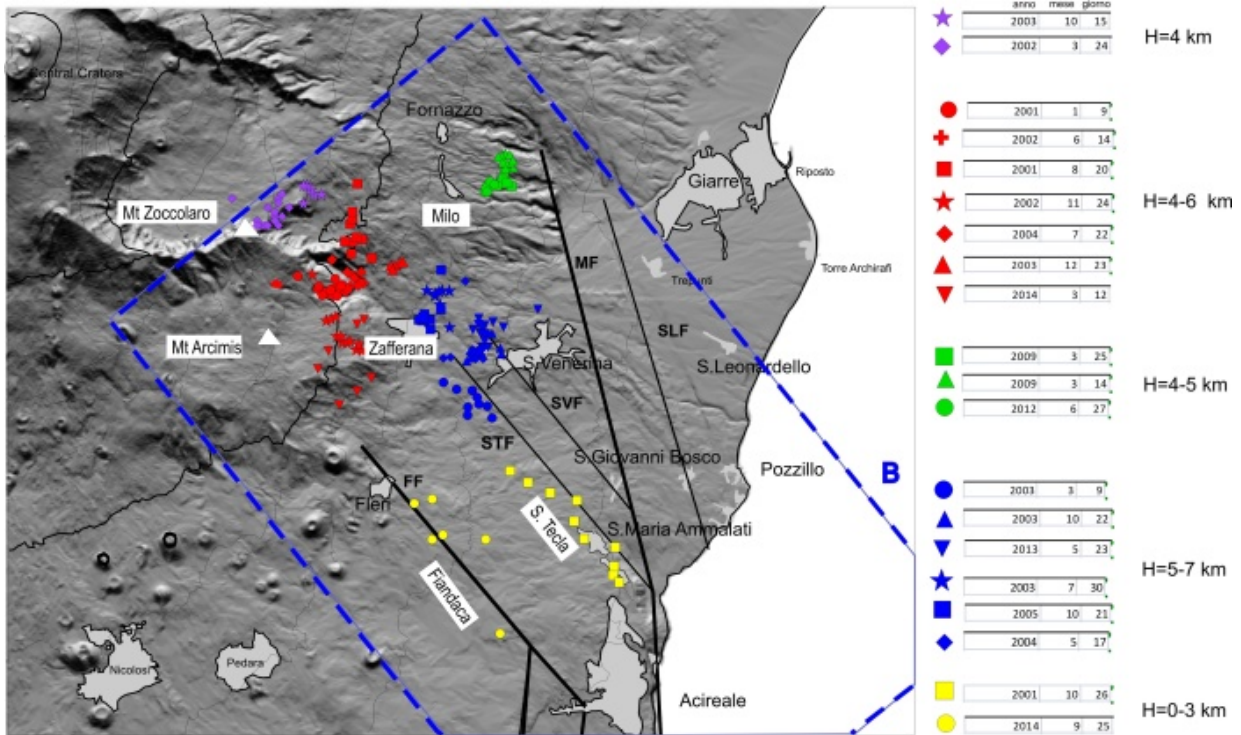


Figure 16. Top: epicentral distribution of the seismic swarms occurred in sector B during the study period (eruptive periods are not considered). Different colors and symbols are used for different seismogenic area and swarms, respectively. For each swarm the date, hour and the mean depth values are also reported. Bottom: time distribution of the swarms compared with the most eruptive phases.

Section 2
Scientific Reports of Research Units (RU 1)

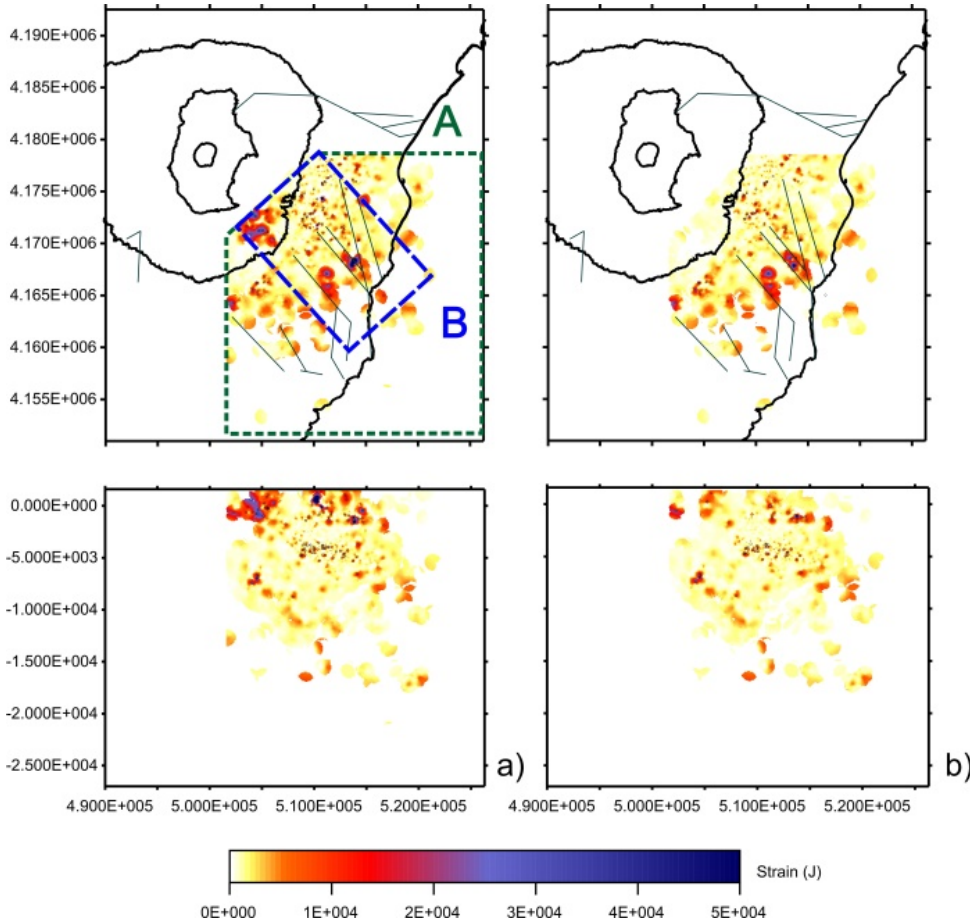


Figure 17. Epicentral maps and vertical sections of the strain release in sector A for the whole dataset (a) and for a subset in which the seismicity related to the 2001, 2002-2003 and 2008 eruptions has been eliminated (b). The main structural elements and sector B are also indicated. Black dots indicate the most energetic seismicity ($M_d \geq 2.8$) in the study period.

The analysis of fault plane solutions (FPS) in sector B (Fig. 18) highlights that in the Timpe area, earthquakes may be due to a right-lateral kinematics on planes oriented roughly NW-SE (blue FPS in Fig. 18). This is congruent with structural field data.

On the other hand, the focal mechanisms in the area north of sector B (red FPS in Fig. 18), where morphological evidences of tectonic structures are not visible, show a totally different kinematics. These may be linked to buried faults with dextral movements on NE-SW oriented planes (Alparone and Gambino, 2003; Alparone et al., 2013). The list of FPS considered in the analysis is reported in Tab. 6.

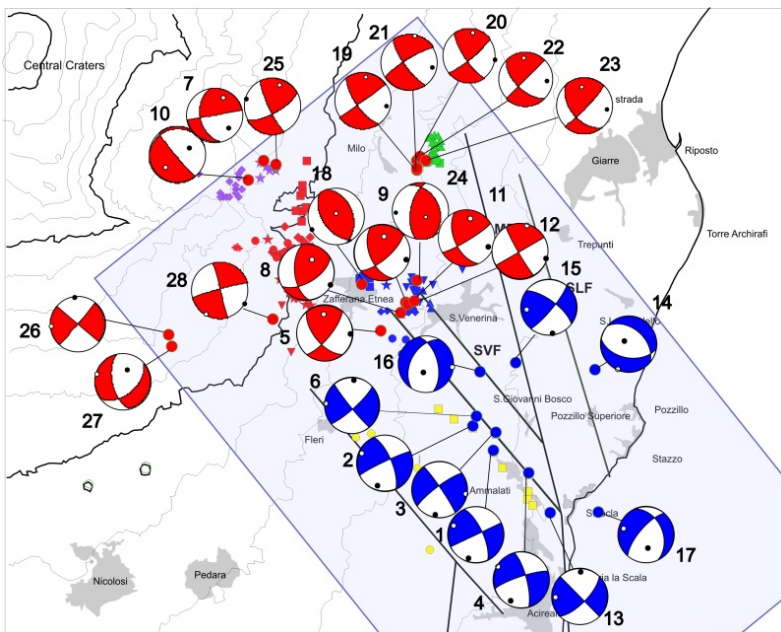


Figure 18. Fault plane solutions of a selected dataset of earthquakes (see Tab. 6) derived from Scarfi et al. (2013) catalogue, integrated with new focal solutions for less energetic earthquakes ($M < 2.7$).

N	date	hhmm	latN	lonE	h (Km)	Md
1	28/10/2001	903	37.649	15.150	1.56	3.5
2	28/10/2001	1505	37.655	15.143	2.08	3.2
3	31/10/2001	2206	37.654	15.151	2.41	2.9
4	31/10/2001	2343	37.643	15.161	3.50	2.8
5	09/03/2003	755	37.680	15.113	4.96	3.0
6	14/03/2003	342	37.658	15.144	2.14	2.9
7	15/10/2003	548	37.724	15.075	4.4	2.7
8	22/10/2003	1206	37.685	15.120	5.53	2.8
9	22/10/2003	1246	37.687	15.122	5.80	2.9
10	15/01/2004	1953	37.719	15.07	4.54	2.8
11	17/05/2004	2152	37.687	15.121	6.69	2.9
12	17/05/2004	2309	37.688	15.124	6.89	2.8
13	06/08/2004	907	37.633	15.168	2.75	2.3
14	19/06/2005	722	37.670	15.183	11.17	2.5
15	01/08/2007	2338	37.672	15.157	2.09	3.3
16	01/07/2009	123	37.669	15.146	1.44	3.0
17	25/08/2010	41	37.633	15.184	6.59	2.5
18	25/03/2012	2102	37.692	15.107	7	3
19	27/06/2012	2158	37.722	15.125	4.48	3.2
20	27/06/2012	2211	37.724	15.125	4.35	2.9
21	27/06/2012	2238	37.722	15.125	4.41	3.1
22	28/06/2012	242	37.725	15.126	4.51	3
23	28/06/2012	818	37.724	15.128	4.71	3.2
24	23/05/2013	1304	37.693	15.125	3.73	3.4
25	24/05/2013	247	37.723	15.079	4.41	3
26	09/10/2013	814	37.679	15.044	2.83	2.7
27	09/10/2013	833	37.676	15.045	2.71	2.7
28	12/03/2014	55	37.683	15.078	5.18	2.9

Table 6. Date, hour, ipocentral coordinates and M_d of FPS shown in Fig. 18.

Sp3 - Comparison among the scalar geodetic, geologic and seismic moments (resp. M. Palano)

Participants: INGV-CT

Raffaele Azzaro, Graziella Barberi, Flavio Cannavò, Ornella Cocina, Mimmo Palano, Luciano Scarfi

The comparison of seismic, geologic and geodetic moment-rates can provide crucial insights for understanding fault behaviour in tectonically active zone, with obvious implications on seismic hazard assessment. It is well acknowledged that when the seismic moment-rate is lower than geodetic or geologic ones, the exceeding moment-rate is released in aseismic mode. In fact, the observed geological and geodetic moment-rates include both elastic and inelastic deformations, and since only the elastic component is responsible for earthquakes, the comparison of these moment-rates with the seismic one does not balance in regions affected by creeping faults. It is the case of Etna, where slow aseismic slip due to fault creep is a common mode of displacement along many of the fault segments in the eastern flank. Therefore, taking advantage of the extensive geological and geophysical dataset available for Mt. Etna volcano, we applied such approach in order to estimate the seismic efficiency of the faults shown in Fig. 19.

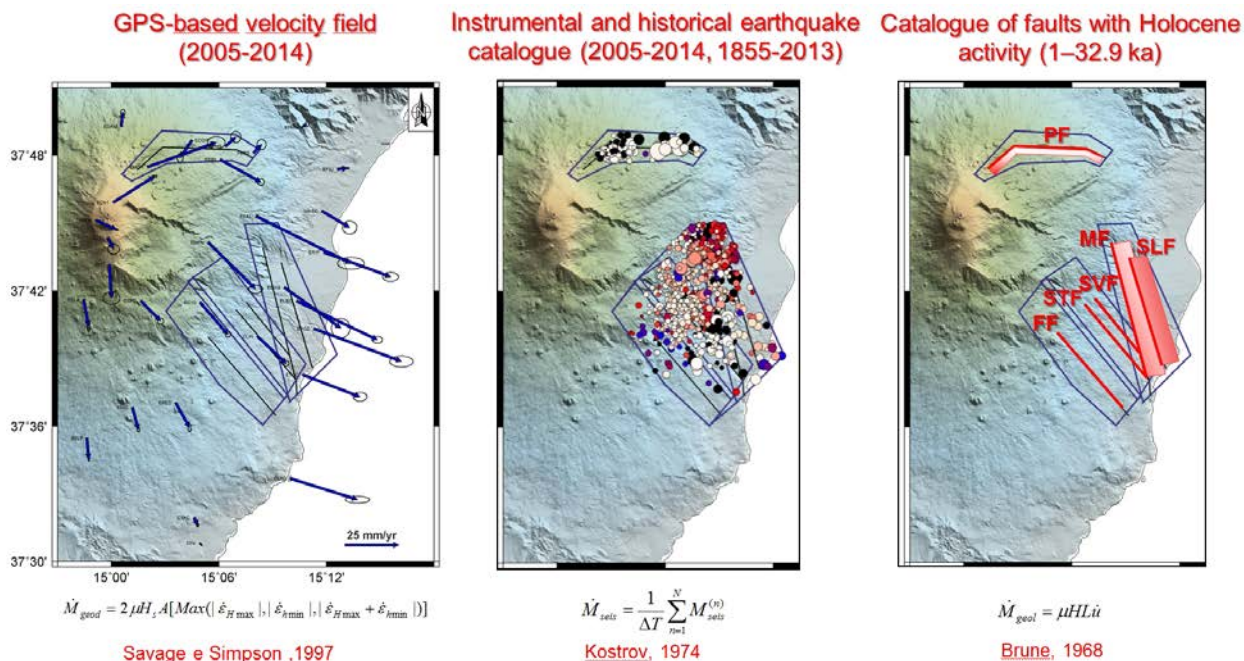


Figure 19. Study area, input data and formulations adopted. Abbreviations as in Fig. 1.

Geologic data

Evidence of active tectonics is mostly distributed over the whole eastern flank, with a number of faults forming two main structural systems: the Timpe faults and the Pernicana fault. The Timpe fault system (TFS) crosses the central part of the eastern flank and forms a wide belt of mainly extensional structures, striking from N to NW. These structures consist of well-developed morphological scarps as well as hidden fault segments. The Moscarello and S. Leonardello faults dissect the lower eastern flank, close to the coastal area and are characterized by prevailing vertical movements. The Fiandaca, S. Tecla and S. Venerina faults displace the middle-low eastern flank and show prevailing right-lateral features. The Pernicana fault consists of some ENE to E-W discrete segments which define a near continuous left-lateral shear zone dissecting the NE flank of the volcano. For each of these structures we collected geometric and kinematic parameters from published and unpublished studies (see Azzaro et al., 2013 and references therein), already used in WP 1 and 4 (see also Fig. 9 and Tab. 5). More in detail, for each structure we considered the following parameters: length, strike, dip, down-dip width, and slip-rate (if available, we used both short- and long-term estimations). Finally, by adopting the Brune's (1968) formulation, we estimated the geologic moment-rate for each of the considered structures.

Seismic data

To better define the seismotectonic features of the faults in the eastern flank of Etna, we considered both long- and short-term seismicity data. As regards the first ones, we used the huge historical data set represented by the macroseismic catalogue of earthquakes occurring at Etna from 1832 to 2013 (CMTE Working Group, 2014). For the analysis we selected major events located in the eastern flank, i.e. 167 shocks with epicentral intensity $I_0 \geq V$ EMS (above the damage threshold) corresponding to an equivalent magnitude $M_L \geq 3.0$ (Azzaro et al., 2011). The above thresholds represent a portion of the catalogue statistically complete, so these earthquakes may be considered representative of the seismic cycle in the long-term (Azzaro et al., 2012b). Regarding the short-term, we used the instrumental data set above presented in *Sp1*, covering the time interval from 2005 to 2014. The choice of this time-span is justified by the development of a modern seismic network, equipped with digital stations and broad-band sensors, allowing the detection of small magnitude events and hence the application of advanced techniques for locating epicenters. Taking into account the spatial distribution of the active faults and their seismogenic thickness we divided the investigated volume into prismatic bodies. In particular, we defined 4 small prismatic bodies containing a single fault (PF and FF in Fig. 19) or a couple of faults (MF-SLF and STF-SVF) and a large prismatic body containing all Timpe faults. The seismic moment-rate was calculated

according to the Kostrov (1984) general formulation which takes into account the number of events occurred in the selected prismatic body during the considered time interval. By considering both instrumental and historical earthquake catalogues, we performed two different computations.

Geodetic data

Available GPS observations collected by the Mt. Etna Permanent GPS Network, spanning 2005 - 2013 time interval and covering the eastern flank of Mt. Etna, have been processed using the GAMIT/GLOBK software. Estimated geodetic velocities refer to the so-called “Etn@ref” reference frame, a local reference frame computed to isolate the Mt. Etna volcanic deformation from the background regional tectonic pattern (see Palano et al. 2010 for details). Taking into account the observed horizontal velocity field and associated covariance information, we computed the expected velocity values at the nodes of the surface projection of each prismatic body and as a second step we derived the average 2D strain-rate tensor at the centre of each selected surface. Finally, by adopting the Savage and Simpson’s (1997) formulation, we estimated the geologic moment-rate for each prismatic body.

Results

Estimated moment-rates are reported in Fig. 20. Main results clearly indicate that i) the geodetic moment-rate estimations are generally larger than the seismic and the geologic ones and ii) the geologic moment-rate estimations are larger than the seismic ones. Although a number of reasons may account for the observed discrepancy - uncertainties on geodetic strain rates estimations related to the station coverage; uncertainties of the geologic slip-rate estimations; not well constrained geometry of modelled faults; limited length of the instrumental earthquake catalogue - it must be also considered the presence of buried/hidden fault segments accommodating a part of deformation, not included in our computation.

In conclusion, the relevant difference among the estimated moment-rates, confirms that a large amount of the deformation at Etna occurs aseismically along faults in the eastern flank, as suggested by field observations. This study provides, for the first time, an analytical estimation of creep processes by means of the deficit of seismic moment-rate calculated with respect the geodetic one. This may be viewed as a proxy of loading processes on locked fault segments prone to seismic failure.

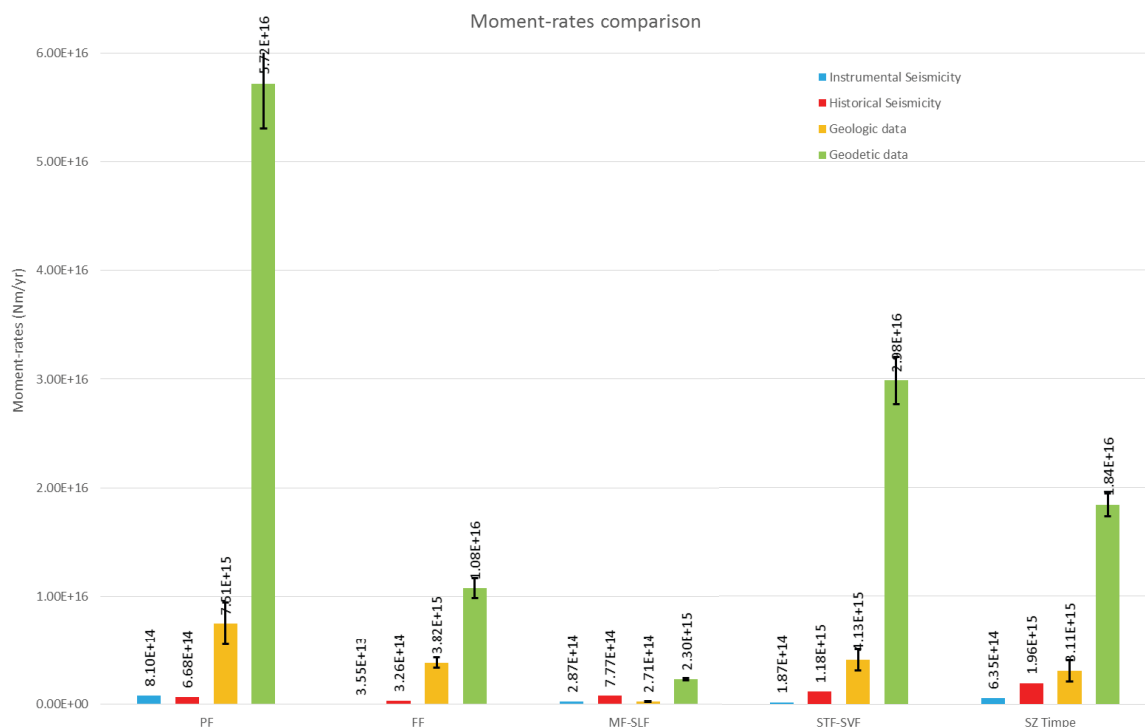


Figure 20. Geological, sismological and geodetic moment-rates obtained for the analysed structures. Fault abbreviations as in Fig. 19.

Task 3 - WP 10, Resp. S. Gambino
Definition of the time-space dynamics of the Lipari-Vulcano tectonic system

Participants: INGV-CT

Salvatore Alparone, Alessandro Bonforte, Salvatore Gambino, Francesco Guglielmino, Antonio Scaltrito, Rosanna Velardita

Other institutions:

INGV-OV Francesco Obrizzo

The WP10 purpose is the geophysical characterization of the different sectors of the Lipari-Vulcano system (Piano, La Fossa Caldera, La Fossa cone, Vulcanello and southern Lipari) in order to define tipology and time-space features of tectonic/volcanic sources active in the last 40 years.

In the first year of the project we reconstructed ground deformation and seismic data series (Fig. 21) covering the 1974-2013 period. We realized a database of the vertical displacements time series for the main benchmarks of precise levelling measured since 1976. We reconstructed the slope distances database since 1974 considering EDM (until 1996) and successively GPS and tilt series (since 1994). Moreover we realized the seismic catalogue of the Aeolian Archipelago starting from 1983

by integrating data from ING, INGV, IIV-CNR.

At the Lipari-Vulcano scale, EDM-GPS and levelling data show strong changes linked the seismic crisis in the late 70s (Bonafede, 1995; Bonaccorso, 2002). Subsequently we recorded a fairly constant slope distances shortening (regional in Fig. 21) linked to transpressive kinematics of the Lipari - Vulcano complex, with a main dextral component of displacement along the NNW - SSE regional tectonic structure (Bonforte and Guglielmino, 2008). No particular changes characterized the Piano area while contraction and subsidence affected La Fossa Caldera and Vulcanello. It is noteworthy the significant increase of subsidence recorded by levelling in the period 1999-2013, also visible in the shortening of lines inside caldera and tilt.

At the small scale of La Fossa cone, EDM measurements showed significant variations, suggesting an inflation of the cone measured on the top of the crater (Fig. 22, phase 1) until 1990, followed by an elongation (phase 2). Levelling data and

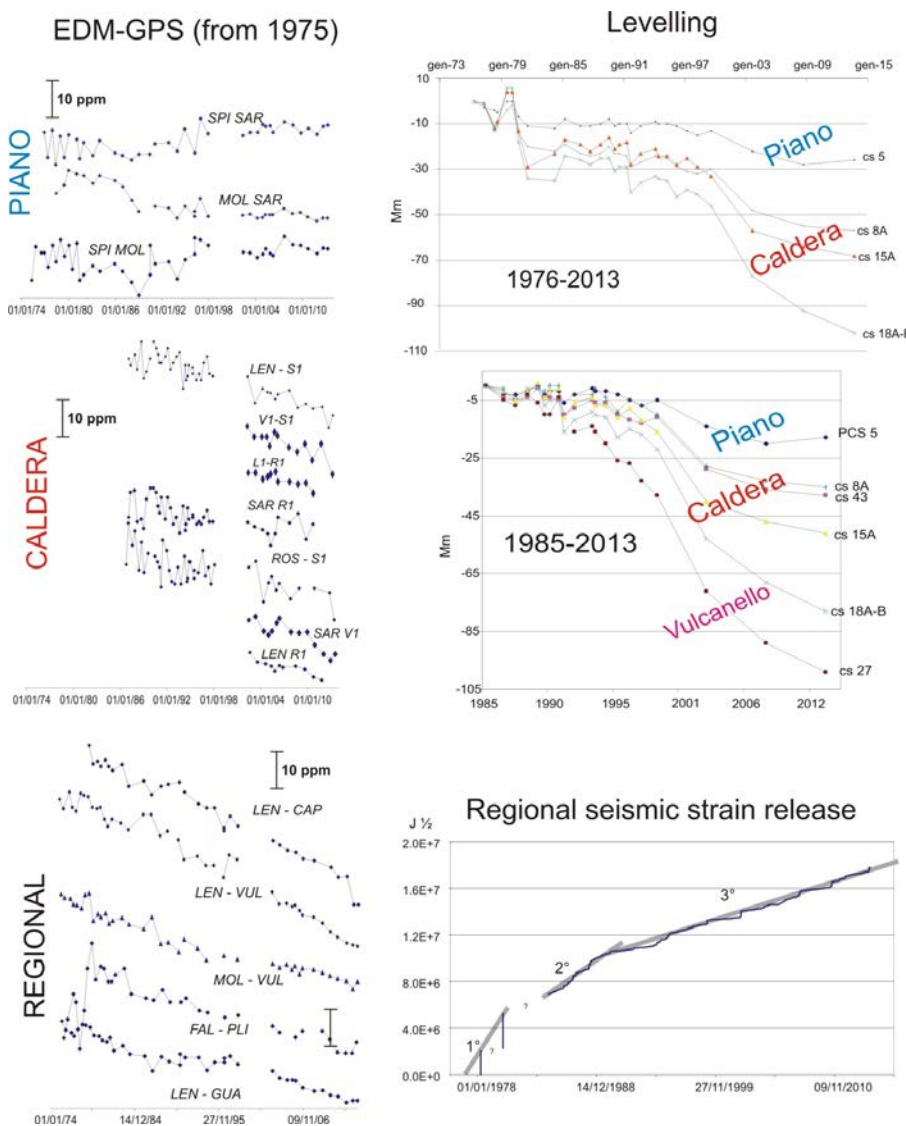


Figure 21. Slope distances measured by EDM/GPS and height variations of reference benchmarks (by levelling) related to the Piano, Caldera and Vulcanello areas. Slope distances crossing the NNW-SSE regional structure are reported in the low graph close to seismic strain release of the Aeolian archipelago. The 1978-1982 strain release considers only the 15/04/1978, M=5.5 and 28/05/1980, M=5.7 events.

measurements of the EDM network installed in 1987 on the cone, showed in 1990-97 a deflation caused by a shallow subvertical source (Gambino and Guglielmino, 2008) positioned below the crater. This model is consistent with an increased activity in a shallow hydrothermal system of water evaporation, as testified by the increase of steam emission and temperature at crater fumaroles. The fluid loss from a shallow geothermal reservoir is the cause of the subsidence recorded. Since the end of 90s, minor variations have affected La Fossa cone.

In short, three main sources act on the Lipari-Vulcano system:

- regional tectonics;
- dynamics of the caldera (unknown);
- dynamics concerning La Fossa cone.

In order to define the caldera related source, we performed a joint data inversions by using 19 slope distances and 14 vertical changes, measured in 1999-2013, and for the minimization process we used a Genetic Algorithm (GA) implemented by Nunnari et al. (2005).

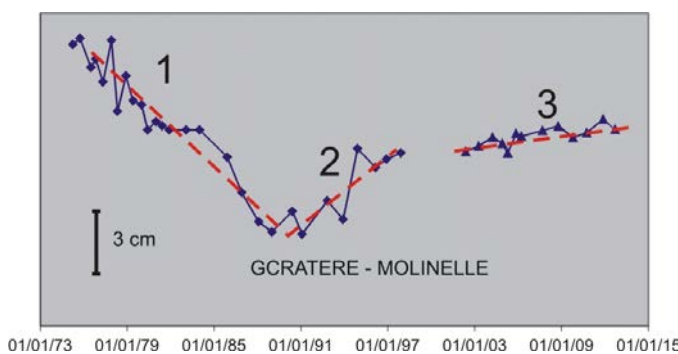


Figure 22. GCratere-Molinelle slope distance changes (EDM until 1996, GPS since 2002).

We obtained two sources, a tabular dislocation consistent with the previous models (e.g. Bonforte and Guglielmino, 2008) and a deflating source located under Vulcanello, 4.6 km b.s.l. deep (Fig. 23). The model fits well the data furnishing mean differences less than 1 mm/year between calculated values and recorded ones.

The volcanic source is located inside the shallow (3-5 km) magma storage zone defined by Peccerillo et al. (2006), fits well with the estimated crustal velocities and Bouguer anomalies of Ventura et al. (1999) and with results of WP 13, which indicate the same geochemical composition of noble gases on fumarolic fluid and the more recent latite lava flows of Vulcanello.

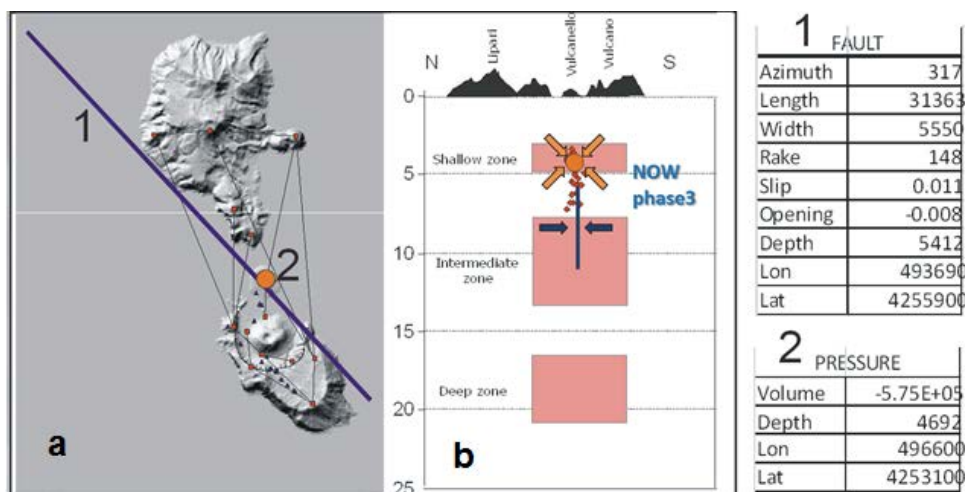


Figure 23. Map (a) and NNW-SSE section (b) of the sources obtained by 1999-2013 data inversion. The section also shows the Peccerillo et al. (2006) model for the internal structure of the magma storage system in the crust, and high precision seismicity (red dots) reported in Gambino et al. (2012).

Task 4 - WP 14

Slope instability hazard maps

Participants: INGV-CT

Luigi Lodato, Francesco Guglielmino, Alessandro Bonforte

Sp3 - FLIR and GB-RAR measurements on the Forgia Vecchia (Vulcano) in order to test the potential applications for detecting slope movements and weak points of rock mass (resp. L. Lodato)

Infrared thermal measurements

In the first year of the project the activity was focused (June 2013, see first annual report) on the acquisition of thermal images in the northern area of La Fossa Crater, particularly the Forgia Vecchia. The methodology had the objective to map the distribution of temperatures for the recognition of weaknesses in the rock mass. They vary according to:

- fumarolic activity;
- primary permeability and secondary permeability due to the presence of fractures and discontinuity;
- lithology of volcanic rocks, in our case of pyroclastic origin, with thickness varying from centimetre to metres;
- discontinuities between layers with different competence and low permeability;
- slope erosion.

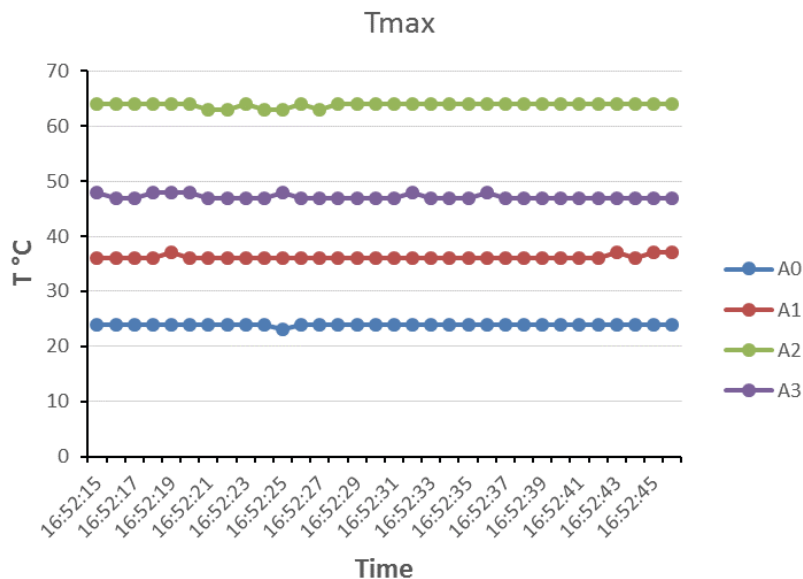


Figure 24. Plot of the areas analysed with thermal images on 20 June 2015, maximum temperature vs. time.

In June 2015, we acquired a new series of data with the same portable thermal camera (FLIR 660) at a distance of 700 metres, with the instrument installed at the terrace of hotel “Faraglione”. The measurements were performed in late afternoon with optimal condition of cloud cover. The data collected during this second campaign were elaborated with the software RESEARCHER IR MAX, obtaining the temperature curves as a function of elapsed time (Fig. 24).

Patterns of different thermal anomalies have been identified near areas of fractures and erosion along the slope. The surveys have confirmed the presence of three areas with significant thermal anomalies, already identified in the first year of the project (Fig. 25). The area A0 is a target at constant temperature, the A2 area affecting the upper part most fractured in 2015, has recorded a temperature of 64° C; the A3 area is affected by two factors:

- in the upper part, as the area A2, the anomalies are related to fracturing occurring in 2015, with temperatures diminished to 47° C;
- in the lower part, slope erosion intercepts lower lithological levels, varying the low permeability and temperature, in this case 45° C.

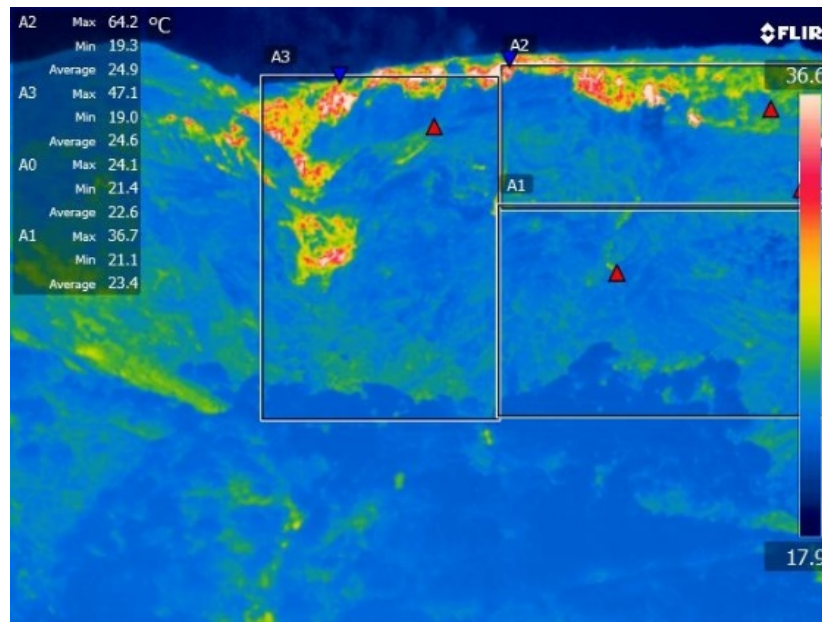


Figure 25. Thermal images of the study area and the identified sectors (white boxes).

Finally, also in area A1, in most erosive engraving points, we localize thermal anomalies with values of 36.5° C.

On the whole, the Forgia Vecchia area is cooling with probable deflection (Tab. 7).

Aree	A2	A3	A3 Monte	A3 Valle	A0	A1	T
2013	70	59	60	55	23	46	°C
2015	64	47	47	45	24	37	°C
Delta T	-0,6	-12	-13	-10		-9	

Table 7. Comparison of temperatures in the different sectors identified and variations between 2013 and 2015.

Ground-Based Radar measurements

In order to integrate the temperature measurements, it was decided to compare thermal data with deformation data obtained through the use of interferometric techniques. The deflection measurements were produced by a radar from the ground, which guarantee the acquisition of the deformation data in continuous, and a resolutions comparable with the temperature measurements made by thermal camera.

The instrument used is the GPRI-II produced by GAMMA, normally used in non-volcanic situations (monitoring of glaciers and landslides rapidly changing). The GPRI-II is a radar Ku-band (about 1 cm in wavelength) having an usege range between 50 m and 10 Km, a resolution of 0.75 m and a resolution in azimuth variable as a function of distance. The GPRI-II is able to measure ground deformations with a precision and accuracy of less than 1 mm.

In our case, thanks to the project VULCAMED, this instrument was recently acquired by INGV-CT but due to a delay in delivery, it was possible only to make a single measurement campaign instead of the two ones scheduled. In practise, we cannot provide the deformation rates of the Forgia Vecchia area but we consider this reference measurement as a test to evaluate the potential applicability of the instrument. In particular, we have installed the GPRI close to the thermal camera in order to provide the interferometric measurements as comparable as possible with the thermal measurements (Fig. 26).



Figure 26. Installation GPRI-II near the thermal camera (terrace of hotel Faraglioni): details of the headframe of the GPRI-II and the equipment (three antennas, one of which transmitter and two receivers).

Interferometric measurements performed in June 2015 will be used as a start measure for future analyses.

The GPRI-II is equipped with a transmitting antenna (Tx1) and two receiving antennas (Rx1 and Rx2) to calibrate and correct the interferometric measurements affected by a high atmospheric noise. Thanks to this particular configuration, it has been possible to generate an interferometric DEM of the examined area, with resolution of 0.75 m x 6 m (Range x Azimuth), which was geocoded using the SRTM DEM (~ 90 m resolution) and subsequently corrected by using an orthoimage having a resolution of 1 m (Figs. 27, 28).

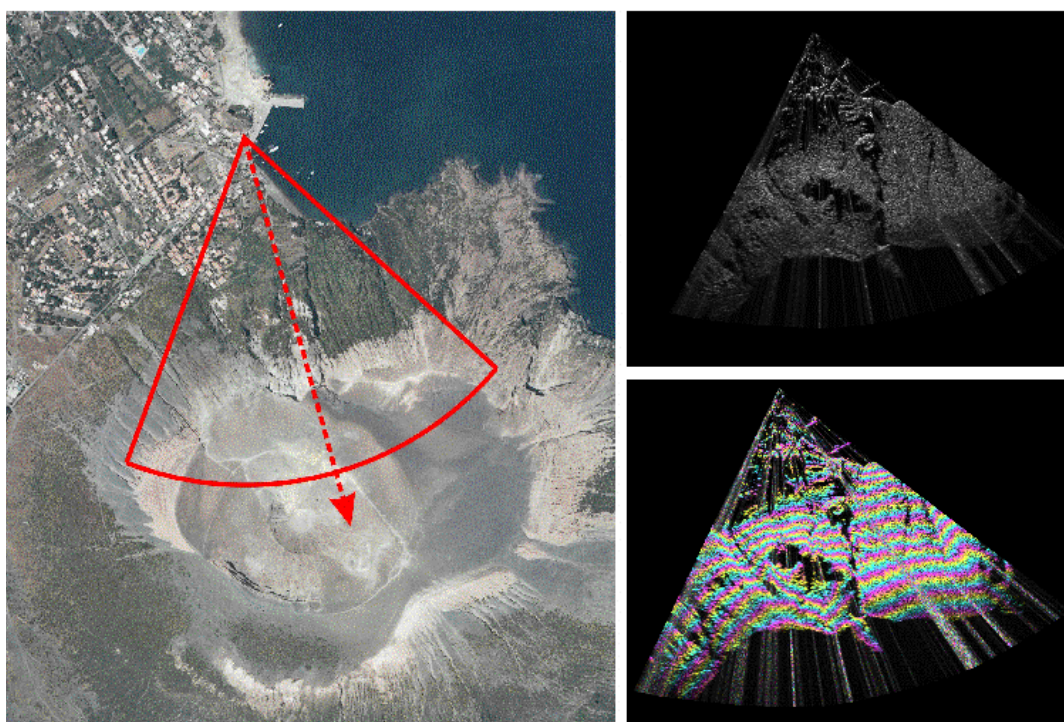


Figure 27. Left: the area of acquisition of GPRI-II; right: images of amplitude (top) and phase (bottom).

The test GPRI-II has been successfully carried out, showing the applicability of this instrument for the study of ground deformation and morphometric analyses of the area of Forgia Vecchia.

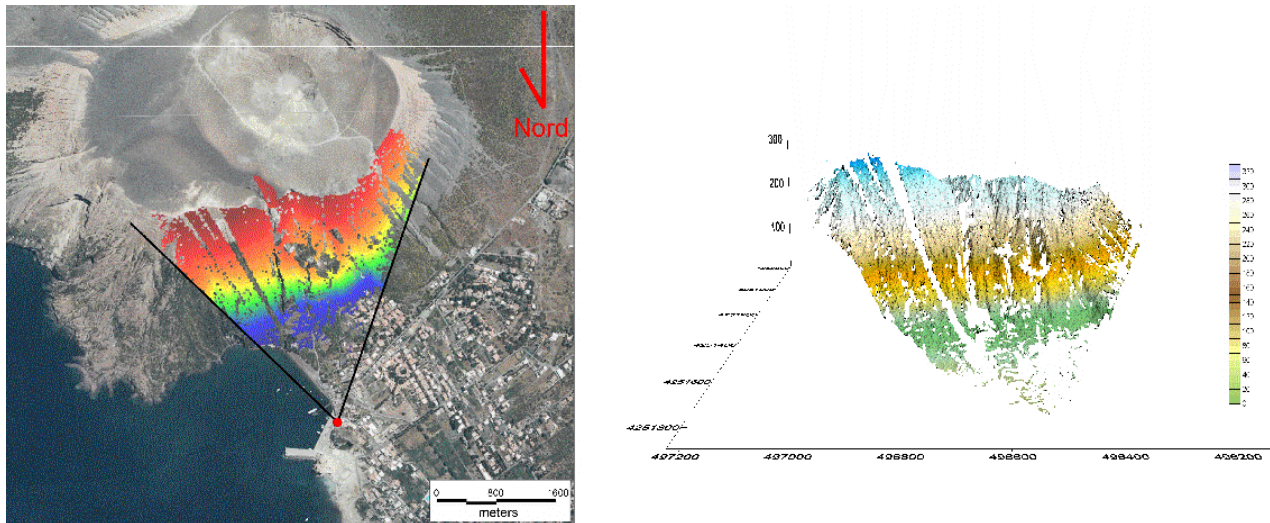


Figure 28. Interferometric DEM of the Forgia Vecchia area.

Deliverables

- WP 1.Sp2 Characterization of the seismic sources: **100%**.
 WP 2.Sp1 Upgrade of spectral GMPE for volcanic earthquakes: **100%**.
 WP 4.Sp1 Fault interaction in the Timpe fault system: implementation of stress simulator: **70%**.
 WP 5.Sp1 Space-time distribution of seismicity and strain release, also in relation with the main recharging phases of the volcano: **100%**.
 WP 5.Sp3 Comparison between the scalar geodetic, geologic and seismic moment: **100%**.
 WP 10.Sp1 Definition of areas with common dynamics: **100%**.
 WP 10.Sp2 Ground deformation maps over different time windows: **100%**.
 WP 14.Sp3 Map of the slope movements and weak points of rock mass in the Forgia Vecchia area from ground-based radar and thermal infrared measurements: **70%**.

Problems and difficulties

- WP 4.Sp1 The activity suffered a delay for administrative problems regarding the approval of contract between INGV-OE and UNI-CT (started on October 6).
 WP 14.Sp3 The Ground-Based Radar, acquired on other funds, has been delivered in May. This caused the first field campaign for reference measurements to be carried out in June, i.e. at the end of the project.

Key publications

- Alparone S., Bonforte A., Gambino S., Guglielmino F., Obrizzo F., Velardita R. (2014). *Dynamics of Vulcano Island investigated by long-term (40 years) geophysical data*. Miscellanea INGV, n 25 Conferenza Rittmann, 29-31 Ottobre 2014.
 Alparone S., Bonforte A., Gambino S., Obrizzo F., Guglielmino F., Scaltrito A., Velardita R. (2014). *Dinamica del sistema Lipari-Vulcano attraverso deformazioni del suolo e sismicità degli ultimi 40 anni*. Convegno GNGTS 2014 Bologna Novembre 2014.
 Azzaro, R., D'Amico S., Pace B., Peruzza L., (2014). *Estimating the expected seismicity rates of volcano-tectonic earthquakes at Mt. Etna (Italy) by a geometric kinematic approach*. Extended abstract presented

Section 2

Scientific Reports of Research Units (RU 1)

at the 33° Convegno Nazionale GNGTS, Bologna (Italy), November 25-27, 2014.

Azzaro R., Barberi G., Cannavò F., Cocina O., Palano M., and Scarfi L. (2015). *Assessing seismic efficiency from scalar moment-rates: an application to Mt. Etna volcano (Italy)*. 6th International INQUA Meeting on Paleoseismology, Active Tectonics and Archaeoseismology. Miscellanea INGV, n. 27, 19-24, April 2015, Pescina, Fucino Basin, Italy, Extended abstracts, p. 32-37.

Barberi G., Cannavò F., Cocina O., Palano M., Scarfi L., and Azzaro R. (2014) *Comparing seismic, geodetic and geologic scalar moment-rates at Mt. Etna volcano (Italy): some preliminary results for seismogenic zones in the eastern flank*. Extended abstract presented at the 33° Convegno Nazionale GNGTS, Bologna (Italy), November 25-27, 2014, 32-37.

Bonforte A., Alparone S., Gambino S., Guglielmino F., Obrizzo F., Velardita R. (2014). *Dynamics of Vulcano Island investigated by long-term (40 years) geophysical data*. DOI: 10.13140/2.1.2133.1205 Conference: Cities on Volcanoes 8, Yogyakarta, Indonesia.

Bonforte A., Alparone S., Gambino S., Guglielmino F., Obrizzo F., Velardita R. (2014). *Investigation of the Volcano-tectonic dynamics of Vulcano Island by long-term (40 years) geophysical data*. Geophysical Research Abstracts, Vol. 17, EGU2015-PREVIEW, 2015 Vienna EGU General Assembly April 2015.

Other references

WP 1

Alparone S., Maiolino V., Mostaccio A., Scaltrito A., Ursino A., Barberi G., D'Amico S., Giampiccolo E., Musumeci C., Scarfi L., Zuccarello L. (2012). *Instrumental seismic catalog of Mt. Etna (Sicily, Italy) in the period between 2000 and 2010*. Miscellanea INGV, n. 15.

Alparone S., Maiolino V., Mostaccio A., Scaltrito A., Ursino A., Barberi G., D'Amico S., Di Grazia G., Giampiccolo E., Musumeci C., Scarfi L., Zuccarello L. (2015). *Instrumental seismic catalogue of Mt Etna earthquakes (Sicily, Italy): ten years (2000-2010) of instrumental recordings*. Annals of Geophysics, 58 (4), S0435.

Azzaro R., Branca S., Gwinner K., Coltelli M. (2012a). *The volcano-tectonic map of Etna volcano, 1:100.000 scale: morphotectonic analysis from high-resolution DEM integrated with geologic, active faulting and seismotectonic data*. It. J. Geosci. (Boll. Soc. Geol. It.), 131 (1), 153-170.

Wiemer S. (2001). *A software package to analyse seismicity: ZMAP*. Seism. Res. Lett., 72, 373-382.

WP 2

Ambraseys N.N., Simpson K.A., Bommer J.J. (1996). *Prediction of horizontal response spectra in Europe*. Earth Eng. Struct. Dyn., 25:371-400.

Bindi D., Pacor F., Luzi L., Puglia R., Massa M., Ameri G., Paolucci R. (2011). *Ground motion prediction equations derived from the Italian strong motion database*. Bull. Earth. Eng., 9:1899-1920. doi 10.1007/s10518-011-9313-z.

Boore D.M., Atkinson G.M. (2008). *Ground-motion prediction equations for the average horizontal component of PGA, PGV, and 5%-damped PSA at spectral periods between 0.01 s and 100 s*. Earth Spectra, 24:99-138.

Joyner W.B., Boore D.M. (1981). *Peak horizontal acceleration and velocity from strong motion records including records from the 1979 Imperial Valley, California, earthquake*. Bull. Seism. Soc. Am., 71: 2011-2038.

Sabetta F., Pugliese A. (1987). *Attenuation of peak horizontal acceleration and velocity from Italian strong-motion records*. Bull. Seism. Soc. Am., 77:1491-1513

WP 5

Alparone S., D'Amico S., Gambino S., Maiolino V. (2013). *Buried active faults in the Zafferana Etnea territory (south-eastern flank of Mt. Etna): geometry and kinematics by earthquake relocation and focal mechanism*. Annals of Geophysics, 56, 1, R0112; doi:10.4401/ag-5758.

Alparone S., Gambino S. (2003). *High precision locations of multiplets on south-eastern flank of Mt. Etna (Italy): reconstruction of fault plane geometry*. Physics of the Earth and Planetary Interiors, 135, 281 -289.

Alparone S., Barberi G., Cocina O., Giampiccolo E., Musumeci C., Patanè D. (2012). *Intrusive mechanism of the 2008-2009 Mt. Etna eruption: constraints by tomographic images and stress tensor analysis*. J. Volcanol. Geotherm. Res., 229, 50-63. doi: 10.1016/j.jvolgeores.2012.04.001.

- Azzaro R., Bonforte A., Branca S., Guglielmino F. (2013). *Geometry and kinematics of the fault systems controlling the unstable flank of Etna volcano (Sicily)*. Journal of Volcanology and Geothermal Research, 251, 5-15.
- Azzaro R., Bonforte A., Branca S. & Guglielmino F. (2013). *Geometry and kinematics of the fault systems controlling the unstable flank of Etna volcano (Sicily)*. Journal of Volcanology and Geothermal Research, 251, 5-15, doi: 10.1016/j.jvolgeores.2012.10.001.
- Azzaro R., D'Amico S. & Tuvè T. (2011). *Estimating the magnitude of historical earthquakes from macroseismic intensity data: new relationships for the volcanic region of Mount Etna (Italy)*. Seism. Res. Lett., 82, 4, 533-544.
- Azzaro R., D'Amico S., Peruzza L. & Tuvè T. (2012b). *Earthquakes and faults at Mt. Etna (southern Italy): problems and perspectives for a time-dependent probabilistic seismic hazard assessment in a volcanic region*. Bollettino di Geofisica Teorica ed Applicata, 53, 75-88.
- Brune J.N. (1968). *Seismic moment, seismicity and rate of slip along major fault zones*. Journal of Geophysical Research, 73 (2), 777-784, doi:10.1029/JB073i002p00777.
- CMTE Working Group (2014). *Catalogo Macrosismico dei Terremoti Etnai, 1832-2013*. INGV, Catania, http://www.ct.ingv.it/macro/etna/html_index.php.
- Cocina O., Barberi G., Giampiccolo E., Milluzzo V., Musumeci C., Sicali S., Patanè D. (2010). *Seismic activity at Mt. Etna from July 2005 to January 2006: evidence of a deep magmatic intrusion leading to the 2006 eruption*. EGU General Assembly 2011. Geophysical Research Abstracts, 12, EGU2010-9267.
- Hirn A., Necessian A., Sapin M., Ferrucci F., Wittlinger G. (1991). *Seismic heterogeneity of Mt Etna: structure and activity*. Geophys. J. Int., 105, 139-153. doi:10.1111/j.1365-246X.1991.tb03450.x.
- Kostrov B. (1974). *Seismic moment and energy of earthquakes and seismic flow of rock*. Izv. Acad. Sci. USSR, Phys. Solid Earth, 1, 23-40.
- Palano M., Aloisi M., Amore M., Bonforte A., Calvagna F., Cantarero M., Consoli O., Consoli S., Guglielmino F., Mattia M., Puglisi B. & Puglisi G. (2006). *Kinematic and strain analyses of the eastern segment of the Pernicana fault (Mt. Etna, Italy) derived from geodetic techniques (1997 - 2005)*. Annals of Geophysics, 49 (4/5), 1105-1117, doi: 10.4401/ag-3103.
- Rasà R., Azzaro R. & Leonardi O. (1996). *Aseismic creep on faults and flank instability at Mt. Etna volcano*. In: Volcano instability on the Earth and other planets (McGuire W.J., Jones A.P., Neuberg J. eds). Geological Society, London, Special Publications, 110, 179-192, doi: 10.1144/GSL.SP.1996.110.01.14.
- Reasenber P., Oppenheimer D. (1985). *FPPFIT, FPLOT and FPPAGE: Fortran computer programs for calculating and displaying fault plane solutions*. US Geol Surv Open File Rep., pp 85-739.
- Savage J.C. & R.W. Simpson (1997). *Surface strain accumulation and the seismic moment tensor*. Bulletin of the Seismological Society of America, 87, 1345-1353.
- Scarfì L., Messina A., Cassisi C. (2013). *Sicily and Southern Calabria focal mechanism database: a valuable tool for the local and regional stress field determination*. Annals of Geophysics, 56, 1, D0109; doi:10.4401/ag-6109.
- Zhang H., Thurber C., and Bedrosian P. (2009). *Joint inversion for V_p , V_s , and V_p/V_s at SAFOD, Parkfield, California*. Geochem. Geophys. Geosyst., 10, Q11002, doi:10.1029/2009GC002709.

WP 14

- Bonforte A., Guglielmino F. (2008). *Transpressive strain on the Lipari-Vulcano volcanic complex and dynamics of the "La Fossa" cone (Aeolian Islands, Sicily) revealed by GPS surveys on a dense network*. Tectonophysics, 457, 64-70.
- De Astis G., Dellino P., La Volpe L., Lucchi F. and Tranne C.A. (2006). (a cura di, Rilevamento ed elaborazione Legenda) *Geological map of the Vulcano Island*, Istituto Nazionale di Geofisica e Vulcanologia, Naples. (La Volpe L. e De Astis G. Eds). Stampa: LAC Firenze.
- Harris A.J.L, Lodato L., Dehn J., Spampinato L. (2009). *Thermal characterization of the Vulcano fumarole field*. Bull. Volcanol., 71, 441-458.
- Harris A., Alparone S., Bonforte A., Dehn J., Gambino S., Lodato L., Spampinato, L. (2012). *Vent temperature trends at the Vulcano Fossa fumarole field: The role of permeability*. Bull. Volcanol., 74, 1293-1311.

RU 2 - INGV - Sezione di PalermoResponsible: **Cinzia Federico****Activity of RU in phase 2**

RU 2 is involved in tasks 2, 3 and 4 of the project:

WP 6 (resp. C. Federico) - Analysis of time series; calibration and maintenance of geochemical stations; field campaigns of measurements; gas and water sampling; chemical and isotope analyses in analytical labs.

WP 13 (resp. C. Federico) - Analysis of time series of temperature and soil CO₂ emissions and comparison with seismic data; field sampling of volcanics; isotope analyses in analytical labs.

WP 14 (resp. P. Madonia) - Field sampling of volcanics; mineralogical and physical analyses; field campaigns for batymetric measurements.

Task 2 - WP 6, Resp. C. Federico***Crustal structures and fluid circulation (Etna)*****Participants: INGV-PA**

Sergio Bellomo, Pietro Bonfanti, Lorenzo Brusca, Walter D'Alessandro, Cinzia Federico, Vincenzo Francofonte, Gaetano Giudice, Marco Liuzzo, Manfredi Longo, Mauro Martelli, Antonio Paonita, Maria Pedone, Antonio Pisciotta, Andrea Rizzo

Sp1 - Assessment of fluid pressure in relation with the tectonic stress and the magmatic activity, based on time series of geochemical data

We have investigated the relationships between the variations in fluid circulation (chiefly groundwater) and the geodetic strain, related to volcanic activity or to earthquakes. According to Roeloffs and Linde (2007), positive variations of volumetric strain (contraction), as well as the increase of the fluid mass, induce the increase of fluid pressure, and viceversa in case of dilation. This in turn produces changes of the water table head and discharge rates. The time record of geochemical data available on the Etnean aquifer (Fig. 1) has been compared with geodetic data of the last 5 years (in cooperation with RU 1). The areal distribution of the theoretical variation of fluid pressure related to the variation of volumetric strain has been computed by applying the relation proposed by Roeloffs and Linde (2007). Data of water table head and yield have been corrected for the effect of rainfall. The comparison between geodetic and hydro-geochemical data has concerned two areas in the eastern flank.

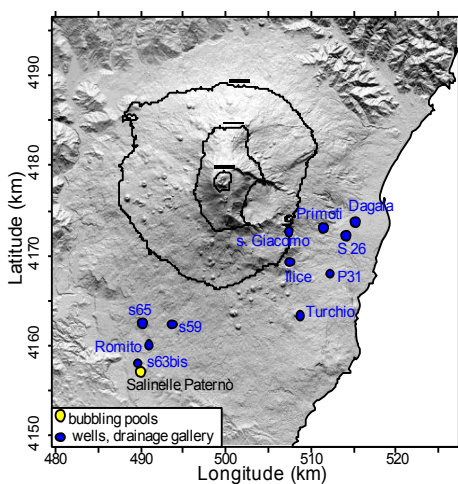


Figure 1. Location of sampling points.

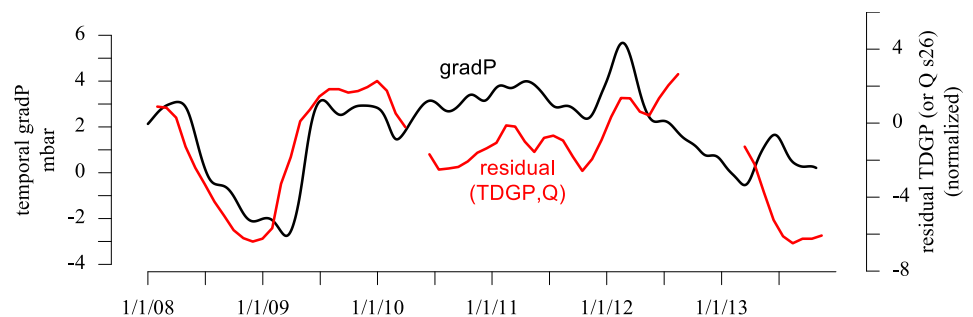


Figure 2. Time trends of fluid pressure, compared with the normalised value of yield and water table head in Primoti and s26 sites (see Fig. 1), corrected for the effect of rainfall.

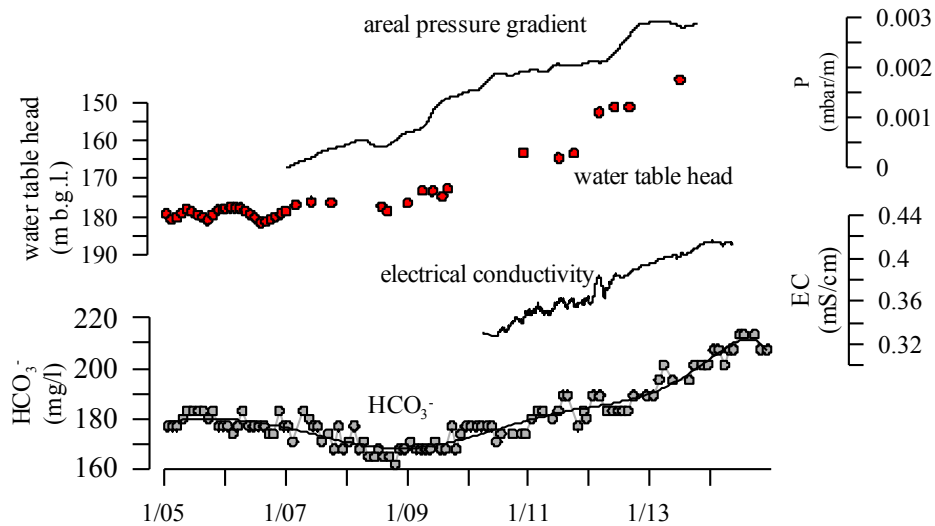


Figure 3. From top to bottom: areal pressure gradient (computed from geodetic strain), water table head in Turchio well, electrical conductivity and HCO₃ contents in Ilice well.

In Fig. 2, the temporal variation of fluid pressure - computed from the geodetic strain and averaged over a 1 km-wide sector close to S. Venerina village - is compared with the normalised value of yield and water table head, assumed as a proxy for fluid pressure, recorded in a well and a drainage gallery (located in the same area) and corrected for the effect of rainfall. The significant correlation between modelled and measured values strongly suggests that changes in fluid circulation in the eastern flank can be ascribed to changes in fluid pressure related to crustal strain.

The change of fluid paths promoted by the changes of crustal strain likely causes the transfer of water in nearby basins and, as a consequence, a further variation of fluid pressure. This has been observed in other wells in the southeastern flank where a significant rise of water levels occurred (Turchio, Fig. 1), which has to be ascribed the fluid mass transfer from nearby basins, induced by dilation strain in this area (Fig. 3). This, in turn, can affect rock properties and ground movement, at least at a shallow depth, where water circulation is more effective (i.e. at the interface volcanics-clays). The changes in water circulation, testified by variations in water table head and/or yield, are paralleled by variations in physico-chemical characteristics of groundwater (Fig. 3), as a water transfer probably occurs among water bodies with different temperature and composition.

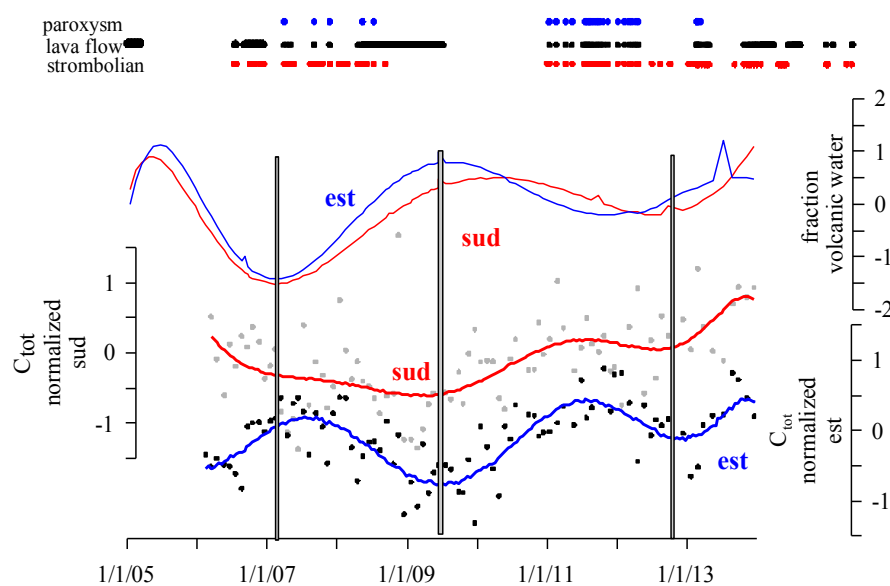


Figure 4. From top to bottom: time trends of the average fraction of volcanic water (normalized), time trends of total dissolved carbon (normalized) in the southern and eastern flanks. Vertical bars indicate the phases of change of water circulation and/or the increase of dissolved carbon.

According to the results of this modelling, the time series of geochemical data available on a network of wells and drainage galleries (Fig. 1) have been analysed to identify the changes related to stress-induced variations of water circulation and those related to the input of volcanic CO₂. With this in mind, the contribution of the different water types has been estimated, according to their chemical composition: it has been assumed that water circulating in the volcanic pile has a typical HCO₃-rich composition, whereas Cl, SO₄ and NO₃ are contributed by rainfall or anthropic pollution. As observed in Fig. 4, the time trends of the fraction of “volcanic water” and the total carbon content (a proxy for the input of CO₂) give complementary information. In particular, in 2007 a first change of water circulation is observed, with the prevailing contribution of the volcanic water, not paralleled by an increase of dissolved carbon, starting later, in 2009. In the same year, a second change in water circulation is observed, testified by the decrease of the fraction of volcanic water. In 2012, a further increase of dissolved carbon is recorded, this time also paralleled by the increasing contribution of the volcanic water end member. We underscore that both in 2009 and 2012, Mattia et al. (2015) have evidenced the increase of the pressure of magmatic fluids in the Etna feeding system, while in 2007 a phase of magmatic recharge has been identified according to He isotopes measured in peripheral gas manifestations (see Sp2 and Fig. 5).

Sp2 - Detection of phases of increased magma degassing, according to chemical and isotopic data (He isotopes) in peripheral gas manifestations (resp. M. Martelli)

The periodic time-monitoring of the ³He/⁴He ratio in gas samples collected every 2-3 weeks in 5 sites at the base of Etna has displayed, as usual, a coherent behaviour in the different sites. For the sake of clarity we here show only the P39 site. During the study period (June 2012 - June 2013), we notice three clear phases of increase of the isotopic ratio, occurred in the following periods: July 2007 - March 2008, June 2010 - June 2011 and finally July 2012 - May 2013 (Fig. 5).

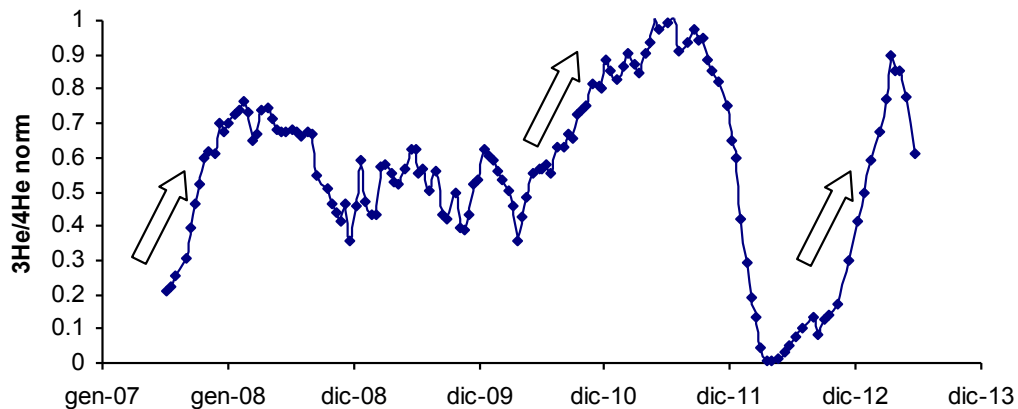


Figure 5. Plot of the ³He/⁴He ratio (expressed as R/Ra normalised between the minimum and maximum values recorded in the study period) in the P39 site (Contrada Pescheria, south-west of Paternò) from June 2007 to June 2013.

These phases are interpreted as an increase of the contribution of a low-degassed magma in the deep portions of the Etna plumbing system (7-13 km below sea level). We notice that these phases can be related to the eruptive phases occurred in 2007-08, 2011-12, and in the first six months of 2013.

Sp3 - Mapping of the gas emission rates in the Salinelle of Paternò and their temporal evolution

Gases and brines emitted in the southern sector of Mt. Etna from mofettes, mud pools and mud volcanoes come from an hydrothermal reservoir hosted within the clayey formations of the sedimentary basement. Gas chemistry and CO₂ and He stable isotopes indicate a clear magmatic origin for these gases and re-equilibration at hydrothermal conditions (Chiodini et al., 1996). Their compositional changes

during either eruptive or rest periods closely parallel those of crater fumaroles (Paonita et al., 2012).

Although these manifestations are the most significant CO₂ emitters outside the crater area, their mass output has never been measured. The monitoring of mud volcanoes in the southern flank of Etna is particularly appealing because the geological setting allows gas pressurization in this area, as an effect of variations of either the stress field or the volcanic activity. Since the first year of the project, we have set up the methodology for direct measurements of the total gas fluxes (Fig. 6), and compared it with other remote technics. We performed gas measurements using two home-made apparatus, able to capture all the bubbles over an area of 0.64 m² or 2.25 m², respectively. The two apparatus are made of stainless-steel funnels (dimensions 0.8x0.8 m and 1.5x1.5m) connected through a tap to a plastic bag, inflated by the bubbling gas. Over an area of about 6,000 m², we measured the flow rate of each bubbling pool, providing that it had a minimum flux rate of 0.5 l/min. Direct measurements of gas flow rate have been compared with in-plume CO₂ measurements. We used an infrared tunable diode transmitter/receiver laser unit to take measurements of volcanic CO₂ path-integrated concentrations along cross sections of the atmospheric plumes over the whole investigated area. During field campaigns, an *ad-hoc* geometry of laser and retroreflectors positions were used in order to scan the atmospheric plumes from different distances and angles. We therefore post-processed the dataset to derive the two-dimensional mapping of CO₂ distribution over the mud volcano (Fig. 7). The difference between the direct flux measurement and the remote in-plume estimate is about 10%.



Figure 6. Sampling apparatus and field activities.

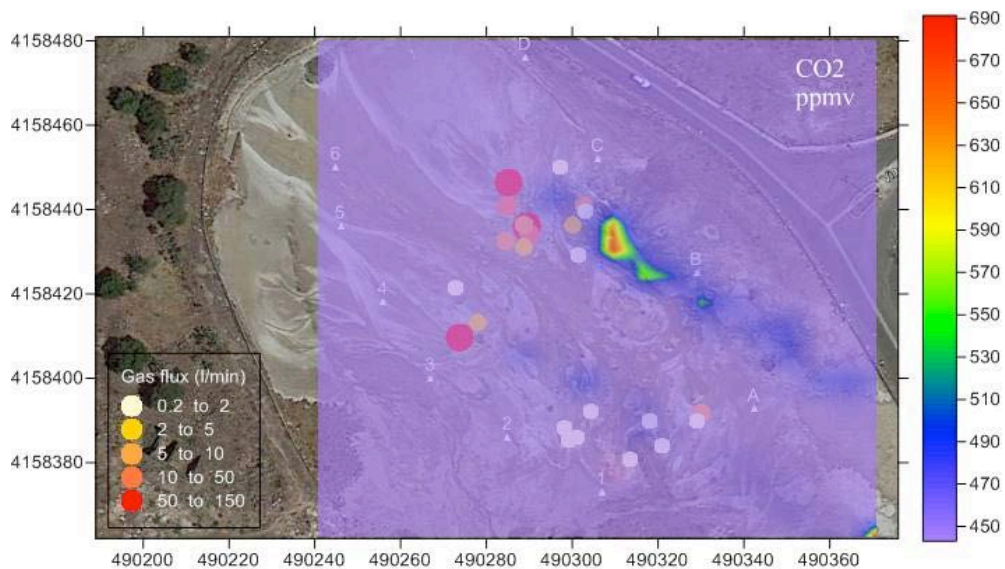


Figure 7. In-plume CO₂ concentration map (April 2014). Classed posts represent the gas flux from each measured pool. Labelled white dots represent the position of laser (letters) and reflectors (numbers).

During the field campaigns performed since December 2013, we have measured a significant change in the gas output rate from the various bubbling pool, paralleled by an evident change in position and dimension of the pools (Fig. 8), which culminated in the formation of a single main pool, emitting increased amount of mud, water and gas (Fig. 9). The total flux from the whole area has varied from a minimum of 4 l/min to 390 l/min. This corresponds to a maximum CO₂ flux of 1.1 ton/d.



Figure 8. Mud pools in the same area in two different field campaigns.



Figure 9. Aerial view of the main pool in June 2014.

Task 2 - WP 13, Resp. C. Federico *Crustal structures and fluid circulation (Aeolian Islands)*

Participants: INGV-PA

Marco Camarda, Giorgio Capasso, Sofia De Gregorio, Iole Serena Diliberto, Cinzia Federico, Vincenzo Francofonte, Gaetano Giudice, Salvatore Inguaggiato, Leonardo La Pica, Marco Liuzzo, Mauro Martelli, Antonio Paonita, Giovannella Pecoraino, Maria Pedone, Andrea Rizzo, Fabio Vita

Sp1 - Steaming ground, mofettes, along the Aeolian-Tindari-Letojanni fault system and assessment of geochemical anomalies related to seismic activity and/or ground deformation

During the first year, we have compared the seismicity with magnitude $M > 2.0$ in a sector of the Patti Gulf (analysis made by UR 1, S. Alparone) with the record of soil CO_2 emissions close to Gioiosa Marea (Northern Sicily). The comparison has shown, for the analysed period (2010-2012), that strain release and soil CO_2 emissions show coeval changes. The soil CO_2 output has been compared with the sum of the normalised values of the cumulative strain and the cumulative number of events, to account for the total seismicity rate. The significant correlation between the two parameters, shown in the scatter plot of Fig. 10, indicates that both gas emissions and seismicity are common effects of the changing tectonic stress in the area.

In the second year, the analysis has been extended to the geochemical anomalies observed in temperature and gas composition in the fumarolic area of La Fossa in Vulcano, to check the eventual

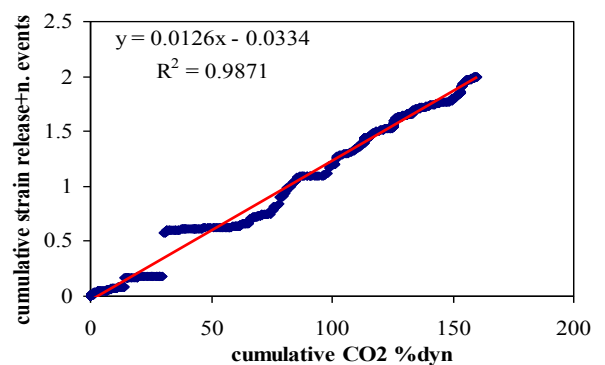


Figure 10. Scatter plot of the cumulative CO_2 emissions and cumulative strain release + n° of events.

relationship between fumarolic activity and seismicity in the Patti Gulf. In Fig. 11, the seismicity with magnitude $M > 2$ in a sector of the Patti Gulf is compared with the de-trended values of temperature of the F5AT fumarole and the CO_2 soil emission close to Gioiosa Marea.

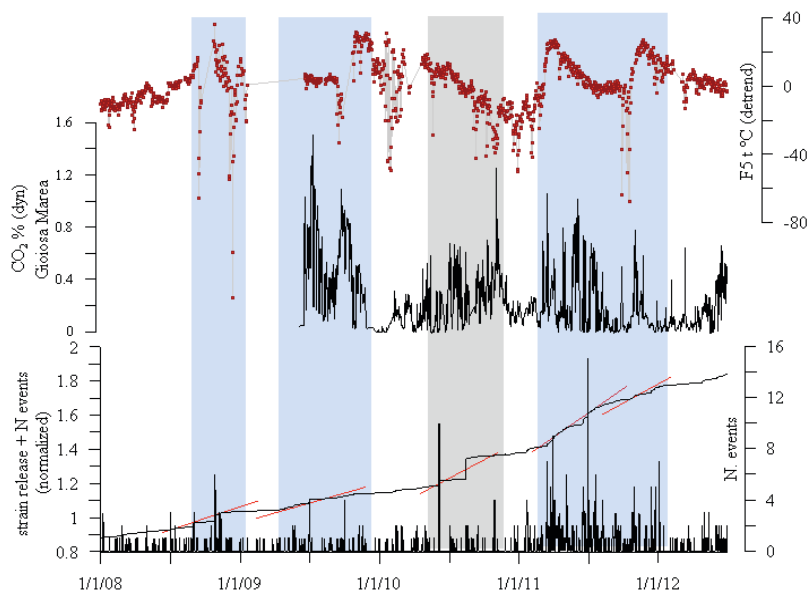


Figure 11. From top to bottom: time trends of temperature in the F5AT fumarole (normalized and de-trended), soil CO_2 degassing in Gioiosa Marea, cumulative strain release + number of events, n° of events.

The shaded blue areas indicate the correspondence of seismicity with both soil degassing in this area of the Sicilian coast and temperature of F5AT fumarole, not verified in the period evidenced by the grey area. Actually, in the latter case, although the high temperature magmatic-fumarolic system has not been affected by seismicity in the studied sector of the gulf, a low temperature fumarole, external to the main exhaling area of La Fossa, has recorded a well-defined anomaly (Madonia et al., 2013). By analysing a longer period, a full synchronism can be envisaged among seismicity, fumarole temperature and CO_2 content (FA fumarole), while not being these parameters proportional between them. This would suggest that the effect of tectonic stress or strain, in a volcanic system, are mediated by the dynamics of the local magmatic-hydrothermal system, related to fluid pressurization, fracture opening, and vapour discharge from fumaroles.

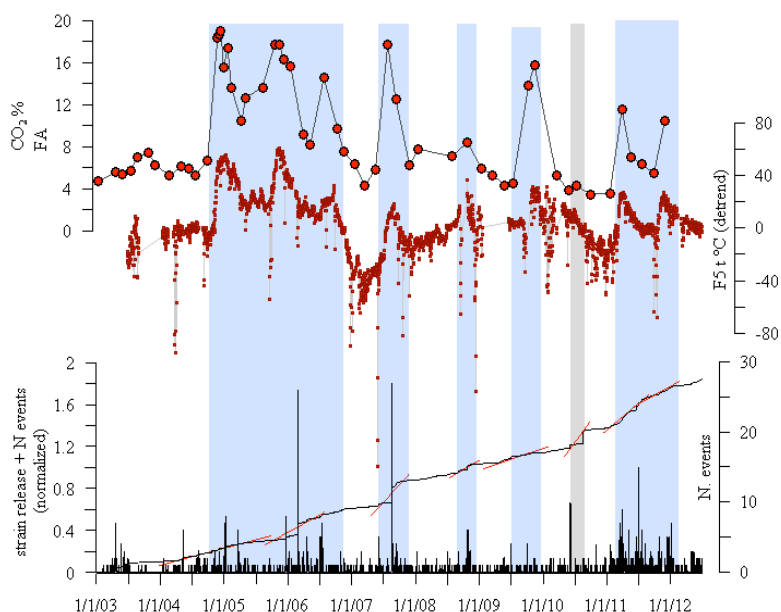


Figure 12. From top to bottom: time trends of CO_2 concentration in the fumarole FA, temperature in the F5AT fumarole (normalized and de-trended), cumulative strain release+ number of events, n° of events.

Sp2 - Mapping of concentrations and fluxes of CO₂, H₂S and HCl in the fumarolic field of La Fossa in Vulcano (resp. C. Federico)

The periods of increased fumarolic activity at La Fossa volcano have been characterized, since early 80's, by changes in the gas chemistry and output rate of fumaroles. Excepting the direct measurements of the steam output from fumaroles performed from 1983 to 1995 (Italiano et al., 1998), the mass output of the single gas species has been recently measured, with various methods, only sporadically or for short periods (Aiuppa et al., 2005; Tamburello et al., 2011; Pedone et al., 2014). Since 2008, a scanning DOAS system is operating in the Palizzi area for the remote measurement of the in-plume SO₂ flux (Inguaggiato et al., 2012). On these grounds, we have envisaged the need of a cross-comparison of different methods for the *in situ* measurement of the output rate of different gas species. In 2015, we have carried out two field campaigns aimed at:

- mapping the concentration of CO₂, H₂S and SO₂ in the fumarolic plume at 1 m from the surface, by using specific open-path tunable lasers (GasFinder Boreal Europe, Fig. 13) and an Active DOAS for SO₂, respectively. These measurements, coupled to simultaneous wind speed data, have been elaborated to obtain the dispersion map and the output rate of single species in the overall fumarolic field;
- mapping the concentrations of CO₂, H₂S, SO₂, H₂O in the fumarolic plume at 0.5 m from the soil, by using an integrated system, including IR spectrometers and specific electrochemical sensors. This has provided the concentration ratios of the analysed gas species and their distribution in the fumarolic field;
- in-fumarole sampling of vapour and measurement of the steam output, to validate the remote measurements.



Figure 13. Retroreflectors (left) and tunable laser (right) on La Fossa cone.

The dispersion map of CO₂ obtained from the tunable laser measurements, is shown in Fig. 14. The maximum CO₂ concentration at 1 m from the soil is 1000 ppmv along the rim, and 1800 ppmv in the inner slopes. As observed, the largest contribution derives from the FA fumarole, despite its present outlet temperature of 230°C, almost 200° lower than those measured at the rim fumaroles. The estimated CO₂ and H₂S fluxes are 320 t/d and 4.4 t/d, respectively. The coeval SO₂ flux, measured by the scanning DOAS system, is 9±1 t/d. The steam output, recomputed from CO₂ flux measurements, is 330 t/d.

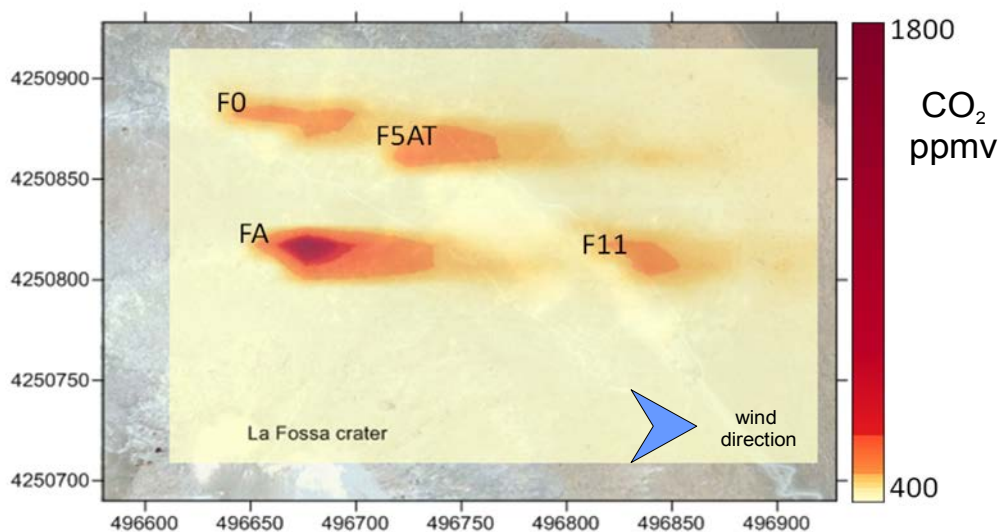


Figure 14. CO₂ dispersion map in La Fossa crater (May 2015).

Section 2

Scientific Reports of Research Units (RU 2)

Sp3 - Helium isotope analysis in melt inclusions and assessment of the evolution of the magma feeding La fossa cone (resp. A. Paonita)

The study carried out by analysing a large number of mafic phenocrysts (olivine and clinopyroxenes) of the Vulcano island, revealed a range of He isotopic ratios between 3.3 and 5.9 Ra (where Ra is the isotopic ratio in the atmosphere). Most of these values (those with $^3\text{He}/^4\text{He}$ between 3.3 and 5.2 Ra) are genetically not compatible with the fluids currently emitted from the fumarolic field, which range from 5.2 to 6.2 Ra (Paonita et al., 2013). The relatively low helium isotopic ratios measured in fluid inclusions are mainly related to crustal assimilation processes of the Calabrian basement, estimated at 10-25% in agreement with previous petrological studies. Our study also revealed that only the basalt of Sommata and latite of Roveto have He isotopic ratio comparable to the fumarolic fluids of La Fossa cone. Taking into account that Roveto is the most recent eruption at Vulcanello (about 400 yr ago) from a presently existing reservoir, the latite is the most plausible magma feeding the current exhalative activity. The Sommata magma (50 ky ago) seems too old to represent a likely magma source. We suggest that deep fluids coming from a primitive reservoir and having high helium isotope ratios, periodically feed the latitic reservoir.

Task 4 - WP 14, Resp. P. Madonia ***Slope instability hazard maps (Vulcano)***

Participants: INGV-PA

Paolo Madonia, Marianna Cangemi, Ygor Oliveri

Other institutions

GFZ, Potsdam (Germany) Sergio Speziale

Sp2 - Maps of the hydrothermal alteration facies in the sector between Forgia Vecchia and the 1988 landslide (Vulcano island), soil permeability, moisture content and fracture network; bathymetry of the slope foot map

As evidenced during the first year of the project (2012-13), the summit area of La Fossa cone is sealed by a hydrothermal alteration crust, fostering condensation of hydrothermal fluids inside the volcanic edifice. The combination of fractures and volcano-stratigraphic discontinuities conveying hydrothermal fluids, makes significant rock volumes prone to slide seaward, as occurred in 1988.

Following these preliminary results, during the second year the activity has been aimed at: i) reconstructing the detailed bathymetry along the La Fossa cone coastline, to assess possible morphological conditions able to trigger flank instability; ii) mapping the fracture field in the area above the Forgia Vecchia craters, to evaluate possible interactions between gravitative movements and hydrothermal fluid circulation; iii) determining mineralogical composition and hydraulic conductivity (under saturated conditions) of volcanic deposits, to evaluate their ability in retaining water, creating favourable conditions for instability.

We retrieved the following results:

- a) a steep submarine scarp has been found immediately SE of the 1988 landslide area

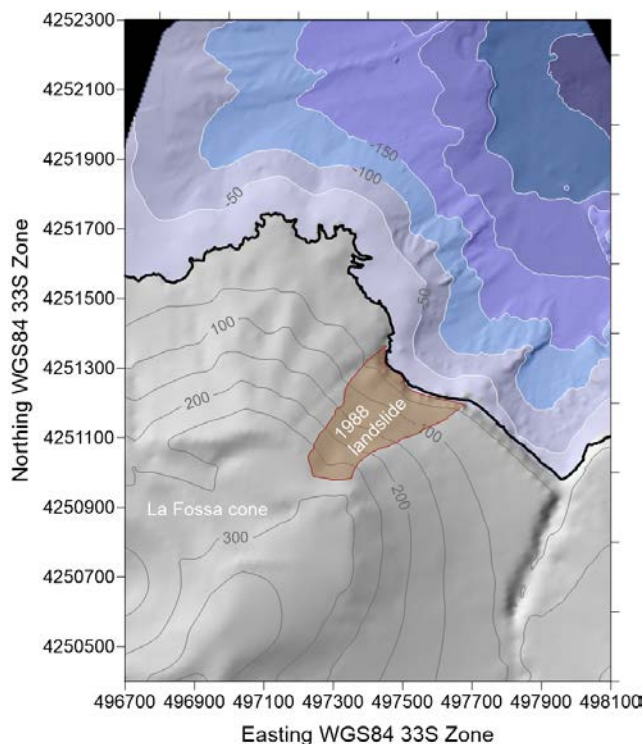


Figure 15. Bathymetry of the NE slope foot of La Fossa cone.

- (Fig. 15), which makes this area susceptible to new landslides;
- b) similar instability conditions have been found above the Forgia Vecchia crater rim area, where tensile fracturing and hydrothermal circulation interact with mutual feedbacks (Fig. 16);
 - c) hydrothermal alteration promotes the formation of clay minerals, significantly reducing the permeability of volcanic deposits (Fig. 17). Argillified volcanic materials with low permeability, show high background water contents, due to the direct condensation of hydrothermal vapor, with impulsive increments after rainfall events (Fig. 18).

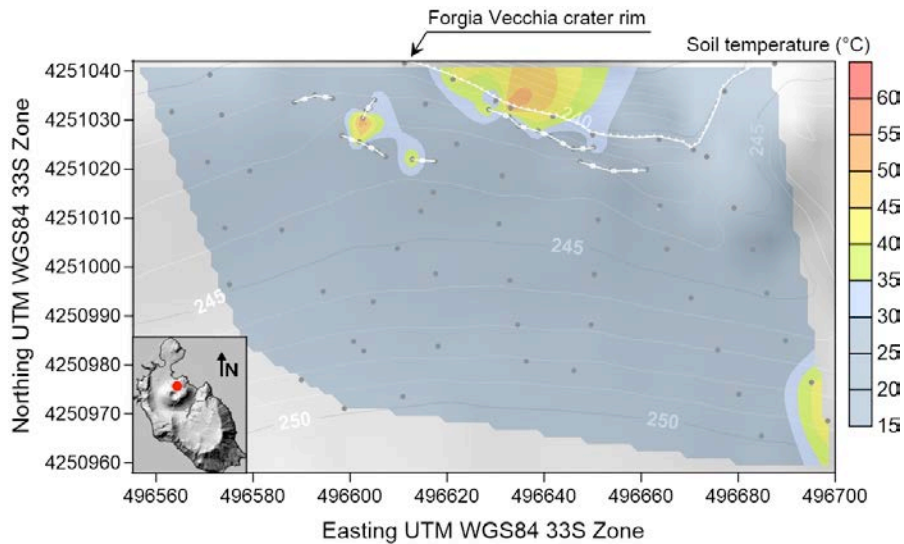


Figure 16. Fracture network (white dotted lines) and soil temperature contour map of the area above the Forgia Vecchia crater rim. Small, black-filled circles are soil temperature measurements.

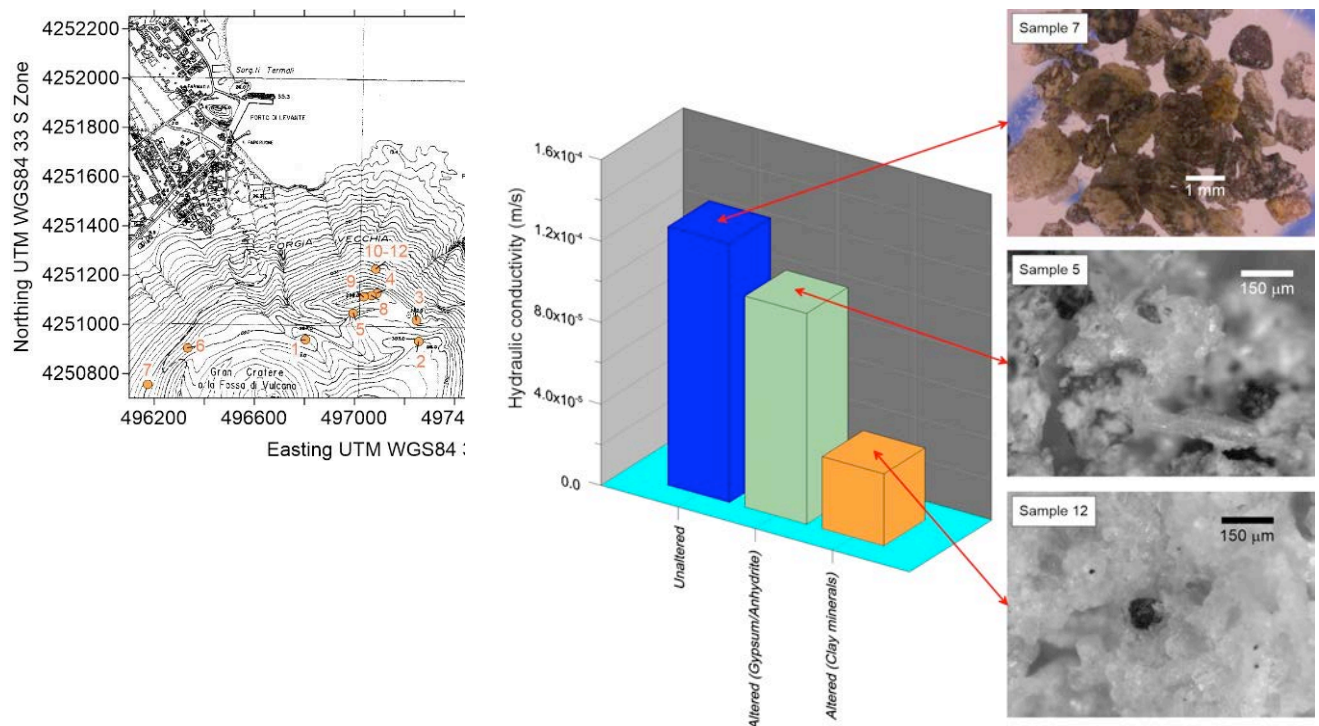


Figure 17. Left: location of rock samples; centre: their average hydraulic conductivity (under saturated conditions) values. Microphotographs on the right illustrate samples representative of each hydrothermal alteration facies used for grouping rock samples.

Section 2
Scientific Reports of Research Units (RU 2)

The abovementioned considerations lead us to conclude that large sectors of the northeastern area of La Fossa cone are prone to potential instability conditions due to circulation of hydrothermal fluids (see deliverable Sp1 in RU 7 report).

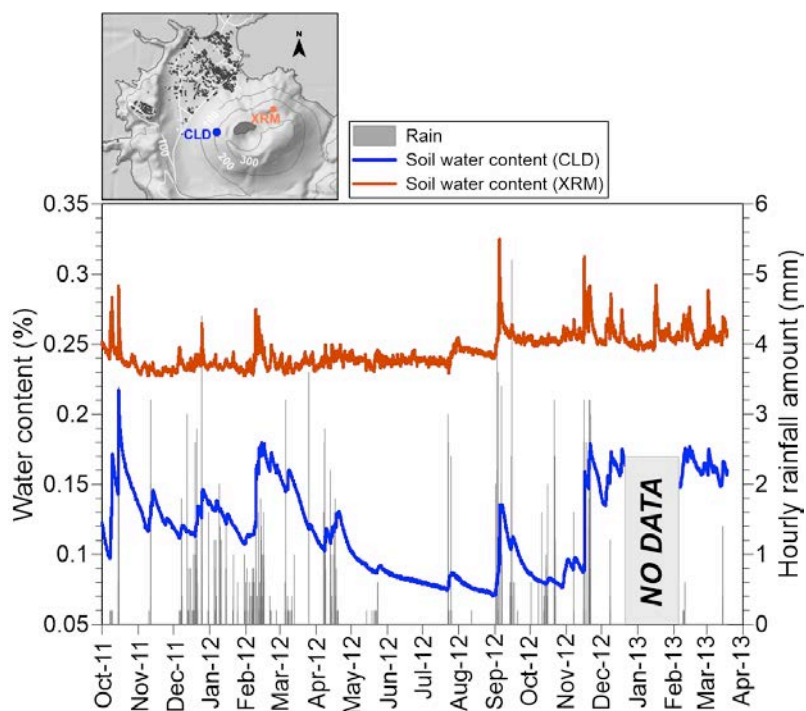


Figure 18. Variations of hourly soil water content and rainfall rate during the period October 2011-March 2013. Stations CLD and XRM (see upper inset for their location) refer to areas without and with active superficial hydrothermal circulation, respectively.

Deliverables

- WP 6.Sp1 Assessment of fluid pressure in the volcano-hydrothermal system in relation with the tectonic stress and the magmatic activity, based on time series of geochemical data: **90%**.
- WP 6.Sp2 Detection of phases of increased magma degassing, according to long-term record of chemical and isotopic data (helium isotopes) in peripheral gas manifestations: **100%**.
- WP 6.Sp3 Mapping of the gas emission rates in the salinelle of Paternò and their temporal evolution: **100%**.
- WP 13.Sp1 Steaming ground, mofettes, along the Aeolian-Tindari-Letojanni fault system and assessment of geochemical anomalies related to seismic activity and/or ground movement: **100%**.
- WP 13.Sp2 Mapping of concentrations and fluxes of CO₂, H₂S and HCl in different portions of the fumarolic field: **90%**.
- WP 13.Sp3 Helium isotope analysis in melt inclusions and assessment of the evolution of the magma feeding La Fossa cone: **100%**.
- WP 14.Sp2 Maps of the hydrothermal alteration facies in the sector between Forgia Vecchia and the 1988 landslide (Vulcano island), soil permeability, moisture content and fracture network; bathymetry of the slope foot map: **100%**.

Problems and difficulties

- WP 6.Sp3 We had unsolved technical problems with the tunable laser for HCl.
- WP 13.Sp2 We had unsolved technical problems with the tunable laser for HCl.

Key publications

- Bruno V., Cannavò F., Federico C., Longo M., Mattia M. (2014). *The effect of crustal strain on fluid circulation in the Mt Etna aquifers*. Conferenza Rittmann, 29-31 October 2014.
- Capasso G., Federico C., Madonia P., Paonita A. (2013). *Response of the shallow aquifer of the volcano-hydrothermal system during the recent crises at Vulcano Island (Aeolian Archipelago, Italy)*. J. Volcanol. Geotherm. Res., 273 (2014) 70-80.
- Diliberto I.S. (2013). *Time series analysis of high temperature fumaroles monitored on the island of Vulcano (Aeolian Archipelago, Italy)*. Journal of Volcanology and Geothermal Research doi: 10.1016/j.jvolgeores.2013.08.003.
- Federico C., Giudice G., Liuzzo M., Pedone M., Cosenza P., Riccobono G., (2014). *First measurements of gas output from bubbling pools in a mud volcano at the periphery of Mt Etna (Italy): methodologies and implications for monitoring purposes*. EGU General Assembly, Wien, 27 April-2 May, 2014.
- Madonia P., Cusano P., Diliberto I.S., Cangemi M. (2013). *Thermal anomalies in fumaroles at Vulcano island (Italy) and their relationship with seismic activity*. Physics and Chemistry of the Earth 63, 160-169, <http://dx.doi.org/10.1016/j.pce.2013.06.001>.
- Mattia M., Bruno V., Caltabiano T., Cannata A., Cannavò F., D'Alessandro W., Di Grazia G., Federico C., Giammanco S., La Spina A., Liuzzo M., Longo M., Monaco C., Patanè D., and Salerno G. (2015). *A comprehensive interpretative model of slow slip events on Mt. Etna's eastern flank*, Geochem. Geophys. Geosyst., 16, 635-658, doi:10.1002/2014GC005585.
- Paonita a., Federico C., Bonfanti P., Capasso G., Inguaggiato S., Italiano F., Madonia P., Pecoraino G., Sortino F. (2013). *The episodic and abrupt geochemical changes at la fossa fumaroles (Vulcano island, Italy) and related constraints on the dynamics, structure, and compositions of the magmatic system*. Geochim. Cosmochim. Acta, 120 (2013) 158-178.

Other references

- Aiuppa A., Federico C., Giudice G., Gurrieri S. (2005). *Chemical mapping of a fumarolic field: La Fossa Crater, Vulcano Island (Aeolian Islands, Italy)*. Geophys Res Lett, 32. doi:10.1029/2005GL023207.
- Chiodini G., D'Alessandro W. and F. Parello, (1996). *Geochemistry of the gases and of the waters discharged by the mud volcanoes of Paternò, Mt. Etna (Italy)*. Bull. Volcanol., 58, 51-58, 1996.
- Inguaggiato S., Calderone L., Inguaggiato C., Mazot A., Morici S., Vita F. (2012). *Long-time variation of soil CO₂ fluxes at the summit crater of Vulcano (Italy)*. Bull. Volcanol., 74, 1859-1863. <http://dx.doi.org/10.1007/s00445-012-0637-6>.
- Italiano F., Pecoraino G. and Nuccio P.M. (1998). *Steam output from fumaroles of an active volcano: Tectonic and magmatic-hydrothermal controls on the degassing system at Vulcano (Aeolian arc)*, J. Geophys. Res., 103, 29,829- 29, 842.
- Madonia P., Cusano P., Diliberto I.S., Cangemi M. (2013). *Thermal anomalies in fumaroles at Vulcano island (Italy) and their relationship with seismic activity*. Physics and Chemistry of the Earth, 63, 160-169, <http://dx.doi.org/10.1016/j.pce.2013.06.001>.
- Mattia M., Bruno V., Caltabiano T., Cannata A., Cannavò F., D'Alessandro W., Di Grazia G., Federico C., Giammanco S., La Spina A., Liuzzo M., Longo M., Monaco C., Patanè D., and Salerno G. (2015). *A comprehensive interpretative model of slow slip events on Mt. Etna's eastern flank*. Geochem. Geophys. Geosyst., 16, 635-658, doi:10.1002/2014GC005585.
- Paonita A., Caracausi A., Iacono-Marziano G., Martelli M., Rizzo A. (2012). *Geochemical evidence for mixing between fluids exsolved at different depths in the magmatic system of Mt Etna (Italy)*. Geochim. Cosmochim. Acta, 84 (2012) 380-394.
- Paonita, A., Federico C., Bonfanti P., Capasso G., Inguaggiato S., Italiano F., Madonia P., Pecoraino G., Sortino F. (2013). *The episodic and abrupt geochemical changes at La Fossa fumaroles (Vulcano Island, Italy) and related constraints on the dynamics, structure, and compositions of the magmatic system*. Geochim. Cosmochim. Acta, 120 (2013) 158-178.
- Pedone M., Aiuppa A., Giudice G., Grassa F., Francofonte V., Bergsson B., Ilyinskaya E. (2014). *Tunable Diode Laser measurements of hydrothermal/volcanic CO₂, and implications for the global CO₂ budget*. Solid Earth, 5:1209-1221. doi:10.5194/sed-5-1209-2014.

Section 2

Scientific Reports of Research Units (RU 2)

- Roeloffs, E.A. and A.T. Linde (2007). Borehole observations of continuous strain and fluid pressure, in *Volcano Deformation: Geodetic Monitoring Techniques*. (D. Dzurisin, ed.), pp. 305-322, Springer, Berlin.
- Tamburello G., Kantzas E.P., McGonigle A.J.S., Aiuppa A., Giudice G. (2011). *UV camera measurements of fumarole field degassing (La Fossa crater, Vulcano Island)*. *J Volcanol. Geoth. Res.*, 199:47-52.

RU 3, INGV - Centro Nazionale Terremoti, RomaResponsible: **Marco Anzidei****Activity of RU in phase 2**

RU 3 is involved in tasks 2 and 3 of the project:

WP 8 (resp. I. Nicolosi) - Field campaigns of measurements and geomagnetic database; preliminary interpretations of the magnetic data of Val Calanna and offshore Etna.

WP 9 (resp. A. Anzidei) - GPS campaign in the Aeolian islands and Nebrodi/Peloritani area in cooperation with RU 1; updated GPS crustal velocity field and strain (with RU 1); multibeam (MB) bathymetric campaign at Lipari; DTM for the whole island of Lipari based on aerial photogrammetry and LIDAR data (with RU 7), with ultra-high resolution for the areas of Marina Corta and Marina Lunga.

Task 2 - WP 8

Tectonic setting of the sedimentary basement (Etna)

Participants: INGV-RM2

Iacopo Nicolosi, Roberto Carluccio, Francesca D'Ajello Caracciolo, Massimo Chiappini

Other Institutions

INGV-CT Stefano Branca; **University of Burgos (Spain)** Isabel Blanco

Sp1 - Magnetic modelling of the Val Calanna area and off-shore coastal sector (resp. I. Nicolosi)Val Calanna area

Using the new high resolution aeromagnetic survey of Etna volcano, carried out during 2012 by the Istituto Nazionale di Geofisica e Vulcanologia (D'Ajello Caracciolo et al., 2014), we performed a detailed study of the Val Calanna area, an inferred dike swarm system of an outcropping sub-volcanic body (Ferlito and Nicotra, 2010) (Fig. 1). From a magnetic point of view, the Val Calanna area is characterized by a low, round shaped anomaly that represents a local magnetization negative contrast considering the volcanic magnetic background. The round shaped low anomaly shows a clear geometry that is spatially larger than the Val Calanna units outcrops. We measured the magnetic susceptibility of some outcrops of Val Calanna area (Tab. 1).

The measures indicate low susceptibility values of the high altered host rocks of Mt. Calanna Unit, as defined by Ferlito and Nicotra, (2010) (Fig. 2). Reduced to magnetic pole anomaly detail of Val Calanna area is represented in Fig. 3, showing the areal distribution of magnetic low that overcomes the outcrops of Mt. Calanna Units.

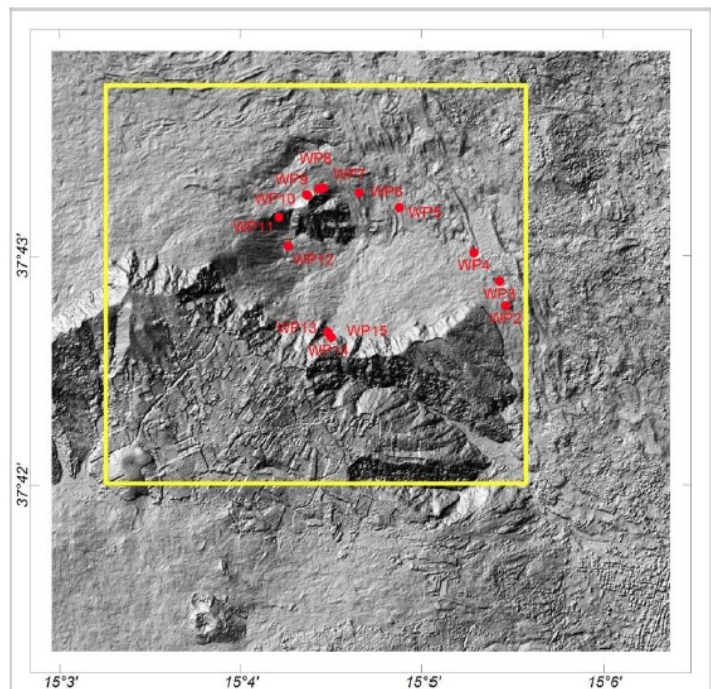


Figure 1. Val Calanna area (yellow square) and sites of measured magnetic susceptibility.

Latitude	Longitude	Site	Susc (10^{-3} SI)	Outcrop
37.71093	15.6923	WP1	20	1991-1993 Lava Flows
37.71305	15.09095	wp2	13.8	1991-1993 Lava Flows
37.71483	15.09039	WP3	26.5	1991-1993 Lava Flows
37.71692	15.08804	WP4	23.6	1991-1993 Lava Flows
37.72021	15.08127	WP5	38	1991-1993 Lava Flows
37.72127	15.07758	WP6	37	1991-1993 Lava Flows
37.72163	15.07429	WP7	27	1991-1993 Lava Flows
37.72158	15.07383	WP8	4.3	altered Mt Calanna Unit
37.72115	15.07272	WP9	40	unaltered Mt Calanna Unit
37.72109	15.07282	WP10_1	23.5	unaltered Mt Calanna Unit
37.7195	15.07019	WP11	0.3	altered Mt Calanna Unit
37.71114	15.07471	WP13	33	unaltered dike cutting Mt Calanna Unit
37.71111	15.07465	WP14	1	altered Mt Calanna Unit
37.71076	15.075	Wp15	30	unaltered post Mt Calanna Unit

Table 1. Location and values of the measured susceptibility.

Mt. Calanna is located close to the northern border of the magnetic anomaly low (blue color tones), while Mt. Fior di Cosimo is close to the central area defined by the magnetic minimum. A borehole (SG6) reached a depth of about 600 meters without crossing the Mt. Calanna altered volcanic material while two drainage galleries intercept these products.



Figure 2. Example of intensely altered breccia, yellowish in color, low susceptibility host rocks and altered dike of Mt. Calanna Unit.

We analyzed the low intensity magnetic anomaly to image the subsurface geometry of the Val Calanna area starting from an existing 3D inversion model that describes the pre-volcanic basement morphology (Nicolosi et al., 2014). In Fig. 4 we show the same magnetic anomaly map in color scale with the superimposition of gravity bouguer anomaly isolines from Loddo et al. (1989).

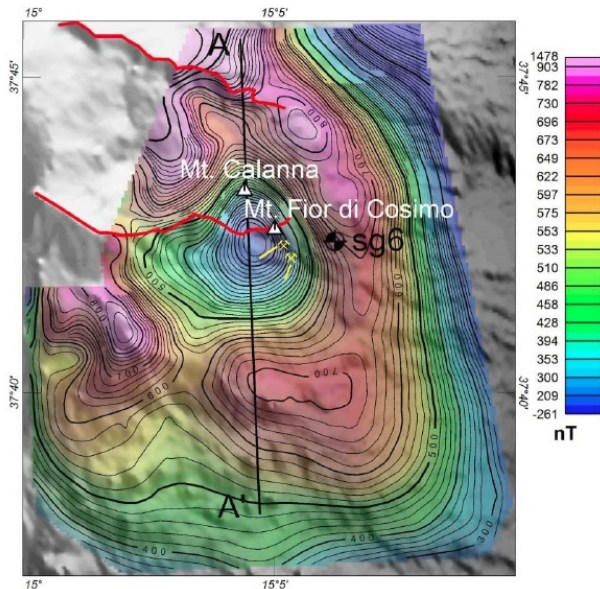


Figure 3. Intensity map of Reduced to magnetic pole Val Calanna Area anomaly. Magnetic Inclination: 55° , Magnetic Declination: 0° . Mt. Calanna and Mt. Fior di Cosimo location are reported. Red lines: Valle del Bove rims. Borehole Sg6 location is shown in the map; drainage galleries are indicated in yellow markers.

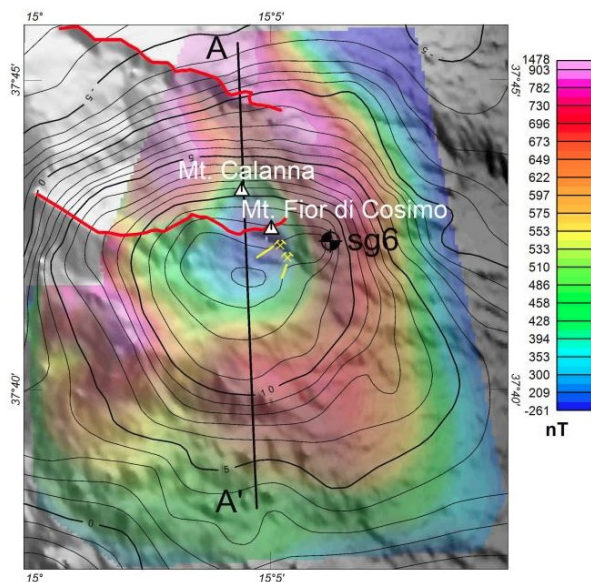


Figure 4. Intensity map of Reduced to magnetic pole Val Calanna area anomaly. Isolines represent the bouguer anomaly intensity values from Loddo et al. (1989).

Fig. 4 shows the perfect matching between the magnetic and gravity anomalies both centered in correspondence of Mt. Fior di Cosimo area. Fig. 5 shows the subsurface extension of the altered sub-volcanic system of Val Calanna inside the magnetized volcanic units. The question marks represents our hypothesis about depth extension of sub-volcanic body that cannot be modelled due to absence of magnetic contrast between pre-volcanic, clay rich basement and altered sub-volcanic material. We compared, along the profile A-A', the magnetic anomaly of the Val Calanna area with subsurface images modeled using different geophysical techniques: gravity (Schiavone and Loddo, 2007), magnetotelluric data (Siniscalchi et al., 2012), magnetic (Nicolosi et al., 2014) and seismic tomography (Villasenor et al., 1998) as shown in Fig. 6.

All these techniques independently confirm the presence of the crustal body responsible for the observed anomalies in the Val Calanna area. We interpret the low magnetized area as the upper portion of an altered feeder system of the earliest Etna central volcanic activity.

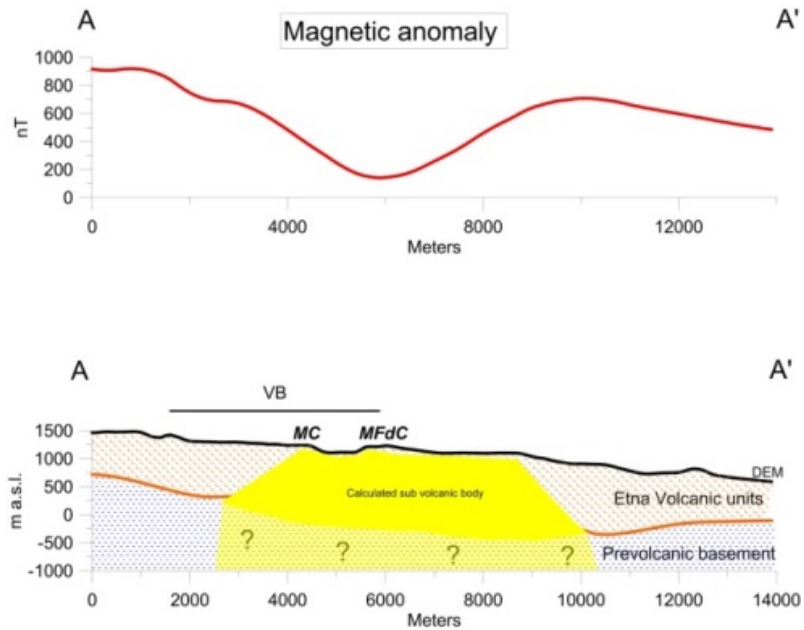


Figure 5. Etna volcano magnetic model along profile AA'. Orange patchwork: magnetic volcanic deposits. Blue patchwork: pre-volcanic, non-magnetic basement. Orange line: basement-volcanic product surface contact. Yellow polygon: sub-volcanic body of Val Calanna. Question marks: area not modellizzabile using magnetic methods. VB: Valle del Bove., MC: Mt. Calanna. MFdC: Mt. Fior di Cosimo.

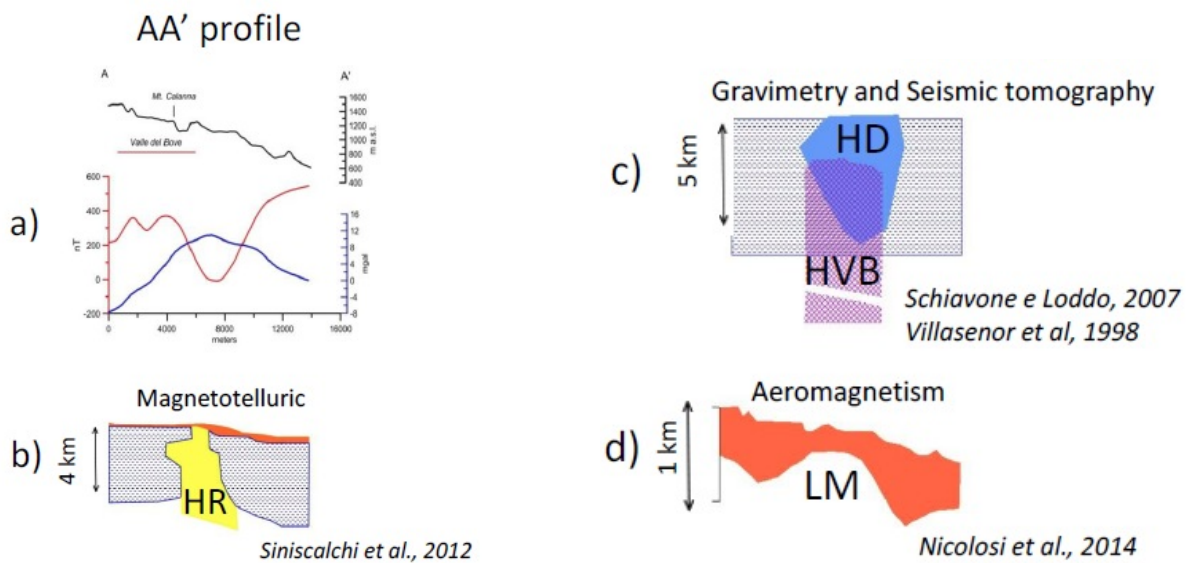


Figure 6. a) Magnetic and gravity anomaly; b) high resistivity body (HR) model; c) High density (HD) and High Velocity Body (HVB) models; d) Low magnetic area (LM) inside highly magnetized volcanic pile.

We highlight the real extension of the low magnetized zone that is characterized by a sub-circular shape of about 5 km diameter centered close to the Mt. Fior di Cosimo area. We interpret the low magnetized area as an altered feeder system of the earliest Etna central volcanic activity. Therefore, the highly weathered and tectonized dyke swarm recognized at Mt. Calanna by Ferlito and Nicotra (2010) represents the only surface evidence of a large sub-circular shallow plumbing system that fed the final stage of the Timpe phase volcanism and the beginning of the construction of the first central edifices in Etna region during the Valle del Bove phase. The plane view extension of the non-magnetic body that defines the Val Calanna system is represented in Fig. 7.

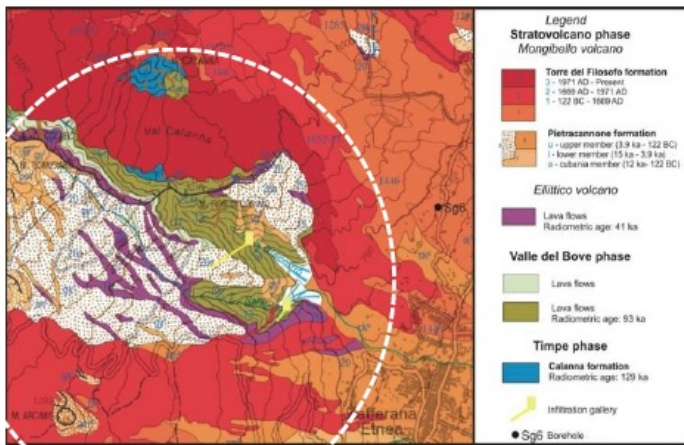


Figure 7. White dotted line represents the maximum areal extension of the altered, non-magnetic, sub-volcanic body of the Val Calanna area shown on the geological map (Branca et al., 2011).

Etna offshore

During the 2012 INGV aeromagnetic survey, we measured at a low altitude of 1000 ft (300 m) the magnetic anomaly signature of the Etna offshore area. Fig. 8 shows the magnetic anomaly represented in color scale. The magnetic anomaly is characterized by a SW area with mainly positive anomaly (purple-reddish tones) and a NW negative area close to the shoreline. The southern positive anomaly starts from a huge aligned anomaly corresponding to the Catania canyon. The negative one (blue tones) clearly represents the offshore continuation of the negative component of the huge dipolar Etna volcano magnetic anomaly. The northern termination of the offshore magnetic anomaly is marked by a positive anomaly located in front of the Alcantara valley. Fig. 9 shows a clear correlation between the magnetic anomaly map and the morphological bulge structure recognized by Chiocci et al. (2011).

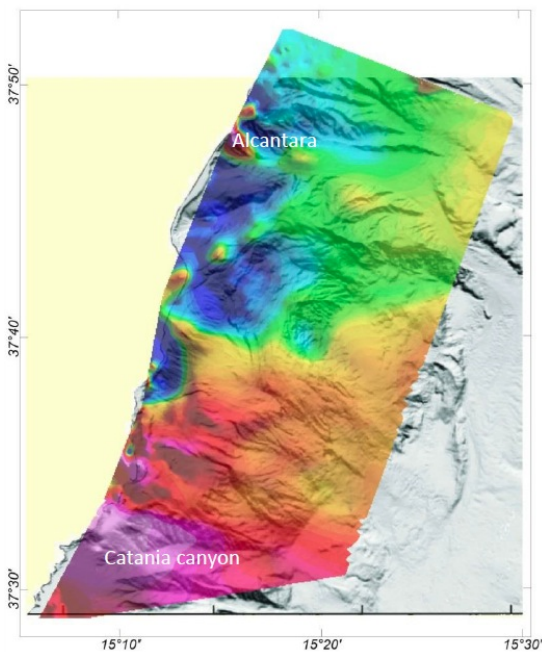


Figure 8. Magnetic anomaly map of the Etna offshore area acquired at an altitude of 1000 ft (300 m). Etna offshore bathymetry modified from Chiocci et al. (2011).

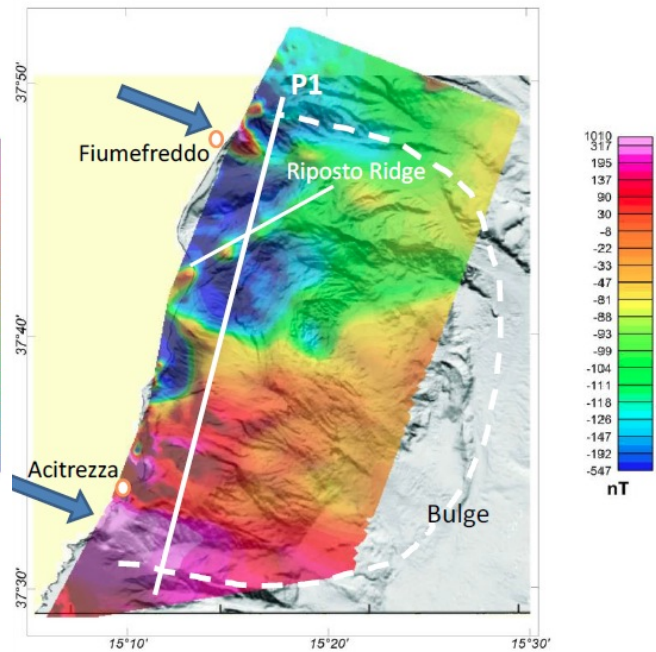


Figure 9. Etna offshore magnetic anomaly. The white dashed line represents the bulge morphology as indicated by Chiocci et al. (2011). The blue arrows indicate the Catania canyon and Alcantara valley positive magnetic anomaly. The white continuous line represents a modeled profile.

Section 2

Scientific Reports of Research Units (RU 3)

Some high frequency magnetic anomalies are aligned along the Riposto ridge; these anomalies represent the effect of superficial volcanic products above a non-magnetic basement that characterizes the ridge. We realized a 2.75D model along the P1 profile shown in Fig. 9, using a constant magnetization value of 8 A/m, according to the value used by Nicolosi et al. (2014) for the volcanic products pile bulk magnetization.

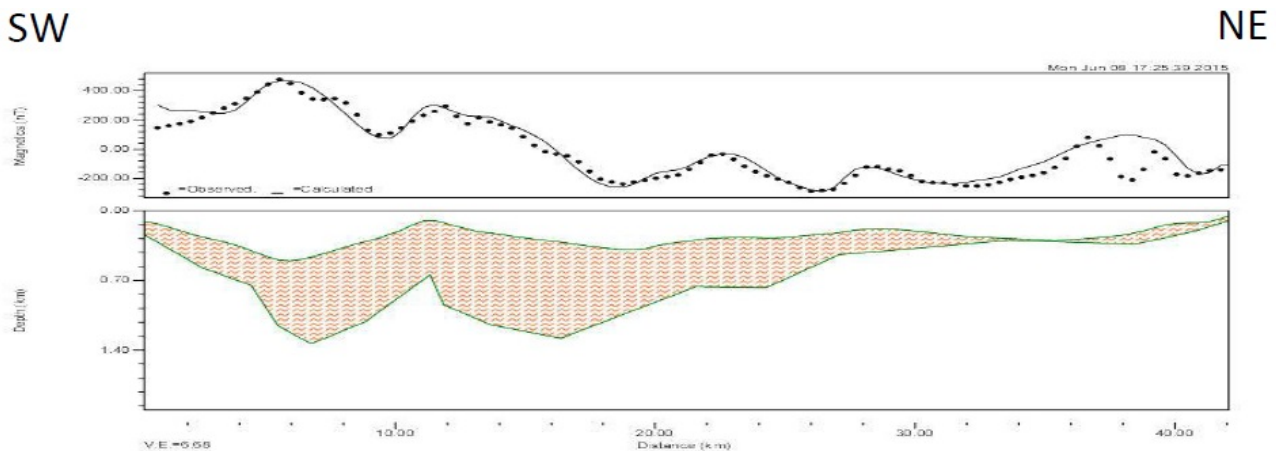


Figure 10. 2.75D magnetic model of the P1 profile. A constant magnetization of 8 A/m was used. The magnetic layer top is represented by the bathymetry and the bottom was modeled to fit correctly the observed magnetic values.

Fig. 10 shows the modeled P1 profile. In general, the high frequency pattern of the magnetic anomaly of the off-shore area indicates the presence of superficial localized volcanic bodies, while the main long wavelength anomaly is due to a tabular body confined between the Catania canyon and the Alcantara valley. In relation with the Catania canyon, it is necessary a thickening of magnetized material to correctly describe the associated magnetic anomaly. Moving toward NE from the Catania canyon, the tabular magnetic body tends to thin and disappears north of the Alcantara valley area.

The presented P1 models suffer from the typical ambiguity that characterizes potential field anomalies interpretation. At the moment we do not have independent data to constrain the profiles models; only shallow structures, about some tens of meters, are currently interpreted independently using seismic tomography data in the picture of this project (see Wp 8 report by Monaco, RU 6). The available data shows a good correlation between magnetic profiles and interpreted shallow volcanic bodies in seismic profiles.

Task 3 – WP 9, Resp. M. Anzidei

Deformation of the Lipari-Vulcano-Gulf of Patti system and implications on coastal hazard

Sp2 – Updated GPS crustal velocity and strain fields

Participants: INGV-CNT

Marco Anzidei, Alessandra Esposito, Angelo Massucci, Grazia Pietrantonio, Vincenzo Sepe, Enrico Serpelloni, Antonio Vecchio

Other institutions

INGV-CT Alessandro Bonforte, Mario Mattia, Francesco Guglielmino, Valentina Bruno, Mimmo Palano, Flavio Cannavò, Salvatore Gambino, Giampiero Aiesi, Francesco Calvagna, Salvatore Consoli, Benedetto Saraceno, Massimo Cascone, Marco Manni; **INGV-NA** Franco Obrizzo; **Ecole Normale Supérieure (Paris, France)** Pierre Briole

GPS surveys in the Aeolian Islands

The GPS data analysis follows a procedure that can be summarized in 3 main steps that include i)

daily processing of the GPS networks located in the Aeolian Islands, ii) combination of daily solutions and iii) definition of the reference frame, time series analysis and velocity field estimation.

Daily processing of the GPS network in the Aeolian Islands

The analyzed dataset consists of GPS data collected in the time span 1996-2013 on 28 survey-style benchmarks located in the area of the Aeolian Islands, 31 survey-style benchmarks located in Northern Sicily and Calabrian Arc and 4 permanent GPS stations on the Vulcano Island (Fig. 1). We included in our analysis 9 European IGS sites, used as “anchor” stations to perform a successive combination of the obtained daily solutions with those of a globally distributed network of IGS stations, that is a preliminary step for the transformation into the ITRF2008 reference frame.

We process data using the Bernese GNSS software 5.0 (Dach et al., 2007), following the EUREF Guidelines for EPN Analysis Centres (http://www.epncb.oma.be/_documentation/guidelines/).

The GPS orbits and the Earth’s orientation parameters are fixed to the combined IGS products and an *a priori* loose constraint of 10 m is assigned to all site coordinates. The elevation-dependent phase centre corrections and absolute phase centre calibrations are applied. The troposphere modeling consists in an *a priori* dry-Niell model fulfilled by the estimation of zenith delay corrections at 1-hour intervals in each site using the wet-Niell mapping function; in addition one horizontal gradient parameter per day in each site is estimated. The ionosphere is not modeled *a priori*, it is removed by applying the ionosphere-free linear combination of L1 and L2. The ambiguity resolution is based on the QIF baseline-wise analysis. The final network solution is solved with back-substituted ambiguities, if integer; otherwise ambiguities are considered as real valued measurement biases. Thus the daily GPS solutions are not estimated in a given *a priori* reference frame but computed in a loosely constrained reference frame. The coordinates are randomly translated or rotated from day-to-day and their covariance matrices have large errors (on the order of meters) as a consequence of the loose constraints applied to the *a priori* parameters.

Combination of daily solutions and reference frame definition

The daily “loose” coordinate solutions, with their complete covariance matrices, saved as SINEX files, are day by day merged with daily loose SINEX files of a global network of 60 IGS stations. Basically, the two sets of solutions share 9 common sites allowing the combination into a unique solution using a classical least-squares approach where the coordinates are both observations and estimated parameters. After these combinations, to express the daily coordinates of the overall network in a unique reference frame and to compute the real covariance matrix, we perform two main transformations. First the loose covariance matrix is projected into a well-defined reference frame imposing tight internal constraints (at the millimeter level), and then coordinates are transformed into the ITRF2008 by a 4-parameter Helmert transformation (translations plus scale factor).

Time series analysis and velocity field estimation

Site velocities are estimated fitting simultaneously a linear drift, episodic offsets and annual sinusoids to all the coordinate time series. Offsets are estimated whenever a change in the GPS equipment induces a significant transient in the time series, whereas seasonal oscillations are accounted for by annual sinusoids. Outliers are rejected whenever the weighted residual exceeds three times the global chi square (χ^2). At this stage we combine the obtained network velocity solution, expressed in the ITRF2008 reference frame, with an independent velocity solution of 171 GPS permanent sites in Southern Italy in the time span 1998 to 2013 (Devoti et al., 2014). Also this latter velocity field is referred to ITRF2008 frame and is derived from data of permanent GPS stations belonging to the RING network of INGV, including also CGPS stations in the Aeolian Islands, and to other different networks in Italy.

The velocity combination procedure consists of a linear least-squares approach. The normal matrix is formed by the two independent velocity solutions, and then it is inverted to estimate the unified velocity field of the entire network. As the covariance matrix is usually known separately from a constant multiplier, we also estimate a solution-scale factor together with the combined velocity solution. This ensures that the individual χ^2 of each velocity solution is equally balanced (individual solutions do not prevail in the combination process) and the total χ^2 is close to unity (realistic errors). The combined solution represents a weighted velocity average that takes into account the correlation matrices of the two solutions.

In the auxiliary electronic materials (Annex 1), the time series and the velocity field in SINEX format derived from our analyses, are reported.

Results

The horizontal GPS velocity field of the Aeolian Islands, which are expressed with respect to a fixed Eurasian plate (Fig. 11, Tab. 2), shows recognizable and slow-varying patterns characterized by shortening gradient from SE to NW and gradually decreasing from S to N. The horizontal crustal shortening is up to several $\text{mmyr}^{-1} \text{Km}^{-1}$ while a diffuse subsidence up to 9 mm/yr^{-1} is estimated. Results are in agreement with previous studies that evidenced how the central Aeolian Islands is the area of transition between the active N-S compression in the northwestern part of the archipelago and the NW-SE trending extension recognized in the eastern part of the Aeolian arc, Eastern Sicily and Calabria.

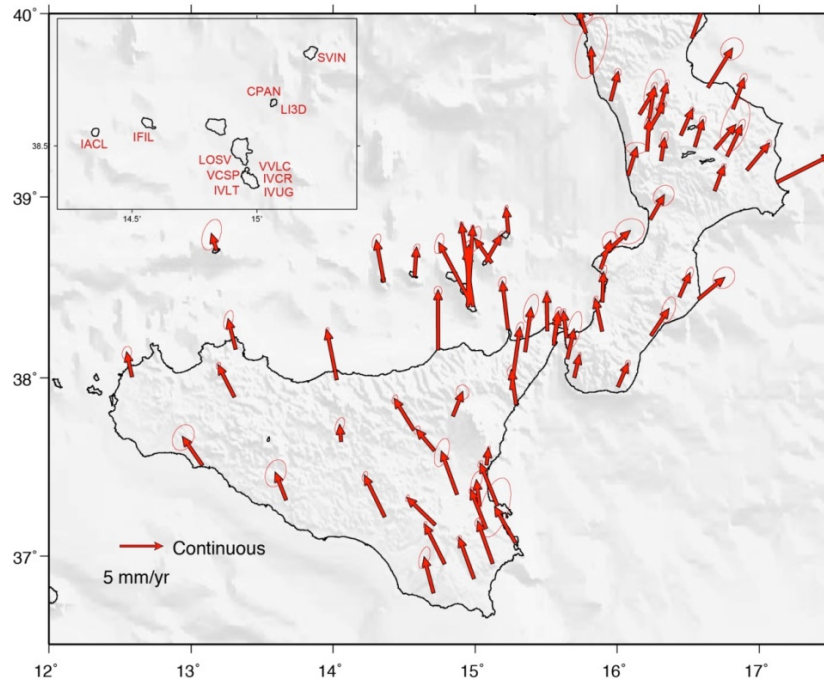


Figure 11. The GPS velocity field for the CGPS regional network. In the inset the CGPS stations for the Aeolian Islands analyzed in this work, are reported.

Island	Islet	Station ID	Lon	Lat	Ht (m)	v East mm/yr	σ vE mm/yr	v North mm/yr	σ vN mm/yr	v Up mm/yr	σ vUp mm/yr	Benchmark type and antenna set up system	Date of construction	time span	additional data
Alicudi		ALCD	14.356	38.531	51.1	-1.2	0.1	4.5	0.1	-1.2	0.4	3DB, 3D	1996	1996-2013	
Filicudi		FILI	14.578	38.563	173.2	0.8	0.3	3.5	0.3	-2.9	1.1	3DB, 3D	1996	1996-2013	
Lipari		LCAP	14.954	38.444	228.7	-3.6	1.1	5.4	0.8	-7.4	3.3			1996-2009	
		LFAL	14.945	38.444	256.1	-0.1	0.6	5.4	0.6	-7.0	2.6			1996-2009	
		LGUA	14.946	38.455	409.3	-1.1	0.6	5.1	0.6	-10.0	2.1			1996-2009	
		LMAZ	14.906	38.483	366.4	1.1	0.5	3.9	0.5	-11.6	1.9			1996-2009	
		LROS	14.977	38.483	282.1	-3.9	0.6	3.4	0.6	-5.5	2.4			1996-2009	
		LSAN	14.934	38.485	580.2	0.1	0.6	3.7	0.6	-11.8	2.0			1996-2009	
Panarea		PA3D	15.074	38.633	145.4	-1.3	0.1	2.0	0.1	2.8	0.6	3DB, 3D	2003	2003-2013	
		PANA	15.074	38.633	145.1	-1.3	0.3	2.0	0.5	2.8	0.9	S, T	1987	1996-2013	1995
		PC3D	15.064	38.639	462.9	0.2	0.4	1.4	0.6	-7.7	1.3	3DB, 3D	2013	2013	
		PCOR	15.064	38.639	465.3	0.2	0.4	1.4	0.7	-7.7	2.2	IGM, T	1970	2003-2013	
	Basiluzzo	BA3D	15.116	38.662	96.4	-2.2	1.6	0.8	1.7	-7.0	6.9	3DB, 3D	2003	2003-2013	
	Bottaro	BOTT	15.111	38.638	54	-1.7	0.2	2.8	0.2	-5.2	0.9	3DB, 3D	2003	2003-2006	
	Lisca Bianca	LIBI	15.113	38.639	75.5	-2.2	1.7	5.1	0.9	0.0	4.2	IGM, T	2003	2003-2013	1997
	Lisca Nera	LINE	15.107	38.635	46.9	-1.4	0.3	2.7	0.3	-4.1	1.2	3DB, 3D	2003	2003-2013	
	Panarelli	PNRL	15.100	38.642	47.3	-1.3	0.4	2.8	0.8	-3.5	1.5	3DB, 3D	2003	2003-2013	
Salina		SALI	14.872	38.559	62.7	1.5	0.1	1.7	0.2	-3.6	0.4	3DB, 3D	1996	1996-2013	1995
Stromboli		STRO	15.242	38.801	50	0.5	0.4	2.9	0.7	0.1	1.3	S, Wild or IGM base	1987	1996-2005	1994
Vulcano		VCRA	14.965	38.403	435.2	-0.5	1.6	10.8	2.8	-7.7	5.8			1996-2009	
		VLEN	14.946	38.408	231.2	0.7	0.6	8.8	0.9	-8.0	1.9			1996-2009	
		VMOL	14.986	38.396	424.1	-1.0	0.9	8.9	1.2	-5.8	2.6			1996-2009	
		VPLI	14.956	38.430	68.6	-0.4	0.9	6.6	1.5	-10.6	3.2			1996-2009	
		VROS	14.974	38.395	369.1	0.6	1.1	9.0	2.1	-6.8	4.2			1996-2009	
		V SAR	14.961	38.390	525.7	-1.3	1.1	9.8	1.6	-7.5	3.2			1996-2009	
		VSER	14.985	38.378	513.5	-1.3	0.4	8.2	0.8	-2.3	1.7	IGM, IGM base & tribrach	1970	1996-2009	1995
		VCUA	14.952	38.417	50.6	0.1	0.6	7.0	1.0	-5.8	2.0	3DB, 3DM	1996	1996-2009	
		VVUL	14.963	38.426	152.4	-0.4	0.9	6.1	1.0	-9.7	2.3			1996-2009	

Table 2. GPS velocities and uncertainties (in mmyr^{-1}). Station name; Longitude; Latitude; ITRFxx velocities; 1σ uncertainties; residual velocities with respect to Eurasia; absolute motion rate and uncertainty. See the text for details.

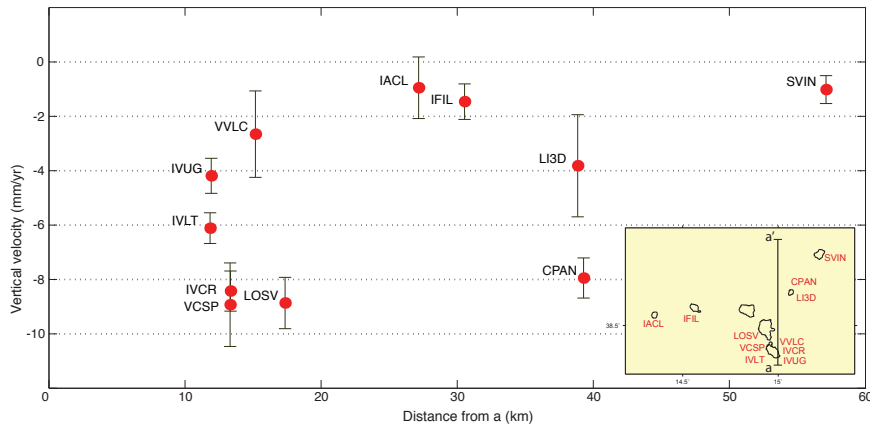


Figure 12. CGPS vertical velocity for the Aeolian Islands.

Anyway, our analysis provides more details with respect to previous studies, i.e. the subsidence of this region (Fig. 12). The GPS network of Lipari-Vulcano shows an overall Northward trending of the ground motion with tiny rotations between NNE to NNW. An active about N-S shortening occurs at $1.0 \times 10^{-13} \text{s}^{-1}$, with a maximum between la Fossa Caldera and Vulcanello, while a diffuse subsidence with values up to 12 mm/yr^{-1} with a gradient of $0.4 \text{ mmyr}^{-1} \text{ Km}^{-1}$ has been estimated between Lipari and Vulcano (Fig. 13).

It is worth noting that the increasing N-S subsidence, is occurring with an increasing N-S contraction, with larger values within the island of Vulcano. Anyway, this pattern is partially dependent from larger uncertainties along the GPS vertical component besides local disturbances. The local network of Panarea shows a general shortening between the archipelago of the Islets and the SE portion of Panarea Island and the NW sector of island along the NE-SW trending structural lineaments (Fig. 14).

Finally, the local networks analyzed in this study, with their several benchmarks distributed over a few km^2 of land and often a few km distant each other, evidenced that the ground velocity field is affected by local disturbances related to the combination of superimposed-volcanic and tectonic signals within this region.

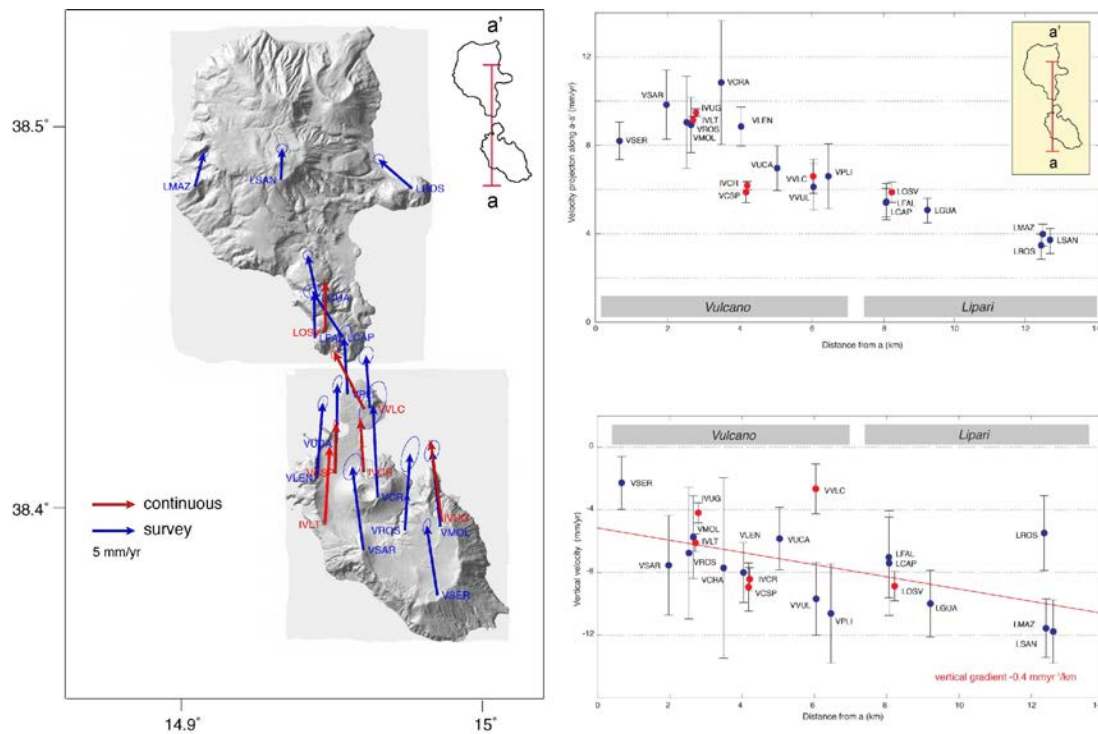


Figure 13. a) The horizontal GPS velocity field for the GPS discrete networks of Lipari-Vulcano; b) upper right: GPS and CGPS horizontal velocities projected along cross section a-a'; c) lower right: CGPS and GPS vertical velocities along a-a'.

Section 2

Scientific Reports of Research Units (RU 3)

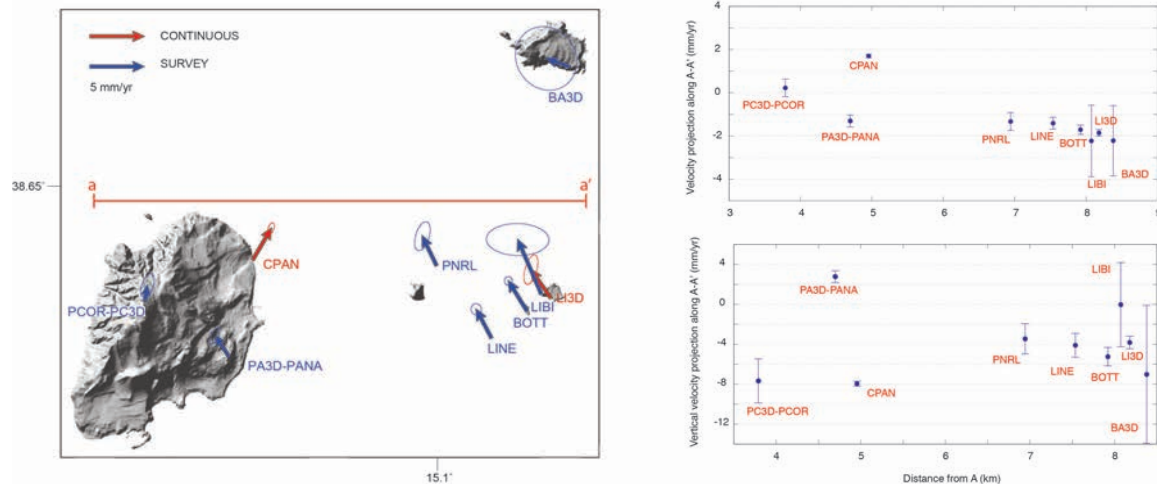


Figure 14. a) The horizontal GPS velocity field for the GPS discrete networks of Panarea; b) GPS and CGPS horizontal velocities projected along cross section a-a'; c) CGPS and GPS vertical velocities along a-a'.

Sp3 – Predictive map of marine ingressión for 2100 for Lipari

Participants: INGV-CNT

Marco Anzidei, Alessandra Esposito, Grazia Pietrantonio, Vincenzo Sepe, Antonio Vecchio

Other institutions

INGV-RM2 Roberto Carluccio, Cosmo Carmisciano, Francesca D'Ajello Caracciolo, Marina Locritani, Filippo Muccini, Iacopo Nicolosi, Riccardo Vagni; **INGV-CT** Marco Manni; **Dipartimento ICEA (UNI-PD)** Massimo Fabris; **Università La Sapienza, Roma** Francesco Latino Chiocci; **IGAG-CNR** Alessandro Bosman, Daniele Casalbore; **Soprintendenza del Mare della Sicilia** Sebastiano Tusa, Roberto La Rocca

To predict the marine ingressión at Lipari in the two areas of Marina Lunga and Marina Corta harbors, we used ultra-high resolution DTMs performed by rapid UAV surveys, in combination with multibeam bathymetric surveys and sea level rise predictions. By adding current isostatic rates, expected climate change from IPCC through the reports Veerner and Rahmstorf model (2009, PNAS) and current rates of land subsidence estimated from historical and GPS data, we provide the first relative sea level rise projections and multitemporal maps of flooding scenarios for the coast of Lipari for the year 2100.

The UAV surveys

Two low-altitude aerial photogrammetric surveys were carried out in October 2014 over the harbors of Marina Corta and Marina Lunga. We used a radio controlled multi rotor DJI S800 multicopter UAV system, equipped with a lightweight nadiral high resolution digital camera (Fig. 15). Equipment included a 10 Megapixel camera (images resolution at 3648x2736 pixels) with horizontal and vertical field of view 53° and 40°, respectively. Surveys were conducted on a windless day and the total time of flight was about 20 minutes. The multi-rotor vehicle, controlled by an autopilot system and flew autonomously through waypoints previously planned on a Ground Control Station system (GCS). To optimize the photogrammetric spatial resolution and coverage of surveyed areas, a constant altitude of 100 m was maintained during the flight with a consequent geometric ground sample distance of 2.5 cm. Surveys investigated 0.14 km² of land and were shot 558 aerial digital photos. Data have been analysed by Agisoft Photoscan Professional software (www.agisoft.com).

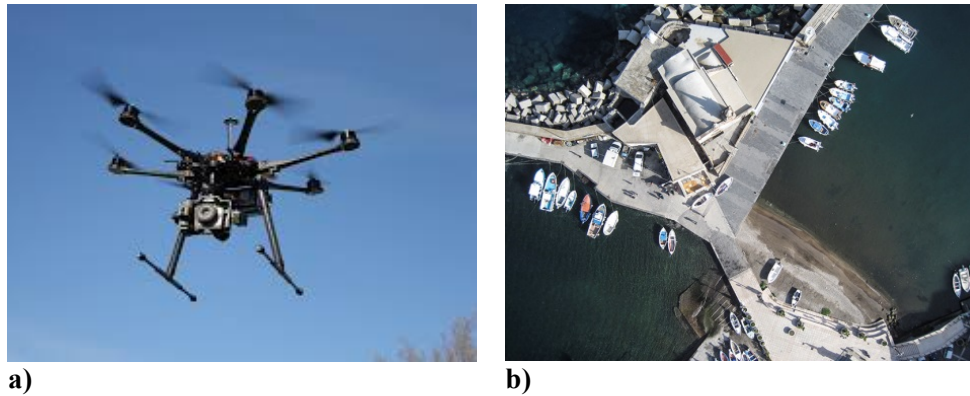


Figure 15. a) The DJI S800 multicopter UAV system and b) a zenithal photo above Marina Corta.

The Multibeam Surveys

The multibeam bathymetric survey was performed during the end of September 2014, covering an area of 17 km² around the coast of the Lipari Island in the depth range between 0.5 and 150 m (Fig. 16). A 7 m long boat named *BigOne* belonging to INGV, was used. The vessel was equipped with a ultra-high resolution Teledyne RESON SeaBat 7125 SV2 multibeam system belonging to the Istituto di Geologia Ambientale e Geoingegneria, National Research Council. This sensor operated at the frequency of 400 kHz, with a cross-track at 1° x 0.5° beam width, and producing up to 512 soundings across a 140°/165° wide swath using equidistance/equiangle configurations.

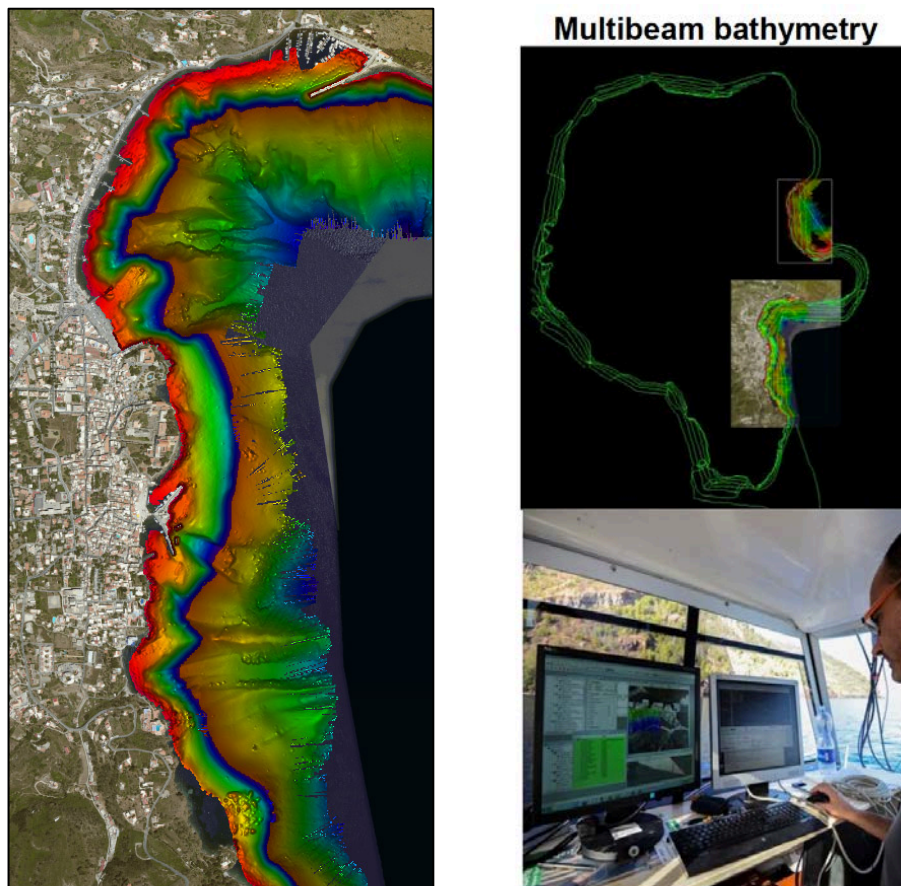


Figure 16. Left: area of the bay of Lipari; right top: investigated areas of the Lipari coast; right bottom: instruments onboard the vessel.

Section 2

Scientific Reports of Research Units (RU 3)

The GPS/RTK and leveling surveys

To scale the images collected during the aerial photogrammetric surveys the coordinates of a set of reference Ground Control Points (GCPs) falling in the investigated areas, were provided. Data were collected using geodetic GPS receivers Leica 1230, equipped with AX1202 antenna and RTK option (Fig. 17 left). GCPs coordinates were estimated in real-time at 1-2 cm accuracy, with respect to the reference continuous monitoring GPS station LOSV located at the INGV Observatory in Lipari. In addition leveling data to measure the elevations of selected features of coastal areas w.r.t sea level (top of piers, docks, streets, groundfloor of houses), were collected (Fig. 17 right). Observations were adjusted for tides using data from the national tidal network (ISPRA).

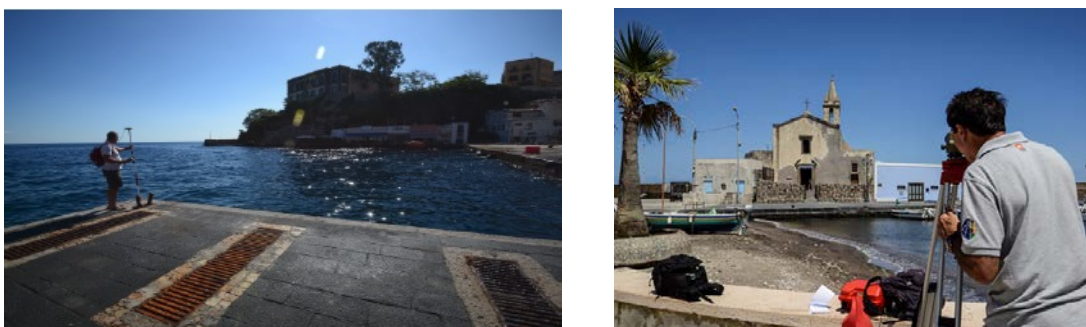


Figure 17. Left: GPS/RTK surveys for Ground Control Points; right: leveling surveys.

Ortophoto creation and DTM extraction

We used the Agisoft PhotoScan Pro software package (<http://www.agisoft.com>) to process the acquired images. Each area was processed separately through a modeling process consisting in three steps: i) camera triangulation with images position and orientation; ii) generation of a dense points cloud and iii) generation of DSM model and orthomosaic photo. The extracted DSMs were then georeferenced by a set of Ground Control Points (GCPs) acquired by GPS/RTK system (Fig. 18).

The shoreline and onshore sectors of the coastal areas are well represented while subsurface bathymetry cannot be modeled, even in shallow waters, due to image noise (reflection and refraction of light) caused by the motion of the sea surface. After georeferencing the two models, a mean point separation resolution at 5.3 cm was achieved. Mean errors are at 4.8 cm and 9.7 cm for Marina Corta and Marina Lunga, respectively. Even if the two surveys have the same point separation resolution, the resulting georeferencing errors are different due to the geometry of Marina Lunga. The georeferenced grid models are calculated using a grid step corresponding to the calculated model errors (5 cm and 10 cm for Marina Corta and Marina Lunga, respectively). The shoreline position at the time of survey is also reported in the maps.

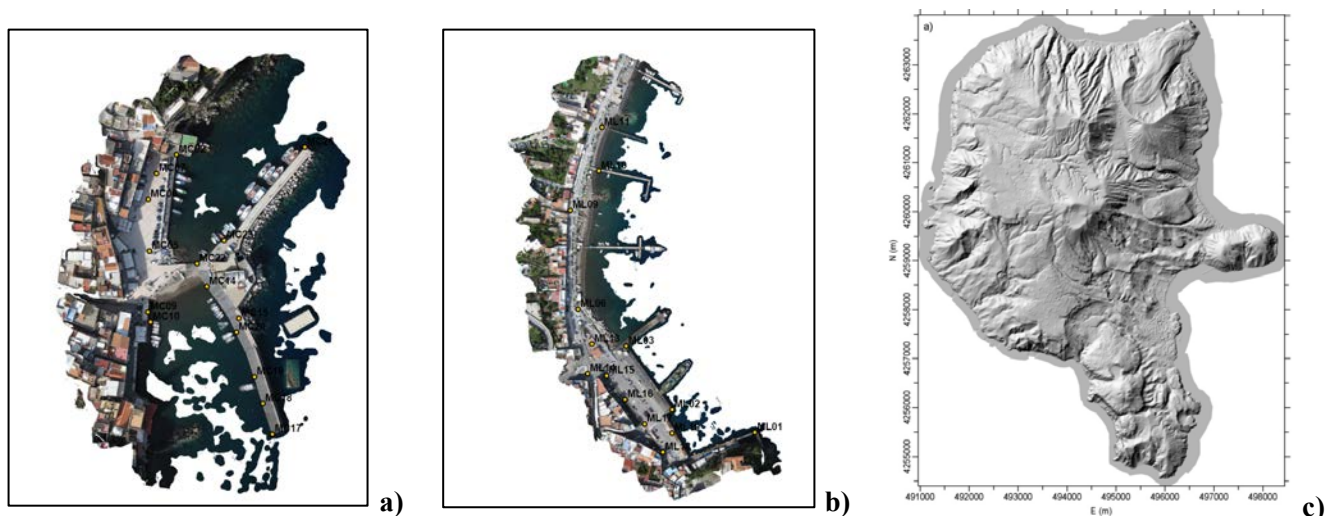


Figure 18. Ortophoto of a) Marina Corta and b) Marina Lunga. Yellow dots are the selected Ground Control Points estimated by GPS/RTK, used to extract the DSM/DTM; c) the DTM extracted from aerial photogrammetric surveys (data from Regione Sicilia).

Land Surface and Bathymetric Data Integration

Digital aerial photogrammetry, LiDAR (Light Detection and Ranging) and multibeam bathymetry provided very high resolution images of topography of land and seafloor surfaces with high accuracy and in a short time (Fig. 19). Point positioning of bathymetric surveys was defined by a GPS/RTK station. The same reference GPS station of LOSV employed to locate the GCPs points during the UAV aerial photogrammetric surveys, were used. To integrate topographic surveys from different datasets into accurate 3D 'digital terrain and marine models' (DTMM), data were co-registered in the same reference system. The topographic dataset consists of aerial photos from Regione Sicilia, Lidar data from Ministero dell'Ambiente (both at the scale of the whole Lipari island), local data from UAV surveys and finally Multibeam bathymetric data, to produce a high resolution DSM/DTM of the coastal area.

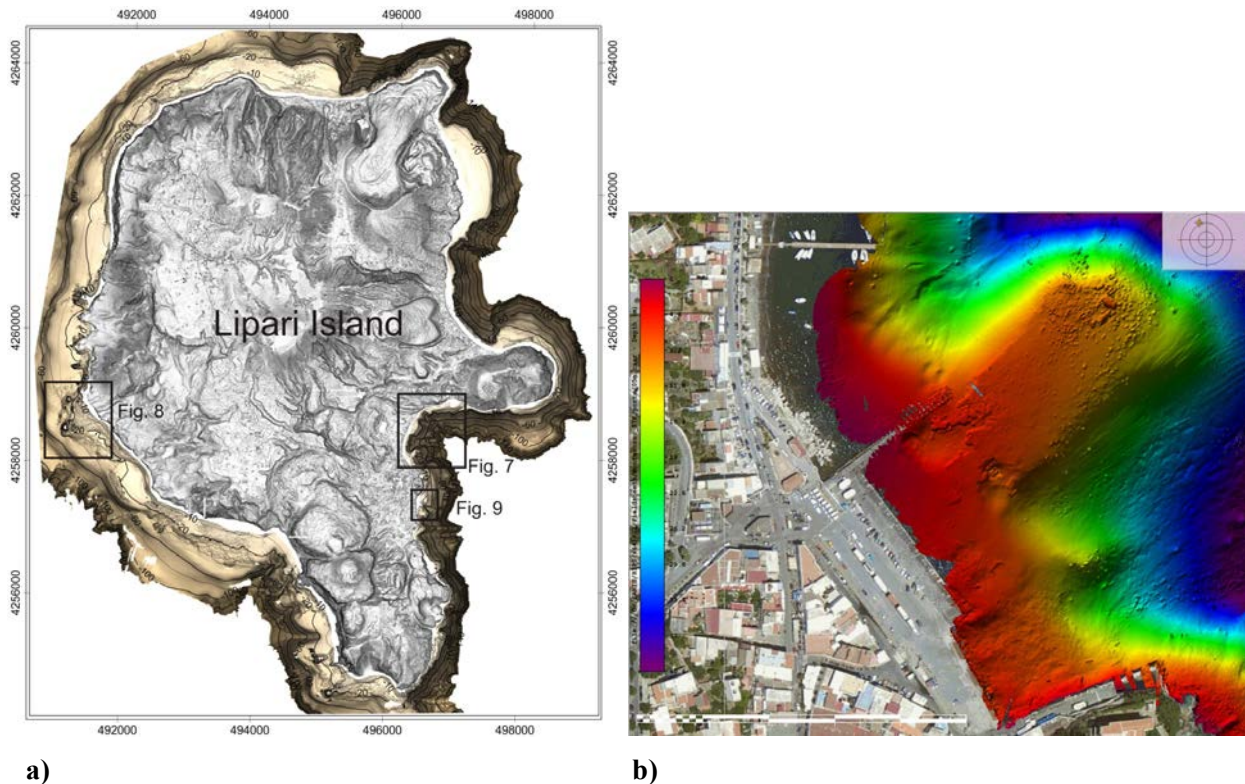


Figure 19. a) DTM of Lipari island from LIDAR data combined with multibeam bathymetric data to a depth up to -150 m; b) the harbor of Marina Lunga with the remains of the Roman age pier that infer a subsidence at -12.7 m in 2.1 ka BP.

Rates of land subsidence at Lipari

Land subsidence at Lipari has been estimated from historical and instrumental data. In the time-span 1996-2013, GPS data shows a diffuse subsidence along the Aeolian arc, but with increasing values across Lipari and Vulcano islands (see Sp2). Particularly, GPS shows a subsidence rate at about 9 mm/yr at Lipari. This value is in good agreement with historical indicators, represented by the Chiesa delle Anime del Purgatorio of the XIII century, the pier of Sottomonastero of the XVIII century and the Roman age pier built in the 100 B.C. The latter was discovered in 2008 during preliminary excavations for the construction of a new pier at Marina Lunga. This is a valuable indicator of the relative sea level changes and vertical land movements since its construction. Archaeological investigations and ultra-high resolution multibeam bathymetry show that its top surface is presently located at -9.1 ± 0.05 m, while the foundations at the outer end of the pier are at -11.6 ± 0.05 m, above a shoreline placed at -13.0 ± 0.05 m.

The current submergence of this pier, as well as for the modern pier at Sottomonastero and the Chiesa delle Anime del Purgatorio, can be explained by the cumulative effect of the relative sea level changes caused by the regional glacio-hydro-isostatic signal, active since the end of the last glacial maximum (18.000 years BP), and the local volcano-tectonic land subsidence. Using glacio-hydro-isostatic model valid for the Aeolian island region (Fig. 20), we have attempted the interpretation of the observed relative sea level change

Section 2

Scientific Reports of Research Units (RU 3)

at 12.3 ± 0.7 m during the last 2100 ± 100 years BP: the total subsidence rate is 5.79 ± 0.01 mm/yr⁻¹, which is partially caused by isostasy at 0.46 mm/yr of rate, and a volcano-tectonic contribution of 5.17 ± 0.01 mm/yr⁻¹. It is worth noting that these rates of relative sea level change likely led to the disuse of the harbor after around the fourth century AD, in agreement with archaeological interpretations.

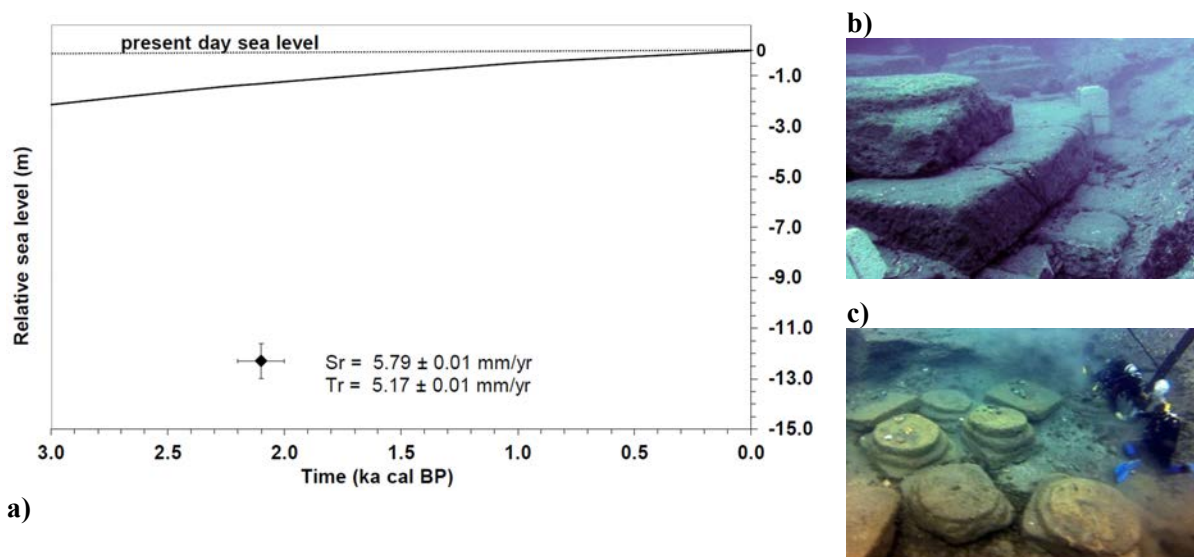


Figure 20. a) Predicted sea level (from Lambeck et al., 2011) compared against the elevation of the Roman age pier at Lipari (black diamond), dated at 2100 ± 100 yrs BP with uncertainties for age and elevation. A relative sea level change of 13.0 ± 0.5 m has been estimated. Sr is the observed subsidence rate of 5.79 ± 0.1 mm/yr⁻¹, while Tr is the rate of the estimated tectonic contribution to the observed subsidence of 5.17 ± 0.1 mm/yr⁻¹. Data have been reduced for the intervening eustatic change at 13 cm as estimated by Lambeck et al. (2004b). b) and c) underwater photos of the Roman age pier with the remnants of the columns and pavements.

Expected sea level rise at Lipari up to 2100

Based on GPS and historical evidence of land subsidence, marine and terrestrial very high resolution DTMs, we provided values of sea level rise for the coastal area for the harbor zones of Marina Corta and Marina Lunga, at specific epochs (Tab. 3). To estimate the future sea level at Lipari, we accounted for current rate of subsidence, global warming trend and long-term natural variability of sea level (at timescales greater than 15 yr). For the eustatic sea level contribution, which is different in the Mediterranean from the Oceans, we used the tidal data of the longest tidal records in the Mediterranean at the stations of Genova, Trieste and Marsiglia. We analysed these records by the Empirical Mode Decomposition (EMD) to build up a simple low order model describing the long-term behavior as a superimposition of a linear trend and a sum of oscillating functions, with constant frequencies derived from the average periods of the EMD modes. This model allows us to estimate the future sea level by including the effects of the long-term variability which may play a relevant role since it can significantly modify the sea level trend when localized sea-level records are considered. Finally, we included into our sea level solutions the climatic scenarios affecting future sea levels, based on the relationship linking global sea level variations on time scales of decades to centuries to global mean temperature. Future sea levels have been estimated for more scenarios: in this report we show the worst scenarios derived from the IPCC RCP 2.6 and RCP 8.5 models and from Veerman and Rahmstorf (2009, PNAS), providing the amounts of sea level rise for 2100 with the following values in Tab. 3.

<i>Year</i>	<i>Climatic model</i>	<i>Minimum sea level rise scenario (m)</i>	<i>Maximum sea level rise scenario (m)</i>
2050	Veermer and Rahmstorf	0.71	0.72
	IPCC 2014	0.58	0.62
2080	Veermer and Rahmstorf	1.34	1.50
	IPCC 2104	0.99	1.14
2100	Veermer and Rahmstorf	1.84	2.21
	IPCC 2104	1.29	1.57

Table 3. Minimum and maximum sea level rise at Lipari for 2050, 2080 and 2100 epochs based on the current rates of sea level trend, subsidence rate and for IPCC (2014) and Veermer and Rahmstorf (2009) climatic predictions.

Maps of flooding scenarios up to 2100

To provide the flooding scenario, we show the upper limit of the marine flooding at different epochs for the two areas of Marina Lunga and Marina Corta. We considered three different scenarios for 2050, 2080 and 2100 epochs, based on the co-registered very high resolution DTMs previously described and on the relative sea level rise prediction as discussed above. We underline that the present sea level is already flooding part of the villages of Marina Lunga and Marina Corta. The water tanks of some houses are already polluted by marine water, beaches are retreating continuously and the roads back of the modern dock are flooded during high tides and storms (Fig. 21).



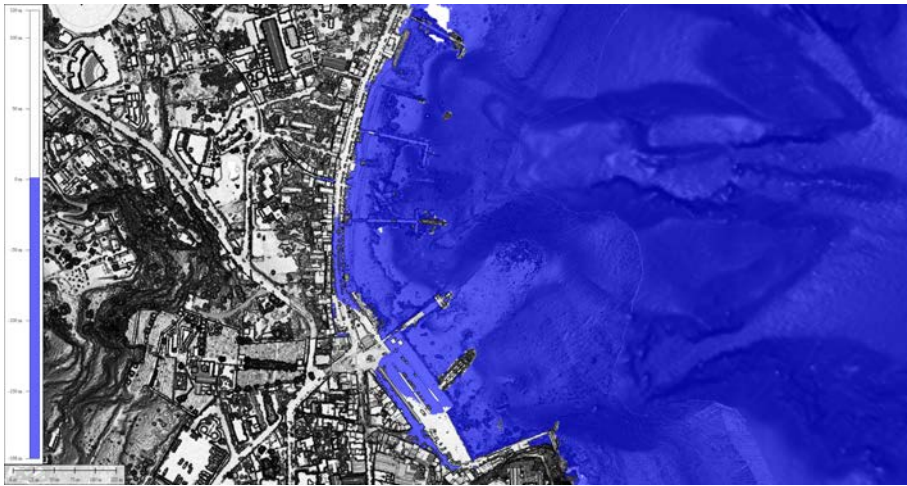
Figure 21. Marina Lunga: a) a flooded groundfloor along via F. Crispi; b) Via Amendola during high tide; c) the submerged pier of the XVIII century, with the bollards at its top.

Results of our predictive maps show that the coast of Lipari will be largely flooded in the next decades with a maximum sea level that will rise at 2.21 m for 2100 for the worst scenario (Veermer and Rahmstorf, 2009). In Tab. 3, we show the maximum and minimum predicted sea level rise for 2050, 2080 and 2100 for IPCC (2014) and Veermer and Rahmstorf (2009) climatic scenarios. In Figs. 22 and 23, we provide multitemporal maps marine flooding at 2050, 2080 and 2100 epochs for Marina Lunga and Marina Corta areas. Shores, commercial infrastructures and touristic coastal installations will be flooded. Land planners and decision makers are solicited to consider this scenario for a conscious coastal management.

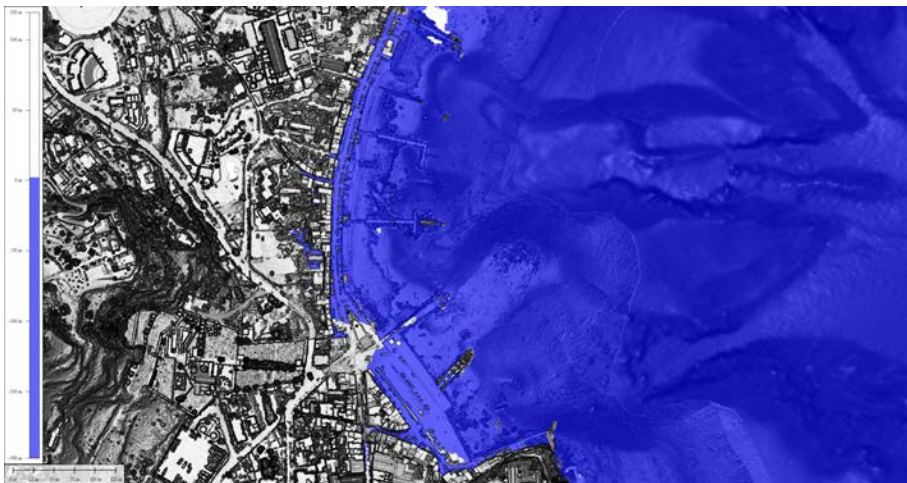
MARINA LUNGA



Epoch: 2050
Sea level rise: 0.72 m
Scenario: maximum
Rahmstorf (2009, PNAS)



Epoch: 2080
Sea level rise: 1.50 m
Scenario: maximum
Rahmstorf (2009, PNAS)



Epoch: 2100
Sea level rise: 2.21 m
Scenario: maximum
Rahmstorf (2009, PNAS)

Figure 22. Maps of multitemporal marine flooding for Marina Lunga. Blue is the sea level with respect to the time of surveys (October 2015). Topography from UAV aerial photogrammetry and bathymetry from multibeam surveys, both performed in this project.

MARINA CORTA



*Epoch: 2050
Sea level rise: 0.72 m
Scenario: maximum
Rahmstorf (2009, PNAS)*



*Epoch: 2080
Sea level rise: 1.51 m
Scenario: maximum
Rahmstorf (2009, PNAS)*



*Epoch: 2100
Sea level rise: 2.21 m
Scenario: maximum
Rahmstorf (2009, PNAS)*

Figure 23. Maps of multitemporal marine flooding for Marina Corta. Blue is the sea level with respect the time of surveys (October 2015). Topography from UAV aerial photogrammetry and bathymetry from multibeam surveys, both performed in this project.

Section 2

Scientific Reports of Research Units (RU 3)

Deliverables

- WP 8.Sp1 Magnetic modelling of the Val Calanna area and off-shore coastal sector: **100%**.
WP 9.Sp2 Updated GPS crustal velocity and strain fields: **90%**.
WP 9.Sp3 Predictive map of marine ingression for 2100 for Lipari: **100%**.

Problems and difficulties

The WP activities have been underfunded.

- WP 9.Sp2 Difficulties to coordinate GPS surveys in Sicily with INGV-CT due to scarce availability of INGV cars at INGV in Rome.
WP 9.Sp3 Aerial photogrammetric surveys for INGV activities need to overcome the current limitations imposed for the use of UAV systems.

Key publications

- Nicolosi I., D'Ajello Caracciolo F., Branca S., Ventura G., Chiappini M. (2014). *Volcanic conduit migration over basement landslide at Mount Etna (Italy)*, Scientific Report, 4, 5293.
- Bosman A., Casalbore D., Anzidei M., Muccini F., Carmisciano C., Chiocci F.L. (2015). *The first ultra-high resolution Digital Terrain Model of the shallow-water sector around Lipari Island (Aeolian Islands, Italy)*. Annals of Geophysics, 58, 2, 2015, S0218; doi:10.4401/ag-6746.
- Anzidei M., Esposito A., Fabris, M., Sepe V. (2015). *Misure GPS rapido statiche ed RTK per la realizzazione di un modello digitale del terreno ad alta risoluzione dell'isola di Lipari*. Quaderni di Geofisica, 124, 32 pp.
- Anzidei M., Bosman A., Casalbore D., Tusa S., La Rocca R. (2015). *New insights on the subsidence of Lipari island (Aeolian islands, southern Italy) from the submerged Roman age pier at Marina Lunga*. Quaternary International, doi:10.1016/j.quaint.2015.07.003.
- Esposito A., Pietrantonio G., Bruno V., Anzidei M., Bonforte A., Mattia M., Puglisi G., Sepe V., Serpelloni E. (2015). *Eighteen years of GPS surveys in the Aeolian islands (Southern Italy): open data archive and velocity field*. Annals of Geophysics, doi:10.4401/ag-6823.
- Carluccio R., Nicolosi I., D'Ajello Caracciolo F., Anzidei M., Sepe V., Chiappini M. (2015). *Fast aerophotogrammetric UAV surveys in coastal areas: the case of Lipari (Aeolian islands, Italy)*. In preparation.
- Anzidei M., Bosman A., Carluccio R., Casalbore D., Chiappini M., D'Ajello Caracciolo F., Esposito A., Fabris M., Nicolosi I., Pietrantonio G., Sepe V., Vecchio A. (2015). *Multitemporal maps of sea level flooding at Lipari for 2100 from very high resolution DTM, sea level data and modelling*. Convegno finale Progetti Vulcanologici Convenzione DPC-INGV, Roma 22-23 Giugno 2015. Aula Magna del Rettorato Università Roma 3.
- Bosman A., Casalbore D., Anzidei M., Muccini F., Carmisciano C., Chiocci F.L., Tusa S. and La Rocca R. (2015). *The first ultra-high resolution Marine Digital Terrain Model of the shallow-water sector around Lipari Island (Aeolian archipelago, Italy): implications on land subsidence from the submerged Roman age pier at Marina Lunga*. Convegno finale Progetti Vulcanologici Convenzione DPC-INGV, Roma 22-23 Giugno 2015. Aula Magna del Rettorato Università Roma 3.
- Esposito A., Pietrantonio G., Bruno V., Anzidei M., Mattia M., Bonforte A., Gugliemino F., Puglisi G., Serpelloni E. and Sepe V. (2015). *Eighteen years of GPS surveys in the Aeolian islands (Southern Italy): results and data*. Convegno finale Progetti Vulcanologici Convenzione DPC-INGV, Roma 22-23 Giugno 2015 Aula Magna del Rettorato Università Roma 3.
- Anzidei M., Bosman A., Carluccio R., Carmisciano C., Casalbore D., Chiappini M., Chiocci L.F., D'Ajello Caracciolo F., Esposito A., Fabris M., Muccini F., Nicolosi I., Pietrantonio G., and Sepe V. (2015). *Very high resolution Digital Terrain and Marine Model for Lipari island: flooding scenario induced by land subsidence and sea level rise*. Geophysical Research Abstracts, Vol. 17, EGU2015-12645, 2015, EGU General Assembly 2015.
- Antonioli F., Amorosi A., Anzidei M., Fontolan G., De Falco G., Lambeck K., Lo Presti V., Mastronuzzi G., Serpelloni E., and Vecchio A. (2015). *Relative sea level change along the Italian coasts and projections for 2100 based on high resolution DTMs and geodetic data: implications for coastal impacts*. Geophysical Research Abstracts, Vol. 17, EGU2015-13701, 2015, EGU General Assembly 2015.

- Anzidei M., Bosman A., Carluccio R., Carmisciano C., Casalbore D., Chiappini M., Chiocci L.F., D'Ajello Caracciolo F., Esposito A., Fabris M., Muccini F., Nicolosi I., Pietrantonio G., Sepe V., Vecchio A. (2105). *Land subsidence and sea level rise at Lipari island (Italy): implications for flooding scenario*. Workshop "Global and regional sea level variability and change", University of the Balearic Islands, Mallorca, Spain June 10-12, 2015.
- Anzidei M., Bosman A., Carluccio R., Carmisciano C., Casalbore D., Chiappini M., Chiocci L.F., D'Ajello Caracciolo F., Esposito A., Fabris M., Muccini F., Nicolosi I., Pietrantonio G., Sepe V. (2105). *Flooding scenario for 2100 at Lipari Island due to land subsidence and sea level rise*. Giornate scientifiche AIQUA - Firenze 18 e 19 giugno 2015.
- Anzidei M., Bosman A., Carluccio R., Carmisciano C., Casalbore D., Chiappini M., Chiocci F. L., D'Ajello Caracciolo F., Esposito A., Fabris M., Muccini F., Nicolosi I., Pietrantonio G., Sepe V., Tusa S. (2105). *Relative sea level rise since Roman times and implications for flooding scenario at Lipari island (Aeolian Islands, Italy)*. PALSEA2 meeting, Tokyo, 2015.
- Anzidei M., Bonforte A., Bruno V., Esposito A., Mattia M., Pietrantonio G., Pisani A.R., Puglisi G., Sepe V. (2014). *Current kinematics of the Aeolian Islands*. Geophysical Research Abstracts, Vol. 16, EGU2014-5262, , EGU General Assembly 2014.
- Anzidei M., Bonforte A., Bosman A., Bruno V., Carluccio R., Carmisciano C., Casalbore D., Chiappini M., Chiocci F.L., D'Ajello Caracciolo F., Esposito A., Fabris M., Marsella M., Mattia M., Muccini F., Nicolosi I., Pietrantonio G., Sepe V., Vagni R.. *Present day kinematics of the Aeolian islands and the case of Lipari*. Conferenza Rittmann, Nicolosi, 2014.

Other references

- Agisoft photoscan professional edition v.1.1.0. www.agisoft.com
- Branca S., Ferrara V. (2013). *The morphostructural setting of Mount Etna sedimentary basement (Italy): implications for the geometry and volume of the volcano edifice and its flank instability*. Tectonophysics, 586, 46-64. doi: 10.1016/j.tecto.2012.11.011.
- Chiocci F.L., Coltelli M., Bosman A., Cavallaro D. (2011). *Continental margin large-scale instability controlling the flank sliding of Etna volcano*. Earth and Planetary Science Letters; 305(1):57-64, doi:10.1016/j.epsl.2011.02.040.
- IPCC, *Climate Change 2014, Synthesis Report*. Edited by The Core Writing Team Synthesis Report IPCC Rajendra K. Pachauri, Chairman IPCC Leo Meyer Head, Technical Support Unit IPCC.
- Lambeck K., Antonioli F., Anzidei M., Ferranti L., Leoni L., Scicchitano G., Silenzi S. (2011). *Sea level change along the Italian coast during the Holocene and projections for the future*. Quaternary International, 232 (2011) 250-257, doi:10.1016/j.quaint.2010.04.026.
- Vermeer M. and Rahmstorf S. (2009). *Global sea level linked to global temperature*. PNAS, December 22, 2009, vol. 106, no. 51, 21527–21532. www.pnas.org/cgi/doi/10.1073/pnas.0907765106.
- Schiavone D. & Loddo M. (2007). *3-D density model of Mt. Etna Volcano (Southern Italy)*. J. Volcanol. Geotherm. Res., 164, 161-175.
- Siniscalchi A., Tripaldi S., Neri M., Balasco M., Romano G., Ruch J. & Schiavone D. (2012). *Flank instability structure of Mt. Etna inferred by a magnetotelluric survey*. Journal of Geophysical Research, vol. 117, B03216.
- Villasenor A., Benz H.M., Filippi L., De Luca G., Scarpa R., Patanè G., Vinciguerra S. (1998). *Three-dimensional P-wave velocity structure of Mt. Etna Italy*, GRL, vol. 25, no.11, pages 1975-1978.

RU 4, Istituto Nazionale di Oceanografia e Geofisica Sperimentale, TriesteResponsible: **Angela Saraò****Activity of RU in phase 2**

RU 4 is involved in tasks 1 and 2 of the project:

- WP 1** (resp. B. Pace, UNI-CH, sub-contractor) - Analysis of the variability of the average time of occurrence of earthquakes along the Timpe faults by a geometric-kinematic approach, through the software code FISH produced in the framework of the project DPC-INGV S2.
- WP 3** (resp. L. Peruzza) - Implementation of PSH codes to take into account the specific needs of Mt. Etna area, in particular topographic effects, scaling laws, GMPE and site effects. The new functionalities have been introduced thanks to the cooperation with the developer team of CRISIS (M.G. Ordaz-Schroeder, M.L. Suarez, UNAM, Mexico City) and OPENQUAKE (M. Pagani, Pavia): a fellowship position for developing and testing models on OPENQUAKE has been activated since Jan. 2015 (R. Gee), partially financed by the V3 Project.
- WP 5** (resp. A. Saraò) - Focal mechanisms by calculation of the moment tensor; relationship between the moment magnitude (M_w) and local magnitude (M_L) for the Etna area.

Task 1 - WP 1, Resp. B. Pace*Time-dependent occurrence probability for strong earthquakes on the Timpe fault system*

Participants: Università “G. d’Annunzio” Chieti-Pescara

Bruno Pace

Other institutions

INOGS-TS Laura Peruzza; INGV-CT Raffaele Azzaro, Salvatore D’Amico

Sp1 – Revision of the average time of occurrence of earthquakes along the Timpe faults

We used a geological approach based on geometric-kinematic parameters of seismogenic faults (3D dimensions and slip rates, Tabs. 1, 2) to estimate the average time and probabilities of occurrence of earthquakes along the Timpe and Pernicana fault systems. The analysis has been carried out through the software code FISH, a Matlab® routine produced in the framework of the projects DPC-INGV S2 in order to quantify the seismic activity from geometry and slip-rates of a fault. The part regarding the input of data is extensively described in the first semester report.

By applying the EP-FISH code, we obtained the most likely values of characteristic expected magnitude (M_{max}) with the associated standard deviation ($sd M_{max}$), the mean recurrence time of the M_{max} (T_{mean}), the aperiodicity factor (CV) and the expected seismic moment rates (M_0_{rate}) for each fault of the Timpe and Pernicana fault systems (Tab. 3). The CV values suggest fault behaviours potentially modelled by a time-dependend approach. Moreover, the M_{max} values calculated by the different methods are comparable each other as well as with the maximum observed historical earthquakes.

Finally, by applying the AR-FISH code we obtained the probabilities to have an earthquake in the range of $M_{max} \pm sdM_{max}$ in the next 5, 10, 20 and 30 years (Tab. 4). The values show the S. Tecla fault (STF) as the most probable fault to have a “characteristic” earthquake in the next years, followed by the Moscarello fault (MF).

Section 2

Scientific Reports of Research Units (RU 4)

Fault	Id	length [km]	width [km]	observed M	sd observed M	elapsed time
Pernicana Fault	PF	8.8	4.2	4.7	0.4	5
Fiandaca Fault	FF	7.7	1.5	4.6	0.4	31
S. Tecla	STF	7.6	5.5	5.2	0.4	101
S. Venerina	SVF	5.6	5.5	4.6	0.4	13
Moscarello	MF	8.0	5.9	4.9	0.4	44

Table 1. Geometrical parameters of the Timpe and Pernicana fault systems used as input for the calculations. Length: length of the fault along strike; width: length of the fault along dip; observed M: magnitude (M_w) of the maximum associated earthquake; sd observed M: standard deviation of the observed magnitude; elapsed time: time elapsed in 2015 from the last “characteristic” earthquake ($M \geq 4.4$).

Fault	Id	Slip-rate max [mm/yr]	Slip-rate min [mm/yr]	Time [Kyr]	Error dating [Kyr]	References
Pernicana Fault	PF	5.4	4.7	9.9	0.7	D'Amato et al., 2015
Fiandaca Fault	FF	2.1	1.7	2.1	0.2	Tanguy et al., 2012
S. Tecla	STF	4.5	2.3	32.9	10.6	Azzaro et al., 2012
S. Venerina	SVF	2.1	1.7			Inferred from FF
Moscarello	MF	2.7	1.4	3.5		Azzaro et al., 2000
S. Leonardello	SLF	2.6	2.6	7.59	0.13	Azzaro et al., 2012

Table 2. Slip-rate values of the Timpe and Pernicana fault systems used as input for the calculations. Time indicate the time window used to evaluate the slip-rates.

Fault	Id	Mmax	sd Mmax	Tmean	CV	M0_rate
Pernicana Fault	PF	5.2	0.4	36	0.6	1.95E+15
Fiandaca Fault	FF	4.9	0.3	148	0.54	1.70E+14
S. Tecla	STF	5.3	0.2	47	0.63	2.13E+15
S. Venerina	SVF	5.1	0.3	57	0.54	8.78E+14
Moscarello	MF	5.3	0.3	69	0.63	1.45E+15

Table 3. EP-FiSH output. M_{max} : characteristic expected magnitude; sd M_{max} : associated standard deviation; T_{mean} : mean recurrence time of the M_{max} ; CV: aperiodicity factor; M_0_{rate} : expected seismic moment rates.

Fault	Id	Mmin	BPT prob. 5 yr	BPT prob. 10 yr	BPT prob. 20 yr	BPTprob. 30 yr
Pernicana Fault	PF	4.8	0.24%	2.63%	17.15%	36.60%
Fiandaca Fault	FF	4.6	0.06%	0.21%	1.01%	2.77%
S. Tecla	STF	5	13.59%	25.29%	44.06%	58.02%
S. Venerina	SVF	4.8	0.54%	2.42%	11.48%	25.18%
Moscarello	MF	5	7.42%	14.78%	28.68%	40.94%

Table 4. AR-FiSH output. M_{min} : minimum magnitude for which is calculated the probability of occurrence ($M_{max} - sd M_{max}$); BPT prob.: time-dependent probability to have an earthquake $\geq M_{min}$ in the next 5, 10, 20 and 30 years.

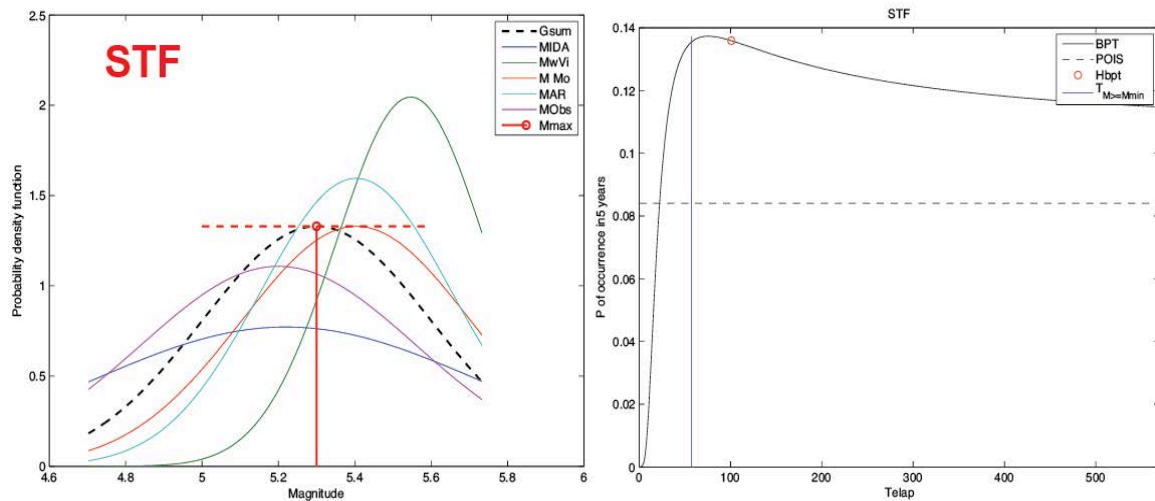


Figure 1. Example of results for the S. Tecla fault (STF). On the left, graph showing the maximum magnitudes estimated by the EP code, following the different used approaches; the dimensions of the curves are in agreement with the relative uncertainties. On the right, graph showing probabilities of occurrence in the next 5 years for an earthquake equal or higher than M_{\min} , following both poissonian and time-dependent BPT behaviours; the red circle represents the time-dependent probability using the elapsed times from the last M_{\max} earthquake, as reported in Tab. 1.

In Fig. 1 we show an example of results obtained by the FISH codes on the S. Tecla fault (STF). In particular, we show the maximum magnitudes estimated by the EP code, according to the different used approaches and the probabilities of occurrence in the next 5 years on an earthquake equal or higher of $M_{\max} - sdM_{\max}$, following both poissonian and time-dependent BPT behaviours. The results of this work suggest that a geological approach based on geometric-kinematic parameters to estimate the expected seismicity rates, can be also adopted with success in the volcanic context of Etna.

Task 1 – WP 3, Resp. L. Peruzza

Probabilistic seismic hazard maps

Participants: INOGS-TS

Laura Peruzza, Robin Gee

Other institutions

UNAM (Mexico) Mario G. Ordaz-Schroeder, Miguel L. Suarez; GEM Pavia Marco Pagani; INGV-CT Raffaele Azzaro, Salvatore D'Amico

Sp1 – Maps including site and topographic effects (30, 20, 10 and 5 yrs)

During the first phase of the V3 Project, with the collaborative work of CRISIS developers, we fixed the problems derived from the rough topography at the small-scale analysis performed at Mt. Etna. In the second semester of the second year, similar implementations have been introduced in OPENQUAKE too, as shown in the example reported in Fig. 2.

Section 2
Scientific Reports of Research Units (RU 4)

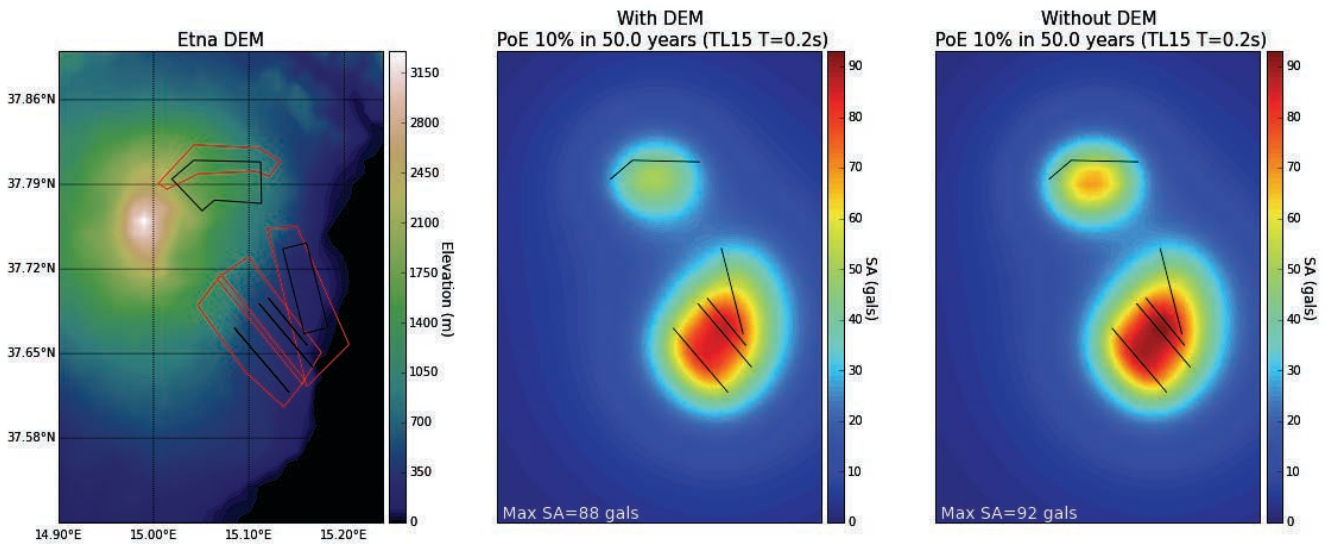


Figure 2. Test on topographic effects using fault sources implemented in OpenQuake during the second phase of the V3 Project; faults are here modelled with their final geometry, but with arbitrary seismicity rates: TL15 means the last GMPE released by Tusa and Langer in the frame of this project.

The effect of topography is controlled by the source characterization, as it influences the source-to-site distance, and by the ground motion prediction equation used: in the performed sensitivity tests we observe that it causes a decrease of expected values locally up to 20%; the role of new topographic distances tends to decrease by increasing the return period the elaborations refer to.

The global scheme of the elaborations so far proposed, is unchanged with respect to the first year of the project, except the inclusion of the geometric-kinematic parametrization of faults described in the previous WP. The conceptual tree is summarized in Fig. 3.

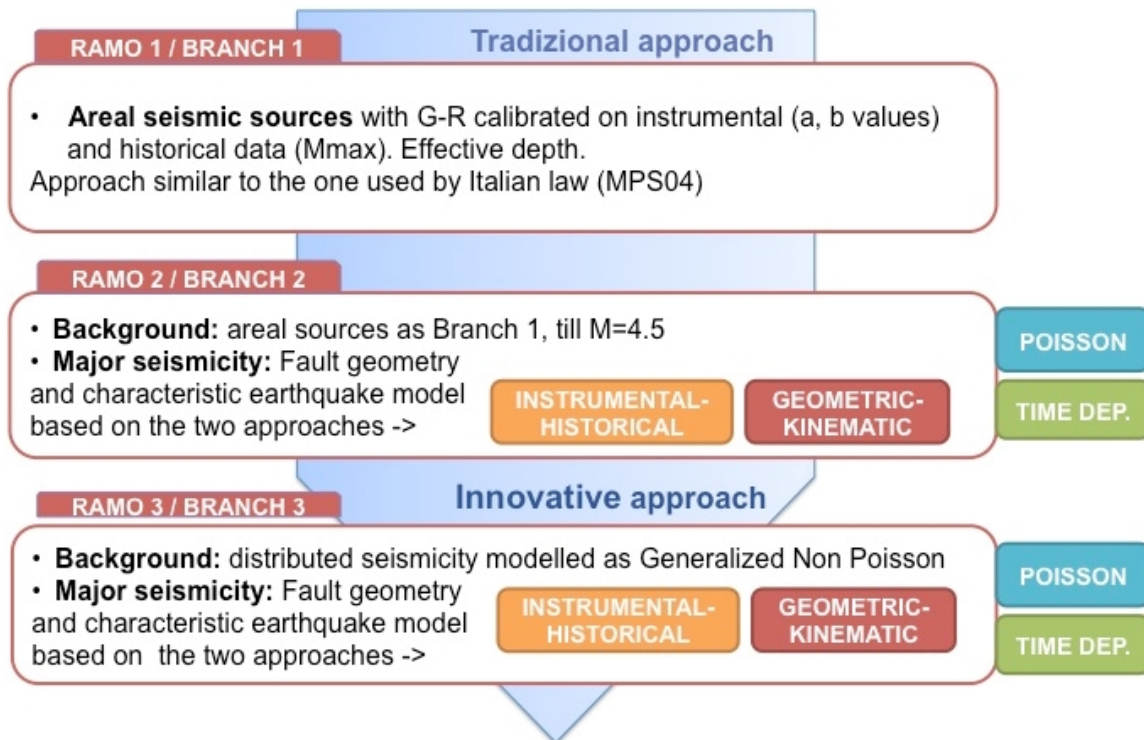


Figure 3. Conceptual scheme of the analyses performed for seismic hazard elaboration, in the V3 Project.

As depicted in the activity report of RU 1 (WP 1, 4), sources characterization went under a significant revision after the relocation of the whole instrumental catalogue using 3D tomographic inversion techniques. Similarly, the attenuation relation calibrated during the first year of the project has been modified in 2015, and several spectral ordinate coefficients are now available. All these novelties became available in the very last months of the project, and have been introduced in the seismic hazard models with some simplifications, for example by implementation of only some structural periods in the analyses (see Tab. 5), in agreement with results given by the team that performed site specific analyses (see report by RU 6, WP 2).

Coeff.	b1>0	b2>0	b3<0	b4<0	b5>0	b6=h	b7<0	b8	b9	rmse e	R2
TUL 13 INV7	Distanza epicentrale fino a 15 km, suoli B										
PGAgeom	1.068	0.666	-0.0089	-3.946	0.091	3.881	0.078	-	-	0.3541	0.686
TUL 15	Distanza ipocentrale fino a 100 km, suoli A										
PGA	-0.033	0.954	-0.083	-2.238	0.311	2.696	-0.006			0.402	0.716
SA 0.2	1.062	0.042	0.080	-2.268	0.019	2.697	0.007	0.472	0.567	0.396	0.858
SA 0.4	-1.803	1.427	-0.105	-1.941	0.050	3.061	0.005	0.491	0.546	0.335	0.883
SA 1	-0.628	0.308	0.064	-1.533	0.239	2.732	0.001	0.465	0.406	0.355	0.869

Table 5. Coefficients used for implementing the GMPE during the first and second phases of the project: the formulation of equation is the one proposed by Bindi et al., 2011 (referred as ITA10).

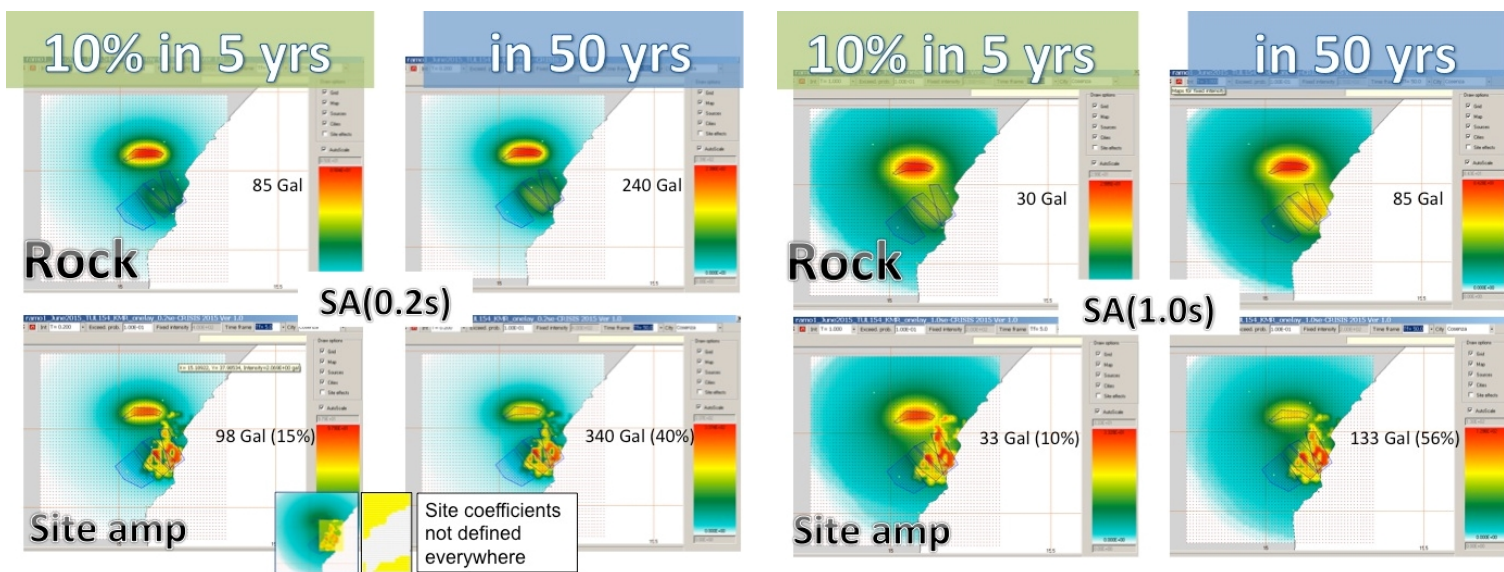


Figure 4. Results obtained by using area sources with G-R calibrated on instrumental and historical data (Branch 1), GMPE derived for the project (Tusa and Langer, 2015, model reported in Tab. 5) and amplification coefficients obtained from site measurements (Panzeria et al., WP2 in RU 6 report). The computations have been done using CRISIS v.2015. Upper frame: spectral acceleration at 0.2 s; lower frame: spectral acceleration at 1.0 s. Note the impact of site effects on the final results.

Given the few time left after the release of the most updated data for running and testing the PSH computations, not all the branches planned in Fig. 3 have been implemented in CRISIS and OPENQUAKE; check on results is still ongoing. The elaborations reported in Fig. 4 are an example of the combination of site amplification coefficients, in a global model of areal sources as depicted in Branch 1; they clearly illustrate how amplification due to local site can jeopardize the expected ground motion at rock reference sites. Even if these results must be considered still preliminary, they represent a first example of new generation, site-specific seismic hazard maps suitable for defining priorities of retrofitting at a local scale.

Task 2 – WP 5

Dynamics and kinematics of the eastern flank from seismological and ground deformation analyses (Etna)

Participants: INOGS-TS

Angela Saraò, Luca Moratto

Other institutions

INGV-CT Ornella Cocina, Luciano Scarfi

Sp2 – Earthquake features through the seismic moment tensor (resp. A. Saraò)

We computed the seismic moment tensor of 50 earthquakes ($3.4 \leq M_L \leq 4.8$) occurred in the period 2005-2013 (Fig. 5) and recorded by the broad-band network of INGV-CT. For our analysis we employed the method developed by Dreger (e.g. Minson and Dreger, 2008), widely adopted in many seismological observatories, with the aim to tune and test this algorithm for computation in near real-time in the Etna area.

The comparison of the best moment tensors with fault plane solutions calculated by first arrival polarities (Scarfi et al., 2013) shows an excellent agreement of solutions (Fig. 6).

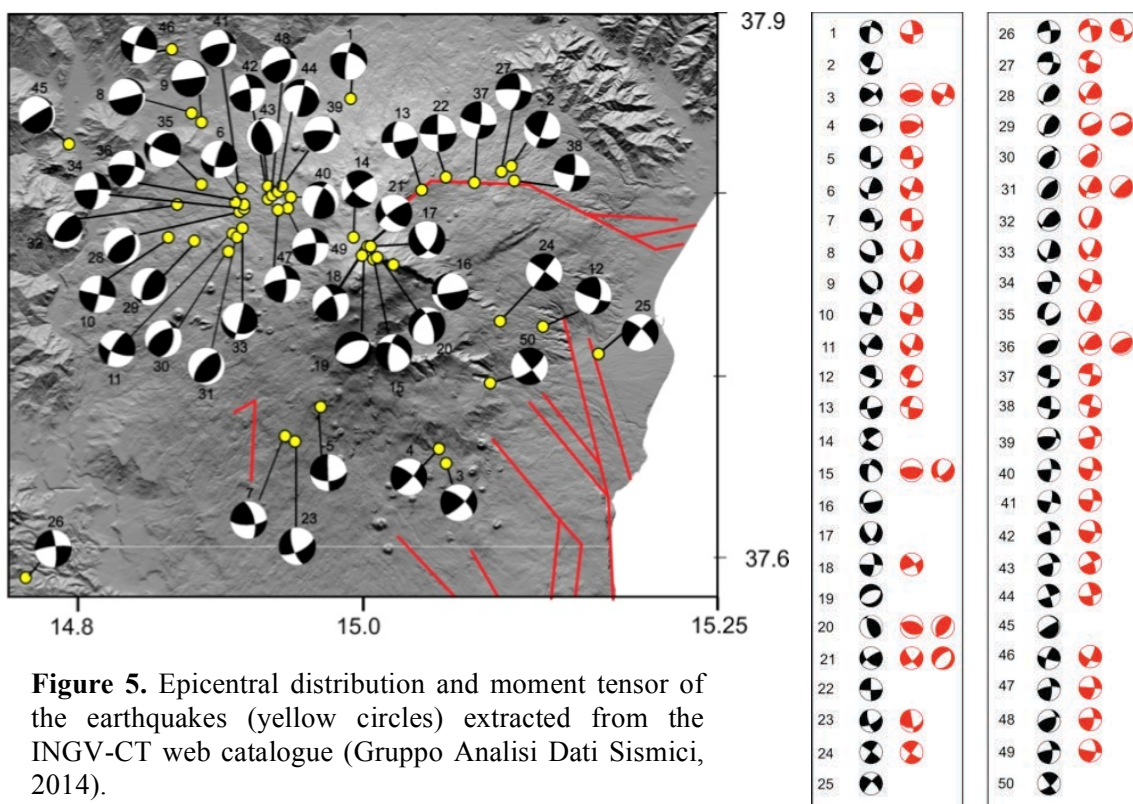


Figure 5. Epicentral distribution and moment tensor of the earthquakes (yellow circles) extracted from the INGV-CT web catalogue (Gruppo Analisi Dati Sismici, 2014).

Figure 6. Comparison of moment tensor (black) with fault plane solutions computed by first polarities (red), published in the INGV-CT web catalogue (Scarfi et al. 2013).

Looking at the percentages of moment tensor component (Fig. 7), we observe an interesting pattern of distribution of the double couple (DC) linked to shear dislocations, and non-DC (CLVD+ISO), possibly related to lenticular crack activation accompanied by possible presence of fluids (CLVD), and volume changes due to implosion or explosion (ISO). In Tab. 6 the solutions obtained by our analysis are listed (Saraò et al, 2014a, 2014b).

We observe that, if we consider the overall dataset (Fig. 7a), the DC component is dominating on the other components but we notice a different trend when splitting the plot in different areas of the volcano; in

the NE area (Fig. 7b), we have a predominance of non-DCs that can be related to the fluids circulation observed also by independent geophysical and geochemical measurements (Siniscalchi et al., 2010). In the NW area (Fig. 7c), the high DC components are associated with deep earthquakes (up to 30 km b.s.l.) and may be due to the activation of the regional tectonic structures related to the Apenninic-Maghrebian Chain compressive regime (Alparone et al., 2010). In the central area (Fig. 7d), the high DCs of the events belonging to the seismic swarm accompanying the 2008 eruption might be related with the formation of the dry eruptive field during the eruption (Aloisi et al., 2009).

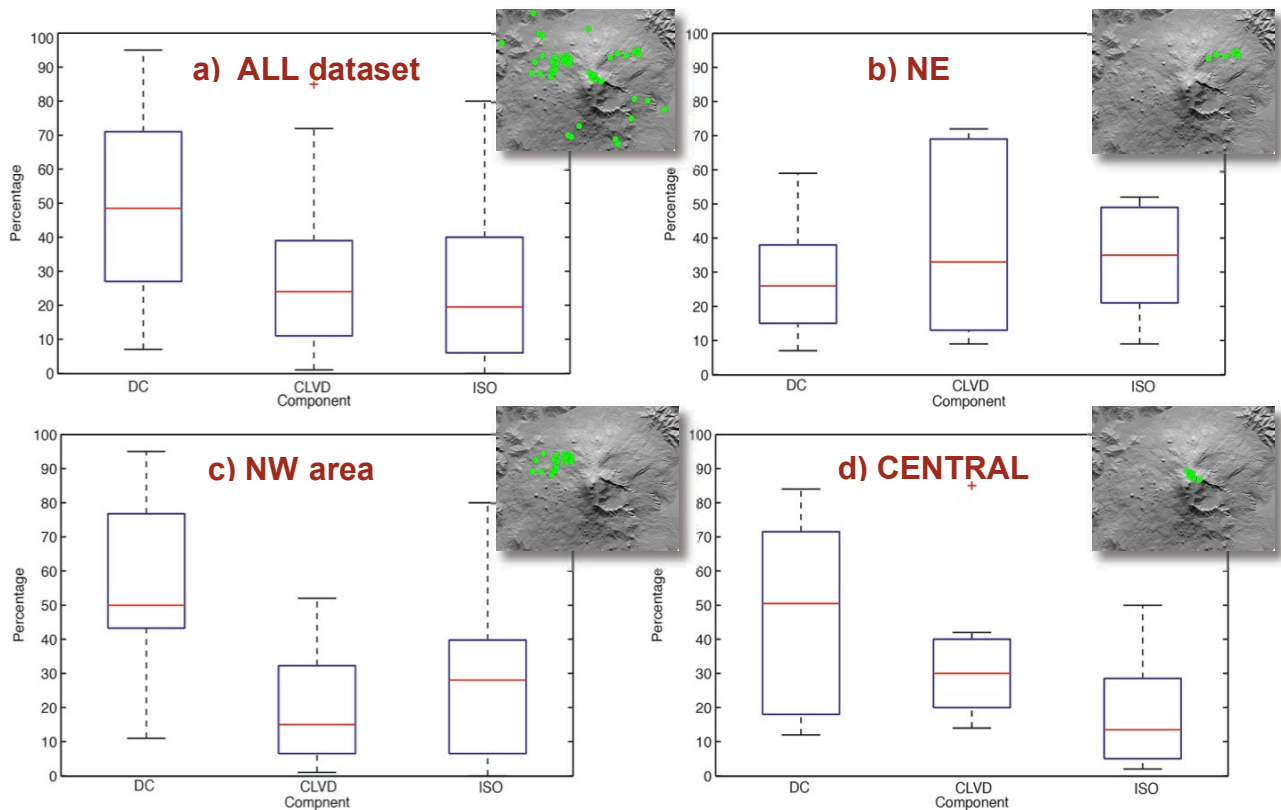


Figure 7. Boxplots with the percentage of moment tensor component (DC, CLVD and ISO) for: a) the whole dataset; b) data of the NE area; c) data of NW sector; d) data of central area (summit) of the volcano. On each box, the central mark (red) is the median, the edges of the box are the 25th and 75th percentiles, the whiskers extend to the most extreme data points not considered outliers.

To obtain a relation M_w vs. M_L , the M_w calculated during this study (red stars in Fig. 8) have been integrated with the M_w obtained by Saraò et al. (2010) through the moment tensor for a selection of earthquakes ($2.0 < M_d < 3.8$), occurred during the early hours of a seismic swarm forerunning the 2001 eruption (blue stars in Fig. 8). For the 2001 data, only the M_d was available, therefore we retrieved the M_L through the empirical relation M_L - M_d by Tuvè et al. (2015). The final data set has been investigated through the generalized orthogonal regression (Fig. 8, black line and black equation). The error associated to the M_w is ± 0.2 . The error associated to the M_L is ± 0.3 .

Section 2
Scientific Reports of Research Units (RU 4)

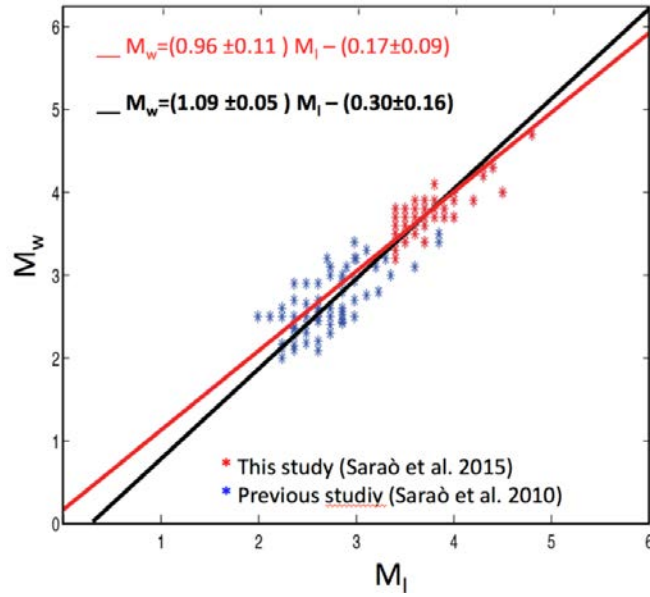


Figure 8. Relation M_L vs. M_w obtained in this study.

N	Date	Time	LAT	LONG	ML	Dep	Q	Str1	Dip1	Rak1	Str2	Dip2	Rak2	DC	CLVD	ISO	Mw	M _e 21
1	2005/07/10	13:38:51	37.852	14.991	3.4	29	2	189	79	-36	287	54	-167	38	39	23	3.4	1.34
2	2005/08/14	21:56:48	37.815	15.104	3.5	2	3	20	87	144	112	54	4	38	13	49	3.7	3.40
3	2005/10/30	06:06:50	37.652	15.058	3.7	9	3	47	74	23	310	68	162	14	53	33	3.8	6.22
4	2005/10/31	00:02:41	37.66	15.053	3.8	4	3	64	63	46	309	50	144	79	15	6	3.8	6.03
5	2006/01/08	16:09:24	37.683	14.97	3.7	12	3	178	87	-142	86	53	-4	75	12	13	3.8	6.34
6	2006/03/02	20:35:38	37.794	14.916	3.4	20	2	195	78	36	96	55	166	24	35	41	3.2	7.48
7	2006/05/20	07:05:56	37.667	14.945	3.8	10	3	87	68	27	346	65	156	27	26	47	3.7	4.21
8	2006/06/19	20:55:34	37.844	14.879	4.0	24	3	102	64	-145	355	59	-31	71	24	5	3.9	8.48
9	2006/06/20	13:16:35	37.839	14.886	3.4	24	1	127	63	-122	2	41	-44	49	8	44	3.3	0.99
10	2006/12/19	14:58:05	37.775	14.862	4.5	26	3	102	89	-174	12	84	-1	50	37	13	4	11.5
11	2006/12/20	01:46:23	37.778	14.908	3.4	24	2	209	71	21	112	70	159	48	19	32	3.7	3.95
12	2008/04/09	04:14:36	37.727	15.126	3.5	8	4	108	81	34	12	57	169	59	25	16	3.8	6.49
13	2008/05/01	21:05:47	37.802	15.041	3.5	1	3	80	85	-29	173	61	-174	29	33	38	3.7	3.82
14	2008/05/13	09:23:04	37.776	14.993	3.6	6	3	232	78	-155	136	66	-13	43	42	16	3.7	4.01
15	2008/05/13	09:28:05	37.764	15.007	3.8	2	3	193	64	-39	303	56	-147	58	25	17	3.8	5.10
16	2008/05/13	09:56:38	37.761	15.021	3.6	5	3	81	85	-59	180	31	-170	73	16	11	3.7	3.37
17	2008/05/13	10:07:48	37.771	15.005	3.9	2	3	142	60	-141	30	57	-36	84	14	2	3.7	4.61
18	2008/05/13	11:03:32	37.768	15.001	3.7	2	3	273	88	159	4	69	2	14	35	50	3.5	1.81
19	2008/05/13	11:52:38	37.766	14.999	3.6	2	3	248	54	-84	58	36	-98	22	38	40	3.5	1.69
20	2008/05/13	12:13:42	37.765	15.009	3.8	1	3	164	62	109	307	33	58	12	85	3	3.9	7.03
21	2008/05/13	13:26:49	37.771	15.003	3.7	2	2	234	77	32	136	59	164	70	24	7	3.7	4.38
22	2008/05/13	21:28:27	37.809	15.058	3.4	1	3	179	88	-174	89	84	-2	15	33	52	3.6	2.75
23	2008/12/16	02:30:14	37.664	14.952	4.0	8	3	162	70	-157	64	68	-22	91	5	4	3.7	3.35
24	2009/03/14	09:26:51	37.73	15.096	3.5	6	3	36	90	-176	306	86	0	45	49	6	3.5	2.18
25	2009/05/13	14:13:46	37.712	15.165	3.6	2	3	220	82	-17	312	73	-172	40	10	51	3.9	8.26
26	2009/07/23	00:10:42	37.589	14.763	3.7	22	2	263	80	-13	355	78	-170	17	62	21	3.6	3.26
27	2009/08/25	16:58:02	37.812	15.097	3.6	2	3	274	80	-29	10	62	-168	7	72	21	3.6	2.43
28	2009/12/19	05:36:00	37.79	14.913	4.4	22	3	205	57	64	66	41	123	47	18	35	4.5	73.9
29	2009/12/19	07:42:25	37.774	14.881	3.7	22	3	203	64	69	63	33	126	43	49	8	3.9	8.1
30	2009/12/19	08:01:10	37.769	14.905	3.6	20	2	239	56	122	11	45	52	55	1	44	3.8	6.61
31	2009/12/19	08:24:57	37.776	14.911	3.8	19	3	223	63	95	31	27	80	57	15	28	4.1	14.3
32	2009/12/19	09:01:14	37.794	14.869	4.8	28	2	217	65	64	87	35	134	87	6	6	4.7	132
33	2009/12/19	12:35:40	37.781	14.915	3.5	20	3	15	88	-55	108	35	-177	30	26	45	3.6	3.33
34	2009/12/19	15:12:35	37.792	14.916	3.8	24	3	269	84	156	1	66	6	58	24	18	3.9	7.51
35	2009/12/19	18:08:33	37.805	14.886	3.5	20	2	186	59	-139	71	55	-38	71	3	26	3.5	1.92
36	2009/12/23	14:24:42	37.795	14.91	3.7	18	2	255	58	106	47	35	67	24	40	36	3.7	3.36
37	2010/04/02	20:04:00	37.806	15.078	4.3	3	3	8	79	163	101	73	12	59	9	32	4.3	26.7
38	2010/04/02	20:21:55	37.807	15.106	3.5	2	2	99	81	13	7	77	171	23	69	9	3.4	1.35
39	2011/05/06	15:12:35	37.804	14.943	4	14	4	274	72	129	24	42	27	44	52	4	4	11.7
40	2011/05/06	15:15:23	37.798	14.949	3.4	23	1	269	83	164	1	74	7	81	14	5	3.4	1.56
41	2011/05/06	15:18:30	37.803	14.914	3.4	20	1	282	89	166	13	76	1	14	6	80	3.4	1.55
42	2011/05/06	19:28:49	37.797	14.933	3.5	20	2	352	76	17	258	74	166	87	8	4	3.5	2.05
43	2011/05/11	01:45:35	37.804	14.933	3.5	20	1	257	81	152	352	63	10	49	11	41	3.8	5.11
44	2011/05/11	02:17:08	37.801	14.94	3.4	20	1	70	85	-173	340	83	-5	11	18	71	3.8	5.57
45	2011/09/09	22:23:44	37.827	14.793	4	26	3	239	84	102	355	14	27	55	43	2	3.9	6.95

N	Date	Time	LAT	LONG	MI	Dep	Q	Str1	Dip1	Rak1	Str2	Dip2	Rak2	DC	CLVD	ISO	Mw	M ₀ e21
46	2012/01/01	04:17:02	37.879	14.865	3.5	32	1	107	83	163	199	73	7	74	23	4	3.8	5.03
47	2012/11/22	09:10:41	37.791	14.94	4.2	12	4	262	71	159	359	71	20	95	5	0	3.9	7.02
48	2012/11/22	11:25:51	37.799	14.936	4.3	20	3	253	70	125	10	39	33	64	6	29	4.2	19.8
49	2012/11/22	11:28:55	37.792	14.947	3.9	12	4	262	76	155	358	66	16	82	10	8	3.8	6.50
50	2013/05/23	13:04:48	37.696	15.089	3.4	4	1	142	89	18	52	72	179	32	50	18	3.4	1.34

Table 6. Earthquakes investigated in this study by moment tensor. For each event are reported: progressive number (N), date (Date), time (Time UTC), Latitude N (Lat.), Longitude E (Long.) in degrees, M_L, depth in km (De), quality of the inversion (Q=4, excellent, Q=0 poor), strike (Str), dip (Dip), rake (Rak) for both planes in degrees, double couple (DC), CLVD, isotropic component (ISO) percentage, M_w and seismic moment (M₀) in 10e+21 dynecm.

Deliverables

- WP 1.Sp1 Revision of the average time of occurrence of earthquakes along the Timpe faults: **100%**.
 WP 3.Sp1 Maps including site and topographic effects (30, 20, 10 and 5 yrs): **90%**.
 WP 5.Sp2 Earthquake features through the seismic moment tensor: **100%**.

Problems and difficulties

The problems and difficulties are due to the compression of a 3-years activity in 2 annual phases only. This fact implies that some of the analyses, mainly related to Task 1-Wp 3, have been performed at the very last minute, and do not have right now an adequate level of cross-checking and controls.

Key publications

- Azzaro R., D'Amico S., Pace B., Peruzza L. (2015). *Is a geometric-kinematic approach valid for estimating the expected seismicity rates in volcano-tectonic areas? Ideas and results from seismogenic sources at Mt. Etna (Italy)*. INQUA Focus Group on Paleoseismology and Active Tectonics 6th International INQUA Meeting on Paleoseismology, Active Tectonics and Archaeoseismology, 19-24 April 2015, Pescina, Fucino Basin, Italy, 3 pp.
- Azzaro R., D'Amico S., Pace B., Peruzza L. (2014). *Estimating the expected seismicity rates of volcano-tectonic earthquakes at Mt. Etna (Italy) by a geometric-kinematic approach*. Extended abstract presented at the 33° Convegno Nazionale GNGTS, Bologna (Italy), November 25-27, 2014.
- Saraò A., Cocina O., Scarfi L. (2014a). *Full moment tensor estimates of seismicity occurred at Mt. Etna in the period 2005-2013*. ESC2014-2468. Abstract presented at the, 2ECEES, Second European Conference on Earthquake Engineering and Seismology. Istanbul (Turkey), 24-29 August 2014.
- Saraò A., Cocina O., Scarfi L. (2014b). *Estimates of complete moment tensor of seismicity occurred at Mt. Etna in the period 2005-2013*. Abstract presented at Conferenza A. Rittmann, Nicolosi (Catania) 29-31 Oct. 2014, Italy. Miscellanea INGV, vol. 25, 160-161. ISSN 2039-6651.

Other references

- Aloisi M., Bonaccorso A., Cannavò F., Gambino S., Mattia M., Puglisi G., and Boschi E. (2009). *A new dyke intrusion style for the Mount Etna May 2008 eruption modelled through continuous tilt and GPS data*. Terra Nova, 21, 4, 316–321.
- Alparone S., Barberi G. Di Grazia G., Giampiccolo E., Maiolino V., Mostaccio A., Musumeci C., Scaltrito A., Scarfi L., Ursino A. (2010). *La sequenza sismica nel versante nord-occidentale dell'etna del 19-27 dicembre 2009: evidenze di ricarica magmatica profonda?* 29 Convegno GNGTS, 26-28 ottobre 2010, Prato.
- Minson S. & Dreger D. (2008). *Stable Inversions for Complete Moment Tensors*. Geophys. J. Int. 174, 585–592.
- Patanè D., Barberi G., Cocina O., De Gori P., Chiarabba C. (2006). *Time resolved seismic tomography detects magma intrusions at Mount Etna*. Science 313, 821.823.
- Saraò A., Cocina O., Privitera E., Panza G.F. (2010). *The dynamic of the 2001 Etna eruption as seen with*

Section 2

Scientific Reports of Research Units (RU 4)

- full moment tensor analysis*. Geophys. J. Int., 181, 951-965, doi: 10.1111/j.1365-246X.2010.04547.x
- Scarfi L., Messina A., Cassisi C., (2013). *Sicily and Southern Calabria focal mechanism database: a valuable tool for the local and regional stress field determination*. Annals of Geophysics, 56, 1, D0109; doi:10.4401/ag-6109. <http://sismoweb.ct.ingv.it/focal/>
- Siniscalchi A., Tripaldi S., Neri M., Giammanco S., Piscitelli S., Balasco M., Behncke B., Magri C., Naudet V., Rizzo E., (2010). *Insights into fluid circulation across the Pernicana Fault (Mt. Etna, Italy) and implications for flank instability*. J. Volcanol. Geotherm. Res. 193, 137-142, doi: 10.1016/j.jvolgeores.2010.03.013
- Tuvè T., D'Amico S. and Giampiccolo E. (2015). *A new Local vs. Duration magnitude relationship for the Mt. Etna seismic catalogue*. Annals of Geophysics, accepted.

RU 5, Dip. Scienze Terra, Università della Calabria, CosenzaResponsible: **Rosanna De Rosa****Activity of RU in phase 2**

RU 5 is involved in task 3 of the project:

WP 11 Sp1 - Field work on the stratigraphy of recent La Fossa and Vulcanello products. Textural, petrographical and melt inclusions studies on selected latitic products from the most recent eruptions of La Fossa volcano. Microdrilling isotopic analyses on selected samples.**WP 11 Sp2** - Field measurements and determinations of slip rates of recent faults on Lipari and Vulcano system; sampling of rocks for radiometric ages determinations of the products along N-S faults and eruptive fractures.**Task 3 - WP 11, Resp. R. De Rosa***Relationships between tectonic features and volcanic activity in the southern sector of the Aeolian Arc***Participants: UNI-CS**

Rosanna De Rosa, Paola Donato.

Other institutions**UNI-RM 3** Joel Ruch, Riccardo Di Lorenzo, Valerio Acocella; **UNI-Insubria** Luigina Vezzoli; **UNI-PI** Anna Gioncada, Mauro Pistolesi; **CNR PISA** Claudia Principe; **UNI-FI** Lorella Francalanci, Sara Di Salvo, Eleonora Braschi, Federico Di Traglia; **UNI-CT** Marco Viccaro, Eugenio Nicotra***Sp1 - Definition of the Lipari-Vulcano feeding system***

The activity has been aimed at the reconstruction of the plumbing system of Lipari-Vulcano in the most recent period (younger than 1 Ka). The last 1000 years represent an important period in the Vulcano-Lipari history for several reasons:

- 1) volcanic activity occurred in the same period at Vulcanello and Fossa vents on Vulcano island, and at Rocche Rosse on Lipari island, along a N-S alignment;
- 2) at least once, in AD 1230±40, eruptions occurred contemporaneously at Lipari and Vulcano;
- 3) since this period, latites have always been erupted, though with different eruptive style and in different amounts, associated or not with rhyolitic magmas.

The stratigraphy of La Fossa and Vulcanello was revised after a detailed geological survey based on the Unconformity-bounded Stratigraphic Units criteria (Fig. 1). Two Eruptive Clusters (EC) have been identified:

- **Lower EC** - Fossa: Palizzi (PEU) and Commenda (CEU) eruptive units. Vulcanello: Vulcanello 1 and 2 cones associated with two lava flows (the Vulcanello platform lava and a submarine pillow lava field);
- **Upper EC** - Fossa: 9 depositional units including the Pietre Cotte lava flow and the 1888-90 deposits. Vulcanello: Vulcanello 3 cone and Roveto-Valle dei Mostri lava flows.

The pyroclastic products of the AD 1230 ± 40 Rocche Rosse eruption (Lipari), are also found interbedded with the products of Vulcano (interbedded with the Breccia di Commenda deposits) and on the Vulcanello platform. This testifies the coeval sedimentation of the XIII cent. Mt. Pilato-Rocche Rosse and La Fossa cone-Vulcanello eruptions. Rocche Rosse can be therefore included in the Lower EC.

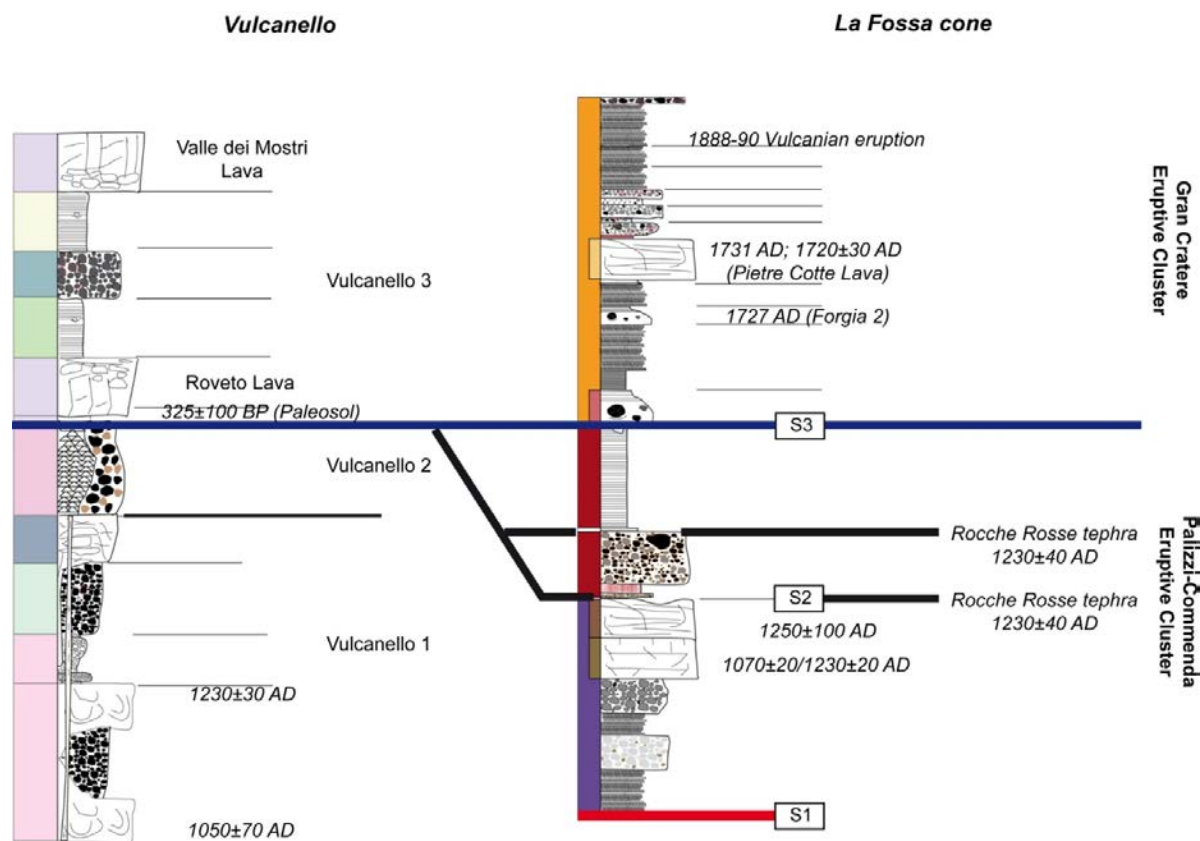


Figure 1. Schematic stratigraphic columns for the last 10 ka of activity at Lipari and Vulcano; the yellow box indicates the last 1000 years of activity at Vulcano (Di Traglia et al., 2013 and new unpublished data).

In the following section we describe in detail the stratigraphy of the last 1 ka activity at Lipari and Vulcano. The older cluster (*PCEC*) comprises the Palizzi (*PEU*) and Commenda (*CEU*) eruptive units: both have a wide areal extent and are clearly distinguishable in the field. The *PEU* comprises several sub-units separated by fourth-order unconformities (Fig. 1). Two sub-units (*Pal E* and *Pal F*) were mapped separately because of their different origin (Fig. 3). *Pal E* comprises at least three sub-units cropping out on the southern (*Palizzi Lava flow*; Frazzetta et al., 1983), northwestern (*Campo Sportivo lava flow*; Frazzetta et al., 1983) and northeastern slopes (*Punte Nere lava flow*; Frazzetta et al., 1983) of the cone. *Pal F*, crops out on the southern slope of La Fossa cone and corresponds to the *Commenda lava flow* described by Frazzetta et al. (1983). The *CEU* consists of a sequence of block-and-ash deposits cropping out at the foot of the cone and in more distal areas (*Breccia di Commenda*; Gurioli et al., 2012) and of a sequence of stratified, accretionary lapilli-rich ash layers characterises the topmost part of the sequence (*Tufi Varicolori*; Frazzetta et al., 1983). The most recent cluster (*GCEC*) comprises nine depositional units, each containing several unconformities.

The entire stratigraphic sequence of the Vulcanello activity has been divided into three lithosomes (*Vulcanello 1*, *Vulcanello 2* and *Vulcanello 3*) that occurred in two clusters. A lithosome is an informal stratigraphic unit defined by lithological and morphological elements having a combination that defines a genetically homogeneous rock body, corresponding to a well-defined volcanic edifice with a recognizable morphology related to a defined eruptive centre (Giordano et al., 2006). The first cluster led to the construction of the main part of the peninsula, with the edification of two cones (*Vulcanello 1 and 2 lithosomes*) associated with two lava flows (the Vulcanello platform lava and a submarine pillow lava field). The second cluster of eruptions built the third cone (*Vulcanello 3 Lithosome*) on the pre-existing two cones after a period of quiescence recorded by the presence of a palaeosol. During the third lithosome, four eruptive units were produced, associated with the *Roveto-Valle dei Mostri lava flows*. The presence of a second cluster of eruptions was also confirmed by historical accounts (De Fiore, 1922).

The fine ash beds related to the Mt. Pilato-Rocche Rosse eruption (Dellino and La Volpe, 1995) were used to assess robust, precise correlations among the studied tephra sequences. Forni et al. (2013) suggested that on Lipari island the *Rocche Rosse tephra*, included within the *Vallone Fiume Bianco Synthem*, were

characterized by a complex sequence of explosive phases that mostly produced a succession of fallout, lithic-rich pumiceous lapilli-tuffs, with minor interlayered beds of lapilli-tuffs with accretionary lapilli deposited from dilute pyroclastic density currents which heralded the emission of a final lava coulee. Archeomagnetic dating on the *Rocche Rosse lava* (Tanguy et al., 2003) and fission track age (Bigazzi et al., 2003) on a coeval pyroclastic sequence (*Lami succession*), suggested the AD 1220 as the most probable age for the Rocche Rosse eruptive sequence. In agreement, the *Rocche Rosse tephra* was found on Vulcano island interbedded with the *Breccia di Commenda* deposit (Gurioli et al., 2012; Di Traglia et al., 2013), dated using paleomagnetic methods on lithic clast by Gurioli et al. (2012) at AD 918-1302, and thus consistent with the AD 1230±40 archeomagnetic dating of Arrighi et al. (2006) of the Vulcanello platform, and with the 0.61±0.02 cal ka BP (ca. AD 1335) 14C dating of Caron et al. (2012) on cryptotephra found in a marine core from the Northern Ionian Sea.

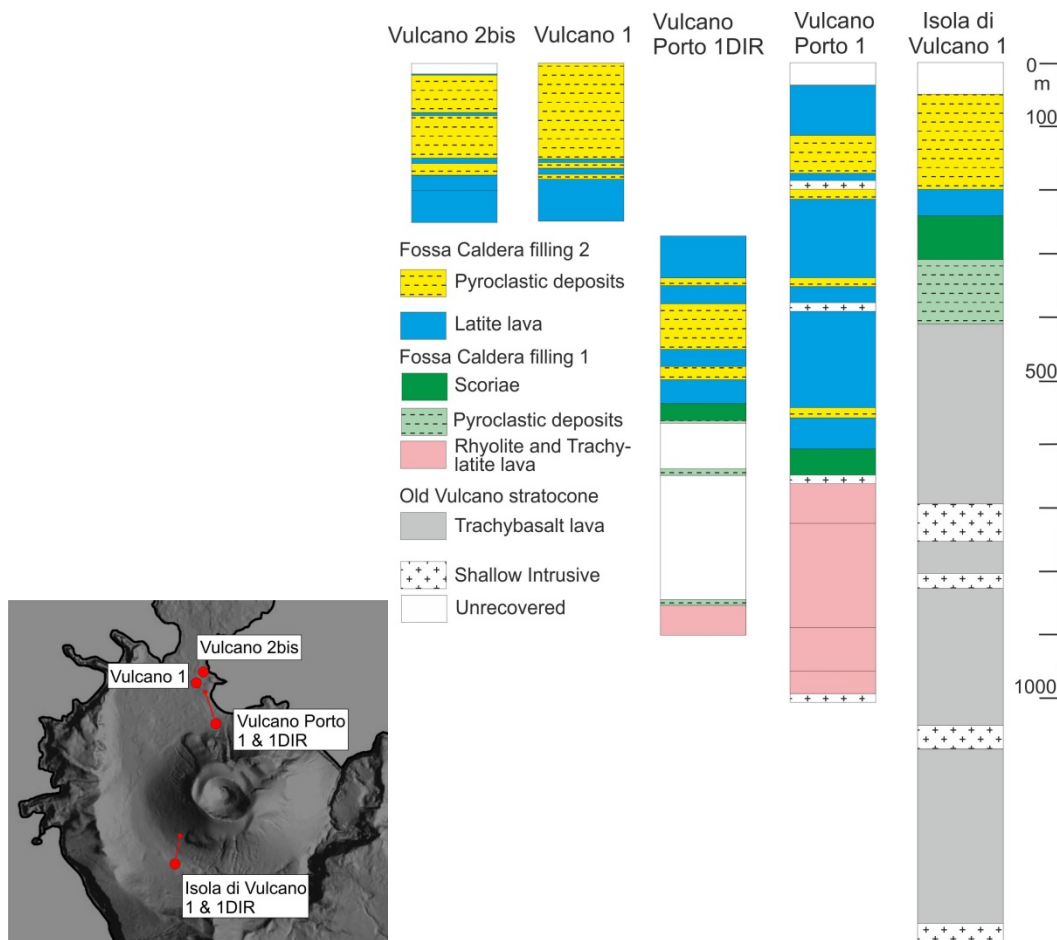


Figure 2. Stratigraphy of ENI geothermal drilling on Vulcano island.

It has been possible to reconstruct the chronological framework by correlating available lava ages with the reconstructed stratigraphic sequence of the lava, pyroclastic and volcanoclastic deposits identified in our field work. Due to the lack of numerical age data on the S1 palaeosol, the age of the onset of *PEU* at the La Fossa cone can only be deduced based on its stratigraphic relationship with the Vulcanello products. The presence of the *Pal B rhyolitic layer* (La Fossa cone) (corresponding to the rhyolitic tephra marker of Frazzetta et al., 1983) on top of the Vulcanello lava platform suggests that the first two units of the *PEU* post-date AD 1230 ± 40, when the Vulcanello lava platform was emplaced (Arrighi et al., 2006). This age is in agreement with other archaeomagnetic data on the *Pal E* (1170 ± 20 AD - 1230 ± 20 AD; Arrighi et al., 2006) and *Pal F* (1250 ± 100 AD; Arrighi et al., 2006). The products of the *CEU* lie directly above the *Pal E* and *Pal F* lavas. The end of the Commenda eruption cannot be precisely constrained. A key feature of the recent Vulcano and Lipari successions is the occurrence of the *Rocche Rosse tephra* interbedded within the

Section 2

Scientific Reports of Research Units (RU 5)

CEU succession. Their stratigraphic position suggests that the *Rocche Rosse tephra* has the same age as the S2 unconformity.

In our tephrostratigraphic framework, the *Rocche Rosse tephra* covered the Vulcanello lava platform and La Fossa cone, where it overlies the products of the PEU and in particular the *Pal E* and *Pal F* lavas. After S3, historical chronicles indicate that activity was renewed in AD 1444 (Mercalli and Silvestri, 1891). Arrighi et al. (2006) also dated the *Pietre Cotte lava* (Frazzetta et al., 1983) to AD 1720 ± 30, in good agreement with the AD 1731 eruption reported by De Fiore (1922). On the basis of historical chronicles, the second explosion of the Forgia craters (*F2*) was attributed to the AD 1727 eruption (Frazzetta et al., 1983 and references therein).

The onset of activity at Vulcanello is still a matter of debate. Some Authors (Keller 1970, 1980; Voltaggio et al., 1995; De Astis et al., 2013) suggested that the early activities of Vulcanello may have occurred in 126 or 183 BC, as reported by the Strabo and Plinius historical chronicles quoted by Mercalli and Silvestri (1891) and De Fiore (1922). By contrast, Arrighi et al. (2006), based on archaeomagnetic studies, suggested that the Vulcanello lava platform was built up during a continuous volcanic activity which occurred from AD 1100 to 1250. A palaeosol dated at 0.397 + 0.097 ka (Keller 1980; De Astis et al. 2013) separates *Vulcanello 2* from *Vulcanello 3* Lithosome. Therefore, the sub-aerial part of Vulcanello could be considered as the final part of a submarine growth process that also involved sporadic sub-aerial activity spaced in time.

The stratigraphy and composition of the subsoil of La Fossa Caldera have been reconstructed by reviewing data of the ENI geothermal drillings (Fig. 2). The results suggest that:

- La Fossa Caldera is infilled by interbedded primary lava and pyroclastic deposits. Effusive activity prevails on explosive one;
- rhyolite-trachylatite lavas similar to Mastro Minico-Lentia units (~28-21 ka BP) is confirmed from a depth of about 650 m near the Porto di Levante, followed by the emplacement of scoriae from fissural vents (indicative of volcano-tectonic deformation?);
- subsequent activity is submarine until very recent times (50 m depth);
- Faraglione is a small stratocone extended until about 200 m depth;
- La Fossa Caldera collapse is differentiated in time and space;
- structural, sedimentological and stratigraphical data exclude the occurrence of huge landslide during La Fossa Caldera collapse or involving the caldera infilling deposits.

Overall compositional data suggest that latites are the most abundant products. A latitic reservoir therefore, was active throughout the entire La Fossa history.

Melt inclusions study

Compositional data of melt inclusions (MI) in olivine, pyroxene and feldspars available for Vulcano, and unpublished data on Vulcanello and La Fossa (data collection in course) have been reviewed and discussed to obtain informations on the magmatic system, integrating information given by fluid inclusions and geological data (Zanon et al., 2003; Peccerillo et al., 2010). The composition of melt inclusions reflects, as regards major elements, the composition of the bulk rock (Fig. 3). The least evolved magmas of La Fossa and Vulcanello activity of the last 1000 years are the shoshonites erupted during the Vulcanello 1 period of activity, both as lava (lava platform) and as pyroclastics; only rare MI with basaltic composition were found in xenocrysts in the 1888-90 eruption and are interpreted as early stages of differentiation of La Fossa and Vulcanello (Davì et al., 2009). The most evolved magmas of the period are La Fossa rhyolites, but in most cases (Pietre Cotte, 1888-90) they are close to the liquidus temperature and do not show phenocrysts in equilibrium. MI with rhyolitic composition can be found only in the crystals of the products of one eruption in the Palizzi cluster.

There are no direct data on the volatile content of primitive melts for La Fossa and Vulcanello, but La Sommata shoshonitic basalt (H₂O up to 5-6 wt%, S 1500-2100 ppm, Cl 3000 ppm) can be taken as a proxy, although the basaltic MI interpreted to represent the parents of Vulcanello and Fossa magmas are more potassic. A deep reservoir at 20 km (Peccerillo et al., 2010) probably collects the primitive melts and allows the first steps of differentiation. The mafic magmas are H₂O-undersaturated at 20 km of depth and reach H₂O saturation during ascent between 10 and 15 km, at about 300 MPa. Shoshonites and latites (H₂O up to 2 wt% but mostly below 1 wt%, S <500 ppm, Cl 3000 ppm) are collected in an intermediate-shallow depth reservoir above the depth of fluid-saturation, as indicated by the decreasing content of H₂O and sulfur and the

constant/slightly increasing content of chlorine in this differentiation step. Important volatile loss occurs: sulfur is lost during differentiation to shoshonite and latite mainly as a gas phase, sporadically as a sulfide; an aqueous fluid conveys chlorine loss. The latitic MI of Vulcanello and those of La Fossa for what concerns Pietre Cotte, and the 1888-90 pyroclastics are similar to each other as regards major elements and volatile content. The latitic MI of one eruption of the Palizzi period, instead, suggest a slightly higher H₂O content. These products show abundant biotite phenocrysts, suggesting hydrous conditions, and evidence of a main sulfide exsolution event (possibly consequent to a mafic recharge?). In the Palizzi period, storage and differentiation to rhyolites occurred at La Fossa in an intermediate depth reservoir, probably at 3-5 km.

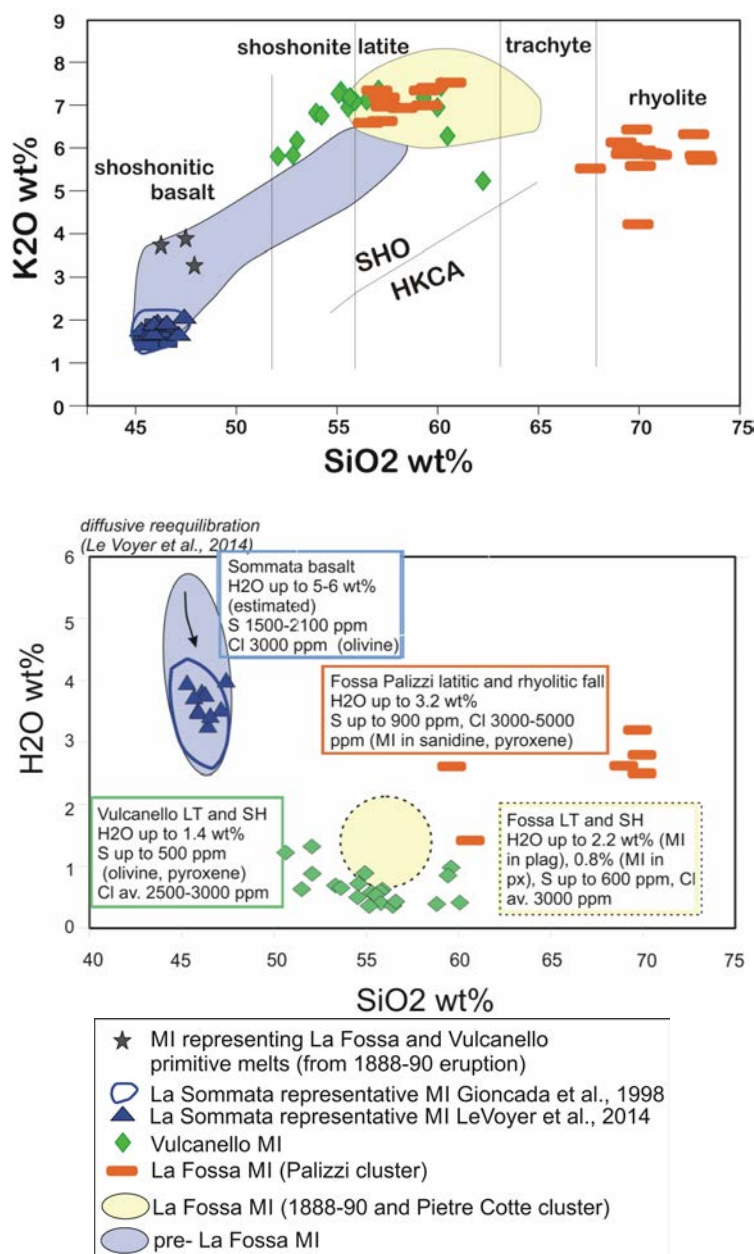


Figure 3. Melt inclusions composition of La Fossa and Vulcanello products.

For La Sommata MI, evidence for diffusive reequilibration of MI in olivine during magma ascent suggest an H₂O content higher than measured (Chen et al., 2013; Voyer et al., 2014). The possibility that this process, as well as other mechanisms influencing H₂O measured in MI, could affect the generally low water content of shoshonitic and latitic MI at Vulcanello and La Fossa, has been considered: for the Vulcanello MI, taking into account the size of MI and size and shape of host olivine, this process had only a minor effect on the H₂O content. For the host olivines of these MI, the lack of rapid crystallization features excludes growth

Section 2

Scientific Reports of Research Units (RU 5)

during rapid ascent. Therefore, a slow ascent/rest at shallow depth shortly before eruption is envisaged for Vulcanello shoshonite and latite magmas.

The major elements composition of melt inclusions reflects that of the bulk rock. The least evolved magmas of La Fossa and Vulcanello are the Vulcanello 1 shoshonites. Evidence of early stages of differentiation are recorded in MI with basaltic composition in xenocrysts in the 1888-90 eruption.

The most evolved magmas are the La Fossa rhyolites. MI with rhyolitic composition can be found only in the crystals of the products of the Palizzi period. Later rhyolites are aphyric.

La Sommata: primitive magmas reach H₂O saturation at about 300 Mpa. S is lost during differentiation to a gas phase and, at times, to a sulfide immiscible phase. Evidence for diffusive reequilibration of MI during magma ascent suggests an H₂O content higher than measured.

Vulcanello: the lack of rapid crystallization features excludes growth during rapid ascent. Therefore, a slow ascent/rest at shallow depth shortly before eruption, is envisaged for Vulcanello shoshonite and latite magmas.

Palizzi: magmas show abundant biotite and higher H₂O content, suggesting hydrous conditions. Storage and differentiation to rhyolites occurred in an intermediate depth reservoir, probably at 3-5 km. The crystals of Palizzi latites register a main sulfide exsolution event, possibly consequent to a mafic recharge.

Latites geochemistry

Field data indicate that in the recent period of Vulcano-Lipari activity, latites were common to most of the eruptive phases and represented the least evolved magmas erupted. Thus, latite is the key composition to be investigated for the purposes of this project.

Trace elements and REEs abundances (Fig. 4) indicate that no significant difference can be appreciated between the latites erupted contemporaneously at Lipari and Vulcano, or between the products of the two Eruptive Clusters of La Fossa and Vulcanello.

We suggest that latites have a common origin from a same shoshonitic basalt by AFC processes, as already proposed for Vulcanello by Davi et al. (2009).

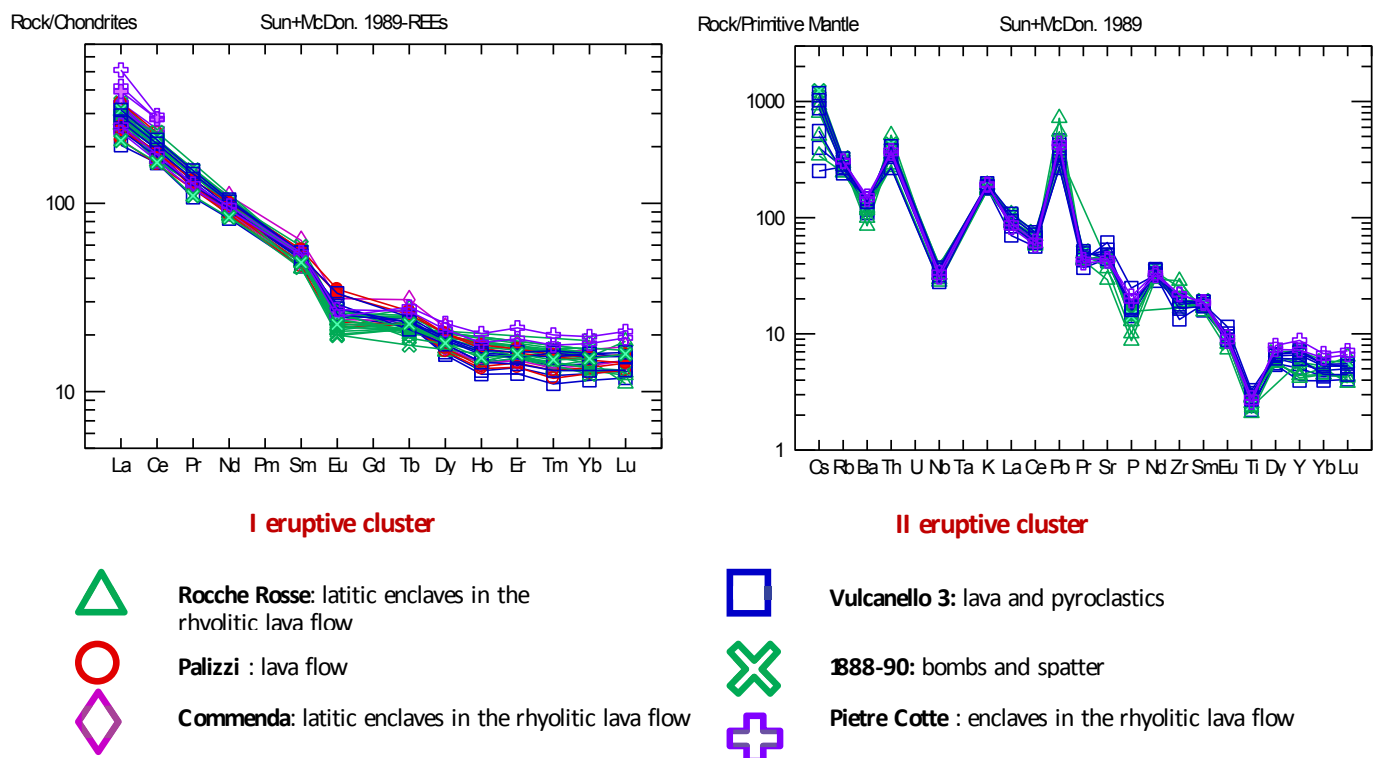


Figure 4. Spiders diagrams of incompatible elements and REE of latites younger than 1 ka.

Timescales of magma residence and migration during the last 1000 years of activity at Vulcano

Within the frame of the project, we present preliminary textural analyses and major and trace element zoning data on plagioclase crystals from selected volcanic products of the Vulcano island, emitted during the last 1000 years (Fig. 5). This new dataset of major and trace elements, which was respectively obtained through SEM-EDS/WDS and laser ablation inductively coupled plasma mass spectrometry (LA-ICP-MS) along core-to-rim, has been used to constrain the signature of the processes occurring in the plumbing systems during the recent activity and the transfer dynamics to the surface. The attention has been focused on the volcanic products emitted during the last 1000 years. At La Fossa cone, these eruptive events have been characterized by the emission of magma with latitic compositions, as lava (e.g. Palizzi lava) or enclaves within rhyolitic lava (e.g. Commenda and Pietre Cotte lava), such as also the 1888-90 eruption. At Vulcanello, it has been considered suitable for analysis the latitic lava at the top of Vulcanello I phase, and those at the top of Vulcanello 3 (Valle dei Mostri lava). Textural observations through polarizing optical microscope, BSE highly-contrasted images and SEM-EDS/WDS core-to-rim, allowed to discriminate four different texture on plagioclase crystals of Vulcano during the last 1000 years:

- Type 1: oscillatory-zoned plagioclase with only minor variation of An and FeO contents. They are attributed to quiet crystallization processes in a magmatic environment where only minor changes in P, T, fO₂ occur;
- Type 2: plagioclases with sieve-textured rims, characterized by an increasing of the An and FeO contents. This texture on plagioclase crystals is attributed to magma mixing processes during pre-eruptive phases with a more basic magma, able to modify both An and FeO values;
- Type 3: plagioclases with dissolved/resorbed cores, with a typical rounded shape. Generally, they present a strong decrease of the An content after the dissolution surface of the crystal. They form due to a rapid ascent of their hosting magmas in water-undersaturated levels of the magma plumbing system;
- Type 4: cores of plagioclase with coarse sieve textures. This texture has the same significance of Type 2 plagioclases, but here the ascent rates of magmas is lower.

Plagioclase with sieve-textured rims and coarsely sieved cores (Types 2 and 4) are the most abundant within the plumbing system during the last 1000 years of activity.

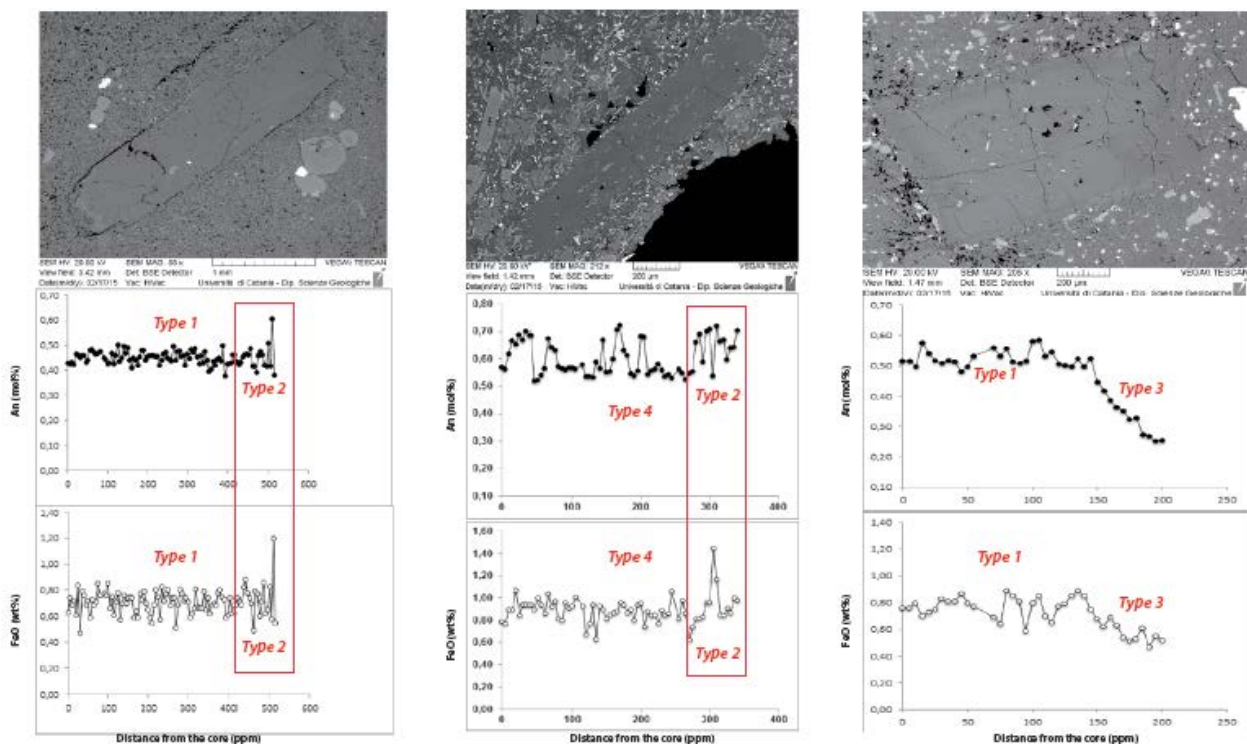


Figure 5. Compositional profiles on plagioclase crystals.

Section 2

Scientific Reports of Research Units (RU 5)

Diffusion modeling and estimated residence time

The residence time estimates have been obtained on crystals with exclusive oscillatory-zoned patterns or portions of crystals not severely affected by μm -sized glass inclusions caused by disequilibrium. The mineral diffusion model provided by Zellmer et al. (1999) requires that parameters, such as An content, temperature and the width over which diffusion occurs, should be fixed. The theoretical approach assumes that, after crystal growth, the initial Sr zoning amplitude decreases over time towards equilibrium conditions, while diffusion does not significantly affect the An content of the crystal. If complete equilibration has not been reached, the observed Sr variation within the crystal lies between the initial and the equilibrium profiles.

One of the primary tasks for the application of diffusion modelling is therefore to test whether or not the observed Sr concentrations are in diffusive equilibrium. To summarize, the chosen parameters include the highest An content (molar fraction) of any crystal and magma temperature of 1075-1175°C (Tab. 1).

Crystal	X _{An} ¹	T (°C)	D _{Sr} (m ² /s)	2w (μm)	Time (yrs)
VL14_1_P11	0.49	1175	1.4*10 ⁻¹⁷	88	4-5
VL14_1_P12	0.55	1175	8.5*10 ⁻¹⁸	69	4-5
VI315_7_P11	0.60	1175	5.8*10 ⁻¹⁸	112	15
VI315_7_P12	0.61	1175	5.3*10 ⁻¹⁸	60	8
VC3b_P11	0.56	1075	8.5*10 ⁻¹⁸	36	2
PC_P12	0.60	1075	5.8*10 ⁻¹⁸	137	19
ROV_P11	0.64	1075	4.0*10 ⁻¹⁸	98	21
ROV_P13	0.60	1075	5.8*10 ⁻¹⁸	120	22
PA_P11	0.62	1075	5.3*10 ⁻¹⁸	60	4
PA_P15	0.58	1075	7.0*10 ⁻¹⁸	120	8-9

¹ maximum anorthite content of the crystal

Table 1. Parameters used for diffusion on plagioclase crystals suitable for calculation with estimation of residence times. Samples refer to: PA=Palizzi; ROV=Valle dei Mostri lavas at Vulcanello; PC=Pietre Cotte enclaves; VC3b=Commenda enclaves; Vi315=initial phases of the 1888-90 eruption; VL14=final phases of the 1888-90 eruption.

Starting from an initial Sr concentration, the time required to reach the measured Sr compositional profile was calculated by means of a standard diffusion equation that depends on the Sr diffusivity and the width over which diffusion occurs. On the basis of published data, the maximum range in the initial Sr concentration within a single plagioclase crystal has been suggested to vary by no more than a factor 2.5. Although much work is needed, diffusion modelling shows that residence times for magmas emitted during the last 1000 years at Vulcano, range between 2 and 22 years.

The most striking features is that residence times are relatively low for the most evolved products (latites or latitic enclaves within rhyolitic magmas), especially at La Fossa eruptive system (2-19 years). Obviously, these timescales cannot account for the total amount of residence time of La Fossa magma within the crust, but only they can reflect the storage time of the most evolved products within the shallowest portion of the feeding system. The Vulcanello products, which are the less evolved products among the analyzed stratigraphic succession, clearly show the highest residence times, being 19-21 years. More than a very slow ascent from the deep magmatic reservoir where they were ponding, obtained data for Vulcanello could reflect a long times of magma storage for shoshonitic magmas in the deep reservoir (ca. 20 km) of the Lipari-Vulcano complex.

Future work should be focused on the analysis of major and trace elements of much more crystals for the considered eruptive events, in order to improve the number of crystals that could be suitable for diffusion modeling. Furthermore, residence times will be related to the volcanological history of Vulcano island and to their relationships with the tectonic structures.

Isotopic studies

1) Sr and Nd isotopic ratios on whole-rocks

These data were performed on whole-rocks of 9 key samples, 4 from Lipari (trachytic and latitic enclaves of Rocche Rosse lava flow) and 5 from Vulcano (eruptions of Palizzi, Commenda, Pietre Cotte, 1888-90). Sr isotopes on a chosen sample from Vulcanello were already available. Lipari and Vulcanello samples were analysed in order to complete the data set performed during the previous year of the project. Micro-Sr isotopes were analysed on plagioclase, clinopyroxene, sanidine and groundmass of these samples.

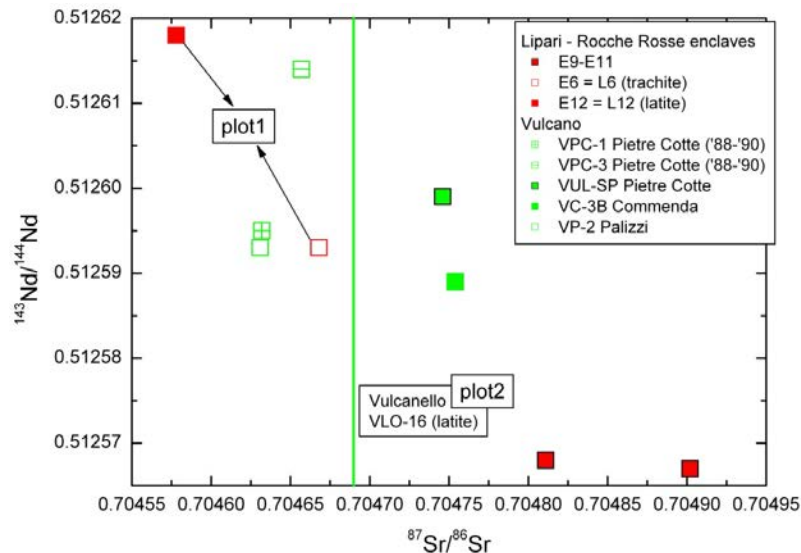


Figure 6. Whole-rocks $^{87}\text{Sr}/^{86}\text{Sr}$ vs $^{143}\text{Nd}/^{144}\text{Nd}$ of latites from Lipari and Vulcano.

Our results indicate that Lipari samples have a large isotopic variation, with a negative correlation between $^{143}\text{Nd}/^{144}\text{Nd}$ and $^{87}\text{Sr}/^{86}\text{Sr}$ (Fig. 6). Sr isotope ratios of whole-rock samples L6 and L12, moreover, are lower than those of the micro-drilled minerals (Fig. 7). Whole-rock isotope ratios of Vulcano and Vulcanello samples are intermediate between those of Lipari and do not show a good Sr-Nd isotope correlation. In the final activity of La Fossa, $^{87}\text{Sr}/^{86}\text{Sr}$ of latitic magmas seems to increase from Palizzi to Commenda, decreasing again toward Pietre Cotte.

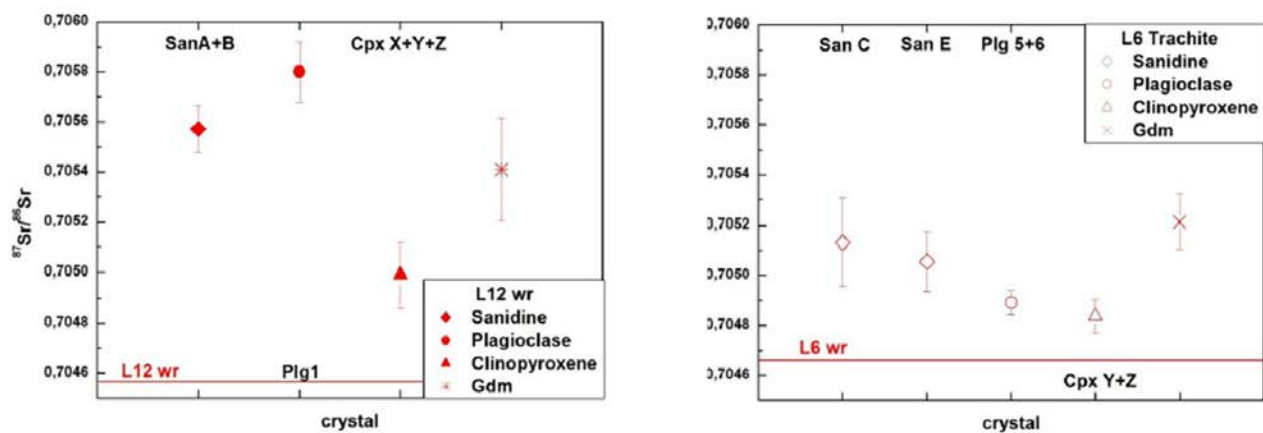


Figure 7. In situ Sr-isotope for Lipari-Rocche Rosse system.

2) Micro-Sr isotope analyses

In the second year of the project, we have analysed micro-Sr isotopes on clinopyroxene, plagioclase

Section 2
Scientific Reports of Research Units (RU 5)

and glassy groundmasses of new samples from Vulcano. Thus, three latitic enclaves (VPC-1, VPC-2, VPC-3) included in the Pietre Cotte rhyolitic lavas (ca. 1730 AD) and a scoriaceous product erupted in the final activity of 1888-90 (Vul-Sp) were selected and prepared for the micro-drilling techniques (Micromill + TIMS instruments). The rocks are quite porphyritic with phenocrysts of plagioclase (plg) and clinopyroxene (cpx). These phenocrysts show complex zoning and variable compositions (Mg-number: 70-87; An₂₂₋₆₀) and textures. Vul-Sp clinopyroxenes seem to be Fe-richer than those of Pietre Cotte enclaves, although the general compositional range is similar to those of Vulcanello and Rocche Rosse enclave clinopyroxenes. Rounded microcrystalline aggregates, with variable proportions between plg and cpx, are present in the Pietre Cotte enclaves and possibly represent batches of more mafic magmas included in these enclave melts.

The chosen crystals (core and rim) and glasses of each thin polish section were micro-milled and the powders (+ Milli-Q purified water) were collected in beakers, in order to apply the usual methods by final TIMS measurements for isotope analyses. In the Pietre Cotte enclaves we have obtained micro-Sr isotope data on 6 plg (cores and rims), 3 cpx, 3 glassy groundmasses and 4 microcrystalline aggregates (micro-milled as bulk samples), whereas in the 1888-90 sample we have analysed Sr-isotopes in 1 plg phenocryst (core and rim), 1 plg of a crystalline aggregate, 2 cpx and 2 glassy groundmasses (1 from the same aggregate of plg).

Results show small but consistent variations of Sr-isotopes (0.70458-0.70492), which generally increase from plagioclase cores to rims and then groundmasses. ⁸⁷Sr/⁸⁶Sr values of clinopyroxenes are in the range of plg Sr-isotopes and all the isotope data mostly fall in the variation field of whole-rock latite isotope data (Fig. 8).

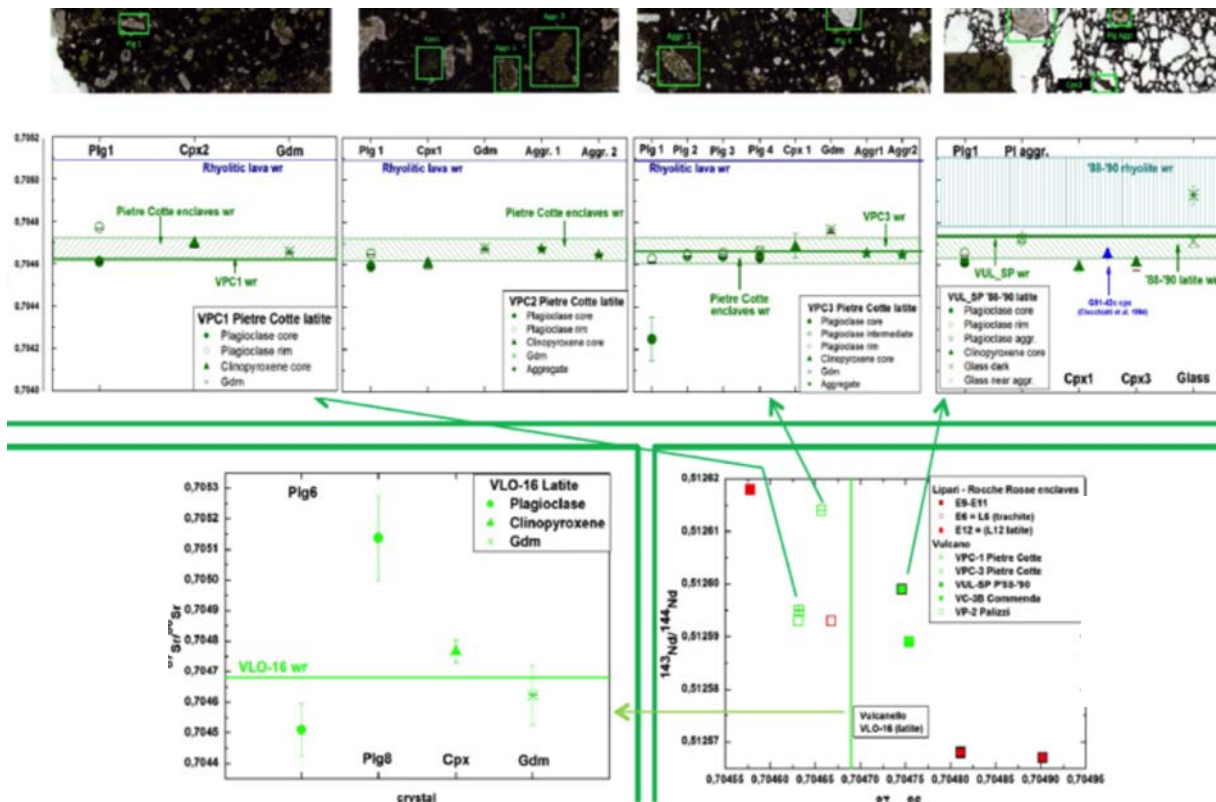


Figure 8. In situ Sr-isotope of Vulcano La Fossa system: Pietre Cotte and 88-90 eruption.

Only some values are different from the whole-rock isotopic range. In particular, a plagioclase core from a Pietre Cotte enclave (VPC3) is found to have a quite low ⁸⁷Sr/⁸⁶Sr value, which is similar to the Sr-isotopes of the older La Sommata activity. Furthermore, a plg rim of enclave VPC-1 has ⁸⁷Sr/⁸⁶Sr higher than the whole-rock isotope range and it is similar to the groundmass isotope value of enclave VPC-3. The rounded microcrystalline aggregates present in the Pietre Cotte enclaves, have Sr-isotopes falling in the general variation range for these samples.

Sr-isotopes of groundmass in the 1888-90 latitic scoria are particularly higher than those of the

analysed minerals, showing an increase with time from Pietre Cotte to 1888-90 activities. This higher groundmass isotope value falls in the isotopic range of 1888-90 rhyolites (Fig. 3), thus suggesting processes of crustal contamination during the evolution from latites to rhyolites.

It is to note that a plagioclase and an interstitial glass of a crystalline aggregate present in the 1888-90 scoria have $^{87}\text{Sr}/^{86}\text{Sr}$ values intermediate between those of the analysed minerals and the two higher groundmass values, possibly testifying a passage stage of magma evolution from the Pietre Cotte enclave magma composition to that of the final activity. The major element composition of the glass in this aggregate also corroborates this hypothesis. Although Lipari and Vulcano crystals show similar trace element ratios, Sr-isotopes of Lipari Rocche Rosse enclaves are higher than those of Vulcanello which in turn are higher than those of Vulcano (Figs. 7, 8), suggesting higher degrees of crustal assimilation during the evolution of shoshonite to latite at Lipari.

In summary, these isotopic data can indicate: i) mixing with more Sr-radiogenic rhyolitic magmas; ii) crustal contamination at varying degrees in the different volcanic systems; iii) crystal recycling from a crystal mush related to the previous and less Sr-radiogenic activity of Vulcano. The latter evidence derives from the quite low $^{87}\text{Sr}/^{86}\text{Sr}$ value of a plagioclase core, similar to the Sr-isotopes of the older La Sommata activity. It is possible that Pietre Cotte mafic enclave magmas use the same reservoir of La Sommata magmas. Alternatively, low Sr-radiogenic magmas were stored in the crust also in more recent periods, but crustal assimilation at lower depth usually hides this evidence on whole-rock composition.

Mixing with more Sr-radiogenic rhyolitic magmas (above point i) can be hypothesised from the isotopic variations among the Pietre Cotte enclaves, with higher values in rims and some groundmasses. This seems to indicate that before the eruption, the two variably evolved magmas remained in contact for a period of time sufficient to vary Sr isotope in the groundmass and to crystallise more Sr-radiogenic plg rims. The rounded microcrystalline aggregates present in the Pietre Cotte enclaves, having Sr-isotopes falling in the general variation range for these samples (Fig. 8), could represent the pristine isotopic composition of the input magmas before their interaction with the rhyolitic melts.

The overall isotopic data contribute to achieve the aims of the project and, in particular, to confirm the presence of a common and deep magma reservoir between Lipari and Vulcano, and to understand the magmatic behaviour of the final system at La Fossa of Vulcano.

The Lipari-Vulcano recent plumbing system: a possible model

The integration of stratigraphic, geochemical and petrological data (published and unpublished ones) allows to propose the following reconstruction. La Fossa, Vulcanello and Lipari volcanic activity in the last 1000 years can be described as two eruptive cluster (EC) (Fig. 9), thanks to the individuation of important unconformities of variable rank (being S1 the oldest).

The Lower EC was opened by Vulcanello 1 and 2 eruptions, characterized by emission of mafic and prevalently degassed magma; differentiation in this period is only minor at Vulcanello. The presence of Rocche Rosse (from Lipari) and Fossa tephra beds on Vulcanello allows the correlation among Lipari, Vulcanello and La Fossa activities. The latter was prevalently explosive and characterized by the eruption of more evolved (latitic and rhyolitic) magmas with respect to Vulcanello. Differentiation to rhyolite occurred in a reservoir at 3-5 km of depth (Palizzi). Interestingly, at the end of the period, a magmatic-hydrothermal system developed at La Fossa, with alteration facies analogous to the present ones, suggestive of a degassing magmatic system with the top at < 2 km of depth. It is worth of note the contemporaneous eruptions of latite-to-rhyolite magmas at Lipari (Rocche Rosse) and at Fossa (Breccia di Commenda).

At Vulcanello the Upper EC occurred with latitic and prevalently degassed magmas and the development of intense hydrothermal alteration and fumarolic activity. At La Fossa, prevalently explosive latitic to rhyolitic eruptions occurred, with possible coeval activity with Vulcanello. The least evolved magmas are latitic. A very shallow storage stage before eruptions is suggested by several lines of evidence: the presence of crustal xenoliths, the high sulfidation character of current alteration requiring the top of the magma chamber releasing fluids at < 2km, the presence of acidic subvolcanic rocks in VP1 drilling at 1 km (Fig. 2).

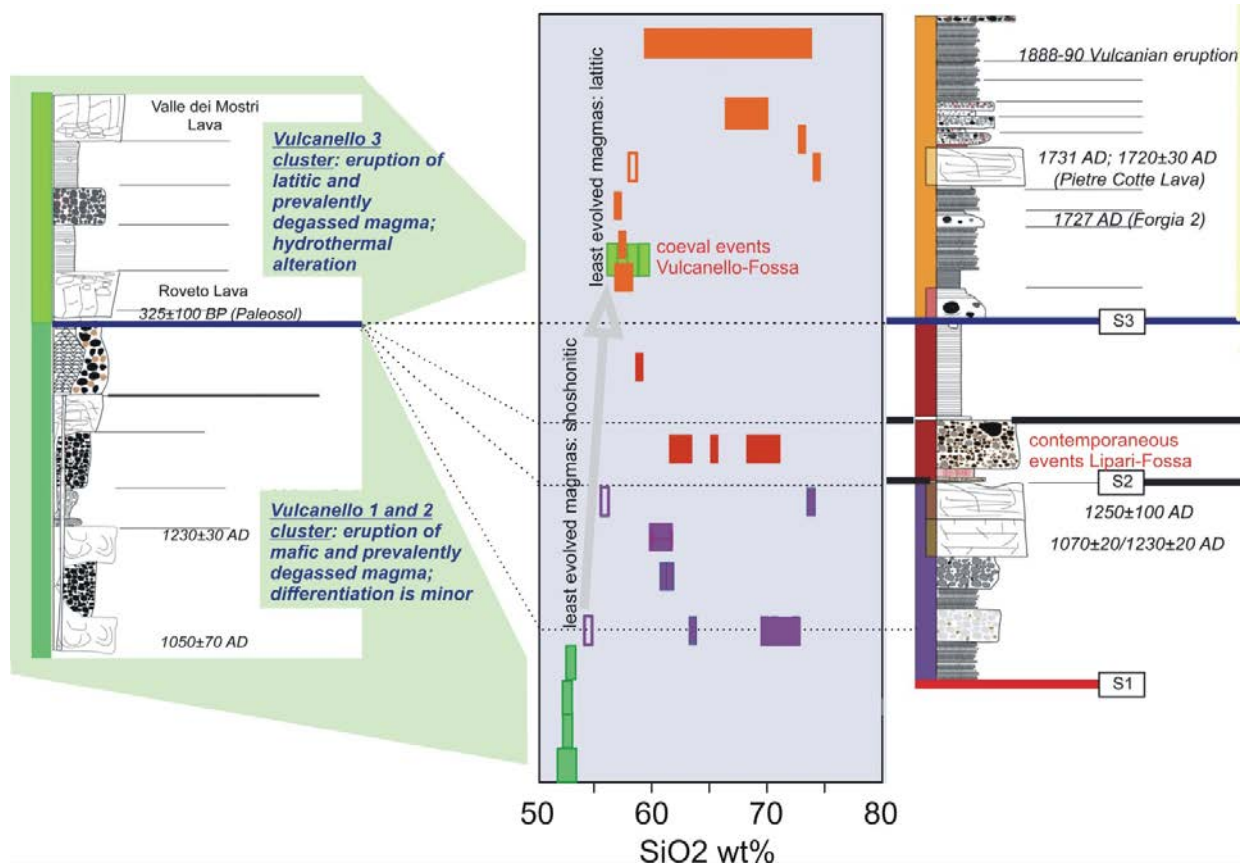


Figure 9. Stratigraphic and compositional relationships among La Fossa, Vulcanello and Rocche Rosse (Lipari).

La Fossa erupted magmas with different degree of differentiation, while Vulcanello erupted the least differentiated magmas for each period of activity: therefore, La Fossa eruptions are, for each cluster, fed both by the same mafic reservoir feeding Vulcanello, and/or by rhyolitic reservoirs repeatedly forming in the last 1000 years. These reservoirs form below La Fossa and are never intersected by the magmas rising at Vulcanello. The ubiquitous presence of mingling evidence in rhyolites demonstrates that the latitic reservoir is always active below La Fossa, also during the periods of rhyolitic activity.

Vulcanello activity is dominated by an effusive behavior, while La Fossa activity in the last 1000 years is characterized by a prevalence of explosive events. This is in agreement with the low volatile content of MI in olivine from Vulcanello activity, and with the volatile build-up observed in some cases with differentiation to rhyolite at La Fossa. The correspondence in the degree of evolution of the erupted magmas indicates that the shoshonitic and latitic magmas very likely rose from a same reservoir. The results of this reconstruction can be summarized as follow (Fig. 10):

- presence of a basaltic shoshonitic to shoshonitic magma chamber under Vulcano and Lipari at about 20 km directly feeding the Vulcanello lower EC shoshonitic eruption;
- differentiation of the shoshonitic magmas in latitic to rhyolitic reservoirs in which AFC processes occur;
- Lower EC, probably fed by a 5 km deep reservoir in which the volatiles contents of magmas increase by evolution (Palizzi) and decreases by degassing (Commenda and Vulcanello);
- Upper EC, probably fed by a shallow reservoir (1 km?) at Vulcano and Vulcanello. Depth of the Rocche Rosse magma chamber unknown. Presently feeding the fumarolic activity at Fossa (Paonita et al., in preparation).

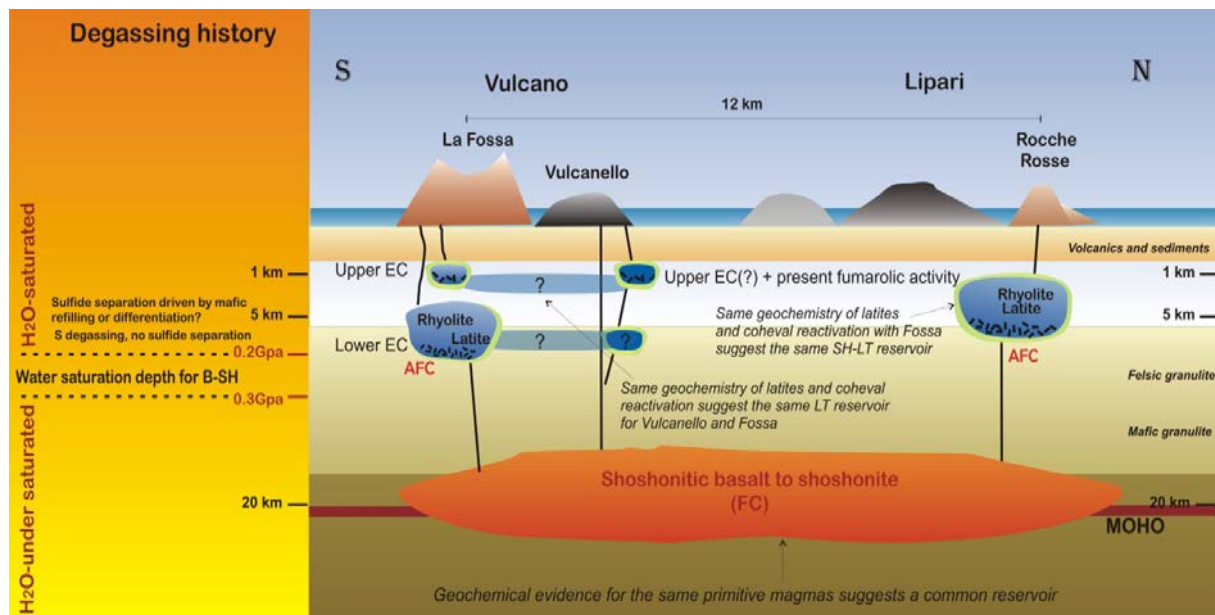


Figure 10. A model for the recent plumbing system of Lipari and Vulcano islands.

Sp2 - Characterization of the Lipari-Vulcano active fault systems

Four structural campaigns have been conducted in 2013 and 2014/2015. We collected ~500 mesoscale (centimeter to meter-scale) structural measurements (e.g. faults, fractures and dikes) at 40 sites (27 stations at Lipari and 25 at Vulcano). Fault strikes, dips and when possible, kinematic indicators have been measured (Fig. 11).

Stratigraphic data show that Vulcano is controlled by a general northward migration of its magmatic activity, from the older Caldera del Piano (~120 ka) to Vulcanello and La Fossa volcano, the latter being in a state of unrest (active fumaroles, seismicity and ground deformation) since the last 1888-1890 eruption. Lipari is subject to a general eastward migration of its activity, with most recent activity characterized by a northward migration of the eruptive events concentrated on the eastern side of the island.

We define five principal units based on the ages and the structures commonly found on both islands. This aims considering both islands as a single magmato-tectonic system, supported by the presence of coeval magmatic and faulting activities on both islands. These units are:

- 1) Unit 1 (>70 ka), comprising the Pre-caldera del Piano at Vulcano and from the Paleo Lipari up to the San Angelo formation at Lipari (SA, Fig. 12);
- 2) Unit 2 (40-50 ka), with Piano Caldera (mafic ash deposits) and Punta Luccia at Vulcano and the old domes located in the southern part of Lipari (e.g. Punta del Levante, PL, Fig. 12);
- 3) Unit 3 (13-22 ka), this comprises the endogenous domes on both islands, with Lentia at Vulcano and Monte Guardia and Monte Giardina at Lipari;
- 4) Unit 4 (~8 ka) represented by the Monte Saraceno and Faraglioni at Vulcano and Gabelotto at Lipari (5);
- 5) Unit 5 (<2 ka), that includes La Fossa and Vulcanello at Vulcano and Forgia Vecchia, Pilato and Rocche Rosse at Lipari.

Outcrops are generally rare on both islands that are densely vegetated; so well exposed outcrops that are not affected by faulting are also discussed (e.g. Pilato deposits, North of Lipari) for future possible measurement campaigns.

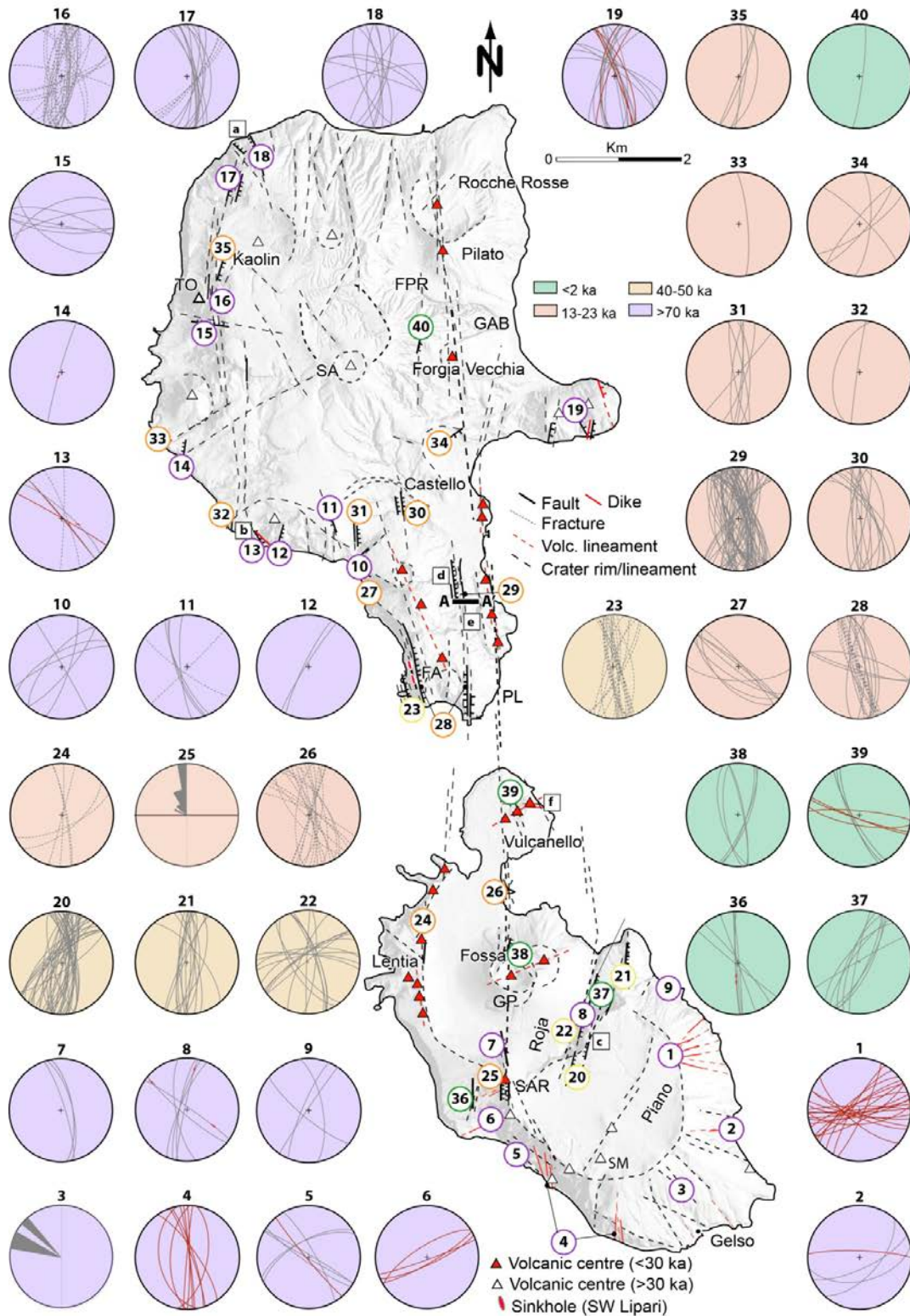


Figure 11. Structural map of Lipari and Vulcano, with all the field measurements plotted using OSXStereonet program. Colors indicate the different Units affected by faulting (see text for details). The grewish NS elongated swath highlights the area containing all the volcanic centers.

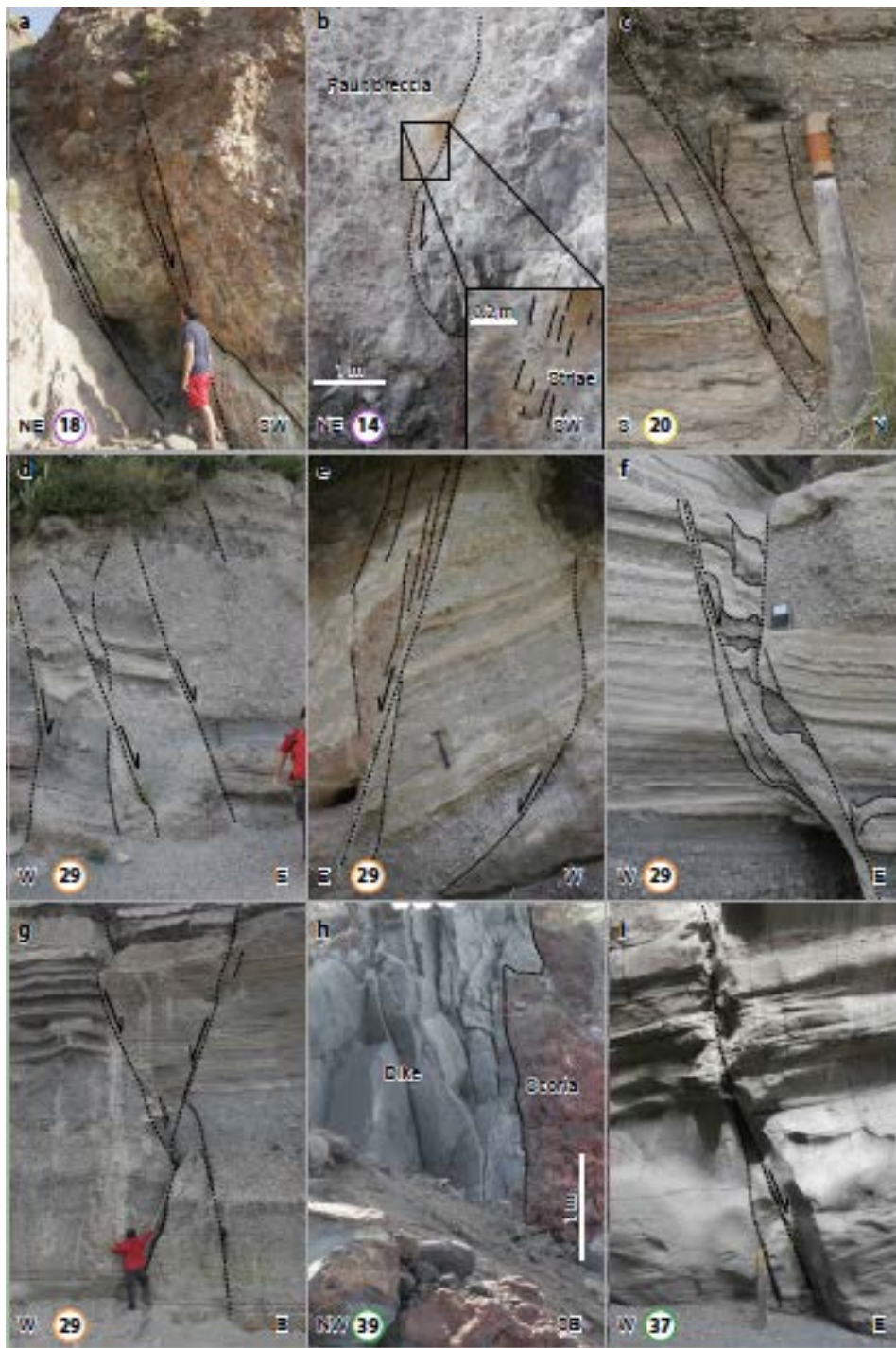


Figure 12. Photographs of different units affected by faults and intrusions. a,b) Unit 1 (>70 ka) located to the North of Lipari, along the shoreline, c) Unit 2 (40-50 ka) with faulted ash fall deposits at Piano caldera, d-f) Unit 3 (13-23 ka) with pyroclastic surges and ash falls located SE of Lipari (CAVA SOUTH), g-h) Unit 4 (<2ka) with, respectively, a dike on Vulcanello Eastern shoreline, La Fossa deposits located on the SE part of the volcano, along the Roja canyon).

To resume, the collected structural data show (Fig. 13) two main fault zones on Vulcano, with (1) a NNE-SSW oriented graben-like structure affecting the deposits related to the Piano caldera and Punta Luccia unit (~50 ka), and (2) a N-S oriented graben-like zone affecting the recent deposits of La Fossa (<2 ka) and Saraceno (~8 ka). The oldest unit (>70 ka; Pre caldera del Piano unit) dominated by dikes, does not show a preferred trend. All together, these results support a dominant NW-SE to E-W extension at Vulcano between 50 ka to Present.

Section 2
Scientific Reports of Research Units (RU 5)

On Lipari, the structures cluster to the South and to the west of the island. This part mainly shows products of Units 1 and 2 (i.e. >50 ka) but also secondary offset younger deposits oriented NS (sites 32-35; Fig. 11). The dome area to the south initially developed along a graben-like structure, oriented NNW-SSE (site 23 and 28; Fig. 11) then further migrated eastwards, denoted by the San Giuseppe and the Castello domes. The products younger than 1 ka migrated northward and took place along a narrow NS corridor.

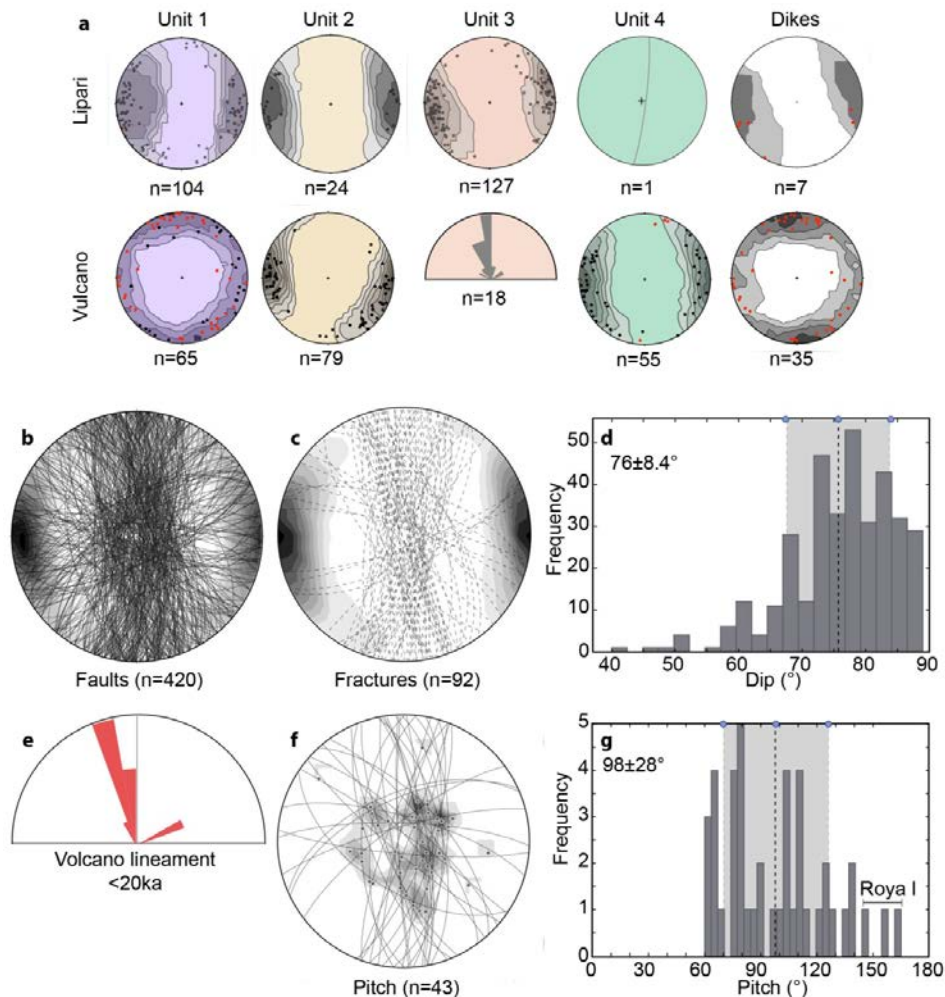


Figure 13. a, b) Principal orientations of faults and fractures are NS. c) Fault dips are ~75°. d) Volcanic lineaments are NNW-SSE oriented. e) Kinematic indicators indicate a dominant dip-slip component, with secondary left and right lateral components. The volcanic material composition being generally poorly consolidated (e.g. fall and surge deposits), we retrieved around 10% of kinematic indicators over the sum of the measured structures.

The stratigraphic and structural data indicate (Fig. 14) that the activity younger than 22 ka on both islands developed exclusively along a narrow structural corridor (15 km long in the N-S direction and 2 km wide in E-W direction), concentrating most of the magmatic and faulting activity during the last 20 ka, and even a narrower structural activity for the last 1 ka.

These results support a constant E-W dominant extensional regime with very limited E-W spatial variation of the activity; any future eruption is thus more likely to occur along this corridor. Geochemical data are in good agreement with the presence of a single, central and elongated deeper magma body that then generates intrusions on both islands with the same magma parental signature.

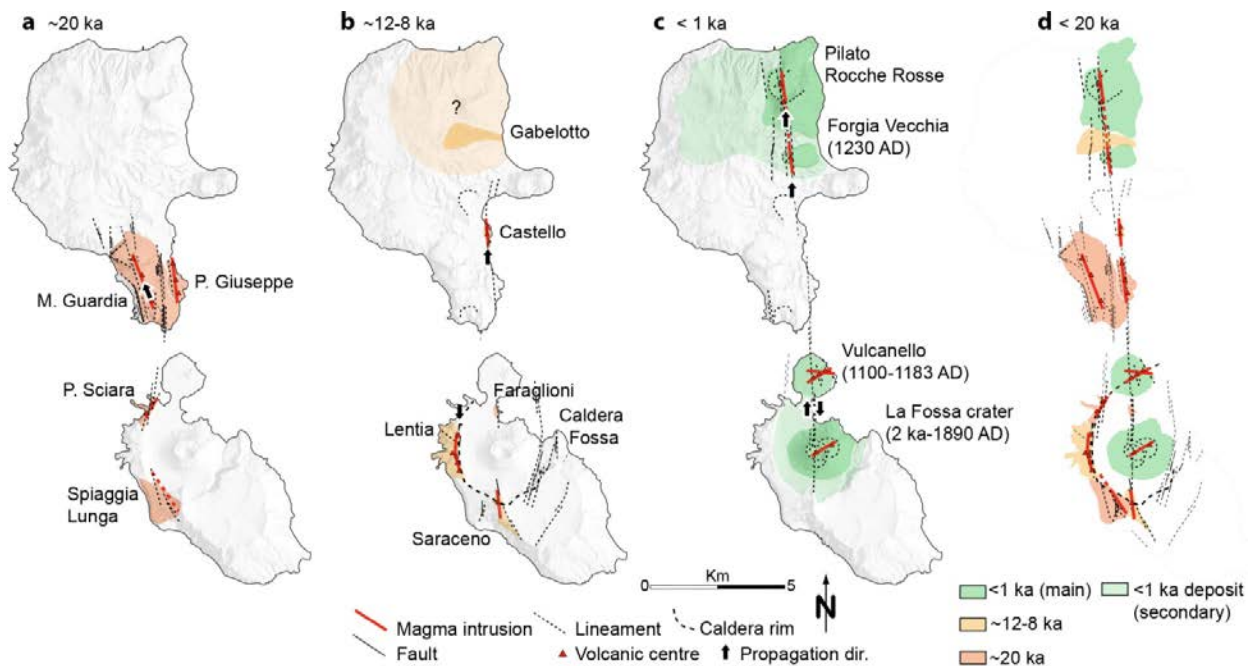


Figure 14. Magmato-tectonic evolution of Lipari and Vulcano during the last 20 ka.

La Fossa and Vulcanello are located along the narrow N-S corridor; however, both craters are aligned on a NE-SW direction, almost orthogonal to the dominant N-S trend. Both systems lie within or at the boundary of La Fossa caldera structure. This may indicate the influence of the caldera structures, providing a preferential pathway for magma ascent, independently of the regional stress field. Other examples of differential stress fields generated by caldera structures are commonly observed, such as at Askja (Iceland) and Long Valley (North USA) calderas, where magmatic intrusions taking place into the caldera structures are controlled by the pre-existing structures (Holohan et al., 2008).

Alternatively, the NW-SE trending structures in Vulcano may be influenced by the opening of the Gioia basin to the East that has a similar orientation, and therefore may influence the Vulcano-Lipari system. Dike intrusions at Vulcano show a somehow preferential E-W orientation, which may support this hypothesis.

Result synthesis

- Structures are oriented from NNE-SSW to NNW-SSE with a dominant NS orientation;
- Faults show dominant eastward immersions (asymmetric graben-like structure of the entire area);
- Kinematic indicators show a predominant dip-slip component (mean pitch $\sim 70\text{-}110^\circ$) supporting an extensive regime (EW-oriented);
- The existence on both islands of a spatial and temporal correlation between faulting and magmatism during the last 13 ka, focusing along a ~ 15 km-long, 1 km-wide NNW-SSE narrow structure (see swath in Fig. 11).
- Faulting periods may occur during transient magmatic activity instead of resulting from continuous regional tectonic processes (syn-eruptive processes and faulting).

Conceptual model

Our results show that both islands are subject to a dominant EW extension and contrast with the surrounding stress field (Fig. 11). We propose a simple model to explain this difference (Fig. 15). The maximum effective stress (σ_1) may rotate from horizontal to vertical, transiting from pure right lateral strike-slip faulting along the Tindari fault zone (tectonic-dominant), to an extensive regime (magmatic dominant) inducing normal faulting and extension during transient magma intrusions.

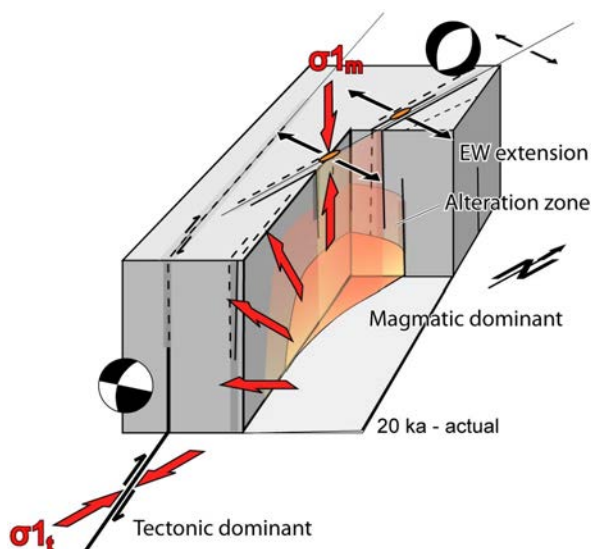


Figure 15. Proposed kinematics model to explain the transition between strike slip faulting (South) to normal faulting (North), transiting from tectonic stress (σ_1 horizontal) to magmatic stress (σ_1 vertical), in response to the presence of a long-lived magma body activity or transient magmatic intrusion.

Our data reflect the overall shallow part of a larger complex system and the stress field may vary significantly at greater depth. The integration with existing geophysical data can be obtained by considering the results from WP 10 (see report of RU 1).

Deliverables

- WP 11.Sp1 Definition of the Lipari-Vulcano feeding system: **90%**.
WP 11.Sp2 Characterization of the Lipari-Vulcano active fault systems: **100%**.

Problems and difficulties

Problems and difficulties are due to the compression of a 3-years activity in 2 annual phases only, and in the delay of funding.

- WP 11 Sp1 Some analyses have been performed late and do not have an adequate level of cross-checking and controls.

Key publications

- De Rosa R., Di Lorenzo R., Donato P., Francalanci L., Gioncada A., Nicotra E., Pistolesi M., Ruch J., Vezzoli L., Viccaro M., Braschi E. (2014). *Insights on the recent magmatic system of Lipari and Vulcano on the basis of new structural and geochemical data*. Miscellanea INGV, n. 25, Conference A. Rittmann, Nicolosi (Ct), Italy.
- Di Traglia F., Pistolesi M., Rosi M., Bonadonna C., Fusillo R., Roverato M. (2013). *Growth and erosion: The volcanic geology and morphological evolution of La Fossa (island of Vulcano, Southern Italy) in the last 1000 years*. *Geomorphology*, 19, 94-107.
- Fusillo R., Di Traglia F., Gioncada A., Pistolesi M., Rosi M., Wallace P.J. (2013). *Volatile Content in Melt Inclusions of Vulcanello's Explosive Activity: Implications for the Last 1000 Years of Activity at Vulcano Island (Aeolian Archipelago, Italy)*. Goldschmidt 2013 Conference Abstracts, p. 1124, DOI:10.1180/minmag.2013.077.5.6.
- Ruch J., Vezzoli L., Di Lorenzo R., De Rosa R., Acocella V. (2014). *Magmatic versus tectonic influence in the Eolian arc: the case of Vulcano and Lipari islands revisited*. EGU General Assembly.
- Ruch J., Vezzoli L., Di Lorenzo R., De Rosa R., Acocella V. (2015). *Transient magmatic control in a tectonic domain: the central Aeolian volcanic arc (South Italy)*. EGU General Assembly.

Other references

- Arrighi S., Tanguy J.C., Rosi M. (2006). *Eruptions Of The Last 2200 Years At Vulcano and Vulcanello (Aeolian Islands, Italy) Dated By High-Accuracy Archeomagnetism*. Phys. Earth Planet. Int., 159, 225-233.
- Caron B., Siani G., Sulpizio R., Zanchetta G., Paterne M., Santacroce R., Tema E., Zanella E. (2012). *Late Pleistocene to Holocene tephrostratigraphic record from the Northern Ionian Sea*. Marine Geology, 311-314, 41.51. Bull Volcanol 56:466-486. Doi:10.1007/S004450050233.
- Davi M., De Rosa R., Barca D. (2009). *A La-Icp-MS Study Of Minerals In The Rocche Rosse Magmatic Enclaves: Evidence Of A Mafic Input Triggering The Latest Silicic Eruption Of Lipari Island*. Bull Volcanol, Aeolian Arc, Italy). J. Volcanol. Geotherm. Res., 182:45-56. Doi:10.1016/J.jvolgeores.2009.02.001.
- De Astis G., Lucchi F., Dellino P.F., La Volpe L., Tranne C.A., Frezzotti M.L., Peccerillo A., (2013). *Geology, volcanic history and petrology of Vulcano (central Aeolian Archipelago)*. Geol. Soc. London Mem., V. 37, P. 281-349.
- Dellino P., La Volpe L. (1995). *Fragmentation Versus Transportation Mechanisms In The Pyroclastic Sequence Of Monte Pilato-Rocche Rosse (Lipari, Italy)*. J. Volcanol. Geotherm. Res., 64: 211-232. Doi:10.1016/0377-0273(94)00084-T.
- Di Traglia F., Pistolesi M., Rosi M., Bonadonna C., Fusillo R., Roverato M. (2013). *Growth and erosion: The volcanic geology and morphological evolution of La Fossa (island of Vulcano, Southern Italy) in the last 1000 years*. Geomorphology, 19, 94-107.
- Forni F., Lucchi F., Peccerillo A., Tranne C.A., Rossi P.L., Frezzotti M.L. (2013). *Stratigraphy and geological evolution of the Lipari volcanic complex (central Aeolian Archipelago)*. Geol. Soc. London Mem., V. 37, P. 213-279.
- Gurioli L., Zanella E., Gioncada A., Sbrana A. (2012). *The historic magmatic-hydrothermal eruption of the Breccia di Commenda, Vulcano*. Italy. Bull. Volcanol., (2012) 74:1235-1254, DOI 10.1007/s00445-012-0590-4.
- Holohan E.P., van Wyk de Vries B., Troll V.R. (2008). *Analogue models of caldera collapse in strike-slip tectonic regimes*. Bull. Volcanol., 70, 773-796.
- Keller J. (1980). *The Island Of Vulcano*. Rendiconti Della Società Italiana Di Mineralogia e Petrologia, V. 36, No. 1, P. 369-414.
- Mercalli G., Silvestri O. (1891). *Le Eruzioni Dell'isola Di Vulcano, Incominciate Il 3 Augusto 1888 E Terminate Il 22 Marzo 1890*. Ann. Uffic. Cent. Meteorol. Geodin., 10(4), 213 Pp.
- Tanguy J.C., Le Goff M., Principe C., Arrighi S., Chillemi V., Paliotti A., La Delfa S., Patanè G. (2003). *Archeomagnetic Dating Of Mediterranean Volcanics Of The Last 2100 Years: Validity And Limits*. Earth Planet. Sci. Lett., 211:111-124. Doi:10.1016/S0012-821x(03)00186-9.

RU 6, Dip. di Scienze Biologiche, Geologiche e Ambientali, Università di Catania

Responsible: **Carmelo Ferlito**

Activity of RU in phase 2

RU 6 is involved in tasks 1 and 2 of the project:

- WP 2** (resp. G. Lombardo) - Description of the local seismic response in test areas of the Etnean territory, in order to single out ground motions features, associating these to the local stratigraphic characteristics.
- WP 7** (resp. C. Ferlito) - Samples analyses by integrating the dataset with the mineral phase analyses performed with the SEM; modelization of the crystallization conditions for the 1928 and 1981 lavas.
- WP 8** (resp. C. Monaco) - Modelling of tectonic structures along the Ionian offshore of Etna from seismic profiles. Defining of tectonic processes and deformation active at the front of the chain in the light of growth of fold and thrust system, and relationships with volcano dynamics.
- WP 12** (resp. M.S. Barbano) - Reconstructing the chronological sequence of volcanic phenomena at Volcano and updating the earthquake catalogue from the 1400s to the 1900s by an historical approach. Focus on poorly known local and regional earthquakes of medium-low energy ($4.2 < M < 5.0$) and seismic sequences, which may provide a better understanding of the relationships between seismicity and eruptive activity.

Task 1 - WP 2

Ground-motion prediction equations (PGA from instrumental seismic data) (Etna)

Participants: UNI-CT

Giuseppe Lombardo, Francesco Panzera

Other institutions

INGV-CT Stefano Branca, Horst Langer, Emanuela Longo

Sp1 - Identification of site correction functions for the prediction of PGA (resp. G. Lombardo)

The features of near surface geology as well as the morphologic setting and the water content of layers play a key role in controlling ground motion. The most common technique of site response estimation is the standard spectral ratio (SSR) that consists in comparing earthquake recordings at two sites, the first of which is located on soft sediments (target site) and the other on hard rock (reference site) (Borcherdt, 1970). The method provides reliable evaluations if the “reference site” is free from any site effect, as for instance if it is located on an un-weathered, horizontal bedrock.

Another extensively used technique, that does not need a reference station, consists in the spectral ratio between the horizontal and the vertical components of the shear wave part of the earthquake recordings (HVSr). This method, first applied by Lermo and Chavez-Garcia (1993) and subsequently by Lachet et al. (1996), exhibits very encouraging similarities with the SSR technique, especially in frequency values of resonant peaks, when the S-waves are used (Chavez-Garcia et al., 1996; Bonilla et al., 1997; Riepl et al., 1998; Parolai et al., 2001). According to the above mentioned studies, HVSr is well correlated with surface geology and much less sensitive to source and path effects. However, peak amplitudes depend on the type of incident waves; consequently, the determination of the absolute level of amplification only through HVSr is not straightforward (Field and Jacob, 1995). A quick estimate of the site effects role in the seismic motion observed at the surface can be provided by the horizontal to vertical noise spectral ratio technique (HVNR). This method, first introduced by Nogoshi and Igarashi (1971), was put into practice by Nakamura (1989) and became widely used in recent years since it provides a reliable estimate of the fundamental frequency of soft soil deposits (Lermo and Chavez-Garcia, 1993; Seekins et al., 1996). The ambient noise appears actually made of an unpredictable brew of different wave fields, and not by Rayleigh waves alone. Many authors (e.g., Mucciarelli, 1998; Rodriguez and Midorikawa, 2002; Maresca et al., 2003) have questioned the existence of simple direct correlation between HVNR spectral amplitude values and the site amplification.

Section 2

Scientific Reports of Research Units (RU 6)

The HVNR from ambient vibrations are sometimes “non-informative”, particularly in the case of significant lateral heterogeneity giving rise to 2D/3D effects and velocity inversion that influence the vertical component of motion (Di Giacomo et al., 2005; Castellaro and Mulargia, 2009; Panzera et al., 2013). It is however commonly accepted that, although the single components of ambient noise can show large spectral variations as a function of natural and cultural disturbances, the HVNR spectral ratio tends to remain invariant, therefore preserving the fundamental frequency peak (Cara et al., 2003).

The selection of specific elastic response spectra according to “soil categories” is the easiest way to account for site effects in engineering projects and general-purpose hazard maps. Most of the international seismic codes make use of the average shear wave velocity of the upper 30 m ($V_{S,30}$) to discriminate soil categories (Eurocode, NEHRP). Some doubts arise about the aptitude of $V_{S,30}$ to predict actual soil amplification in Etna volcano as well as in different part of the world. Recent studies pointed out that the main problems are: alternating outcrops of sediment and lava (Panzera et al., 2011), oriented fractures linked to the fault fabric (Rigano et al., 2008; Di Giulio et al., 2009; Panzera et al., 2014, 2015), velocity inversion (Panzera et al., 2015). Then, a possible solution is to adopt a “Predominant-Period Site Classification”. We tested the reliability of using both ambient noise and earthquake recordings in a rather complex geologic and topographic setting, characterized by velocity inversion as well as strong vertical and lateral heterogeneities. The seismic site response of the study area was investigated by adopting the most commonly used techniques to evaluate the site response properties, such as the HVSR and the HVNR. Moreover, a detailed analysis of the geologic setting to reconstruct the stratigraphic sequence of 19 seismic stations of the INGV-CT, was performed. These data, with a velocity model built through literature information, were used to achieve 1D amplification function for the Etnean area.

Earthquake spectral ratio

The HVSRs were performed selecting local earthquake records, extracted from the INGV-CT database. The location and magnitude of the recorded events were taken from the bulletins (Tab. 1). The data set includes 30 earthquakes with local magnitude greater than 2.5, which occurred in the volcanic area.

Recorded earthquakes were base-line corrected, with the purpose of removing spurious offsets and band-pass filtered in the range 0.08-20 Hz, with a fourth order causal Butterworth filter. The analysis was performed by using 20s time windows, starting from the S-wave onset, including part of the coda and using a 5% cosine-tapered window. First of all, Fourier spectra, smoothed using a Konno-Ohmachi filter, of the S-wave time window were compared with the pre-event noise, in order to select good quality data on the basis of the Signal/Noise ratio. For each recording, only those signals with $S/N \geq 3$ were considered for analysis. The spectral ratio were evaluated at each station for the selected events and a geometric mean of all spectral ratios were computed to obtain the mean HVSR curve and the corresponding standard deviation.

Time origin (UTC)	Magnitude	Latitude	Longitude	Depth (Km)
08/01/2009 15:42:47	3.2	37.782	14.974	26.9
14/03/2009 09:26:51	3.4	37.797	15.151	3.4
13/05/2009 14:13:48	3.4	37.779	15.127	2.3
25/08/2009 16:58:03	3.1	37.771	14.954	24.7
19/12/2009 05:36:19	3.1	37.771	14.929	24
19/12/2009 07:42:27	3.5	37.793	14.966	25.9
19/12/2009 08:01:12	3.5	37.793	14.963	25.7
19/12/2009 08:24:58	3.7	37.813	14.873	28
19/12/2009 12:35:41	3.2	37.772	14.953	24.7
19/12/2009 12:43:11	3.6	37.794	14.965	27.3
19/12/2009 14:02:31	3.2	37.787	14.962	24.3
19/12/2009 14:37:33	3.2	37.784	14.946	29.9
19/12/2009 17:24:36	3.2	37.784	14.947	26.8
19/12/2009 18:08:34	3.4	37.673	14.966	16.4
23/12/2009 14:24:42	3.6	37.793	14.962	26.5
11/01/2010 22:15:45	3	37.773	14.932	27.5
03/04/2010 00:05:13	3.4	37.791	14.963	24.8
16/03/2011 17:34:06	3.2	37.788	14.955	27.3
05/05/2011 15:58:06	3.2	37.782	14.947	27.6
06/05/2011 19:28:50	3.5	37.791	14.962	26.7
11/05/2011 01:45:36	3.5	37.791	14.968	25.3
11/05/2011 01:46:48	3.4	37.796	14.98	26.6
11/05/2011 02:12:26	3.2	37.79	14.968	24.7
11/05/2011 02:17:08	3.4	37.788	14.96	25
09/09/2011 22:23:44	4	37.712	15.166	1.3

Time origin (UTC)	Magnitude	Latitude	Longitude	Depth (Km)
27/09/2011 07:52:54	3	37.898	14.809	12.71
01/01/2012 04:17:03	3.4	37.793	14.953	24.9
25/03/2012 21:02:30	3	37.772	14.939	27.5
27/06/2012 22:38:57	3.1	37.743	14.886	20.3
22/11/2012 11:28:56	3.7	37.859	14.909	30.4
30/12/2012 12:14:29	2.5	37.686	14.958	11
23/05/2013 13:04:48	3.4	37.696	15.089	3.9
24/05/2013 02:47:00	3	37.723	15.079	4.4
09/10/2013 08:33:22	2.7	37.676	15.045	2.7
12/03/2014 00:55:37	2.9	37.683	15.078	5.2
04/05/2014 17:25:55	2.6	37.876	14.912	25.6
02/06/2014 01:15:01	2.5	37.781	14.947	20.5
11/07/2014 12:44:11	2.5	37.628	15.068	7.2
09/08/2014 07:07:00	2.7	37.609	15.161	17.78
09/08/2014 11:26:24	2.5	37.614	15.184	23.5

Table 1. Etnean earthquakes used for the analysis (from Gruppo Analisi Dati Sismici, 2014, <http://www.ct.ingv.it/ufs/analisti/catalogolist.php>).

Noise spectral ratio

Microtremor recordings were selected from the stations of INGV-CT. The signal length was of about 1 hour at each stations. To check the stability of the HVNR, the signal was selected in two different days. The first day, in summer, was characterized by a low level of noise, whereas the second one was taken in winter, with an high level of noise, due to the weather conditions and the start of lava fountains in the last hours of the day.

The microtremor recording were de-trended, band-pass filtered and subdivided in 30s, 5%cosine tapered, time windows. Through an anti-trigger algorithm based on STA/LTA (Short Time Average over Long Time Average), only the most stationary parts were selected and transients associated to very close sources were excluded. In particular, STA was settled to 1s and LTA to 20s. After the necessary processes of signal cleaning were completed, the spectral ratio technique was then applied to obtain the mean spectral ratios and corresponding standard deviation. Once the HVSR and HVNR were performed, they were overlapped and it was observed a strong similarity between the obtained results (Fig 1).

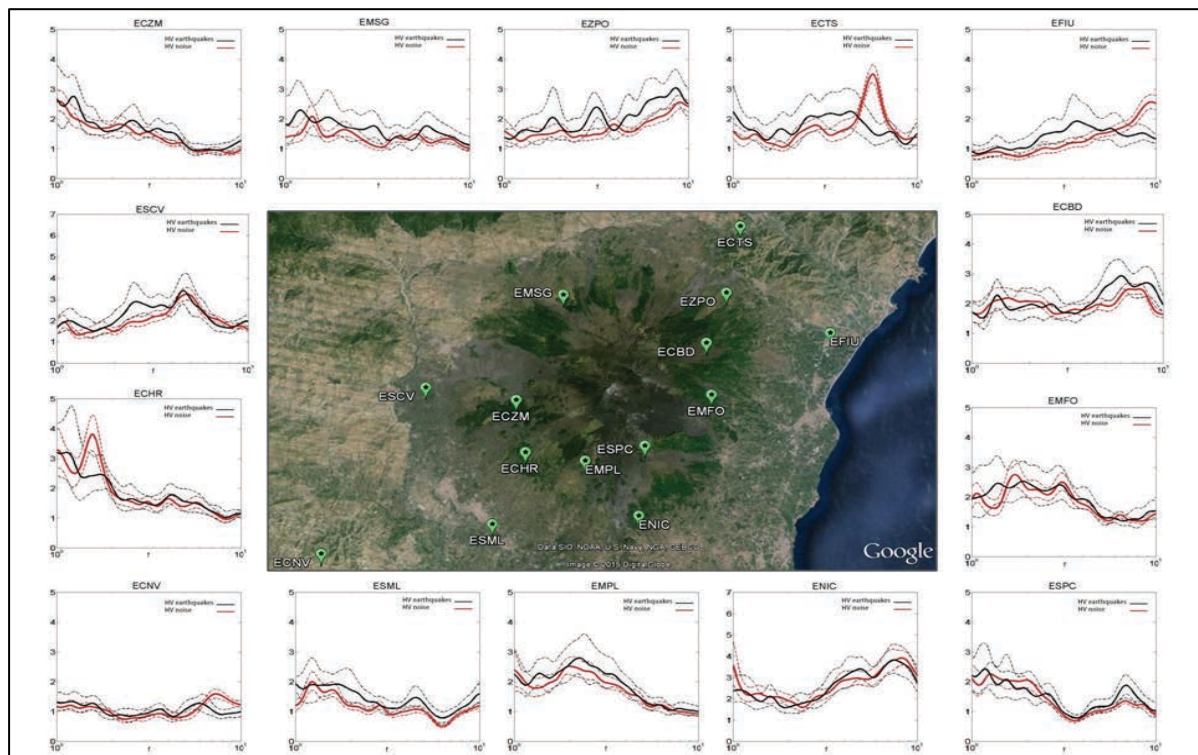


Figure 1. Mean HVSR (black line) and mean HVNR (red line) at each considered seismic station with the corresponding standard deviation, dashed black and red respectively.

Numerical modelling

The modelHVSR Matlab routines (Herak, 2008) was adopted to compute theoretical HVSR in a homogeneous and isotropic layer. The soil model consists of a number of visco-elastic layers, stacked over a half-space, each of them being defined by the thickness (h), the velocity of the body waves (V_P and V_S), the density (ρ), and the Q-factor, which controls the inelastic properties. The incoming waves are assumed to be travelling vertically and assuming that horizontal and vertical motions at the bedrock have no amplification, the HVSR at the surface is then obtained as the ratio between the theoretical transfer functions of S and P waves. In particular, the observed HVSR is inverted through a Monte Carlo simulation aiming to find soil models that minimize the misfit function with theoretical HVSR. The Monte Carlo search is started with an initial model whose parameters are randomly perturbed within the bounds defined by the user. In our case, the number of random tries was settled to 10,000 and the initial model of body wave velocities (V_P and V_S) and layers thickness was perturbed by $\pm 5\%$ and $\pm 25\%$ respectively, to obtain a good fit with the experimental results.

For all the considered seismic stations of Mt. Etna, stratigraphic sequence were made by integrating literature information (Branca et al., 2011; Branca and Ferrara, 2013) and observations (Fig. 2). This procedure made possible to estimate the thicknesses of the layers and then, using geotechnical and geophysical literature data (Priolo, 1999; Azzaro et al., 2010), body wave velocities, density as well as Q_p and Q_s were assigned to each layer (Tab. 2). Fig. 3 shows an example of inversion procedure at two of 19 considered seismic stations.

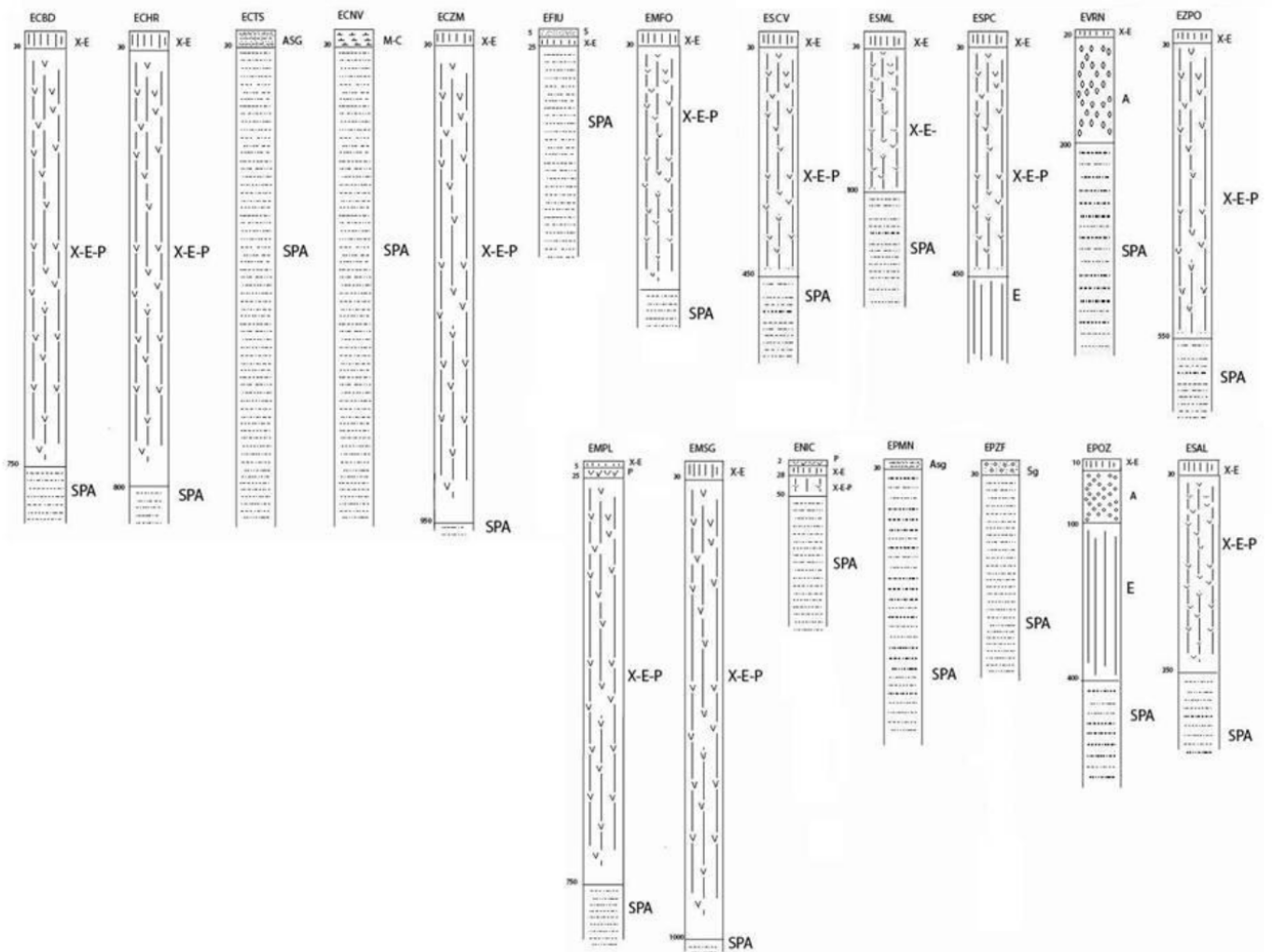


Figure 2. Stratigraphic sequence obtained for each seismic station used for HVSR and HVNR inversion.

Lithology	Symb	V _{S min} (m/s)	V _{S max} (m/s)	Density (kg/cm ³)
Scoriaceous lava	X	225	380	1.83
Massive lava	E	900	1250	2.24
Bullous fractured lave passersby to massive lave	E2	413	598	2.24
Sandstones with clayey silt elements	Cc	500	800	2.14
Silty sand with volcanic elements	S	367	497	2.04
Alluvial conglomerate from cemented to un-cemented	A	170	800	2.00
Pyroclastic deposits	P	217	433	1.63
Marly clay	M-C	250	650	1.95
Yellowish sandy clay and silt with interbedded sand	Asg	250		1.95
Quartzly sand, coarse gravel and conglomerate	Sg	450		2.00
Pliocenic sediments and alloctonous (flysch, clay, silt and sand)	Spa	1316		2.10

Table 2. Geotechnical and geophysical parameters of the main geological formation outcropping in the Etna region.

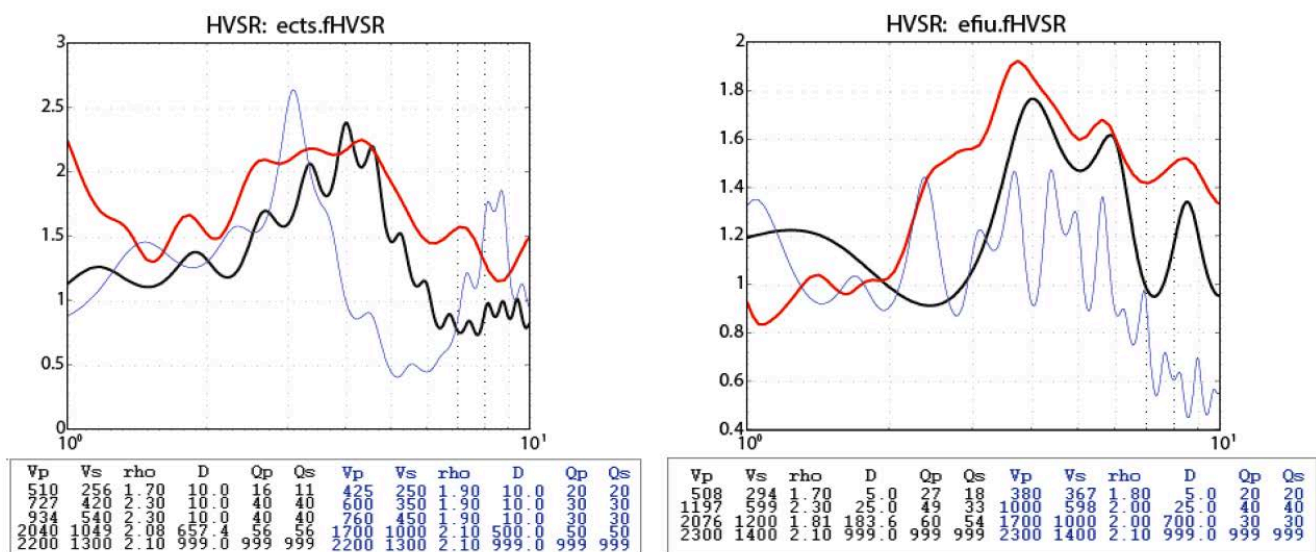


Figure 3. Measured (red), 1D start model (grey) and 1D final model (black) HVSR curves, with inferred geotechnical and geophysical parameters, obtained from seismic stations ECTS and EFIU, localized on Etna volcano. Note the good agreement between experimental and obtained curves.

Site amplification functions

The amplifications were computed from frequency-domain calculations, using the programs SITE_AMP and NRATTLE (Boore, 2003) that convert a velocity and density model into site amplifications. In particular, the NRATTLE Fortran routine calculates the Thomson-Haskell plane SH-wave transfer function for horizontally stratified constant velocity layers at a specific incidence angle over a uniform velocity halfspace. The input parameters of NRATTLE are the V_S, density (ρ) and Q. The halfspace is settled equal to the deepest measured layer and the NRATTLE solution is exactly equivalent to the solution computed by the equivalent linear site response program SHAKE for linear modulus reduction and damping curves (Schnabel et al., 1972). The code compute amplifications at specified frequencies or at frequencies corresponding to the “breakpoints” in the velocity model.

Section 2

Scientific Reports of Research Units (RU 6)

To compile the input file for the programs SITE_AMP and NRATTLE we used the output model of modelHVSR obtaining as output the amplification function (AF) for 14 seismic stations. Five stations of the selected 19 seismic stations were eliminated due to lack of convergence in the modelHVSR inversion. Therefore, a classification scheme alternative to that based on V_{S30} was adopted. To discriminate among classes, as proposed by many authors (Zhao et al., 2006; Luzi et al. 2011; Di Alessandro et al., 2012), the predominant soil period was adopted subdividing the AF into groups. Taking into account the frequency at which the first peak of corresponding HVSR occurs, the following classes were considered:

- ET-1 class: flat spectral ratios showing amplitude values not exceeding 2 units (including standard deviation);
- ET-2 class: HVSR having fundamental period $T \leq 0.2$ s with amplitude exceeding 2 units;
- ET-3 class: HVSR with fundamental period $0.2 < T \leq 1.0$ s with amplitude exceeding 2 units;
- ET-4 class: HVSR showing broad band amplitude exceeding 2 units.

The mean AF of each class was obtained by averaging the AF of all stations included in the considered classes (Fig. 4). The obtained curves show a good match with those proposed by Luzi et al. (2011) for the whole Italian territory. It is however important to specify that the present results do not consider the long period seismic site effects and the obtained amplification functions display values higher than those achieved by Luzi et al. (2011). This last evidence could be related to the low shear wave velocity values assigned to the fractured lavas.

ET-1	ET-2	ET-3	ET-4
ECNV	ECBD	ECHR	ECTS
	ENIC	EMPL	ECZM
	EPMN	ESCV	EFIU
	EZPO		EMFO
			ESML
			ESPC

Table 3. Seismic stations sorted using the proposed classification for Mt. Etna.

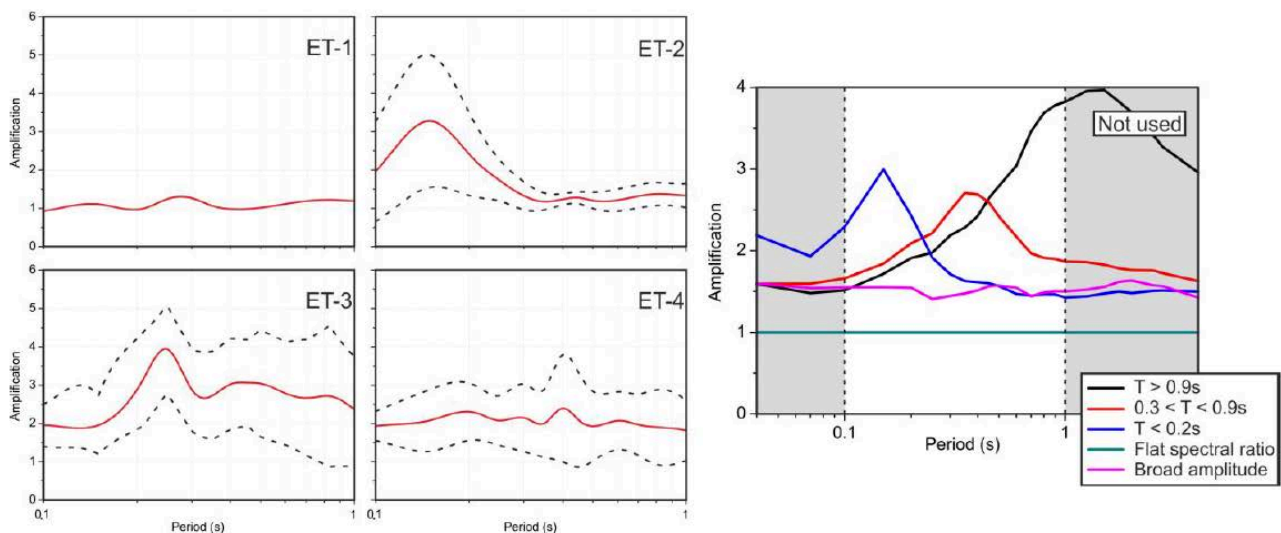


Figure 4. Left: mean site amplification (red curve) and standard deviation (dashed black curve) for the Etnan area. Right: Luzi et al. (2011) amplification function for the whole Italian territory.

A classification proposed for the eastern flank of Etna

The comparison of HVSR and HVNR obtained at each considered seismic station, located all around the volcano, allowed us to verify that the noise can be used as a valid alternative to the earthquakes data. It is

therefore possible to use the HVNR technique as a quick and inexpensive procedure to evaluate the fundamental period of an investigated site.

An extensive noise measurements campaign was made in the eastern flank of Etna, to classify the investigated sites through the proposed classification. In particular, using a three components velocimeter, 130 noise measurements were performed. By means of a GPS, each recording site, homogeneously spaced along a grid having size of about 1x2 km, was geo-referenced. The study area includes the municipalities of Piedimonte Etneo, Fiumefreddo di Sicilia, Mascali, Giarre, Riposto, Sant'Alfio, Milo, Zafferana, Santa Venerina, Acireale, Aci Catana, Aci Sant'Antonio, Viagrande and Trecastagni (Fig. 5).

Time series of 30 minutes length were recorded using a sampling rate of 128 Hz and processed through the HVNR. Time windows of 30 s were considered and the most stationary part of the signal was selected excluding transients associated to very close sources. In this way, the Fourier spectra were calculated in the frequency range 0.1-30.0 Hz and smoothed using a proportional 20% triangular window. Following the criteria suggested by the European project Site EffectS assessment using Ambient Excitations (SESAME, 2004), only the spectral ratio peaks having amplitude greater than two units, in the frequency range 0.5-10 Hz, were considered significant. To summarize the obtained results, the HVNR were subdivided into 16 groups showing a similar shape using the cluster analysis (Fig. 6). The cluster analysis was computed taking into account only the HVNRs amplitudes in the 0.5 - 10.0 Hz frequency range. Higher frequency values ($> 10\text{Hz}$) were not included, being not interesting from the engineering point of view. The analysis was performed taking into account the 130 HVNR ($i=1\dots 130$) whose amplitude was computed at 100 frequency values (M) in the range 0.5-10.0 Hz, expressing them by a vector y_{iM} . The degree of similarity between the HVNR observed at two sites (e.g. i and j) was calculated using the Euclidean distance:

$$d_{ij} = \sqrt{\sum_{M=1}^{63} (y_{iM} - y_{jM})^2} \quad (1)$$

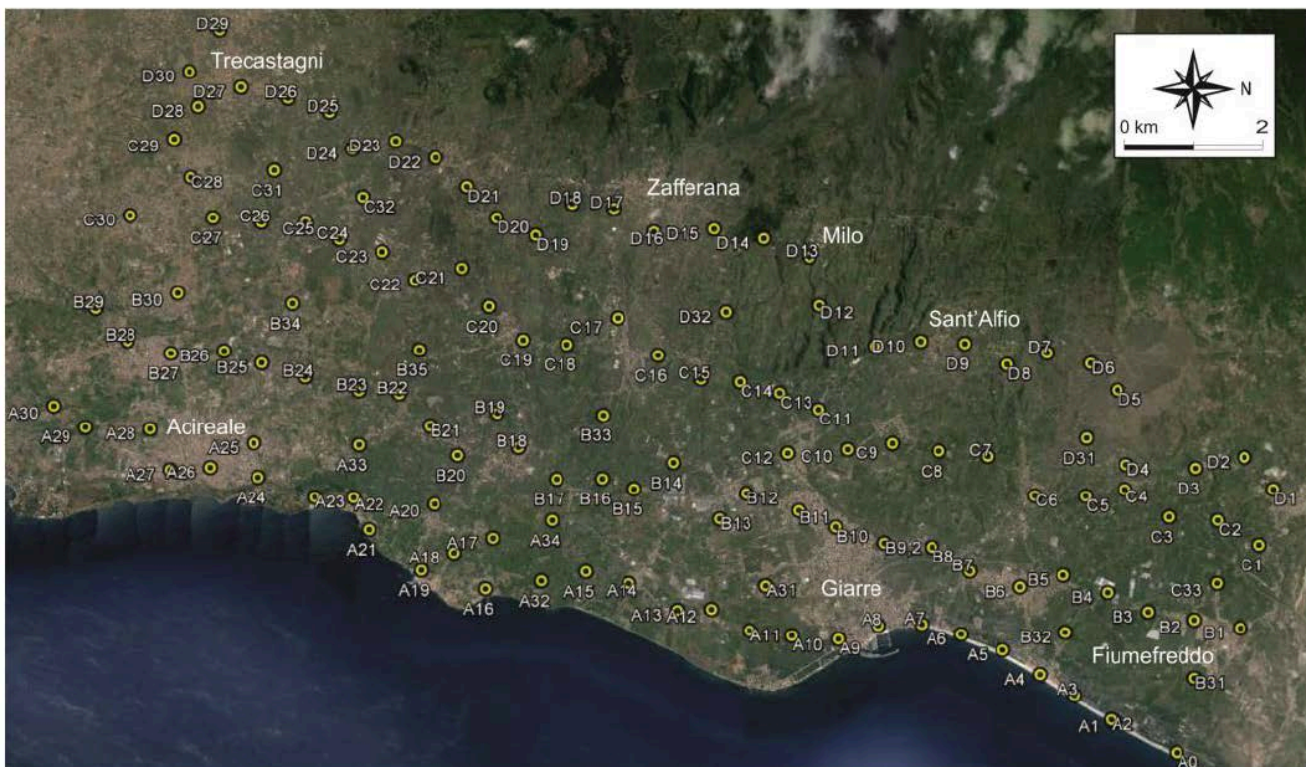


Figure 5. Map showing the HVNR measurement locations in the eastern flank of Mt. Etna.

Section 2
Scientific Reports of Research Units (RU 6)

Finally, the use of *k-means* clustering approach (MacQueen, 1967) has led to the recognition of the clusters. This technique consists in ranking into N_C clusters, chosen by the user, the N_K measurement points and evaluating the quality of the clustering by computing the sum of the squared error (SSE):

$$SSE = \sum_{i=1}^{N_K} \sum_{j=1}^M (y_{ij} - y_{C_{kj}})^2 \quad (2)$$

where y_{C_k} is the centroid of the vectors y_i in the cluster, calculated through:

$$y_{C_{kj}} = \frac{1}{N_K} \sum_{i=1}^{N_K} y_i \quad (3)$$

The *k-means* algorithm directly attempts to minimize the SSE, assessing each measurement point to its nearest cluster and repeating the computation until the points do not change the cluster any longer.

The identification of the best solution from a group of acceptable models was achieved through the Akaike information Criterion (AIC, Akaike, 1974). This procedure does not require particular assumptions on the experimental data and it is suitable for solving the model decision problem in many applications (Burnham and Anderson, 2002). To find the optimal partition, the cluster analysis was run for increasing values of N_C (ranging from 5 to 15) and selecting the N_C value for which the AIC is minimized. Assuming that the model error is normally distributed, the AIC formula is:

$$AIC = N_K \ln \left(\frac{RSS}{N_K} \right) + 2k + \frac{2k(k+1)}{(N-k-1)} \quad (4)$$

where N_K is the total number of HVNR, \ln indicates the natural logarithm, RSS is the residual sums of squares and k indicates the number of free parameters as N_C-1 . In the present study, RSS is defined as the sum of the SSE of all the clusters of each partition.

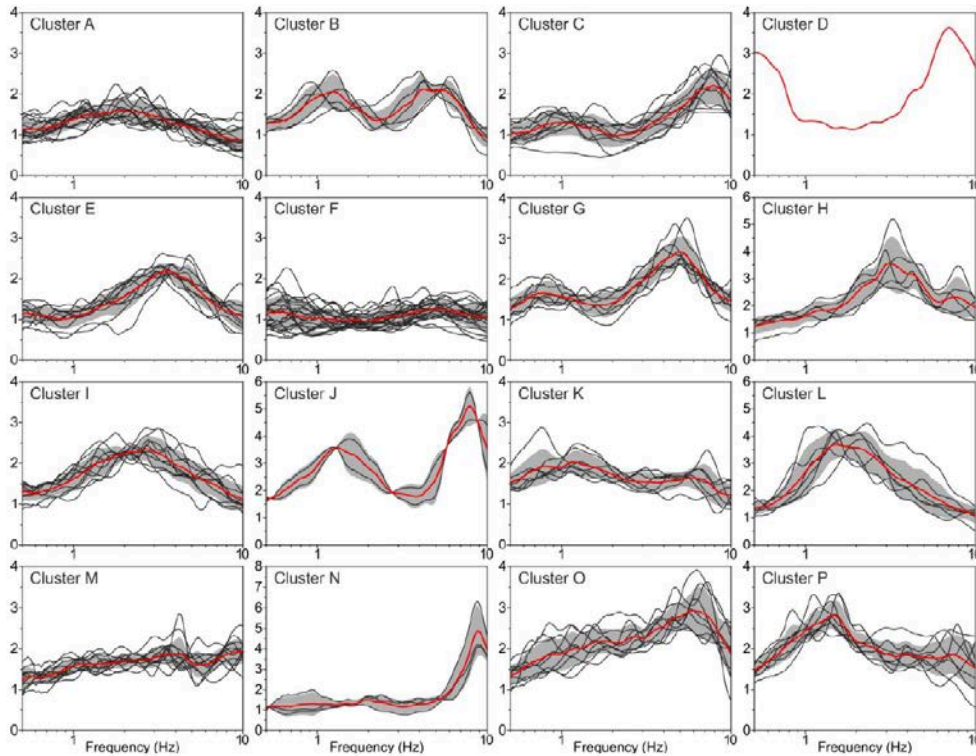


Figure 6. Clusters obtained from the measurements performed in the eastern flank of Mt. Etna. Red line is the centroid, whereas grey shadowed area is the standard deviation.

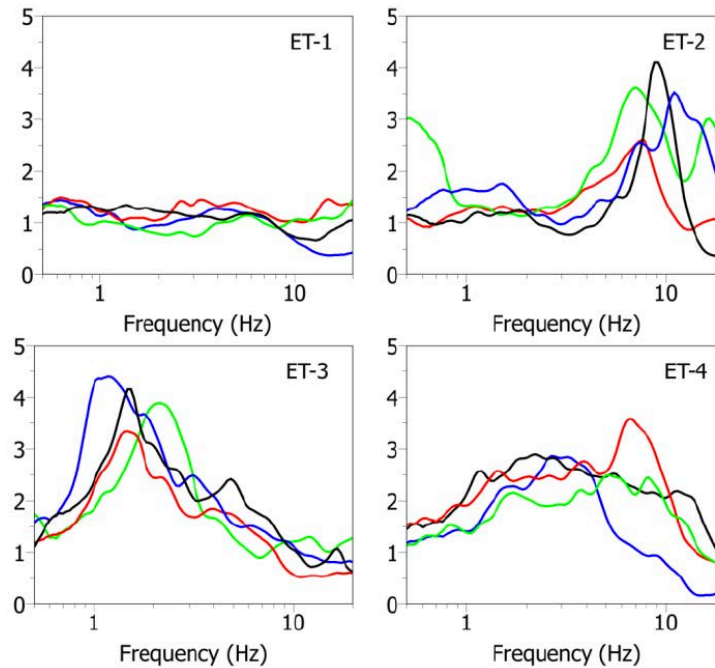


Figure 7. Examples of classification based on the use of HVNR. The coloured curves refer to selected examples of HVNR from the 130 microtremor measurements for each class.

Each co-author manually classified the HVNRs using the adopted predominant period classification (see examples in Fig. 7). Different classifications were made only for stations close to the limits of the site classes. When co-authors opinions differed, the sites were re-classified.

In Fig. 8 (left) the space distribution of site classes for the investigated area, is shown whereas the central panel depicts a macro-zones map of the studied area, achieved by interpolating these information through the Nearest Neighbor algorithm. The obtained results highlight that the main fault systems existing in the studied area play an important role in the seismic site response features of the lower eastern flank of Mt. Etna (Fig. 8, right).

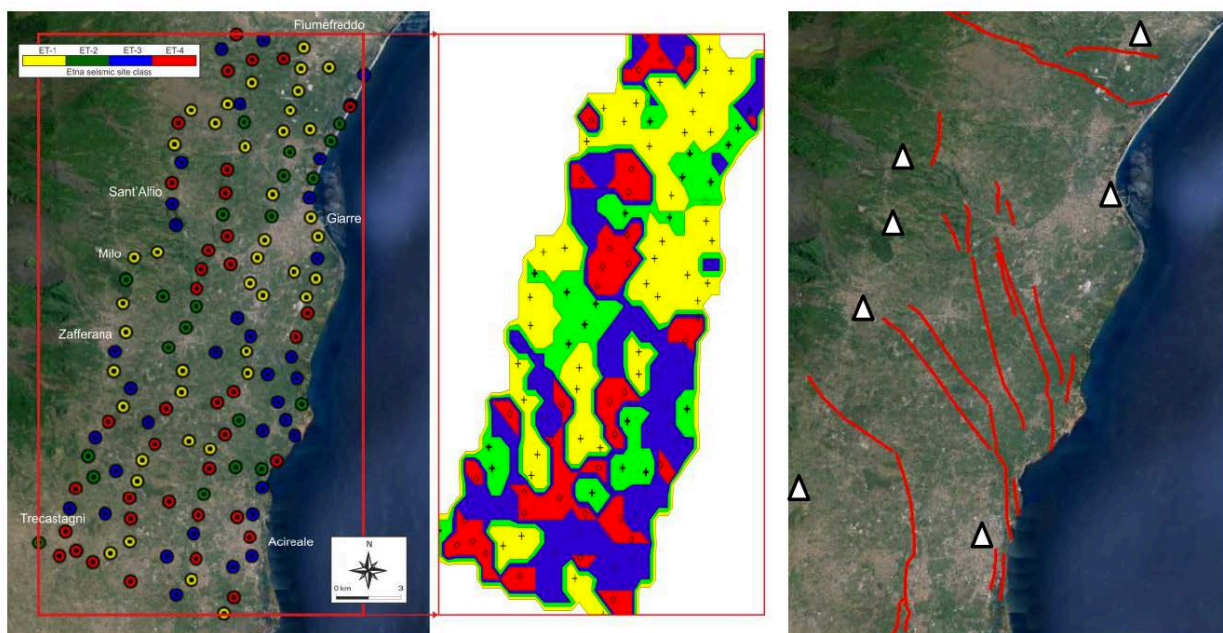


Figure 8. Map showing the class assigned to each measurement point (left panel). Map of the studied area obtained by interpolating the class assigned at each measurement point using the algorithm Nearest Neighbor (central panel). Main faults existing in the studied area (right panel).

Section 2

Scientific Reports of Research Units (RU 6)

Conclusions

- A preliminary characterization of the local seismic response in the Etnean territory was performed;
- Literature data were achieved in order to get information on elastic parameters and lithology;
- HVSR and HVNR were compared to test the reliability of ambient noise in the Etnean area to obtain information on the soil fundamental period;
- Through a simple 1D model, preliminary site amplification functions were achieved and assigned to 4 classes of a predominant-period site classification to overcome the problems related to the average shear wave velocity of the upper 30 m ($V_{S,30}$);
- The classification was applied to map site effects in the lower eastern flank of Mt. Etna;
- Long period seismic site effects corresponding to ET3 and ET4 classes seem to match the area of the Timpe faults system and the Pernicana fault;
- These results highlight, besides stratigraphic effects, a strong role of the oriented fractures linked to the fault fabric; this means that further analysis are needed to better constrain the achieved amplification functions.

Task 2 - WP 7, Resp. C. Ferlito

Geochemistry of magmas and feeding structures (Etna)

Participants: UNI-CT

Carmelo Ferlito, Giulia Maria Maugeri, Gabriele Lanzafame, Luca Samuele Capizzi

Other institutions

INGV-CT Stefano Branca, Rosa Anna Corsaro, Lucia Miraglia

Sp1 - Analyses of textures and compositions of crystalline phases (1928-1981 eruptions)

The feeding system of Etna volcano is very articulated allowing magma residence along its way up. Seismic patterns of earthquakes associated to magma rises at times display a correlation between the shift of the hypocentres and the upward magma rising through the crust along tectonic structures. Analyses of the products erupted in recent lateral events have evidenced not negligible geochemical differences in lavas erupted by distinct tectonic segments (Ferlito et al., 2008); this implies that the differentiation processes could be influenced, even in the short period, by the conditions and rising times. The work carried out during the first year of the project has made evident how the products of two case eruptions (1928, 1981) (cfr. Ponte, 1929,a-b; Scott, 1983 Coltelli et al., 2012), have displayed syn-eruptive compositional variations. The reason of such a pattern can be found alternatively either in eruptions fed by compositionally distinct magmas or in changes of the feeding conditions (e.g. increase of the magma output due to a more active tensile tectonics). We have realized that there exists a strict relationship between the type and size of mineral phases and the degassing associated, which in turn is directly correlated with the tectonic activity.

For the selected eruptions, 16 samples have been collected (9 for 1928 and 7 for 1981); analyses of whole-rock major and trace element are reported in Tabs. 4 and 5, respectively.

	SiO ₂	TiO ₂	Al ₂ O ₃	Fe ₂ O ₃	FeO	MnO	MgO	CaO	Na ₂ O	K ₂ O	P ₂ O ₅	LOI	TOT
E81-3	47,23	1,68	17,21	1,69	8,46	0,18	5,05	10,36	3,53	1,93	0,49	0,91	98,73
E81-4	46,86	1,68	17,12	1,69	8,43	0,18	5,04	10,36	3,52	1,90	0,49	0,90	98,16
E81-1	47,08	1,67	17,32	1,68	8,39	0,18	4,80	10,07	3,64	1,96	0,50	0,70	97,99
E81-2	47,07	1,67	17,25	1,68	8,42	0,18	4,99	10,29	3,58	1,92	0,49	0,66	98,20
E81-5	47,02	1,65	17,30	1,68	8,40	0,18	4,93	10,20	3,61	1,92	0,49	0,70	98,08
E81-6	46,86	1,66	17,14	1,70	8,48	0,18	5,09	10,35	3,46	1,89	0,48	0,68	97,97
E81-7	47,03	1,69	17,02	1,72	8,59	0,18	5,18	10,34	3,65	1,92	0,49	0,68	98,48
EMAS-1	47,89	1,66	17,08	1,68	8,39	0,18	5,19	10,11	3,64	1,68	0,48	1,00	98,97
EMAS-2	47,74	1,66	17,26	1,70	8,49	0,18	5,18	10,20	3,68	1,62	0,47	1,00	99,19
EMAS-3	47,70	1,66	17,25	1,69	8,45	0,18	5,22	10,30	3,54	1,61	0,47	0,94	99,01
EMAS-4	47,59	1,67	16,87	1,72	8,58	0,18	5,38	10,19	3,46	1,67	0,47	0,76	98,53
EMAS-5	47,81	1,69	17,03	1,74	8,68	0,18	5,45	10,37	3,51	1,56	0,47	0,78	99,27
EMAS-6 II	47,67	1,69	16,81	1,74	8,68	0,19	5,56	10,38	3,51	1,56	0,46	0,75	99,00
EMAS-7	47,60	1,70	16,91	1,74	8,68	0,19	5,50	10,38	3,49	1,59	0,46	1,10	99,32
EMAS-8	47,65	1,67	17,21	1,71	8,56	0,18	5,18	10,22	3,67	1,64	0,48	1,10	99,27
EMAS-9	47,55	1,69	17,00	1,74	8,69	0,18	5,53	10,32	3,60	1,52	0,47	1,22	99,50

Table 4. Composition (wt%) of whole rock major elements for the 1928 and 1981 lavas.

Compositional variations within each lava flow are not significant, especially for trace elements, whose variability is within the analytical error (Figs. 9, 10). Moreover, lava emitted at the upper fissures during the 1928 eruption is slightly more evolved than the lava erupted at lower fissures; on the contrary, during the 1981 eruption, lavas emitted at the intermediate fissures are more primitive than lavas emitted at the lower fissures.

	EMAS1	EMAS3	EMAS6	EMAS8	EMAS9	E81-2	E81-3	E81-6
Th	9,273	8,916	8,543	8,914	8,767	8,485	8,388	8,352
Ba	682,4	658,6	639,6	652,7	647,9	663,3	652,5	660,4
Co	38,62	49,51	40,21	38,91	41,52	38,87	37,42	40
Cr	30,79	30,19	28,96	27,56	29,77	23,2	21,58	22,88
Cu	108,7	114,4	109,3	108,6	113	125,7	132,7	129,9
Dy	5,101	4,989	4,866	4,924	4,988	5,12	4,954	5,01
Er	2,389	2,326	2,262	2,28	2,299	2,318	2,283	2,32
Eu	2,695	2,631	2,554	2,601	2,586	2,673	2,622	2,678
Ga	22,33	22,44	21,87	22,32	22,33	22,16	21,61	22,06
Gd	7,077	6,931	6,805	6,809	6,879	7,119	6,939	7,054
Ge	1,408	1,342	1,394	1,353	1,397	1,32	1,295	1,322
Hf	4,515	4,351	4,165	4,33	4,356	4,306	4,199	4,231
Ho	0,914	0,892	0,87	0,887	0,883	0,887	0,894	0,888
La	63,64	61,4	59,66	61,28	60,7	60,12	59,28	59,61
Lu	0,307	0,305	0,305	0,304	0,304	0,302	0,298	0,307
Nb	51,73	50,91	48,35	50,26	49,37	47,29	46,23	46,31
Nd	49,11	47,85	46,83	47,55	47,22	48,08	47,06	47,06
Ni	24,82	25,04	28,1	25,97	29,02	25,17	23,02	24,23
Pb	7,4186	6,0587	6,1959	6,0296	6,8205	6,408	6,352	6,41
Pr	13,17	12,78	12,46	12,75	12,59	12,72	12,52	12,59
Rb	33,24	32,38	30,81	32,72	25,47	41	40,24	41,03
Sm	8,921	8,707	8,56	8,679	8,683	8,924	8,753	8,817
Sr	1140	1165	1105	1143	1130	1244	1212	1239
Ta	3,01	2,944	2,789	2,894	2,801	2,712	2,653	2,644
Tb	0,973	0,95	0,936	0,939	0,942	0,964	0,962	0,969
Th	9,273	8,916	8,543	8,914	8,767	8,485	8,388	8,352
U	2,606	2,415	2,406	2,507	2,464	2,428	2,397	2,415
V	263,7	269,2	272,7	270,1	268,9	275,4	273,8	278,8
Y	26,06	25,39	24,65	25,15	24,94	25,64	25,45	25,54
Yb	2,149	2,085	2,033	2,029	2,03	2,021	2,026	2,02
Zr	214,6	208,8	199,7	207,1	206,4	207	202,3	203,9

Table 5. Composition of whole-rock (ppm) trace elements for samples referred to the 1928 and 1981 lavas.

Section 2
Scientific Reports of Research Units (RU 6)

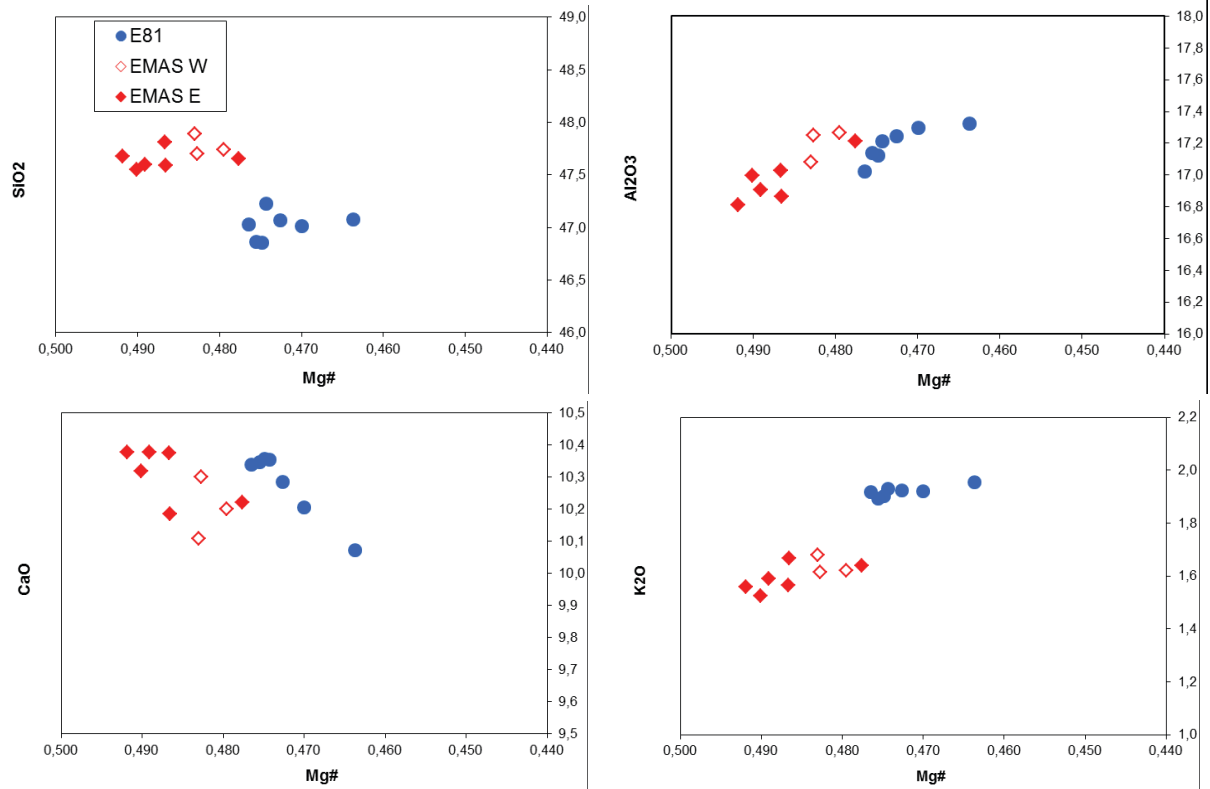


Figure 9. Variation diagrams for major elements.

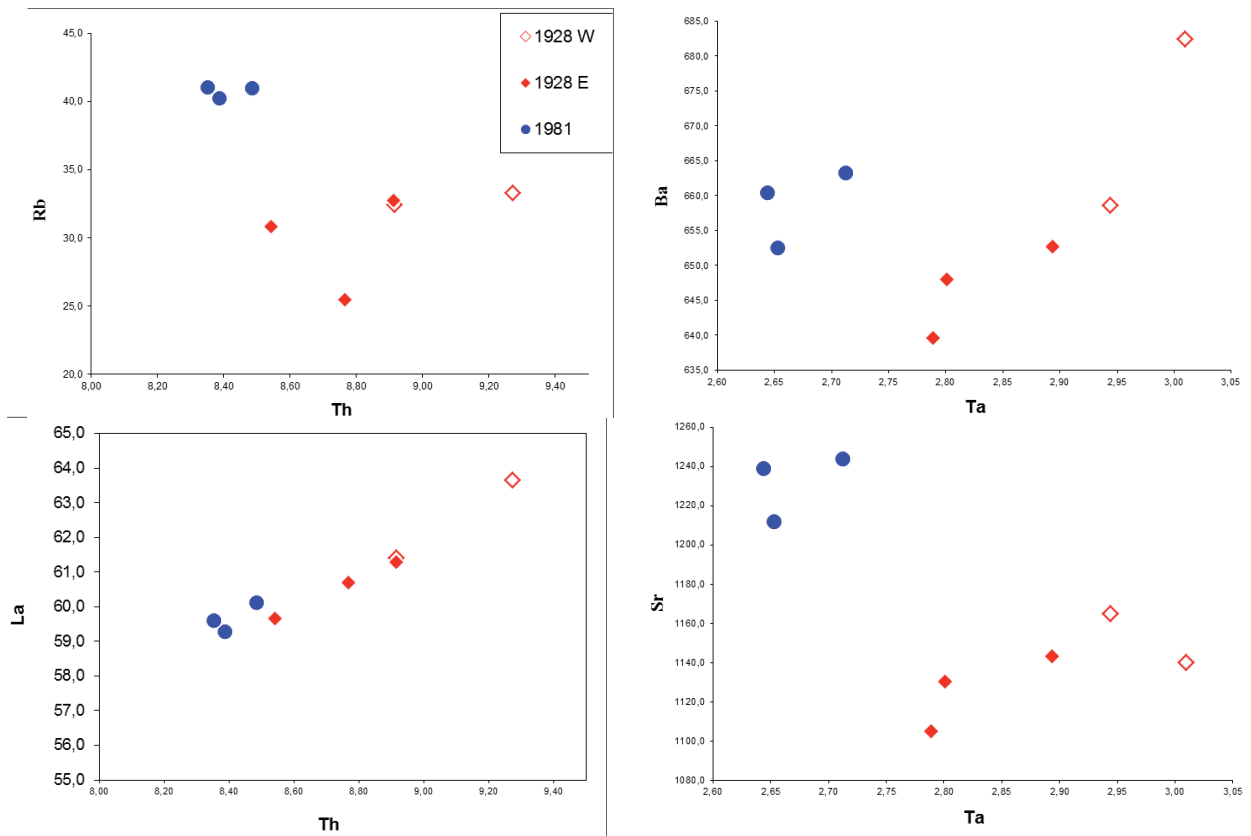


Figure 10. Variation diagrams for trace elements.

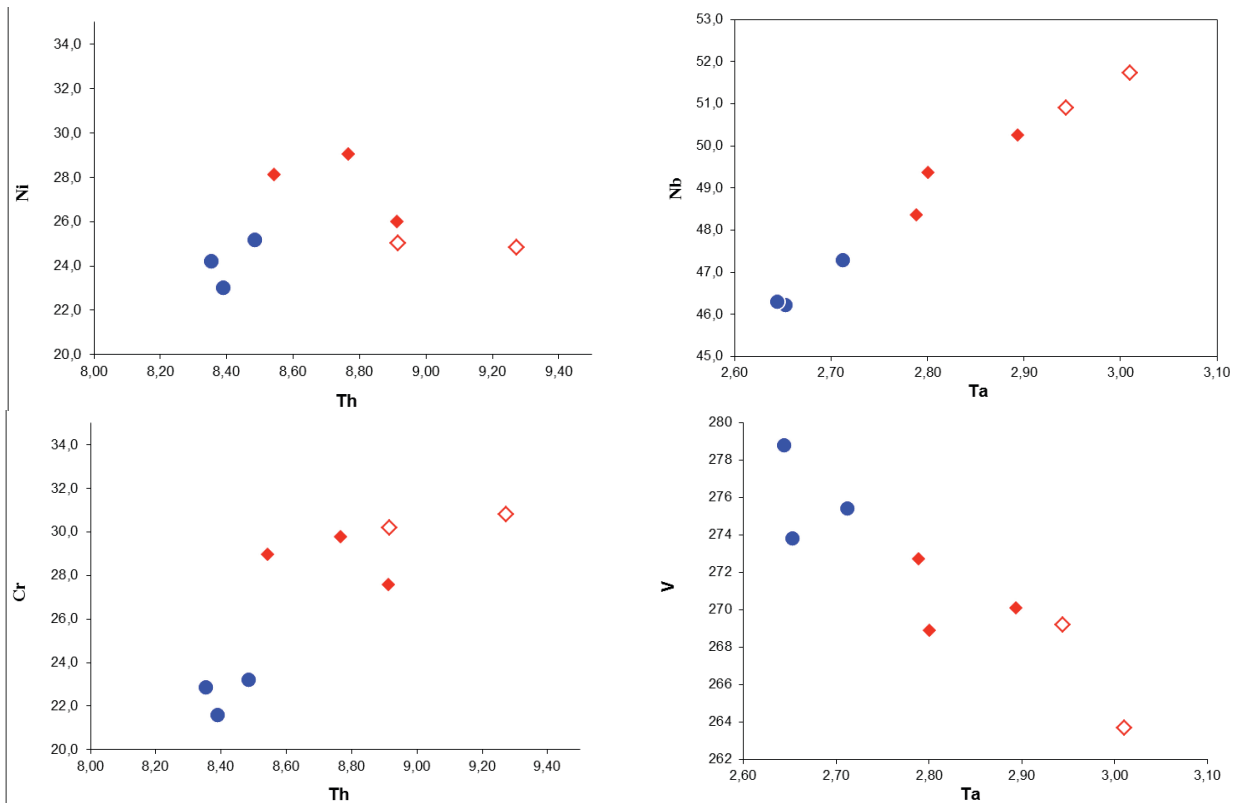


Figure 10. (continued).

On the base of the classificative diagram TAS (Total Alkali Silica), all samples fall in the trachybasalt field (Fig. 11).

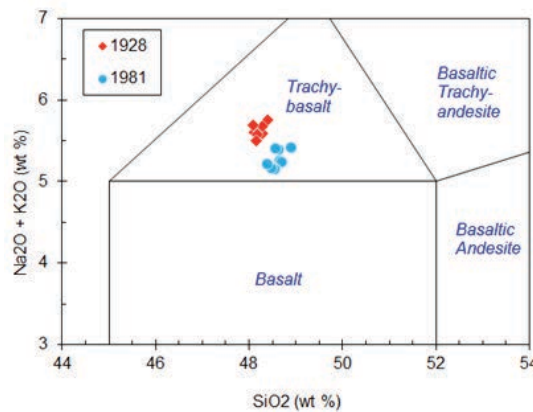


Figure 11. Classificative diagram TAS (Total Alkali Silica).

In Fig. 12 it is reported the phenocrysts content for different samples for 1928 and 1981 eruptions: products of the 1928 eruption have a generally high porfircity (P.I.>30), which increases for lavas emitted at the lower fissures (P.I. ca. 50). Instead, products of the 1981 event have a generally high porfircity (P.I.>30), without a comparable strong increment at the lower fissures.

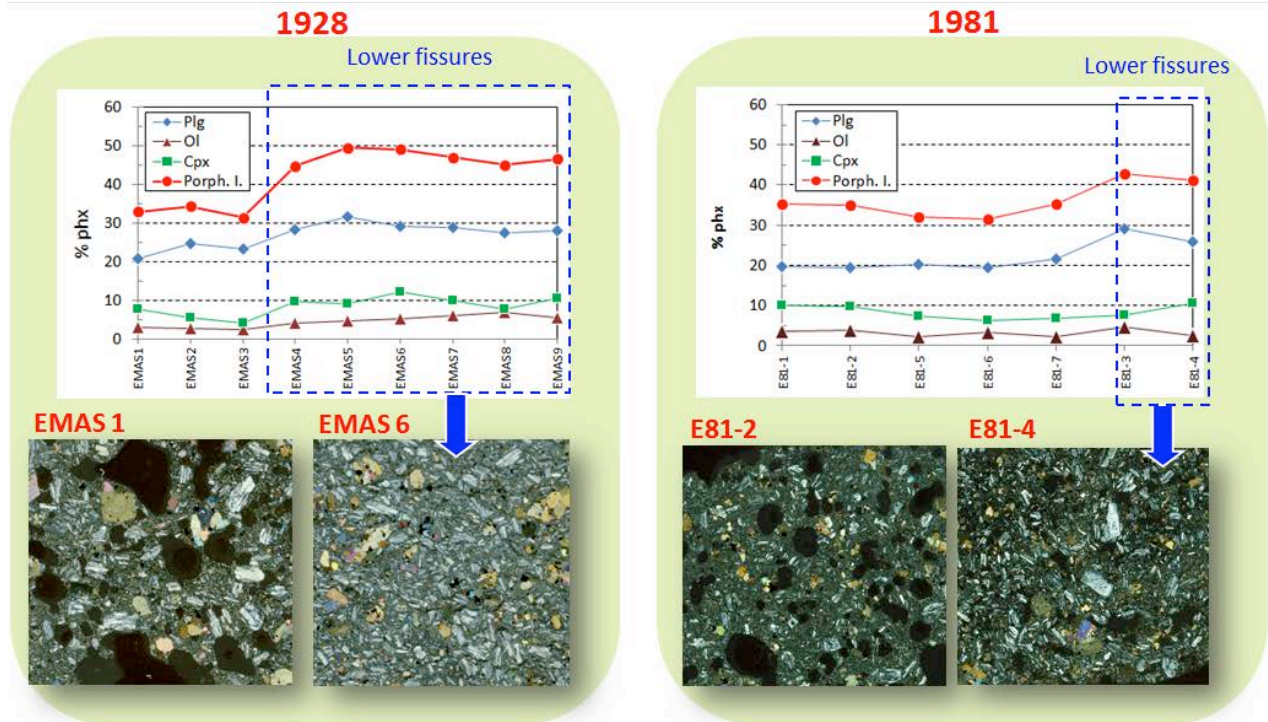


Figure 12. Phenocrysts content for a different samples of the 1928 and 1981 eruptions.

Sp2 - Pre- and sin-eruptive magma differentiation models and relationship with volcanological evolution and syn-eruptive tectonics

The modelization of magma rise during the two events was attempted by imputing in the model data on phases compositions, which have been obtained with scanning electron microscope analyses of 2 samples for each event. The most significant phases taken into consideration are olivine and plagioclase (Figs. 13, 14). The compositions of most of the olivine phenocrysts (>200 mm) erupted during the 1928 event show cores (Fo 79-82) in disequilibrium with the host magma (Fo 72-76); rims of phenocrysts and groundmass microlites are more fayalitic (Fo 59-73), as expected in the late stages of the melt crystallization, they were in equilibrium with a more evolved liquid. Correlations between the characteristics of the upper and lower fissures are not evident.

In the case of the 1981 eruption, the cores of olivine phenocrysts (Fo 73-76) are in equilibrium with the host magma (Fo 72-76); rims of phenocrysts and groundmass microlites are more fayalitic (Fo 59-73) in equilibrium with a more evolved liquid. Also in this case, differences between intermediate and lower fissures are not significant.

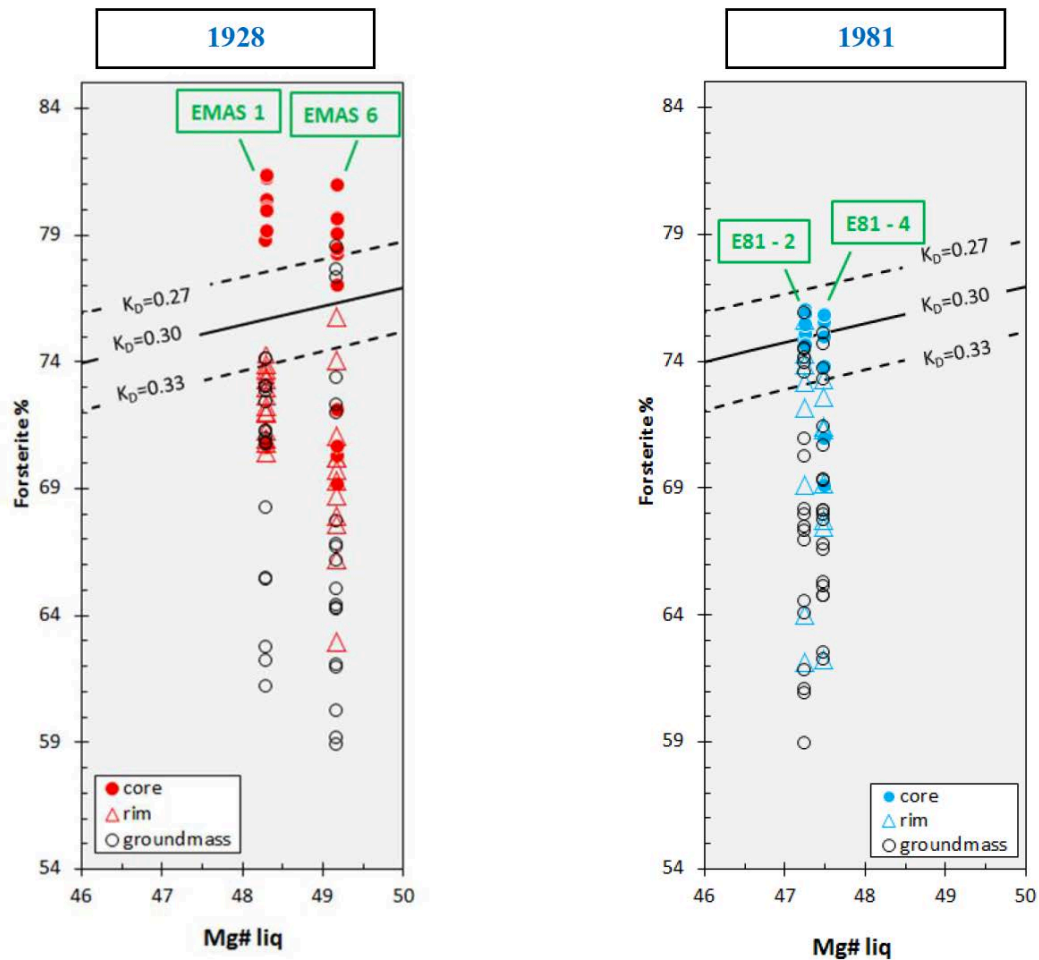


Figure 13. Forsteritic content of the 1928 and 1981 olivines; equilibrium fields are obtained by using the distribution coefficient (K_D Roeder and Emslie, 1970).

Analyses for plagioclase phases (Fig. 14) point out that during the 1928 and 1981 eruptions the cores of plagioclase phenocrysts (An_{74-86}) are in equilibrium with the host magma; rims of phenocrysts and groundmass microlites are more albitic (An_{50-65}) and, as expected during crystallization, they are in equilibrium with a more evolved liquid. As displayed by the olivines, there are not differences between characteristics of upper and lower fissures.

Data of mineral compositions have been used to simulate the conditions of ascending magmas (Fig. 15), hypothesizing that the starting magma could have been a more primitive basalt, whose composition chosen as analogue is the Mt. Maletto lavas, which represent one of the most primitive lavas ever emitted in the Etnean area.

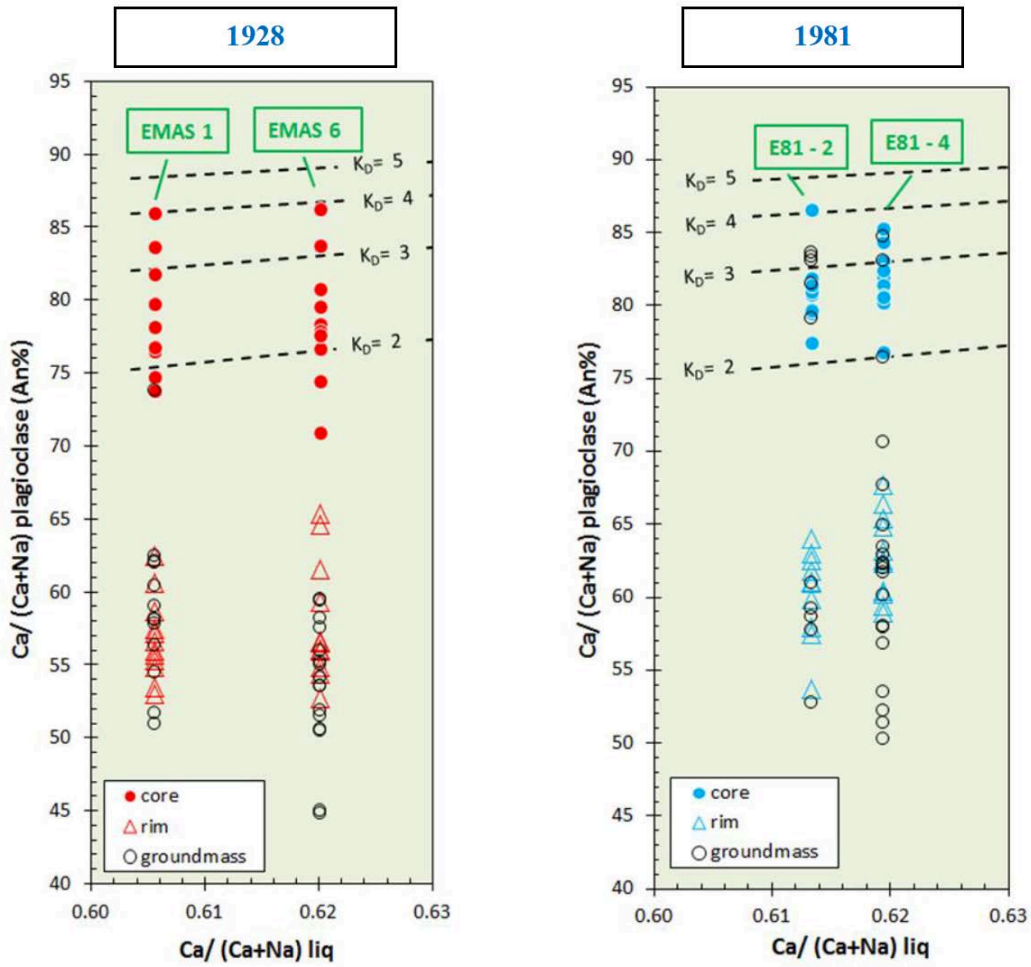


Figure 14. Ca/(Ca+Na) in plagioclases and in the melt of the 1928 and 1981 lavas; equilibrium fields are obtained by using the distribution coefficient (K_D Wallace and Carmichael, 1994).

Conditions used to simulate fractional crystallization of ascending magma, are:

- Composition of the starting magma= Mt. Maletto lavas from Tanguy et al. (1997)
- $T= 1220$ to 1060 °C
- $P= 3000$ to 0 bar
- $\Delta P/\Delta T= 20$
- Oxygen fugacity Buffer Ni-NiO
- $H_2O=1\%$

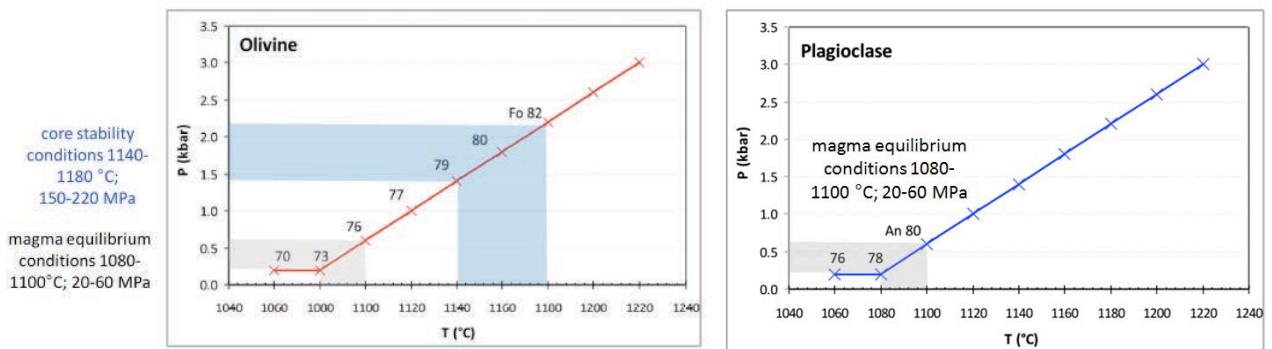


Figure 15. Temperature and pressure conditions allowing the crystallization of olivines and plagioclases.

For the 1981 eruption, which presented crystalline phases in equilibrium with its melt, the ascent to the surface could have occurred without any appreciable residence time at depth. On the contrary, MELT's simulations, indicate that the cores of the 1928 olivines formed at considerable pressure (150-220 MPa), suggesting that magma could have reached the surface through a more complex history, which includes intracrustal residence for a significant period of time.

In conclusion, for the 1928 eruptive event which, in order to fill the lack of recent data and interpretations has been studied more in depth, our data could be interpreted by envisaging that the magma feeding the eruption was associated to a compositionally zoned dyke, but that its ascent was slow enough to allow the crystallization of forsteritic olivines at about 5-7 km below the sea level.

For the 1981 eruptive event, our data underline that the mineral phases (olivine cores and plagioclase cores) are in equilibrium with the magma composition, indicating that the ascent must have been without any appreciable interruption. Both flank eruptions were almost purely effusive (Branca and Del Carlo, 2005) and fed by trachybasaltic dykes characterized for being compositionally zoned, with more evolved magma in the upper and the more primitive magma in the lower section of the dyke. The compositions of the 1928 and 1981 products very alike highlight that the different syn-eruptive tectonics is not related to the petrologic features of magmas.

Task 2 - WP 8, Resp. C. Monaco

Tectonic setting of the sedimentary basement (Etna)

Participants: UNI-CT

Giovanni Barreca, Fabrizio Cultrera, Giorgio De Guidi, Sabrina Grassi, Sebastiano Imposa, Carmelo Monaco, Salvatore Scudero

Other institutions

INGV-CT Graziella Barberi, Stefano Branca, Gianni Lanzafame, Mario Mattia, Luciano Scarfi, Valentina Bruno; UNI-PA Fabrizio Pepe

Sp2 - Seismic profiles in the offshore south-east of Etna

The eastern Sicily continental margin extends from the coastline of Sicily to the Ionian Abyssal Plain. From west to east, a continental shelf, continental slope, and continental rise can be recognized. The shelf is generally narrow and locally is absent. The whole continental margin is affected by large deformation that develops from the base of the slope up to the shoreline. Evidence of active tectonics near the coastline was documented on the basis of multibeam data (Chiocci et al., 2011). It is well accepted that high-resolution seismic surveys that image in the 30 m to 1 km depth range with vertical resolution up to 0.5 m in the near sub-seafloor, are of fundamental importance, for i) active tectonic studies at basin to margin scales, ii) mapping the offshore prolongation of shallow portions of major (seismogenic) faults recognized inland, iii) estimating vertical movements at 10 Kyr scale and, sometimes, iv) measuring the shallow impedance structure and estimating the local amplification of seismic energy.

A literature review indicates that no high-resolution seismic profiles have been previously acquired in the study area using a high-resolution (multi-tips Sparker) source. It is thus not a coincidence that the final aim of the WP 8 was to verify if the tectonic processes acting in the substratum of the

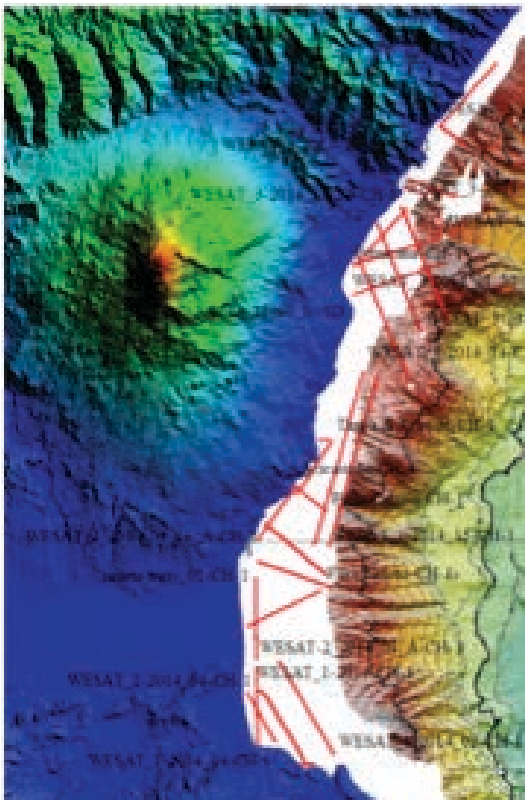


Figure 16. Location map of the high-resolution seismic profiles acquired between Capo Sant'Alessio and Castelluccio-Agnone.

Section 2
Scientific Reports of Research Units (RU 6)

volcanic edifice of Mt. Etna (i.e. normal faulting along the coastal sector, fold growth at the front of the chain) may determine the measured vertical deformation, or if it is partially related to volcano dynamics, by using new acquired high-resolution seismic profiles. For this purpose, a grid of about 400 km of reflection seismic data was recorded along the continental shelf and part of the upper slope in the offshore area between Capo Sant’Alessio and Agnone-Castelluccio, in August 2014 (Fig. 16).

The acoustic sources for seismic prospecting was a 1 kJ Sparker power supply with a multi-tips Sparker array. Data were recorded with a single-channel streamer having an active section of 2.8 m. Profiles are mostly oriented in the NE-SW to NNW-SSE directions. Navigation was controlled by a DGPS system.

Data processing was performed running a series of mathematical operators including: a) true amplitude recovery using a T^2 spherical divergence correction; b) band-pass (300-2000 Hz) “finite impulse response” filter using a filter length of 256 samples; c) de-ghosting, d) swell-filter; e) time migration; f) trace mixing of three traces for enhancing horizontal signal; g) time variant gain to boost amplitudes of deeper arrivals; h) mutes to eliminate the signal noise on the water column. Signal penetration was found to exceed 250 ms t.w.t.

Examples of the acquired and processed seismic lines are presented hereinafter. The seismic line between Capo Mulini and Acitrezza runs in a SSW-NNE direction along the continental shelf (Fig. 17). Seismo-stratigraphic analysis tools and methods were used to define seismic units and infer their lithologies.

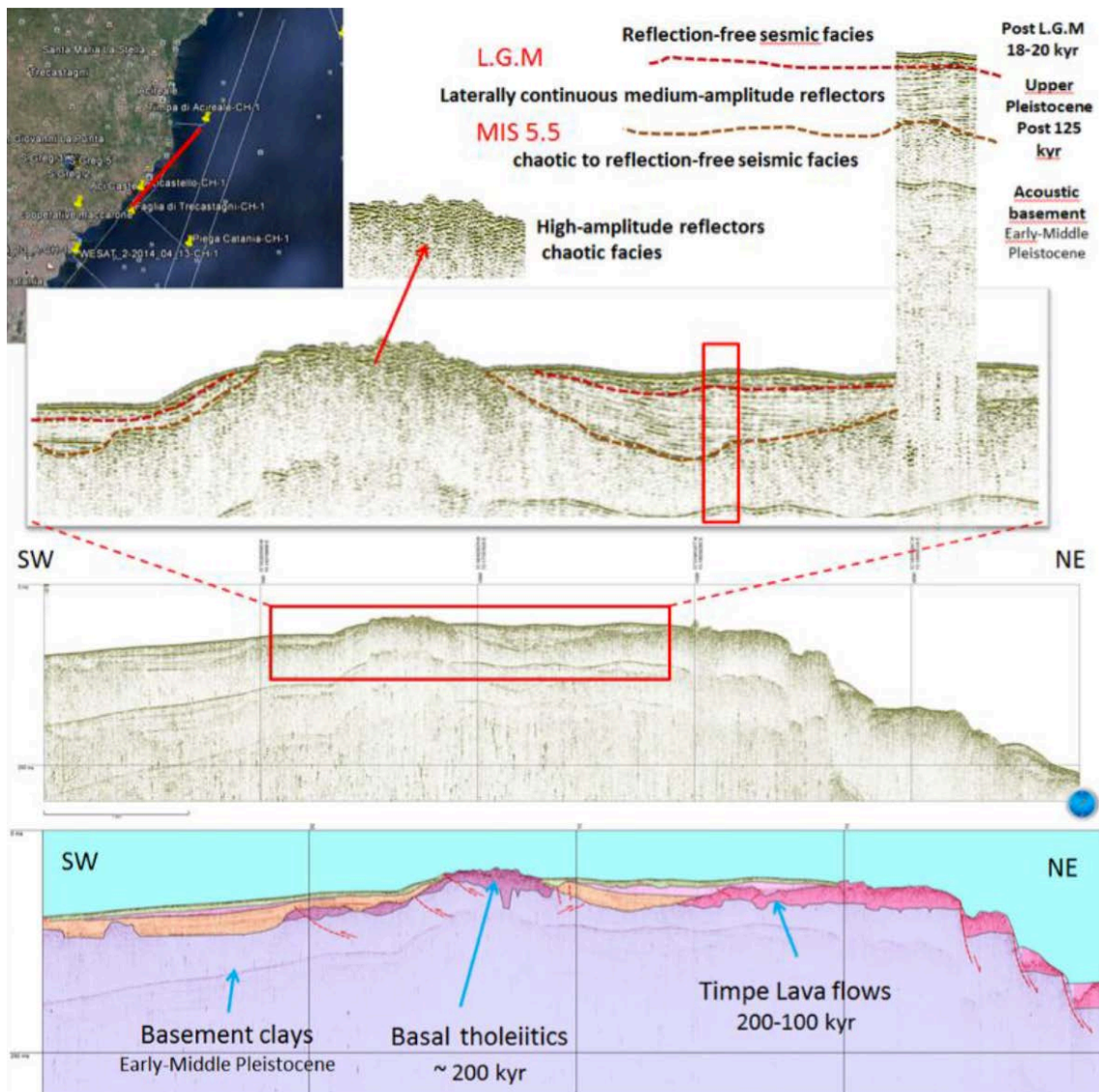


Figure 17. Seismostratigraphic interpretation performed on a NE-SW oriented sparker line acquired between Capo Mulini and Acitrezza passing very close to the Ciclopi rocky islets. Note the erosive truncations and unconformities between the several identified seismic units. The lower erosive truncation separates the acoustic basement from a well-bedded sedimentary succession upwards.

Five seismic units limited by marker reflections were recognized. The lowermost appears as reflection-free limited upwards by an erosive truncation and should correspond to the Lower-middle Pleistocene clayey Etnean substratum. A seismic unit characterized by a zone of disturbed reflections with shield geometry, limited upward by high-amplitude reflectors was found in the sector corresponding to the submerged portion of the Acitrezza rocky islets formed by Basal Tholeiithics (~500-200 kyr). A seismic unit characterized by high to medium-amplitude reflectors forms a plateau East of the Acireale cliff where the Timpe volcanic unit (200-100 kyr) outcrop. The seismic units associated with volcanic products are covered by deposits seismically characterized by laterally continuous reflectors that can be correlated to an Upper Pleistocene sedimentary sequence. This latter is limited upwards by an erosive surface that separates it from a thin and chaotic seismic unit, probably corresponding to the sedimentary succession that can be correlated to the transgressive and highstand stages of the last eustatic cycle.

Tilted and folded Upper Pleistocene deposits suggest that shortening occurred in the Acitrezza offshore. Reflectors with divergent geometry suggest syn-tectonic deposition into a piggy-back basin setting (growth folding). Asymmetric folding, which appears also to involve the younger erosive truncation, is observed and it has been related to thrust propagation, being some reflectors displaced in reverse mode. North-eastwards, a belt of normal faults (the seaward extension of the transtensional Timpe fault system) dislocates the 200-100 ky volcanic plateau producing also ruptures in the seafloor. Other two parallel seismic lines have been acquired between Catania and Stazzo in a SSW-NNE direction along the continental shelf as well (Fig. 18). Here, active normal faults have been detected, accompanied by the ascent of mud diapirs.

They bound triangular-shaped basin with growing Holocene strata. Line interpolation allowed us to reconstruct a NW-SE direction for the extensional structures that seems to connect with the S.Venerina-S. Tecla seimogenic fault system onshore (Fig. 18) The analysis of the profiles shows active contractional deformation, probably related to frontal thrusts of the chain in correspondence of Aci Castello-Acitrezza, along the offshore extension of the Catania Anticline (Fig. 19). Conversely, extensional structures bound to the NE the contractional system, along the offshore extension of the Timpe fault system. Thrusting and folding can be related to the late migration of the Sicilian chain front, whereas extensional faulting to the east (oblique onshore) is probably part of the major kinematic boundary located in eastern Sicily (Polonia et al., submitted).

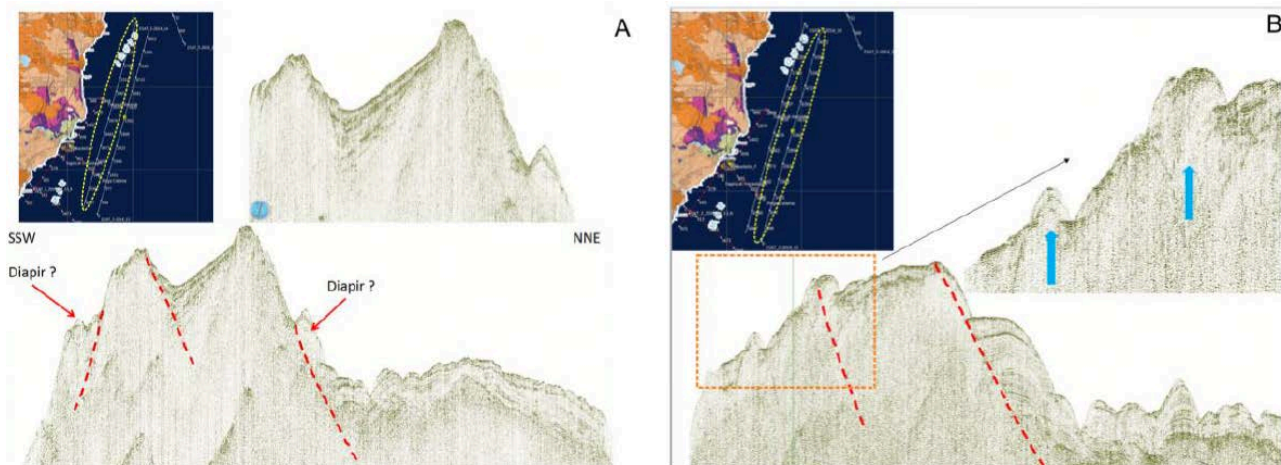


Figure 18. a) Active horst structure detected along a NNE-SSW trending line. Note that faulting is accompanied by the ascent of probably mud diapirs. Top-zoom displays a small triangular-shaped basin with growing strata. b) The same pattern of deformation has been observed on a parallel seismic line.

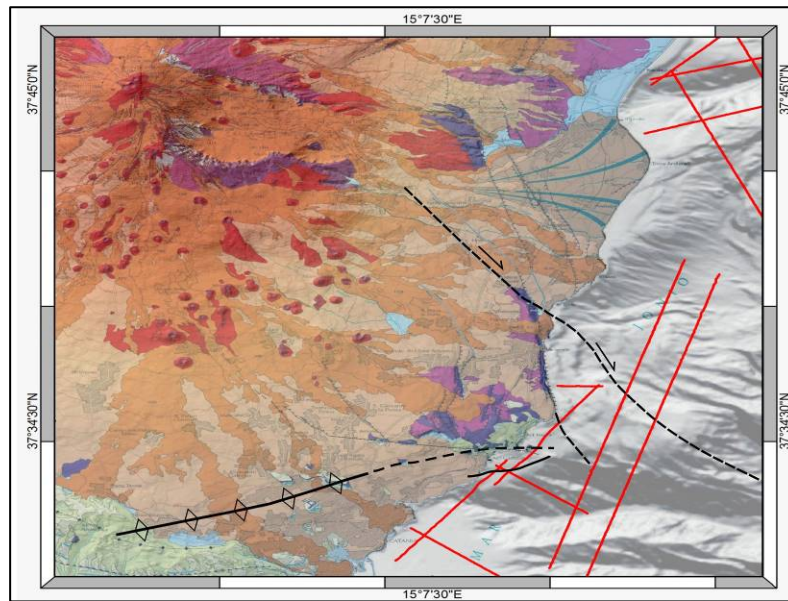


Figure 19. Map view of the identified tectonic structures (geology from Monaco et al., 2010, modified; bathymetry from Chiocci et al., 2011).

Sp3 - Relationships between on- and offshore structures and definition of deformation processes

Geological and morphological analyses, compared with seismological and geodetic data, suggest that a compressive regime currently occurs at crustal depth in the western sector of Mt. Etna, accommodated by shallow thrusting and folding at the front of the chain, south of the volcanic edifice. In particular, a large WSW-ENE trending anticline, interpreted as a detachment fold, is growing west and north of Catania city (the Catania anticline, see black line in Fig. 19). Geological data suggest that during the last 6,000 years the frontal fold has been characterized by uplift rates of ~6 mm/yr along the hinge, consistent with the interferometric data recorded in the last 20 years.

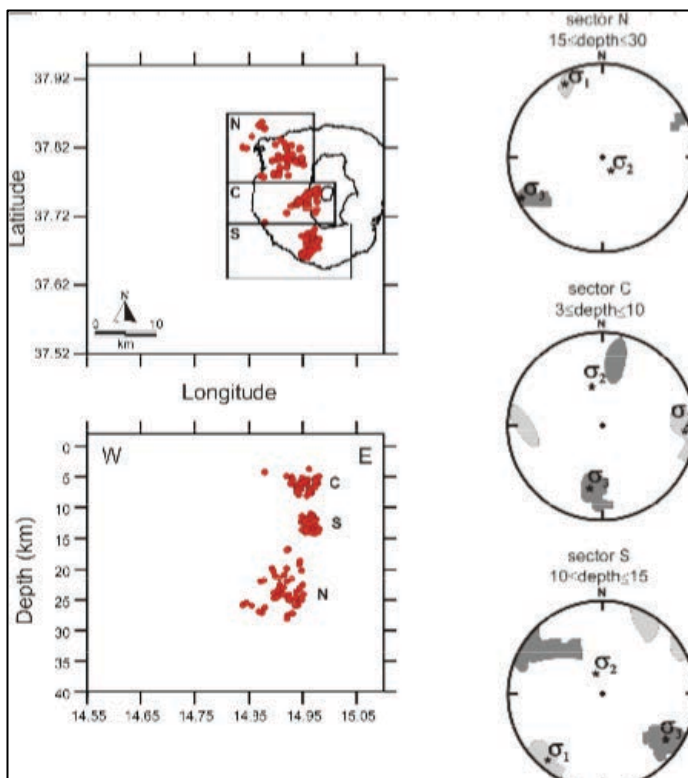


Figure 20. A roughly N-S oriented axis of compression has been obtained by seismological data. Besides the activity related to the volcanic feeding system (see sector c), the seismic pattern under the Mt. Etna edifice can be certainly related to the regional dynamics.

Moreover, a roughly N-S oriented axis of compression has been obtained by seismological data (Fig. 20), which is consistent with GPS measurements over the last 20 years that have revealed shortening along the same direction (Fig. 21). The obtained velocity field shows that two GPS stations south of the anticline (UNIG, S114) move with velocities of about 4 mm/yr along NNW to NNE directions, whereas the station located north of the structure (TIRI) moves to the SSW with velocity of about 2 mm/yr. These results are consistent with NNW-SSE vectors obtained by permanent stations (Mattia et al., 2012), related to the Africa-Europe convergence process, with the exception of the TIRI benchmark that could be affected by the dynamics of the volcano (inflation/deflation processes; e.g. Bruno et al., 2012). Accordingly, the volcano acts as a buttress to the propagation of ground deformation related to tectonic processes. Recently Cianetti et al. (2012) applied a numerical model to calculate normalized horizontal and vertical displacements for analytical models of magmatic sources and from this analysis is possible to deduce that benchmarks placed at distance of 20-25 km from the craters (e.g. TIRI), are potentially still affected by the action of the inflation/deflation cycles typical of the discharge/recharge process of an active volcano, while increasing this distance the effects are negligible (e.g. UNIG, S114).

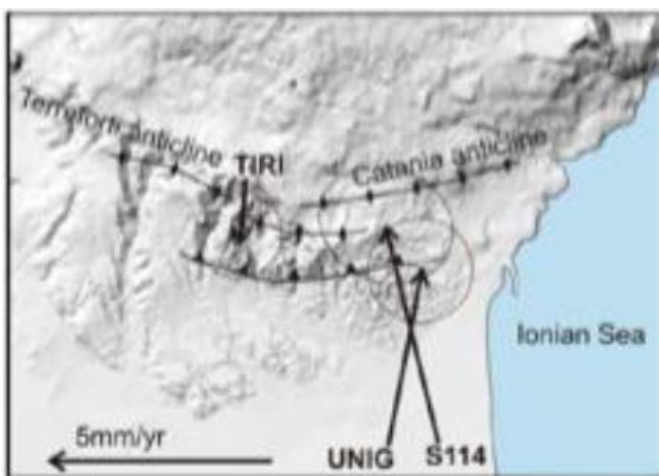


Figure 21. In 1992 the Italian IGMI (Istituto Geografico Militare Italiano - www.igmi.org) started the GPS measuring of a network made up of 1260-benchmarks, extended over the whole Italian area. The main target of this network was the cartographic framing of the Italian territory. We re-surveyed three of these IGMI benchmarks north and south of the Catania Anticline in order to calculate the velocities of some benchmarks very close to the alignment revealed by SAR data (Bonforte et al., 2011).

Geological and morphological analyses, compared with seismological and geodetic data, suggest that a compressive regime currently occurs at crustal depth in the western sector of Mt. Etna, accommodated by shallow thrusting and folding at the front of the chain, South of the volcanic edifice. Active tectonics in this part of the Sicilian fold-and-thrust belt are mainly controlled by the ~NNW-SSE compression caused by the Nubia - Eurasia convergence. The orientation of the P-axes at a depth > 10 km, where seismogenic processes related to the volcano activity can be considered less relevant, and geological evidence at surface are both consistent with these regional dynamics. It's worth noting that at shallow crustal level the inflation/deflation processes could act as a buttress to the underthrusting of the Hyblean slab, amplifying the shortening rate (Fig. 22). The seismicity distribution and the slip rate velocities indicate a coexistence and interaction of thick and thin-skinned deformation across this domain. The basement is involved in crustal thrusting along relatively high-angle shear zone (the SBT; Lavecchia et al., 2007), while the frontal and shallow part of the belt is affected by low-angle blind thrust and detachment folds.

In conclusion, besides the activity related to the volcanic feeding system, the seismic pattern under the Mt. Etna edifice can be certainly related to the regional dynamics. The compressive stress is converted into elastic accumulation and then in earthquakes along the ramps to the rear of the chain, whereas on the frontal area it is accommodated by aseismic deformation along an incipient detachment within the clayish foredeep deposits. In fact, despite the high rates of convergence, the seismicity is moderate at the front of the chain and the "seismic efficiency" of the SBT is greater in correspondence of ramps at the rear, where strong earthquakes can occur.

Section 2

Scientific Reports of Research Units (RU 6)

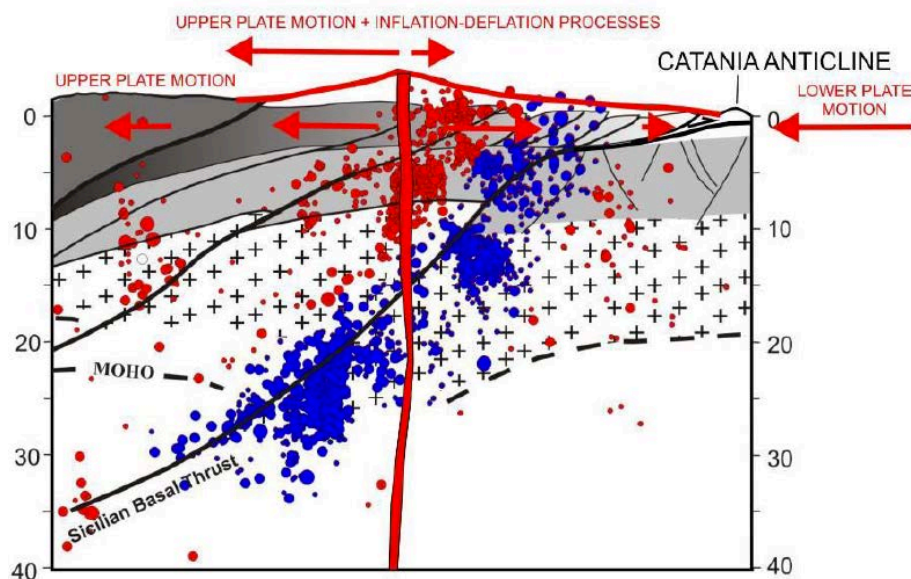


Figure 22. Model showing as at shallow crustal level the inflation/deflation processes of Mt. Etna volcano could act as a buttress to the underthrusting of the Hyblean slab, amplifying the shortening rate at the front of the chain (the Catania anticline).

Task 3 - WP 12, Resp. M.S. Barbano

Historical analysis on the space-time relationships between regional earthquakes in the Gulf of Patti-northern Sicily and seismic-volcanic phenomena at Vulcano

Participants: UNI-CT

Maria Serafina Barbano, Claudia Pirrotta

Other institutions

INGV-BO Viviana Castelli

Sp1 - Short monographs of volcanic events and the main earthquakes

In order to compile the catalogues of Vulcano eruptions and earthquakes in the Gulf of Patti-northern Sicily, we analyzed seismological and volcanological repertories containing lists and brief descriptions of eruptions, earthquakes and their effects, consistently available since the second half of the 15th century (e.g. Mongitore, 1743; Ferrara, 1810; Mercalli, 1883, 1891; Baratta 1901; the complete list is in the file “repertory_june_2015” in Annex 1). The second phase of the analysis focused on a survey of historical serial sources such as gazettes and diaries. Finally, we scrutinized memories of travelers visiting Sicily and Aeolian Islands, such as Antoine de La Sale (1406); Hieronimo Maurando (1544); Jacques-Philippe D’Orville (1764); Déodat de Dolomieu (1783); Lazzaro Spallanzani (1792-1795) (the complete list is in the file “references_june_2015” in Annex 1). The research was conducted with fast criteria trying to combine the in-depth investigation with the economy of time, resources and energy. The planned activity was completed. However, for some events, given the large amount of material to be analyzed and the impossibility to find all sources located in various libraries in Italy, we have not been found some primary sources, that are reported in other documents.

For each events - eruptions, earthquakes or seismic sequence - we compiled a short monography, which includes the description of the earthquake effects (or seismic sequence) and/or eruptions, a list of localities with the associated macroseismic intensities, the transcription of texts and related references. At present, the catalogues of eruptions and earthquakes are comprehensive with respect to the expeditious analysis, but certainly, the possibility to continue research on archival sources can improve the quality of information.

Sp2 - Final release of the database on earthquakes and volcanic activity

The main results are:

- a list of historical eruptions, whose occurrence was mostly already known to Mercalli (1883; 1891), but for which we improved the available base of data, solving the doubts on the occurrence of some of them and achieving a better definition for others;
- a list of historical earthquakes, most of which were already included in the parametric earthquake catalogues compiled since the 1970s but that - in many cases - had no reference study. We produced reference studies for all the earthquakes that did not have one and updated the older ones.

We identified a total of forty eruptions or secondary effects at Vulcano. We report described fumarolic activity more or less strong, to trace periods when the volcano was not in eruptive activity. Most descriptions concern the explosive activity typical of Vulcano (*vulcaniana*, according to the term coined by Mercalli to describe the activity of this volcano). We also collected some evidence of volcanic activity at Stromboli, which can be considered a by-product of the study, as a systematic search on this subject was not in the goals.

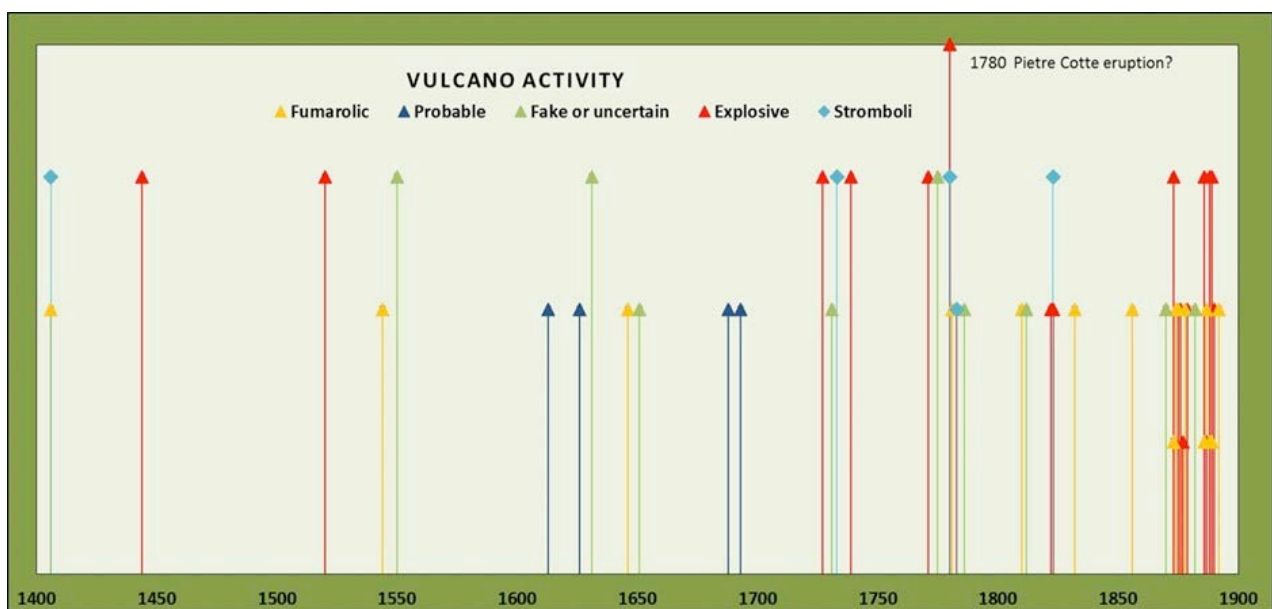


Figure 23. Chronology of eruptive events at Vulcano. The last eruption was in 1888-90. Red: Explosive activity; blue: probable activity; green: fake or uncertain; yellow: fumarolic activity; sky-blue: Stromboli activity.

The eruptions are clustered in periods of 10-20 years (Fig. 23), separated by intervals of 30-40 years of dormancy, excluding the period from 1400 to 1600 during which the interval between the eruptive activity and the principally fumarolic activity was 70-90 years (lack of data or cyclic behaviour? In the last century, we observe an equally long period of quiescence). For the last eruption in 1888-1890, it is reported major damage to buildings and farming. For previous eruptions, damage is due to the strong emissions of ash that covered Vulcano and Lipari, in some cases reaching the coasts of Sicily and Calabria.

The number of earthquakes after the study is significantly increased, with several earthquakes and new seismic sequences identified mainly in the period 1717-1783. Seismicity seems to migrate over time from the Sicilian coast to the smaller and far islands (Fig. 24), whereas it is simply an improvement in the completeness of the catalogue. As regards for earthquakes in northern Sicily, it is very likely that the archival sources (the Archbishops of Patti and Lipari) already identified, but analyzed and/or transcribed only partially, may provide more information. However, for the Aeolian Islands it seems quite difficult to find more evidence since only Lipari was inhabited until the end of 1700s.

Section 2

Scientific Reports of Research Units (RU 6)

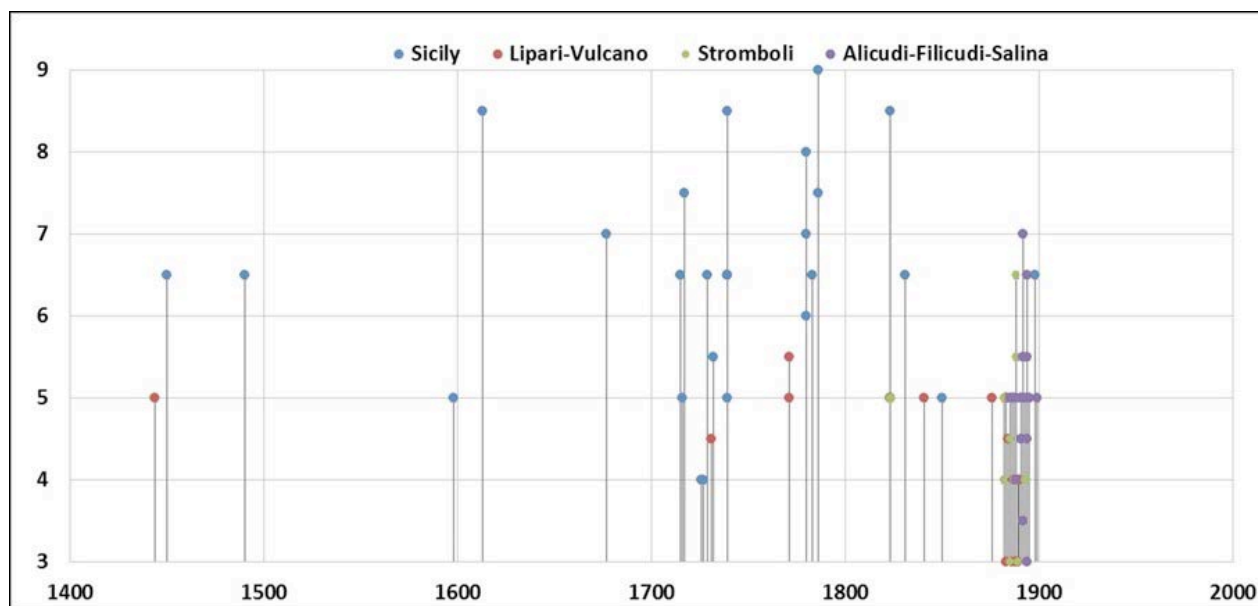


Figure 24. Earthquakes (new catalogue) in the Aeolian Islands and nearby Northern Sicily, distinguished according to their epicentral area: blue dots, earthquakes with damage or felt in the Sicilian Tyrrhenian area; red dots, earthquakes felt in Lipari and Vulcano; green dots, Stromboli earthquakes; purple dots, earthquakes with damage or felt in other Aeolian Islands (Alicudi, Filicudi, Salina).

Historical research shows that in the 14th-19th centuries the eruptive phenomena of Vulcano are adequately documented, while earthquakes that occurred in the same area are less clearly reported. This can be partly explained by the fact that earthquakes of volcanic origin can be felt in small areas, while eruptions are clearly visible from afar, and may cause trouble and damage due to the fallout of ash even at a considerable distance (as it happened for example during the 1771 and 1888 eruptions). Moreover, in the studied period urbanization was very sparse both in the Aeolian Islands and on the Sicilian coast facing the archipelago.

Seismicity, which affected the area facing the Aeolian Islands, is better documented and information is available from the end of the 15th century. Most earthquakes are reported in the catalogues, such as the Naso earthquakes of 1613, 1739, 1786, 1823, which are among the strongest of the area, and the Patti seismic sequences of 1780 and 1786. Another area often affected is that of Castoreale. Interesting are some earthquakes felt in Milazzo in connection with activities in Vulcano as in 1727. The majority of earthquakes in Northern Sicily does not seem connected with seismic activity of Vulcano. After the unrest of the May 1739 eruption, there were strong earthquakes in Naso. Eruptive activity in Vulcano is reported after the strong earthquakes in Calabria and in one case even after the earthquake of 1688 in Campania (Mercalli, 1883). Finally, it's worth mentioning several earthquake that affected the islands of Salina, Alicudi and Filicudi in the years following the last eruption in 1890.

We retrieved a fairly extensive bibliography from volcanological and seismological sources, and also historical maps and images depicting Sicily and Vulcano. The latter shows fumarolic activity or explosive activity at La Fossa, while it seems that Vulcanello did not present any manifestations of activity at least since 1544. The historical data does not give a clear picture to interpret the relationship between earthquakes and eruptions. However, it has allowed us to understand that at Vulcano the eruptive activity, mainly explosive, is not accompanied by strong volcano-tectonic earthquakes, unlike Stromboli where these are documented. The activity at Vulcano is preceded by an increasing of fumarolic temperature and by roars. The collected information is very interesting for its descriptions of explosive activity, in particular for researchers who deal with risk and evacuation plans in the event of a future eruption.

For the 1888-1890 eruptive period, we found several sources that have been scanned so they are available in pdf format. Key information can be found in the monography. There is also a list of sources and photographic documentation.

The following materials are available in electronic form (Tab. 6): 1) table of repertoires; 2) chronological table of surveyed eruptive activity (since 1400) in the repertoires and the sources found; 3)

monographs of major volcanic events and related earthquakes; 4) chronological table of major earthquakes and main earthquakes and sequences; and monographies of main earthquakes; 5) list of sources consulted and photographic documentation; 6) sources of the 1888-90 eruption in pdf format.

1	Table of analyzed repertories	Repertory_june_2015
2	Table of eruptive activity	Eruptive-event_june2015
3	Monographs of eruptions and associated earthquakes	scheda 1406, 1444, 1626, 1688, 1727, 1731, 1732, 1739, 1771, 1780, 1783, 1873, 1886-1888-90
4	Table of earthquakes and monographies of main earthquakes	equ_aeol-northsicily_june_2015; earthquake 1450, 1490, 1598, 1613, 1717, 1729, 1771, 1780, 1786, 1823, 1831, 1841, 1888, 1892
5	Sources and iconographic documentation	ref_june_2015
6	Sources of the 1888-1890 eruption	Eruzioni Vulcano_Mercalli 1889, Mercalli_1888_L'isola di Vulcano e lo Stromboli dal 1886 al 1888; Isola di Vulcano_Silvestri 1889; Stromboli e Vulcano_Platania 1889 Mercalli_1891

Table 6. Materials in electronic form.

Deliverables

- WP 2.Sp1 Identification of site correction functions for the prediction of PGA: **100%**.
 WP 7.Sp1 Analyses of textures and compositions of crystalline phases (1928, 1981 eruptions): **100%**.
 WP 7.Sp2 Pre- and sin-eruptive magma differentiation models and relationship with volcanological evolution and syn-eruptive tectonics (1928, 1981 eruptions): **100%**.
 WP 8.Sp2 Seismic profiles in the offshore south-east of Etna: **100%**.
 WP 8.Sp3 Relationships between on- and offshore structures and definition of deformation processes: **100%**.
 WP 12.Sp1 Short monographs of volcanic events and the main earthquakes (Vulcano-Gulf of Patti): **100%**.
 WP 12.Sp2 Final release of the database on earthquakes and volcanic activity (Vulcano-Gulf of Patti): **100%**.

Problems and difficulties

- WP 7 Redefinition of the target on the 1928 and 1981 eruptions.

Key publications

- Barbano M.S., V. Castelli, C. Pirrotta (2014). *Eruzioni storiche e terremoti dell'isola di Vulcano*. 33° GNGTS Meeting, Bologna, 25- 27 November 2014.
 Barbano M.S., V. Castelli, C. Pirrotta (2015). *Materiali per un catalogo di eruzioni di Vulcano e dei terremoti dell'area siciliana antistante dal 1400 al 1899*. Quaderni di Geofisica, in prep.
 Barreca G., Monaco C., Pepe F. (2015). *High-resolution seismic exploration in the Mt. Etna offshore: preliminary results and implications with regional tectonics*. Abstract Congresso congiunto SIMP-AIV-SoGeI-SGI, Il Pianeta Dinamico: sviluppi e prospettive a 100 anni da Wegener, Firenze 2-4 Settembre 2015.
 Branca S., De Guidi G., Lanzafame G., Monaco C. (2013). *Holocene vertical deformation along the coastal sector of Mt. Etna volcano (eastern Sicily)*. In Epitome FIST GeolItalia 2013 - IX forum italiano di Scienze della Terra, Pisa 16-18 settembre 2013, 133.
 Branca S., De Guidi G., Lanzafame G., Monaco C. (2014). *Holocene vertical deformation along the coastal sector of Mt. Etna volcano (eastern Sicily, Italy): implications on the time-space constrains of the*

Section 2

Scientific Reports of Research Units (RU 6)

- volcano lateral sliding*. J. of Geodynamics, 82, 194-203, Doi: [org/10.1016/j.jog.2014.07.006](https://doi.org/10.1016/j.jog.2014.07.006).
- Branca S., De Guidi G., Lanzafame G., Monaco C. (2014). *Holocene Vertical Deformation along the Coastal Sector of Mt. Etna Volcano (eastern Sicily, Italy): Implications on the Time-Space Constrains of the Volcano Lateral Sliding*. Riassunti estesi Conferenza A. Rittmann, Nicolosi (Catania) 29-31 Ottobre 2014, Miscellanea INGV (ISSN 2039-6651), 25, p. 23.
- De Guidi G., Barberi G., Barreca G., Bruno V., Cultrera F., Grassi S., Imposa S., Mattia M., Monaco C., Scarfi L., Scudero S. (2015). *Geological, seismological and geodetic evidence of active thrusting and folding south of Mt. Etna (eastern Sicily): revaluation of "seismic efficiency" of the Sicilian Basal Thrust*. J. of Geodynamics, in print.
- De Guidi G., Barberi G., Barreca G., Bruno V., Cultrera F., Grassi S., Imposa S., Mattia M., Monaco C., Scarfi L., Scudero S. (2013). *Active thrusting and folding south of Mt. Etna (eastern Sicily)*. Note Brevi e Riassunti Riunione Annuale Gruppo Italiano Geologia Strutturale, Milano, 28-29 Ottobre 2013, Rend. Online Soc. Geol. It., 29, 35-38.
- De Guidi G., Barberi G., Barreca G., Bruno V., Cultrera F., Grassi S., Imposa S., Mattia M., Monaco C., Scarfi L., Scudero S. (2013). *Geological, seismological and geodetic evidence of active thrusting and folding south of Mt. Etna (eastern Sicily)*. Atti del 32° Convegno Nazionale G.N.G.T.S., Trieste 19-21 Novembre 2013, Tema 1: Geodinamica, 48-53.
- De Guidi G., Barberi G., Barreca G., Bruno V., Cultrera F., Grassi S., Imposa S., Mattia M., Monaco C., Scarfi L., Scudero S. (2014). *New Geological, seismological and geodetic evidence of active thrusting and folding south of Mt. Etna (eastern Sicily): revaluation of "seismic efficiency" of the Sicilian Basal Thrust*. Rend. Online Soc. Geol. It., Suppl. n. 1 al Vol. 31 (2014) Congresso SGI-SIMP Milano 10-12 Settembre 2014, p. 17.
- Ristuccia G.M., Di Stefano A., Gueli A.M., Monaco C., Stella G., Troja S.O. (2013). *OSL chronology of Quaternary terraced deposits outcropping between Mt. Etna volcano and the Catania Plain (Sicily, southern Italy)*. Physics and Chemistry of the Earth, 63, 36-46, <http://dx.doi.org/10.1016/j.pce.2013.03.002>.
- Spampinato C.R., Braitenberg C., Monaco C., Scicchitano G. (2013). *Analysis of vertical movements in eastern Sicily and southern Calabria (Italy) through geodetic levelling data*. Journal of Geodynamics, 66, 1-12, <http://dx.doi.org/10.1016/j.jog.2012.12.002>.
- Spampinato C.R., Braitenberg C., Monaco C., Scicchitano G. (2013). *Analysis of vertical movements in eastern Sicily and southern Calabria (Italy) through geodetic leveling data*. In Epitome FIST GeoItalia 2013 - IX forum italiano di Scienze della Terra, Pisa 16-18 settembre 2013, 137.

Other references

WP 2

- Akaike H. (1974). *A new look at the statistical model identification*. IEEE Transactions on Automatic Control, 19, 716-723.
- Azzaro R., Carocci C.F., Maugeri M., Torrisi A. (2010). *Microzonazione sismica del versante orientale dell'Etna studi di primo livello*. Ed. Le nove Muse, Catania, pp. 181.
- Boore D.M. (2003). *Prediction of ground motion using the stochastic method*. Pure Appl. Geophys., 160, 635-676.
- Bonilla L.F., Steidl J.H., Lindley G.T., Tumarkin A.G., Archuleta R.J. (1997). *Site amplification in the San Fernando valley, California: variability of site-effect estimation using the S-wave, coda, and H/V methods*. Bull. Seism. Soc. Am., 87(3), 710-730.
- Borcherdt R.D. (1970). *Effects of local geology on ground motion near San Francisco Bay*. Bulletin of the Seismological Society of America, 60, 29-61.
- Burnham K.P., Anderson D.R. (2002). *Model selection and multimodel inference: a practical information-theoretic approach*. 2nd edn. Springer, New York.
- Branca S., Coltelli M., Gropelli G. (2011). *Geological evolution of a complex basaltic stratovolcano: Mount Etna, Italy*. Ital. J. Geosci., 130 (3), 306-317, DOI: 10.3301/IJG.2011.13.
- Branca S., Ferrara V. (2013). *The morphostructural setting of Mount Etna sedimentary basement (Italy): implications for the geometry and volume of the volcano edifice and its flank instability*. Tectonophysics, doi: 10.1016/j.tecto.2012.11.011.
- Castellaro S., Mulargia F. (2009). *Vs30 estimates using constrained H/V measurements*. Bull. Seism. Soc. Am., doi: 10.1785/0120080179.

- Chávez-García F.J., Sanchez L.R., Hatzfeld D. (1996). *Topographic site effects and HVSR. A comparison between observations and theory*. Bull. Seism. Soc. Am., 86, 1559-1573.
- Di Alessandro C., Bonilla L.B., Boore D.M., Rovelli A., Scotti O. (2012). *Predominant Period Site Classification for Response Spectra Prediction Equations in Italy*. Bulletin of the Seismological Society of America, 102(2), 680-695.
- Di Giacomo D., Gallipoli M.R., Mucciarelli M., Parolai S., Richwalski S.M. (2005). *Analysis and Modeling of HVSR in the Presence of a Velocity Inversion: The Case of Venosa, Italy*. Bull. Seism. Soc. Am., 95(6), 2364-2372.
- Di Giulio G., Rovelli A., Cara F., Azzara R.M., Marra F., Basili R., Caserta A. (2003). *Long-duration asynchronous ground motions in the Colfiorito plain, central Italy, observed on a two-dimensional dense array*. J. Geophys. Res., 108(B10): 2486, doi:10.1029/2002JB002367.
- Eurocode8 (2003). *Design of structures for earthquake resistance-Part 1: general rules, seismic actions and rules for buildings*. EN 1998. European Committee for Standardization, Brussels.
- Field E.H., Jacob K. (1995). *A comparison and test of various site response estimation techniques*. Bull. Seism. Soc. Am., 85(4), 1127-1143.
- Herak M. (2008). *ModelHVSR-A Matlab® tool to model horizontal-to-vertical spectral ratio of ambient noise*. Computers Geosciences, 34, 1514-1526.
- Lachet C., Bard P.-Y. (1994). *Numerical and Theoretical Investigations on the Possibilities and Limitations of Nakamura's Technique*. J. Phys. Earth, 42, 377-397.
- Lermo J., Chavez-Garcia F.J. (1993). *Site effect evaluation using spectral ratios with only one station*. Bulletin Seismological Society of America, 83, 1574-1594.
- Lermo J., Chavez-Garcia F.J. (1994). *Are microtremors useful in the site response evaluation?* Bulletin Seismological Society of America, 84, 1350-1364.
- Luzi L., Puglia R., Pacor F., Gallipoli M.R., Bindi D., Mucciarelli M. (2011). *Proposal for a soil classification based on parameters alternative or complementary to VS30*. Bull. Earthquake Eng. doi 10.1007/s10518-011-9274-2.
- MacQueen J.B. (1967). *Some methods for classification and analysis of multivariate observations. Proceedings of the Fifth Symposium on Math, Statistics, and Probability*. Berkeley, CA: University of California Press, pp. 281-297.
- Maresca R., Castellano M., De Matteis R., Saccorotti G., Vaccariello P. (2003). *Local Site Effects in the Town of Benevento (Italy) from Noise Measurements*. Pure appl. geophys., 160, 1745-1764.
- Mucciarelli M. (1998). *Reliability and applicability of Nakamura's technique using microtremors: an experimental approach*. J. Earth. Eng., 2, 625-638.
- Nakamura Y., (1989). *A method for dynamic characteristics estimation of subsurface using microtremor on the ground surface*. Quarterly Rept. Railway Tech. Res. Inst., 30, 25-33.
- Nogoshi M., Igarashi T. (1970). *On the propagation characteristics of microtremors*. J. Seism. Soc. Japan, 23, 264-280.
- Panzerà F., D'Amico S., Lotteri A., Galea P., Lombardo G. (2012). *Seismic site response of unstable steep slope using noise measurements: the case study of Xemxija bay area, Malta*. Natural Hazard and Earth Science System, 12, 3421-3431.
- Panzerà F., D'Amico S., Galea P., Lombardo G., Gallipoli M.R., Pace S. (2013). *Geophysical measurements for site response investigation: preliminary results on the island of Malta*. Bollettino di Geofisica Teorica ed Applicata, 54 (2), 111-128
- Panzerà F., Lombardo G., Monaco C., Di Stefano A. (2015). *Seismic site effects observed on sediments and basaltic lavas outcropping in a test site of Catania, Italy*. Natural Hazards, doi: 10.1007/s11069-015-1822-7.
- Panzerà F., Pischiutta M., Lombardo G., Monaco C., Rovelli A. (2014). *Wavefield polarization in fault zones of the western flank of Mt. Etna: Observations and fracture orientation modeling*. Pure and Applied Geophysics, 171 (11), 3083-3097
- Panzerà F., Rigano R., Lombardo G., Cara F., Di Giulio G., Rovelli A. (2011). *The role of alternating outcrops of sediments and basaltic lavas on seismic urban scenario: the study case of Catania, Italy*. Bulletin of Earthquake Engineering, 9 (2), 411-439.
- Parolai S., Bindi D., Troiani L. (2001). *Site response for the RSM seismic network and source parameters in the central Apennines (Italy)*. Pure Appl. Geophys., 158, 695-715.
- Priolo E. (1999). *2-D spectral element simulation of destructive ground shaking in Catania (Italy)*. J. Seismol., 3, 289-309.

Section 2

Scientific Reports of Research Units (RU 6)

- Riepl J., Bard P.-Y., Hatzfeld D., Papaioannou C., Nechtschein S. (1998). *Detailed evaluation of site response estimation methods across and along the sedimentary valley of Volvi (EUROSEISTEST)*. Bull. Seism. Soc. Am., 88(2), 488-502.
- Rigano R., Cara F., Lombardo G., Rovelli A. (2008). *Evidence for ground motion polarization on fault zones of Mount Etna volcano*. J. Geophys. Res., 113, B10306, doi: 10.1029/2007JB005574.
- Rodriguez V. H., Midorikawa S. (2002). *Applicability of the H/V spectral ratio of microtremors in assessing site effects on seismic motion*. Earthqu. Eng. Struct. Dyn., 31(2), 261-279.
- Schnabel, P.B., Lysmer J. and Seed H.B. (1972). *Shake a computer program for earthquake response analysis of horizontally layered sites*. Report No. EERC 72 - 12, Earthquake Engineering Research Center, University of California, Berkeley, California.
- Seekins L.C., Wennerberg L., Margheriti L., Liu H.P. (1996). *Site amplification at five locations in San Francisco, California: a comparison of S waves, codas, and microtremors*. Bull. Seism. Soc. Am., 86(3), 627-635.
- SESAME (2004). *Guidelines for the implementation of the H/V spectral ratio technique on ambient vibrations: Measurements, processing and interpretation*. SESAME European Research Project WP12, deliverable D23.12, at <http://sesame-fp5.obs.ujfgrenoble.fr/Deliverables>, 2004.
- Zhao J.X., Irikura K., Zhang J., Fukushima Y., Somerville P.G., Asano A., Ohno Y., Oouchi T., Takahashi T., Ogawa H. (2006). *An empirical site-classification method for strong-motion stations in Japan using H/V response spectral ratio*. Bull. Seismol. Soc. Am., 96, 914-925.

WP 7

- Branca S. & Del Carlo P. (2005). *Types of eruptions of Etna volcano ad 1670-2003: implications for short-term eruptive behaviour*. Bulletin of Volcanology, 67(8), 732-742.
- Coltelli M., Marsella M., Proietti C. & Scifoni S. (2012). *The case of the 1981 eruption of mount Etna: an example of very fast moving lava flows*. Geochemistry, geophysics, geosystems, 13(1).
- Ferlito C., Coltorti M., Cristofolini R. & Giacomoni P.P. (2009). *The contemporaneous emission of low-k and high-k trachybasalts and the role of the NE rift during the 2002 eruptive event, mt. Etna, italy*. Bulletin of Volcanology, 71(5), 575-587.
- Ponte G., (1929a). *L'eruzione etnea del novembre 1928*. Atti Acc. Gioenia Sci. Nat. Catania, v 16 mem XII bis: 1-6.
- Ponte G., (1929b). *L'eruzione etnea del novembre 1928 e l'Istituto Vulcanologico etneo*. Boll. Comitato nazionale geodet. Geofis., XVII: 1-7.
- Roeder P.L. & Emslie R. (1970). *Olivine-liquid equilibrium*. Contributions to mineralogy and petrology, 29(4), 275-289.
- Scott S.C. (1983). *Variations in lava composition during the march 1981 eruption of mount Etna and the implications of a compositional comparison with earlier historic eruptions*. Bulletin of Volcanology, 46(4), 393-412.
- Wallace, P.J. & Carmichael, I.S. (1994). *Petrology of volcán Tequila, Jalisco, Mexico: disequilibrium phenocryst assemblages and evolution of the subvolcanic magma system*. Contributions to mineralogy and petrology, 117(4), 345-361.

WP 8

- Bonforte A., Guglielmino F., Coltelli M., Ferretti A., Puglisi G. (2011). *Structural assessment of mount etna volcano from permanent scatterers analysis*. Geochem. Geoph. Geosyst., 12 (2). Doi: 10.1029/2010gc003213.
- Bruno V., Mattia M., Aloisi M., Palano M., Cannavò, F. and Holt W.E. (2012). *Ground deformations and volcanic processes as imaged by cgps data at mt. Etna (italy) between 2003 and 2008*. J. Geophys. Res., 117, b07208, doi:10.1029/2011jb009114.
- Chiocci L.F., Coltelli M., Bosman A., Cavallaro D. (2011). *Continental margin large-scale instability controlling the flank sliding of etna volcano*. Earth planet. Sci. Lett., 305, 57-64.
- Cianetti S., Giunchi C., Casarotti E. (2012). *Volcanic deformation and flank instability due to magmatic sources and frictional rheology: the case of mount etna*. Geophys. J. Int., 191 (3), 939-953, doi:10.1111/j.1365-246x.2012.05689.x.
- Lavecchia G., Ferrarini F., De Nardis R., Visini F., Barbano M.S. (2007). *Active thrusting as a possible seismogenic source in sicily (southern italy): some insights from integrated structural-kinematic and seismological data*. Tectonophysics, 445, 145-167.

Mattia M., Bruno V., Cannavò F., Palano M. (2012). *Evidences of a contractional pattern along the northern rim of the Hyblean plateau (sicily, italy) from gps data*. Geol. Acta, 10, 1-9.

Monaco C., De Guidi G., Ferlito C. (2010). *The morphotectonic map of mt. Etna*. Ital. J. Geosci., 129, 408-428.

WP 12

Baratta M. (1901). *I terremoti d'italia*. Torino, 950 pp., rist. Anastatica, Bologna 1972.

De Dolomieu D. (1783). *Voyage aux iles de lipari fait en 1781 ou notices sur les iles æoliennes pour servir a l'histoire des volcans*. Paris, 208 pp.

De La Salle a. (1406). *Sa vie et ses ouvrages apres des documents inedits, champion, paris, falk fils Bruxelles, (appendice, excursion aux iles Lipari, extrait de la salade, d'apres l'edition de Philippe Le Noir*. Paris, 1527, corrige d'apres le ms. 18210 de la Bibliotheque Royale de Belgique, pp. 159-172), Neve j. (ed.), 1903.

D'Orville J.P. (1764). *Sicula, quibus siciliae veteris rudera, additis antiquitatum tabulis illustrantur*. Amsterdam, g. Tielenburg, 2 voll.

Ferrara F. (1810). *I campi flegrei della Sicilia e delle isole che le sono intorno e descrizione fisica e mineralogica di queste isole*. Messina, stamp. dell'Armata Britannica, 424 pp.

Mercalli G. (1883). *Vulcani e fenomeni vulcanici in Italia*. Milano, ristampa anastatica, forni ed. 374 pp.

Maurando H. (1544). *Itinerario di Hieronimo Maurando da Antibes a Costantinopoli (1544)*, ed. L. Dorez (1904).

Mercalli, G. (1891). *Cenni topografici-geologici dell'isola di Vulcano e storia delle sue eruzioni*. Ann. Uff. Centr. Meteor. Geodin., 10, pp. 7-50.

Mongitore A. (1743). *Istoria cronologica de' terremoti di Sicilia*. In: id., della Sicilia ricercata nelle cose più memorabili, Palermo, 2 vv., 345-445.

Spallanzani L. (1792-1795). *Viaggi alle due Sicilie e in alcune parti dell'appennino*. 1a ed. Pavia, b. Comini, 5 voll. [consultata edizione di milano, società tipogr. De' classici italiani, 1825-1826, vol. 1.

RU 7, D.I.C.E.A., Università La Sapienza, RomaResponsible: **Maria Marsella****Activity of RU in phase 2**

RU 7 is involved in task 4 of the project:

WP 14 Sp1 - Analysis of instability phenomena (shallow or deep-seated) affecting La Fossa cone in response to volcanic activity or other triggering processes. Collection and processing of detailed topographical data through proximal-sensing techniques based on digital camera and laser scanning sensors, historical photogrammetric datasets, DInSAR results. In collaboration with RUs 1 and 2, extraction of maps describing the hydrothermal active areas, fracture fields, subaerial slope morphology network.

Task 4 - WP 14, Resp. M. Marsella***Slope instability hazard maps*****Participants: UNI-RM**

Peppe Junior Valentino D'Aranno, Maria Marsella, Silvia Scifoni, Alberico Sonnessa

Other institutions

INGV-RM Gianfilippo De Astis; **UNI-Padova** Massimo Fabris; **UNI-RM3** Guido Giordano, Paola Molin, Romanella Vio; **UNI-Granada (Spain)** Jose Baena Palenzuela; **CNR-IREA** Susi Pepe, Eugenio Sansosti, Giuseppe Solaro, Piero Tizzani

Sp1 - Vector and thematic maps in GIS formats (La Fossa cone and selected sites at Lipari) (WP14_Sp1a); report on the characteristics of past and active instability phenomena and associated hazard (Vulcano and Lipari) (WP14_Sp1b) and on stability analysis of the potential failures detected at La Fossa cone (WP14_Sp1c)

Summary

The activity was focused on the analysis of instability phenomena affecting La Fossa cone (Vulcano) and Lipari Island. An integrated approach was applied for identification of area subjected to landslide events. The main steps can be resumed in:

1. quantitative analysis to detect and map slope failures occurred in the past using a multi-temporal spatial approach; this step was carried out by expanding the data available from previous projects with numerical maps (Digital Elevation Models, DEMs and orthophotos) derived from the photogrammetric analysis of IGMI historical aerial photos (1954-1995) (WP14_Sp1b);
2. evaluation of the active processes based on the outcomes of the DinSAR analysis updated to 2013 (WP14_Sp1b);
3. landslide-susceptibility analysis by implementing an automatic GIS procedure that was validated using the outcomes of traditional geomorphological analysis (WP14_Sp1a, WP14_Sp1b);
4. stability analysis of the potential failures identified at La Fossa cone (Vulcano) (WP14_Sp1c).

Multi-temporal photogrammetric and DinSAR analyses

The historical photogrammetric dataset was processed in order to obtain DEM (Digital Elevation Model) and orthophotos. The new data were added to the GIS geodatabase that collects all the geographic datasets analysed during the first year of activity.

Field work

A GPS survey was necessary in order to create a Ground Control Points (GCPs) database for external orientation of historical photogrammetric data. The GCPs were selected around the La Fossa cone and Forgia Vecchia on which the analysis was focused (Fig. 1).



Figure 1. GCPs collected with GPS survey.

In Fig. 2 the elevation residuals for three different time intervals on the NE flank of Gran Cratere (Vulcano) are shown. This data were compared with DinSAR dataset (2009-2013) and the maps describing the hydrothermal activity to identify the most critical areas along the slope and on crater rim.

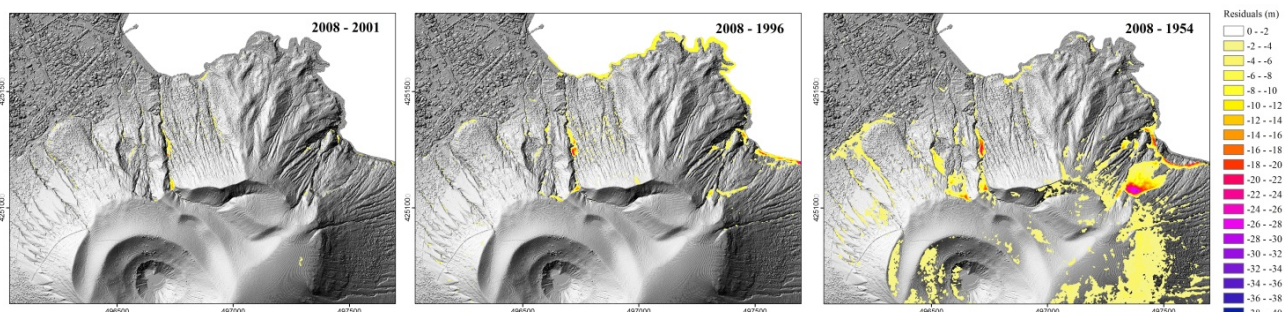


Figure 2. Residual maps for different time steps.

Landslide-susceptibility analysis

A first analysis to evaluate the level of landslide susceptibility was carried out by processing raw Lidar data. The intensity parameters were correlated to slope values to obtain a preliminary zoning of the susceptibility areas. The outcomes of this analysis was combined with the other information (lithology, landslide features, etc) to implement an advanced automatic analysis that provided landslide susceptibility maps based on a GMM method. This GIS based method permits an evaluation of the instability index in a given zone, although it is not capable of predicting the susceptibility to slope movements in terms of absolute probability. The approach was applied to obtain susceptibility maps due to landslide events for the entire Lipari island and La Fossa cone (Vulcano) (Fig. 3), that were validated using an internal quality check and by comparison with the evidence coming from geomorphological and DEM multi-temporal analyses.

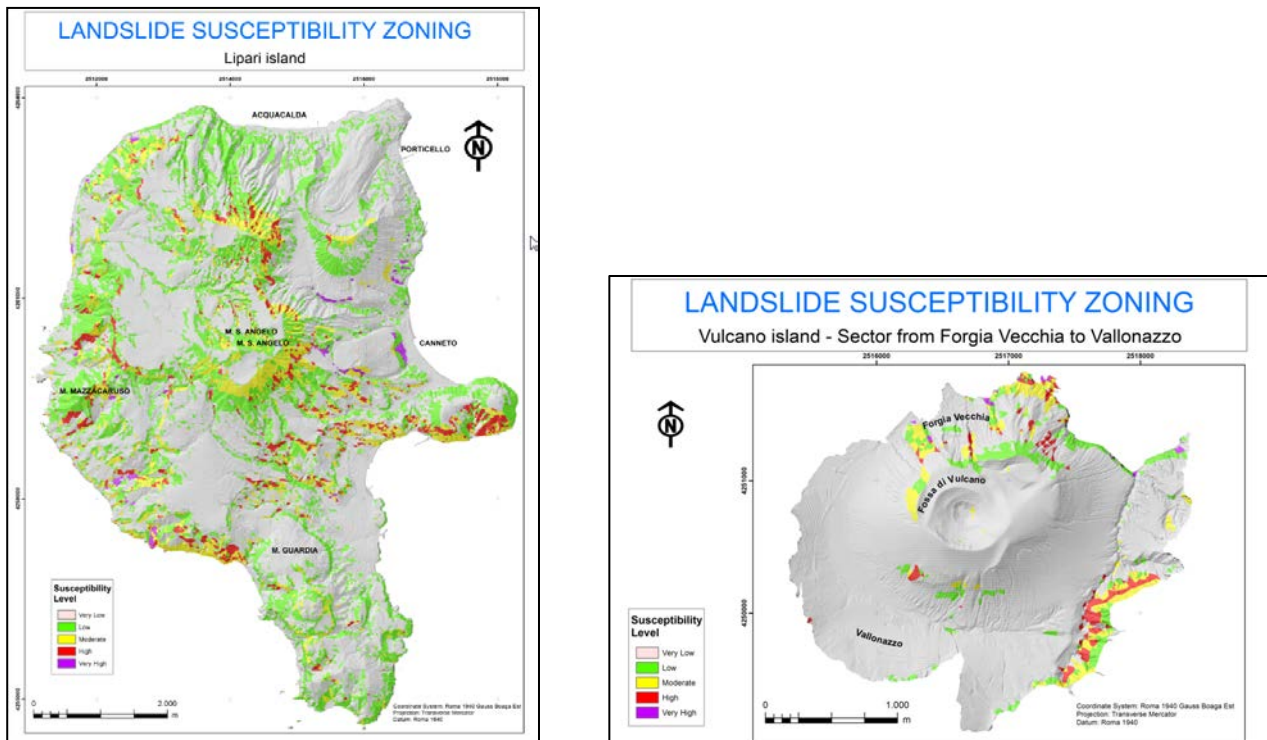


Figure 3. Landslide susceptibility maps for La Fossa (Vulcano) cone and Lipari island.

Stability analysis

A stability analysis was conducted on the La Fossa cone area to evaluate a potential failure of a sector along the NE flank. The Limit Equilibrium analysis using the scientific code CLARA-W developed by O. Hungr (University of British Columbia, Vancouver) was conducted to simulate the slope behavior under gravitative stresses. Evaluation of the slope stability under gravity stress puts in evidence that the slope is near the equilibrium in absence of external actions.

Deliverables

WP 14.Sp1

- Vector and thematic maps in GIS formats (La Fossa cone and selected sites at Lipari): **100%**.
- Report on stability analysis of the potential failures detected at La Fossa cone: **100%**.
- Report on the characteristics of past and active instability phenomena and associated hazard (Vulcano and Lipari): **100%**.

Problems and difficulties

Key publications

- Corsetti M., D'Aranno P.J.V., Marsella M., Salino A., Scifoni S., Sonnessa A. (2013). *Application of Laser Scanning Surveying to rock slopes risk assessment analysis*. The International Archives of the Photogrammetry, Remote Sensing and Spatial Information Sciences, Volume XL-5/W3, 2013 The Role of Geomatics in Hydrogeological Risk, pp.27-32 DOI:10.5194/isprsarchives-XL-5-W3-27-2013.
- Solaro G., Castaldo R., Casu F., De Luca C., Marsella M., Pepe A., Pepe S., Ruch J., Sansosti E., Scifoni S., Tizzani P., Zeni G. (2014) *Insights Into The Dynamics Of Aeolian Volcanic Islands From DInSAR COSMO-SkyMed Observations*. EGU General Assembly 2014, held 27 April - 2 May, 2014 in Vienna, Austria, id.6689.
- Marsella M., D'Aranno P.J.V., Scifoni S., Sonnessa A., Corsetti M. (2015). *Terrestrial laser scanning survey*

Section 2

Scientific Reports of Research Units (RU 7)

in support of unstable slopes analysis: the case of Vulcano Island (Italy). Nat Hazards DOI 10.1007/s11069-015-1729-3. 2015.

Marsella M., Salino A., Scifoni S., Sonnessa A., Tommasi P. (2011). *Stability conditions and evaluation of the runout of a potential landslide at the northern flank of La Fossa active volcano, Italy*. Proceedings of the Second World Landslide Forum, 3-7 October 2011, Rome.

Palenzuela J.A., Marsella M., Nardinocchi C., Pérez J.L, Fernández T., Chacón J., Irigaray C. (2014). *Landslide detection and inventory by integrating LiDAR data in a GIS environment*. Landslides, vol. Ottobre 2014, ISSN: 1612-5118, doi: 10.1007/s10346-014-0534-5.

ANNEX 1

Notes

This annex contains the list of the **deliverables** obtained at the end of the PROJECT V3 “Multi-disciplinary analysis of the relationships between tectonic structures and volcanic activity” (Agreement DPC – INGV 2012).

The products are reported hereinafter as indicated in the proposal for the second year of project activity (see also Annex 2 in this document):

- D1** - Probabilistic time-dependent seismic hazard maps of Mt. Etna, expressed in PGA for different exposure times (30, 20 10 and 5 yrs), including topographic and site effects;
- D2** - Maps and sections of seismicity, ground deformation maps and strain parameters analysis for Etna and Lipari-Vulcano-Gulf of Patti-Peloritani areas;
- D3** - Reports on magma ascent processes in relation with the tectonic setting, petrological and geochemical features at Etna and Vulcano-Lipari-G. di Patti;
- D4** - Flank instability hazard maps due to gravity processes at La Fossa cone (Vulcano) and Lipari.

It must be stressed that many of the reports expected for the deliverables (mainly D3), are already included in the RU reports. Therefore, in this annex we mainly refer to databases, metadata and georeferenced maps.

Files are grouped according the RU responsible for delivery.

Format of files:

- tables and numerical data = Excel, ascii;
- maps = geotiff (WGS84, lat-long o UTM, 300 dpi);
- other documents = *.pdf.

D1

RU 4

WP 3

Time-dependent seismic hazard maps calculated for exposure times of 10, 20, 30, 50 years, and spectral acceleration at 0.0, 0.2, 0.4 and 1.0 seconds (the latter also with site effect corrections); the values of expected PGA (in gal) refer to an exceedance probability $\geq 10\%$.

WP 3_hazard maps (folder)

RU 6

WP 2

Sp2

Map of noise measurements in the south-eastern flank of Mt. Etna

NoisePointGeotiff.tiff/tiffw

List of noise measurement points with coordinates

Noise_points.csv

Monographs of all measurement sites, including location and HVSR (red line is the mean and black dotted lines are the standard deviations), contour of HVSR amplitudes as a function of frequency (x-axis) and azimuth (y-axis), and Fourier spectra for each component

Monographs of sites (folder)

D2

RU 1

WP 5

Instrumental catalogue of earthquakes (Etna)

Catalogue 3D_Etna.xlsx

Epicentral map of earthquakes (Etna)

Epicentral map (folder)

N-S and E-W vertical sections (Etna)

Vertical sections (folder)

Strain distribution maps: 1999-2014 catalogue and only non-eruptive period

Distribution of strain (folder)

WP 10

Database of the $M \geq 3.0$ seismic events located in the Aeolian Archipeago area in the period 1984-2013

1984 2014 seismic catalogue_Eolie.xlsx

Changes in slope distance measured on the Lipari-Vulcano EDM-GPS network in 1975, 1985 and 2013 (for each distance the coordinates and quote of the two benchmarks are reported)

1985-2013 EDM-GPS distances.xls

Levelling and GPS surveys integrated ground deformation map of Vulcano island, from 2008 to 2013

LiVul0813_vel_Liv&GPS.tif

2008-13 Vulcano deformation GIS metadata (folder)

RU 3*WP 9*Sp2**Regional crustal velocity field from CGPS stations**

Eolie_3_new.tif/tif.ovr/tif.aux.xml

Horizontal GPS velocity field for the GPS discrete networks of Lipari-Vulcano

Lipvul_3_039.tif/tif.ovr/tif.aux.xml

horizontal GPS velocity field for the GPS discrete networks of Panarea

Panarea.tif/tif.ovr/tif.aux.xml

Sp3**Maps of multitemporal (2050-2080-2100) marine flooding at Lipari (bay), Marina Lunga, Marina Corta, estimated with different subsidence rate (5.79 and 9 mm/yr), for a stationary eustatic level or maximum and minimum predicted sea level rises for IPCC (2014) and Veermer and Rahmstorf (2009) climatic scenarios**

Baia di Lipari.zip (folder)

Marina Corta_TR-5.79mm.zip (folder)

Marina Corta_TR-9mm.zip (folder)

Marina Lunga_TR-5.79mm.zip (folder)

Marina Lunga_TR-9mm.zip (folder)

High resolution Multibeam bathymetry map of Lipari island (Marina Lunga and Marina Corta bay)

Bathymetry.zip (folder)

RU 6*WP 12***Catalogue of eruptive activity**

Eruzioni_Vulcano.xls

Historical catalogue of earthquakes (Eolie-G. of Patti)

Catalogo_terremoti.xls

Monographs of main earthquakes: 1450, 1490, 1598, 1613, 1667, 1715, 1717, 1726, 1729, 1731, 1732, 1780, 1831, 1841, 1888, 1892, 1893, 1894

Monographs of earthquakes (folder)

Monographs of eruptions with associated seismicity: 1406, 1444, 1626, 1688, 1693, 1727, 1731, 1739, 1771, 1780, 1783, 1786, 1823, 1873-90

Monographs of eruptions (folder)

Sources and iconographic documentation

References.pdf

Table of analysed repertories

Repertory.pdf

Sources of the 1888-1890 Vulcano eruption: Mercalli, Platania, Silvestri

1888-90 sources (folder)

D3**RU 2***WP 6*Sp1**Average of normalized data of total dissolved carbon in monitored sites in the SW and E sectors of Mt. Etna**

Table Ctot.xls

Time trends of the total dissolved carbon in monitored sites and fraction of "volcanic" water

Plot-Ctot.pdf

ANNEX 1

Sp2

Time trend of the He isotopic ratio in P39

He isotopes.pdf

Sp3

Total CO₂ output rate in the Salinelle of Stadio (Paternò)

Table Salinelle.doc

Dispersion map of CO₂ in the Salinelle area

CO₂-map-georeff.tif

WP 13

Sp1

Chemical composition of the fumarole FA (1999-2011)

Tabella_FA.xls

CO₂ concentration in the fumarole FA, temperature in the fumarole F5AT, soil CO₂ emission in Gioiosa Marea (N Sicily), cumulative of strain release+number of events in a sector of the Gulf of Patti

Seismicity, T_fumarole, CO₂.jpg

Sp2

Dispersion map of CO₂ on La Fossa crater

CO₂.tif

Dispersion map of H₂S on La Fossa crater

H₂S.tif

Values of CO₂, H₂S, H₂O and SO₂ fluxes measured at la Fossa in 2015 and comparison with some literature data

Table Vulcano flux.doc

Sp3

Analyses of concentration and isotope composition of He and Ar in some rock samples of Vulcano Island

Vulcano noble gases.docx

He isotopes in olivine and clinopyroxene

Melt inclusions.pdf

RU 3

WP 8

Reduced to magnetic pole anomaly map of Val Calanna

valcalanna_magnetic_anomaly_RP.tif/tif.gi/tif.xml

Magnetic anomaly map of the Etna offshore acquired at an altitude of 300 m

etna_offshore_magnetic_anomaly_map.tif/tif.gi/tif.xml

RU 5

WP 11

Sp1

Database of melt and fluid inclusions of Vulcano and Vulcanello products

Melt_fluid inclusions.xls

Database of whole rocks and mineral compositions of Lipari-Vulcano latites

Whole rocks_mineral compositions.xlsx

Database of compositional and isotopic data on selected latitic samples of Lipari Rocche Rosse

Lipari Rocche Rosse_compositions_isotopes.xlsx

Database of compositional and isotopic data on selected latitic samples of La Fossa and Vulcanello

Vulcano-Vulcanello_compositions_isotopes.xlsx

Sp2**Lipari-Vulcano structural map**

Structural_data_map.pdf

Structural data of Lipari island

Lipari_Structu.xlsx

Structural data of Vulcano island

Vulc_Structu.xlsx

Database of morfostructural and volcano-tectonic data of Vulcano and Lipari islands (with DEM, 5 m-resolution)

Gis Database (folder)

RU 6*WP 7***Location of samples from 1928 and 1981 Etna eruptions**

Sample location.tiff

Database of chemical analyses of mineral phases (olivines, clinopyroxenes) of 1928 lavas

oliv-cpx_1928.xls

Database of chemical analyses of mineral phases (olivines, clinopyroxenes) of 1981 lavas

oliv-cpx_1981.xls

Database of whole rock chemical analyses of 1911-1928-1981 lavas

whole rock_1911-28-81.xls

*WP 8***Map of the tectonic structures in the pre-volcanic basement of Etna (S flank, Ionian offshore)**

structural map_SE Etna.tif/tfw/ovr/aux.xml

D4**RU 1***WP 14*Sp3**Raw data of Ground-Based Radar measurements in the Forgia Vecchia area**

Dati_Raw (folder)

Coherence map (WGS84, lat/long)

COE_map.mli.bmp/kml

Interferogram (WGS84, lat/long)

Int.map..bmp/kml

DEM obtained from interferogram data (UTM 33, 1 m-resolution)

dem_gpri_utm1m_LEE6.tif/tfw/grd

RU 2*WP 14*Sp2**Bathymetry of the slope foot map**

Bathymetry.TIF

Soil temperature contour map of the area above Forgia Vecchia craters

Forgia Vecchia (temperature).TIF

Forgia Vecchia crater rim

Rim.shp

ANNEX 1

Fracture network in the area above Forgia Vecchia craters

Fracture.shp

Soil hydraulic conductivity and hydrothermal alteration facies

Soil.shp

Soil.xlsx

Instability susceptibility (due to hydrothermal fluid circulation) map

Instability-susceptibility.shp

Quantum Gis (release 2.8.1) Project including all the above listed GIS raster and vector layers

CARTO.qgs

RU 7

WP 14

Sp1

Report on the characteristics of past and active instability phenomena and associated hazard

WP14_sp1b_FINAL.pdf

Report on stability analysis of the potential failures detected at La Fossa cone

WP14_sp1c_FINAL.pdf

Landslide susceptibility zoning of Lipari island

Lipari_susceptibility_map.pdf/tif/tfw

Lipari_susceptibility_map_Lidar.pdf/tif/tfw

Lipari_intensity_map./tif/tfw

Landslide susceptibility zoning of Vulcano island – sector from Forgia Vecchia to Vallonazzo

Vulcano_susceptibility_map.pdf/tif/tfw

Vulcano_susceptibility_map_Lidar.pdf/tif/tfw

Vulcano_intensity_map./tif/tfw

ANNEX 2

Description of WPs for the second phase of the project (from approved proposal)

Task 1 – Probabilistic seismic hazard assessment in the eastern flank of Mt. Etna, due to local volcano-tectonic earthquakes

WP 1. Time-dependent occurrence probability for strong earthquakes on the Timpe fault system

The activity will entail revising the average time of recurrence of major earthquakes generated by the Timpe fault system, in light of new data of historical seismology and by using a geological approach based on the estimation of fault activity from geometric-kinematic parameters (dimension, slip-rates etc). The calculation will be performed through a software code produced in the framework of the project INGV-DPC S2. Results will be compared with the estimations obtained in the first year of the project from a purely statistical approach in order to verify the variability of mean occurrence times. The revised values will be used to calculate a more constrained occurrence probability to be applied in the hazard maps (cfr. WP 3).

RUs: 1, 4

2nd year Sp: WP1-sp1) revision of the average time of occurrence of earthquakes along the Timpe faults.

WP 2. Ground-motion prediction equations (PGA from instrumental seismic data)

The estimation of site effects is a crucial aspect of strong ground motion prediction. A versatile method for characterising site conditions is the analysis of ambient noise, in particular the use of the H/V spectral ratios. The project will exploit the abundant material recorded by the continuously operating seismic network of INGV-OE with stations deployed in different geological units. Ambient noise measurements will be exploited for the inversion of the subsurface conditions beneath the seismic stations, allowing a fine tuning of both synthetic simulation as well as the empirical GMPEs. Subsurface models inferred from noise analysis will be compared to results from existing geotechnical information. For selected sites the results obtained from the single station approaches will be compared with those acquired from seismic array analyses.

RUs: 1, 6

2nd year Sp: WP2-sp1) identification of site correction functions for the prediction of PGA.

WP 3. Probabilistic seismic hazard maps

The activity will be dedicated to computing probabilistic time-dependent maps, taking account of effects related to the topography of the steep slopes of the volcano. This analysis is particularly relevant in the case of very shallow events on the PGA attenuation, and the geotechnical characterization of the area. In fact, the estimation of site effects will be introduced (cfr. WP 2) considering the litho-stratigraphic features obtained by integrating a geological model derived from the recent “Geological Map of Etna” and the “Studies of seismic micro-zoning of the eastern flank of Etna”. The maps will be calculated for exposure periods of 30,

ANNEX 2

20, 10 and 5 years, using the source model and the logical tree structure already outlined in the first year of the project.

RUs: 1, 4

2nd year Sp: WP3-sp1) time-dependent probabilistic maps including site-topographic effects, for exposure periods of 30, 20, 10 and 5 years.

Task 2 – Relationships between local tectonic structures and volcanic system at Mt. Etna

WP 4. Coulomb stress transfer

The analysis will be focused on the interaction between faults after the occurrence of an earthquake or an intrusion related to the volcanic activity. The experience of 2002 has shown that the process of stress transfer is a dramatic reality and its consequences must be explored through a FEM (Finite Elements Modeling) approach. Starting from the 3D grid of the faults in the eastern flank of the volcano (the sector most exposed to the destructive effects of local seismicity), historical cases (1865, 1984) of earthquakes triggering other events on nearby faults will be modelled, also in the hypothesis of stress field variations due to dike intrusions. The availability of large datasets of geodetic measurements also enables a comparing simulated ground deformations patterns and observed ones.

RU: 1

2nd year Sp: WP4-sp1) fault interaction case-histories in the Timpe fault system.

WP 5. Dynamics and kinematics of the eastern flank from seismological and ground deformation analyses

The activity will be focused on the seismogenic structures of the lower eastern flank of Etna (Timpe system), by analysing the space-time distribution of the seismic strain release and improving the available dataset of fault plane solutions. Results will be compared with those of well-known nearby areas (e.g. Zafferana). The characterisation of the seismic source will also be carried out through the seismic moment tensor method. Moreover, an analysis of the relationship between the seismicity and the main recharging phases of the volcano will be carried out. The analyses integrating seismological and geodetic data will be performed at the scale of individual fault (S. Leonardello f.) as well as the whole eastern flank. In this latter case, the analysis will be carried out by comparing the scalar geodetic, geologic and seismic moment in order to estimate the seismic efficiency of the area. The obtained parameters will be used to improve the seismotectonic model.

RUs: 1, 4

2nd year Sp: WP5-sp1) space-time distribution of seismicity and strain release, also in relation with the main recharging phases of the volcano; WP5-sp2) earthquake features through the seismic moment tensor; WP5-sp3) comparison between the scalar geodetic, geologic and seismic moment.

WP 6. Crustal structures and fluid circulation

The analysis of the time record of geochemical data on the Etnean aquifer has indicated that changes can be attributed to variations in fluid circulation linked to pressure gradients (which cause fluid movement) which, in turn, follow trends of seismic and geodetic strains. To gather further information and gain a deeper understanding of the relationship between geodetic/seismic strains and variations in water chemistry, we apply the analysis to the geochemical monitoring in the neighbourhood of S. Venerina and Zafferana, measuring the water table head, temperature and gas pressure. Furthermore, the pressurization of gases which can be ascribed to variations of the stress field or the increased input of magmatic-hydrothermal gas will be studied at the mud volcanoes of Paternò by a new sampling technique.

RU: 2

2nd year Sp: WP6-sp1) assessment of fluid pressure in relation with the tectonic stress and the magmatic activity, based on time series of geochemical data; WP6-sp2) detection of phases of increased magma degassing, according to chemical and isotopic data (helium isotopes) in peripheral gas manifestations; WP6-sp3) mapping of the gas emission rates in the salinelle of Paternò and their temporal evolution.

WP 7. Geochemistry of magmas and feeding structures

The activity will focus on the 1928 and 1981 eruptions, both characterised by relevant volcanic hazard in terms of lava-flow fields and fast eruptive dynamics. Products linked to these events present syn-eruptive compositional variations allowing verifying whether these changes are dependent on the presence of originally distinct magmas or, as an alternative, there is also a role of tectonics in modifying the magma ascent process. The investigations will include isotopic analyses, petrographic and textural analyses of the sampled rocks and composition of major elements in minerals in order to detect magma differentiation processes (crystal fractionation, magma mixing, etc.).

RUs: 1, 6

2nd year Sp: WP7-sp1) isotopic analyses, analyses of textures and compositions of crystalline phases; WP7-sp2) pre- and syn-eruptive magma differentiation models and relationship with volcanological evolution and syn-eruptive tectonics.

WP 8. Tectonic setting of the sedimentary basement

The activity will focus on some key areas of the volcano-tectonic system of Etna, following two methodological approaches. The interpretation of the Etna magnetic anomaly map obtained in the first year, will be implemented by a detailed study of the Val Calanna system, an inferred dike swarm of an outcropping sub-volcanic body. In order to constrain the model magnetic parameters of the outcrops in this area will also be measured by means of a dedicated campaign. Moreover, a detailed analysis of off-shore dataset will be made in order to delineate the main structural and geomorphological elements in the Ionian Sea, and to correlate them with the Timpe fault system. The same off-shore area will also be investigated by high-resolution seismic profiles (Sparker and Chirp) recorded along the continental shelf between Capo Mulini and the Simeto River mouth, in order to identify in the sea-bottom the shallower portions of the Misterbianco-Catania anticline recognized in the first year. The final aim is to verify if the tectonic processes at the front of the chain may determine the growth of this fold system, or if it is partially related to volcano dynamics.

RUs: 1, 3, 6

2nd year Sp: WP8-sp1) magnetic modelling of the Val Calanna area (RU 3); WP8-sp2) magnetic modelling of the off-shore coastal sector (RU 3); WP8-sp3) seismic profiles in the offshore south-east of Etna (RU 6); WP8-sp4) relationships between on- and offshore structures and definition of deformation processes.

Task 3 - Relationships between regional tectonic structures and the Vulcano-Lipari system

WP 9. Deformation of the Lipari-Vulcano-Gulf of Patti system and implications on coastal hazard

The deformation patterns will be characterized by analysing the possible interactions between the volcano-tectonic systems of Panarea-Lipari-Vulcano and the Aeolian-Tindari-Letojanni line. The areal distribution of the deformation will be improved by a new GPS campaign (with RU 1) on the discrete network of the Mts. Nebrodi-Peloritani, not investigated since 2006. Two new GPS benchmarks to be installed in the northern part of Lipari will also be used for this purpose. The crustal velocity field will be updated together with the strain maps for the Aeolian islands, highlighting areas with minimum and maximum deformations at different spatial scales. We will also focus on the vertical component of deformation to quantify subsidence at regional and local scales. The extension of the expected marine ingression at Lipari for the year 2100 (Marina Corta and Marina Lunga) will be mapped on a new DTM (with RU 7), calibrated with GCPs measured by GPS. Available aerial photogrammetric data will be also improved through laser scanner and UAV aerial photogrammetry surveys.

RUs: 3, 1, 7

2nd year Sp: WP9-sp1) GPS surveys of the Mts. Nebrodi-Peloritani network and Lipari; WP9-sp2) Updated GPS crustal velocity and strain fields for the Aeolian islands and the Lipari-Vulcano-Gulf of Patti system; WP9-sp3) predictive map of marine ingression for 2100 for Lipari Marina Grande and Marina Corta, based on models integrating historical data, DTM and photogrammetric data.

WP 10. Definition of the time-space dynamics of the Lipari-Vulcano tectonic system.

The analysis will consider ground deformation (EDM, GPS, precise leveling, tilt) and seismic data collected in the 1974-2013 period in order to analyze changes that have characterized the different sectors of the Lipari-Vulcano system during the last 40 years. Also taking account of the previous geochemical, structural and geophysical results, the main anomalies recorded will be identified, discerning changes linked to geothermal system from magmatic and/or tectonic dynamics sources. These studies aim to give a full geophysical overview of the volcanic-structural system and its link with regional scale dynamics and volcanic processes.

RU: 1

2nd year Sp: WP10-sp1) definition of areas with common dynamics; WP10-sp2) ground deformation maps over different time windows.

WP 11. Relationships between tectonic features and volcanic activity in the southern sector of the Aeolian Arc

The activity will focus on the relationships between the geometry of feeding system and ascent dynamics of magmas erupted during the historical activity of Lipari and Vulcano. Processes the magma has been subject to during its upraise from 20 km of depth (differentiation, mixing, storage and ascent dynamics) will be investigated in order to define ascent rates models and storage timescales. The historic activity of La Fossa volcanic system will be studied by means of state of the art analytical techniques on phenocrysts that are able to record the chemical and physical changes of magma during its ascent into the feeding system, and their hosted melt inclusions (major and trace elements and volatile components). Sr-isotope data obtained through microdrilling will be used to constrain the origin of mafic magmas erupted during post-mediaval activity of La Fossa while models of intra-cristalline diffusion will be applied on plagioclase crystals to reconstruct the timescales of magma residence in the plumbing system and its ascent rate. The interactions between the magmatic reservoirs of the Lipari-Vulcano feeding system and the main regional and local tensile tectonic features will be analysed exploiting new radiometric ages on the Mt. Saraceno products (Vulcano) and the rhyolitic domes of the southern part of Lipari. The results of this analysis will allow defining the timing of fault activity.

RU: 5

2nd year Sp: WP11-sp1) definition of the Lipari-Vulcano feeding system (geometry, physical and chemical conditions, timescales of magma ascent and storage); WP11-sp2) characterization of the Lipari-Vulcano active fault systems (regional and local stresses, dating, slip-rates).

WP 12. Historical analysis on the space-time relationships between regional earthquakes in the Gulf of Patti-northern Sicily and seismic-volcanic phenomena at Vulcano

The analysis aims at reconstructing the chronological sequence of volcanic and seismic phenomena in the area from the 16th to 20th centuries. by using the historical research approach. Following the results obtained in the first year, the study will focus on poorly known local and regional earthquakes of medium-low energy ($4.2 < M < 5.0$) and seismic sequences, which may give a better understanding of the relationship between seismicity and eruptive activity. The integrated database including information on seismic and volcanic events will be completed. The earthquake source parameters and possible seismic patterns and volcanic phases of activity will also be defined and characterized.

RU: 6

2nd year Sp: WP12-sp1) Short monographs of volcanic events and the main earthquakes or sequences (G. Patti-Vulcano-Lipari); WP12-sp2) final release of the database on earthquakes and volcanic activity.

WP 13. Crustal structures and fluid circulation

The analysis of $M > 2$ seismicity occurring in a sector of the Gulf of Patti and the record of soil CO₂ emissions close to Gioiosa Marea has shown, for the period (2010-2012), that the strain release and soil CO₂ emissions have synchronous variations. We plan to extend the study to the geochemical anomalies observed in temperature and gas composition in the fumarolic area of La Fossa in Vulcano. Furthermore, we will set up methods for the multi-parametric mapping of the fumarolic field (gas chemistry, emission rates, temperature) to detect the areas mostly affected by the magmatic vapour and those with the higher emission rates, which are not necessarily overlapping, due to the uneven shallow permeability. Finally, we will also perform the analysis of isotope composition of helium in fluid inclusions in the products of various eruptions of La

ANNEX 2

Fossa, with the aim of studying the evolution of the magmatism and characterising the magma actually feeding La Fossa.

RU: 2

2nd year Sp: WP13-sp1) steaming ground, mofettes, along the Aeolian-Tindari-Letojanni fault system and assessment of geochemical anomalies related to seismic activity and/or ground deformation; WP13-sp2) mapping of concentrations and fluxes of CO₂, H₂S and HCl in the fumarolic field of La Fossa in Vulcano; WP13-sp3) helium isotope analysis in melt inclusions and assessment of the evolution of the magma feeding La Fossa cone.

Task 4 – Hazard due to gravity flank instability at Vulcano and Lipari

WP 14. Slope instability hazard maps

The main activity aims at analysing instability phenomena (shallow or deep-seated) that may affect La Fossa cone at Vulcano, in response to volcanic activity or other triggering processes. Multidisciplinary approaches will be applied to extend and refine the investigations carried out in the first year of the project. The collection and processing of detailed topographical data (through proximal-sensing techniques based on digital camera and laser scanning sensors), historical photogrammetric datasets (back to the mid-1900s), DInSAR results, analyses of the past instability phenomena, geological surveying and radar measurements will allow to better constrain the geometry of potential detachment areas and geomorphic modification in time. In particular, the susceptibility to flank failures induced by hydrothermal fluids in the sector between the Forgia Vecchia craters and the 1988 landslide, will be investigated by mapping the alteration facies, temperature, soil permeability and moisture content, bathymetry of the slope foot and m-scale fracture network. Additional studies will be conducted in the SE sector of Vulcano and Lipari to verify and assess the deformation patterns previously evidenced by the DTM and DInSAR analyses. This will allow to classify the areas potentially affected by debris avalanches/flows and rock falls. The results from different methodologies will be integrated in order to estimate the slope stability conditions and provide hazard maps.

RUs: 1, 2, 7

2nd year Sp: WP14-sp1) Vector and thematic maps in GIS formats (La Fossa cone and selected sites at Lipari); report on stability analysis of the potential failures detected at La Fossa cone, and on the characteristics of past and active instability phenomena and associated hazard (Vulcano and Lipari); WP14-sp2) Maps of the hydrothermal alteration facies in the sector between Forgia Vecchia and the 1988 landslide (Vulcano island), soil permeability, moisture content and fracture network; bathymetry of the slope foot map; WP14-sp3) Map of the slope movements and weak points of rock mass in the Forgia Vecchia area from ground-based radar and thermal infrared measurements.

Quaderni di Geofisica

ISSN 1590-2595

<http://istituto.ingv.it/l-ingv/produzione-scientifica/quaderni-di-geofisica/>

I Quaderni di Geofisica coprono tutti i campi disciplinari sviluppati all'interno dell'INGV, dando particolare risalto alla pubblicazione di dati, misure, osservazioni e loro elaborazioni anche preliminari, che per tipologia e dettaglio necessitano di una rapida diffusione nella comunità scientifica nazionale ed internazionale. La pubblicazione on-line fornisce accesso immediato a tutti i possibili utenti. L'Editorial Board multidisciplinare garantisce i requisiti di qualità per la pubblicazione dei contributi.

Rapporti tecnici INGV

ISSN 2039-7941

<http://istituto.ingv.it/l-ingv/produzione-scientifica/rapporti-tecnici-ingv/>

I Rapporti Tecnici INGV pubblicano contributi, sia in italiano che in inglese, di tipo tecnologico e di rilevante interesse tecnico-scientifico per gli ambiti disciplinari propri dell'INGV. La collana Rapporti Tecnici INGV pubblica esclusivamente on-line per garantire agli autori rapidità di diffusione e agli utenti accesso immediato ai dati pubblicati. L'Editorial Board multidisciplinare garantisce i requisiti di qualità per la pubblicazione dei contributi.

Miscellanea INGV

ISSN 2039-6651

<http://istituto.ingv.it/l-ingv/produzione-scientifica/miscellanea-ingv/>

La collana Miscellanea INGV nasce con l'intento di favorire la pubblicazione di contributi scientifici riguardanti le attività svolte dall'INGV (sismologia, vulcanologia, geologia, geomagnetismo, geochimica, aeronomia e innovazione tecnologica). In particolare, la collana Miscellanea INGV raccoglie reports di progetti scientifici, proceedings di convegni, manuali, monografie di rilevante interesse, raccolte di articoli ecc..

Coordinamento editoriale e impaginazione

Centro Editoriale Nazionale | INGV

Progetto grafico e redazionale

Laboratorio Grafica e Immagini | INGV Roma

© 2016 INGV Istituto Nazionale di Geofisica e Vulcanologia

Via di Vigna Murata, 605

00143 Roma

Tel. +39 06518601 Fax +39 065041181

<http://www.ingv.it>



Istituto Nazionale di Geofisica e Vulcanologia